VNIVERSITAT DE VALÈNCIA

Search for new physics in single-top-quark production with the ATLAS detector at the LHC

Tesi Doctoral
Programa de Doctorat en Física

Laura Barranco Navarro

IFIC (Universitat de València - CSIC)
Departament de Física Atòmica, Molecular i Nuclear

Sota la supervisió de

Dra. Mª José Costa Mezquita
Dr. José Enrique García Navarro

València, Setembre 2018

La Dra. **María José Costa Mezquita**, científica titular del Consell Superior d'Investigacions Científiques i el Dr. **José Enrique García Navarro**, científic titular del Consell Superior d'Investigacions Científiques

Certifiquen:

Que la present memòria "Search for new physics in single-top-quark production with the ATLAS detector at the LHC" ha sigut realitzada sota la seua direcció en l'Institut de Física Corpúscular, centre mixt de la Universitat de València i del CSIC, per **Laura Barranco Navarro** i constitueix la seva Tesi per optar al grau de Doctora en Física per la Universitat de València.

I per a que així conste, en compliment de la legislació vigent, presenten en el departament de Física Atòmica, Molecular i Nuclear de la Universitat de València la referida Tesi Doctoral, i firmen el present certificat.

València, a 10 de setembre de 2018

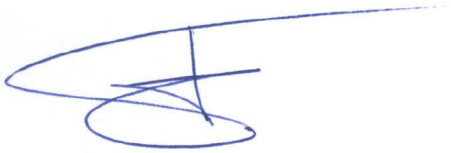

María José Costa Mezquita

José Enrique García Navarro

A totes les persones que m'heu acompanyat al llarg d'aquest camí.
En especial a Pablo, Antonio i Esther.

Acknowledgements

There's a lot of people who directly or indirectly made it possible for me to reach this important milestone in my career. A huge thanks to all of you!

Four years ago started my adventure in high energy physics research. My success couldn't have been possible without the dedication and guidance of my supervisors, María José and José Enrique. I always felt supported and respected while working with you, and it is respect and admiration what I developed for you. From María I've learned to be thorough with my work and to always be demanding with my own results. José is the one who's allways there to help students to solve any technical difficulty and my coding skills have vastly improved thanks to him. I'm deeply thankful for all what I've learned with you two. I can't either forget the guidance and patience from Salva in my first steps in ATLAS when I hardly knew what all this was about. Finally, I cannot finish this paragraph without mentioning Carmen, who gave me the opportunity to join the group.

I would like to thank the IFIC for providing the institutional support to complete my thesis. I acknowledge the FPI contract as well, for the financial support during these years. Thanks to the ATLAS Collaboration, in particular to the analyses teams who made possible the completion of the two analyses that lead to this manuscript. Thanks also to the CERN laboratory for creating a collaborative and respectful environment to do science.

A key ingredient of IFIC is its students. I will never thank Javi enough for the first assistance with alignment and to Sebas, for accompanying me in the transition to his analysis that also became mine. Working with other students makes working less heavy and more fun. It has been lovely to work with Oscar, Galo, Pablo, Florencia and Jesús. Although we haven't work together, sharing lunches, dinners and beers with the "Escuadrón IFIC" has made the last years more enjoyable. Talking about lunch, I'll miss the lively discussions about everything with the "Escape Room" group, Marija, Javi, Antonio and Pablo. I hope that anywhere we go in the future, we continue meeting up and escaping.

I want to thank Carlos and Mercedes for the warmest welcome during my first stay at CERN. Thanks for introducing me to people and make me feel comfortable there. Those cold months in Geneva were nicer also thanks to Costanza, Alex, Tim, Theo and Filip. Thanks for the coziest evenings with wonderful homemade dinner. Also, with Oscar, Sergi and Florencia, I discovered that Geneva is much more nice in summer. Thanks for the amazing experiences we managed to find time for.

I keep very good memories from my years during the physics degree. Courses and exams were tough, but everything was easier when shared with my classmates. The huge amount of hours at the library and at the labs can only make me smile now. Special thanks go to my classmates who also became good frieds, Javi and Esther.

One of the greatest experiences in my life was my year abroad as an Erasmus student at the University of Copenhagen. I'm deeply thankful for having been given this opportunity of personal growing. Among the tons of people who made me feel *hygge* in such a cold city, I keep a very warm place for my dear friends Frederika and Sarah.

I cannot forget those outside of physics who have always been there. Thanks to my family for being always caring and supportive. To my parents, Imma and Miguel, for being the best example for me to follow. Thanks for always encouraging me to pursue my dreams while keeping my feet on Earth. To my sister, Bibi, even though we are far, it never feels like that. There is a very special place here for my grandma, my *iaia*, who could hardly pronouce physics but who was always so proud of me.

My family has increased in past years. Thanks to Fernando, Isabel and Fernando, for making me feel part of your family right away.

Music has been a key ingredient to keep me sane over the past years. The orchestra has seen me grow and there's no space enough in this manuscript to name all the people who have made it worth it to get up early every single Saturday since I was 12. I need to mention, though, my two *horchata in the veins* violin mates, Sofía and Elvira, who have become very dear friends.

Thanks to my flatmates, Antonio and Pablo. The past years, specially the writting period, have been more bearable thanks to you. Thanks for your friendship, for all the travels, the hiking trips, all your support in the toughest moments, the cooking and the endless hours of board games. And here I also need to include my very best friend, Esther. Thanks four your friendship, your understanding and support the past years. Because it doesn't matter how far we are, or what little free time we have, we always find a spot to talk.

Last but no least, I can only say thanks to my partner, Pablo. Thanks for your smiles, for always looking at the bright side of things. Thanks for always being there, in the easy and the difficult times. Thanks for your love, support and encouragement to always get the best of me out. We started this adventure together and so we close it. A new chapter starts now, and we'll write it four-handed.

Contents

Preface

The work documented in this thesis encompasses a wide period of the LHC operation, giving rise to two physics analysis performed on data collected by the ATLAS detector in the Run-1 and Run-2 of the LHC. The LHC is nowadays the most powerful particle accelerator designed to prove the Standard Model of particle physics and to search for new physics.

The Standard Model of particle physics, developed in the 1960's and finalized in the 1970's, has been tested up to the TeV scale and has given encouraging results in an extensive variety of phenomena. Not only does it provide a successful explanation for a range of observations but also predictions which have later been observed. Such predictions include the existence of the $W^{\pm}$ and Z bosons, the top quark and the Higgs boson, whose discovery at the LHC was one of the major milestones of the accelerator. In spite of its great success, it is believed that there must be a more general theory underlying the Standard Model which sheds light to unanswered questions such as the existence of Dark Matter and Dark Energy, the neutrino masses or the matter-antimatter asymmetry of the Universe.

Among all the elementary particles that conform the Standard Model of particle physics, the top quark deserves special attention given its unique properties. The importance of the top quark lies on its large mass, which translates in a very short lifetime, therefore rapidly decaying through EW interactions before it has time to hadronize. As a result, it offers the possibility of studying its properties through its decay products. Another consequence of its large mass is that it is the only quark with a Yukawa coupling to the Higgs boson of the order of one; an accurate

knowledge of its properties can therefore provide key information on fundamental interactions at the electroweak symmetry-breaking scale and beyond.

This thesis explores two different approaches in the search for new physics beyond the Standard Model in the top sector. On the one hand, the presence of new physics can be inferred through the precision measurements of specific properties of the elementary particles. Deviations from the Standard Model predictions would point to the presence of new physics. This is the strategy followed by the first analysis presented in this document and published in [1]. In this work, the Wtb vertex is proved through the measurement of asymmetries in the angular distributions of the decay products of polarized top quarks produced in the t-channel via electroweak interaction. Differences from the Standard Model predictions would imply anomalous couplings in the Wtb Lagrangian. Measurements with polarized top quark decays allow to set limits in the complex phase of the couplings, being therefore sensitive to CP violation effects in the top quark decays. This analysis is carried out using data from the LHC Run-1 period taken during 2012 at a center of mass energy of 8 TeV and collected by the ATLAS detector, resulting in a total integrated luminosity of 20.2 fb^{-1}.

A different approach consists on direct searches for new physics processes. This is the action plan taken in the second analysis reported in this thesis, which uses data from the early Run-2 period gathered in 2015 and 2016 at a center of mass energy of 13 TeV and collected by the ATLAS detector, resulting in a total integrated luminosity of 36.1 fb^{-1}. This dissertation presents the search for events with final states constituted by one top quark and missing transverse momentum known as mono-top, which can be interpreted in the context of generic models of Dark Matter production. In the event of not observing an excess of data, these kind of searches are used to set upper limits on the corresponding production cross-sections.

The quality of the physics analyses performed with data collected by the ATLAS experiment relies on the accurate performance and calibration of the detector. This thesis also presents some contributions to the alignment of the inner detector done during the Long Shutdown 1, the period during the end of the Run-1 and the beginning of the Run-2 in which the detector was upgraded in preparation for the new phase of operation. Precisely, this work was done during the cosmic

ray campaign prior to the first Run-2 collisions and is documented in [2] and [3]. During this period, cosmic-rays data were used to study the alignment of the new installed pixel IBL layer. In addition, the alignment process was implemented in the calibration loop and a web display was created to monitor the output from the alignment.

1 Theoretical framework

The Standard Model (SM) of particle physics is the theoretical framework that so far describes best the subatomic world. Since its development in the 1960's it has proved to be very successful in describing experimental observation. Moreover, it has had the ability to predict new phenomena which has later been confirmed by experiments, the last one being the observation of the Higgs boson at the proton-proton Large Hadron Collider (LHC) in July 2012 [4,5]. The present chapter gives a basic introduction to the building blocks of the SM. This theory can not however be final, as it will be seen later in the chapter. The work of this thesis is devoted to the search of new physics using events involving the top quark. This chapter also describes the main production mechanisms of this particle in hadron colliders and its decay modes. New physics searches can be done with two different strategies, and both are used in this thesis. A first class of studies involve the searches of new states through decay processes involving top quarks. This is the basis of the search of mono-top final states in the context of Dark Matter (DM). Alternatively, if the new states are too heavy to be directly produced, they can still be inferred from deviations from the SM predictions in the strength of the top-quark couplings to other SM particles. This requires accurate predictions and precision measurements which need to be accommodated in the framework of an effective field theory (EFT). The Wtb vertex is studied in this context.

1.1 The Standard Model of particle physics

The SM of particle physics is a quantum field theory which describes the interactions between the elementary constituents of matter through fundamental forces. It is one of the most successful scientific theories developed so far, with excellent precision and predictive power. The SM provides a unified picture where the interactions among the constituents of matter (fermions) are described through the exchange of 'force carrier' particles (bosons).

The four fundamental forces are the electromagnetic interaction, described by Quantum Electro-Dynamics (QED); the strong interaction, described by Quantum Chromodynamics (QCD); the weak interaction and the gravitational interaction. According to the SM, all of the fundamental interactions derive from one general principle, the requirement of local invariance (the invariance of the Lagrangian under a local gauge transformation of a given symmetry group). The weak and the electromagnetic interactions are unified in the Electroweak Theory (EW), proposed by Glashow, Weinberg and Salam [6–8], via the gauge group $SU(2)_L \times U(1)_Y$. The combination of QCD, described via the $SU(3)_C$ with EW theory forms the SM of particle interactions. Gravity is not described by the SM and its implementation is one of the major goals in the field of particle physics.

The mediator particles are spin-1 [1] particles obeying Bose-Einstein statistics. There exist four types of bosonic particles associated to each of the fundamental forces described by the SM. The photon (γ) mediates the interactions between electrically charged particles (QED interactions). The weak interaction is mediated via $W^{\pm}$ (charged weak interactions) and Z (neutral weak interactions) bosons. Finally, eight gluons (g) mediate the strong interaction between colored particles (quarks and gluons). Table 1.1 summarizes the classification of bosons in the SM.

The building blocks of matter, fermions, are spin-$1/2$ particles obeying Fermi-Dirac statistics. They are classified in quarks and leptons and subdivided in three families or generations. Quarks and leptons of different generations differ in their masses. The lightest and most stable particles make up the first generation

[1] Bosons are particles with integer spin. If their spin is 1, the are called vector bosons, whereas they are know as scalar bosons when their spin is 0.

Boson	Interaction	Mass	Electric charge	Color
γ	Electromagnetic	$< 1 \times 10^{-18}$ eV	0	-
$W^{\pm}$	Weak	80.385 ± 0.015 GeV	± 1	-
Z	Weak	91.1876 ± 0.0021 GeV	0	-
g	Strong	0	0	8 combinations

Table 1.1: Overview of the gauge bosons of the SM, given with their properties and associated interactions [9].

and form all stable matter in the universe, whereas the heavier and less stable particles belong to the second and third generations.

Each generation of leptons consists on a charged particle (electron, muon and tau) accompanied by a neutral and massless neutrino. Charged leptons are subject to the weak and electromagnetic interactions while the neutrinos only interact weakly. In the case of quarks, each generation contains a positively charged quark ($+\frac{2}{3}$) and a negatively charged one ($-\frac{1}{3}$). Moreover, as in the case of gluons, all quarks carry color charge (red, green, blue). Quarks can interact via strong, weak and electromagnetic interactions. Table 1.2 summarizes the classification, masses and electric charge of the three families of fermions in the SM. Apart from the particles listed in this table, each fermion counts with an antifermion with its exact same properties but with opposite quantum numbers.

All in all, the SM is conformed by at least 31 elementary particles, if we add the Higgs boson, which will be introduced in the following and which discovery at the LHC in 2012 [4, 5] entailed one of the biggest successes of the SM.

1.1.1 The electroweak interaction

The EW theory combines the $U(1)_Y$ electromagnetic interactions with the $SU(2)_L$ weak interactions. Y refers to the weak hypercharge ($Y/2 = Q + I_3$, with I_3 the third component of the weak isospin) and L stands for the chirality [2] of the weak interactions.

[2] Something is chiral if it is distinguishable from its mirror image; that is, it cannot be superposed into it. Human hands are an example of chiral objects

	Generation	Name	Symbol	Mass	Electric charge	Color
Leptons	1^{st}	Electron	e	$0.5109989461 \pm 0.0000000031$ MeV	-1	-
		Electron neutrino	ν_e	< 2 eV	0	-
	2^{nd}	Muon	μ	$105.6583745 \pm 0.0000024$ MeV	-1	-
		Muon electron	ν_μ	< 2 eV	0	-
	3^{rd}	Tau	τ	1776.86 ± 0.12 MeV	-1	-
		Tau electron	ν_τ	< 2 eV	0	-
Quarks	1^{st}	Up	u	$2.2^{+0.6}_{-0.4}$ MeV	$+2/3$	rgb
		Down	d	$4.7^{+0.5}_{-0.4}$ MeV	$-1/3$	rgb
	2^{nd}	Strange	s	96^{+8}_{-4} MeV	$+2/3$	rgb
		Charm	c	1.28 ± 0.03 GeV	$-1/3$	rgb
	3^{rd}	Top	t	173.1 ± 0.6 GeV	$+2/3$	rgb
		Bottom	b	$4.18^{+0.04}_{-0.03}$ GeV	$-1/3$	rgb

Table 1.2: Summary table of the SM fermion families with their mass and electric charge [9].

The allowed vertexes by electromagnetic interactions are the γ-lepton-antilepton and the γ-quark-antiquark depicted in Figure 1.1. The allowed vertexes by electroweak interactions are depicted in Figure 1.2 and include the charged $W^{\pm}$ boson going to a pair of charged lepton and its corresponding neutrino or to a quark-antiquark pair with quarks from the same family (flavor changing weak currents are not forbidden, but have in general low probabilities of occur). The neutral currents, mediated via the Z boson, include fermion-antifermion pairs (charged lepton-antilepton, neutrino-antineutrino, quark-antiquark). Flavor changing neutral currents (FCNC), such as $Z \rightarrow d\bar{s}$, are not allowed. Triple and four-gauge vertexes are also allowed ($Z/\gamma \rightarrow W^+W^-$, $W^+W^- \rightarrow W^+W^-$, $ZZ/\gamma\gamma \rightarrow W^+W^-$ and $\rightarrow W^+W^-$).

Charged-flavor-changing-weak decays are possible since the eigenstates that interact through the weak interaction, known as weak eigenstates (d',s' and b'), are different from the physically observed mass eigenstates (d,s,b). These states are related by the Cabbibo-Kobayashi-Maskawa (CKM) matrix [10,11] as

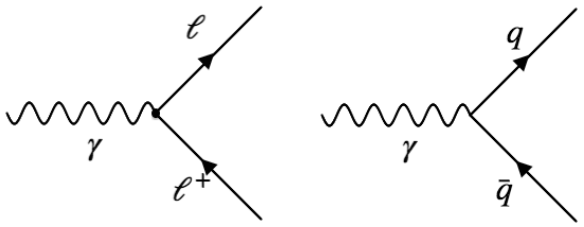

Figure 1.1: The two vertexes of electromagnetic interactions: γ - lepton - antilepton (*left*) and the γ - quark - antiquark (*right*).

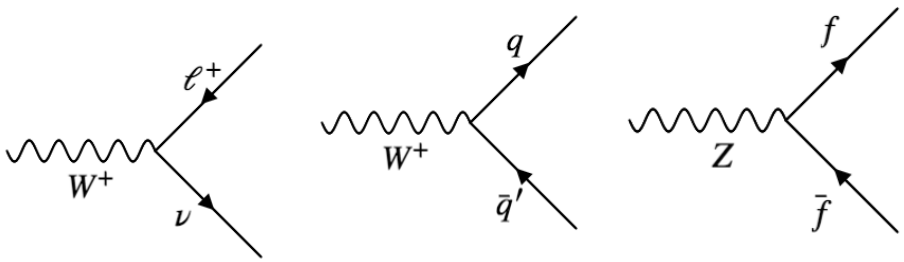

Figure 1.2: The three vertexes of weak interactions involving fermions: charged $W^{\pm}$ boson going to a pair of charged lepton and its corresponding neutrino (*left*) or to a quark-antiquark pair with quarks from the same family (*center*) and neutral currents mediated via the Z boson, fermion-antifermion pairs (charged lepton-antilepton, neutrino-antineutrino, quark-antiquark).

Matrix Element	Global fit value
$\lvert V_{ud}\rvert$	$0.97434^{+0.00011}_{-0.00012}$
$\lvert V_{us}\rvert$	0.22506 ± 0.00050
$\lvert V_{ub}\rvert$	0.00357 ± 0.00015
$\lvert V_{cd}\rvert$	0.22492 ± 0.00050
$\lvert V_{cs}\rvert$	0.97351 ± 0.00013
$\lvert V_{cb}\rvert$	0.0411 ± 0.0013
$\lvert V_{td}\rvert$	$0.00875^{+0.00032}_{-0.00033}$
$\lvert V_{ts}\rvert$	0.0403 ± 0.0013
$\lvert V_{tb}\rvert$	0.99915 ± 0.00005

Table 1.3: Global fit values of the CKM matrix [9].

$$\begin{pmatrix} d' \\ s' \\ b' \end{pmatrix} = \begin{pmatrix} V_{ud} & V_{us} & V_{ub} \\ V_{cd} & V_{cs} & V_{cb} \\ V_{td} & V_{ts} & V_{tb} \end{pmatrix} \begin{pmatrix} d \\ s \\ b \end{pmatrix}. \tag{1.1}$$

In general, the coupling of two quarks a and b to a W boson is proportional to the corresponding CKM matrix element V_{ab}. The values of the matrix elements are determined experimentally, and the most recent values of the global fit provided by the PDG [9] are listed in Table 1.3. As seen from this table, diagonal elements have by far the largest values, so transitions of quarks within a generation are favoured over transitions into quarks of others. For example, the top quark can decay into any of the three down-type quarks, but $|V_{tb}^2| = 99.83\%$ of the times will do it to a b quark.

The CKM matrix can be parametrized in terms of three angles (θ_{12}, θ_{13}, θ_{23}) and one complex phase, δ_{13}. The appearance of this phase results in the violation of the charge and parity symmetries of the weak interactions (CP-symmetry). With the notation $c_{ij} = \cos\theta_{ij}$ and $s_{ij} = \sin\theta_{ij}$, the CKM matrix is written as

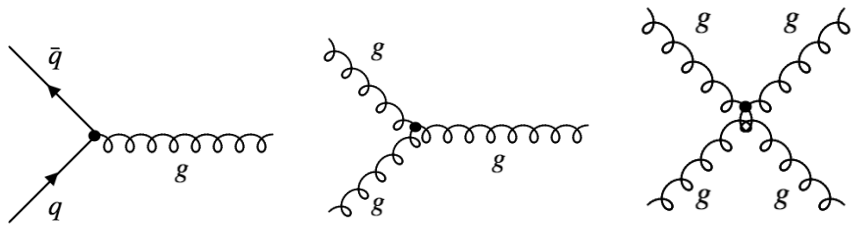

Figure 1.3: The three vertexes of QCD: quark-antiquark-gluon (*left*), three-gluon (*center*) and four-gluon (*right*).

$$V_{CKM} = \begin{pmatrix} c_{12}c_{13} & s_{12}c_{13} & s_{13}e^{-i\delta_{13}} \\ -s_{12}c_{23} - c_{12}s_{23}s_{13}e^{\delta_{13}} & c_{12}c_{23} - s_{12}s_{23}s_{13}e^{\delta_{13}} & s_{23}c_{13} \\ s_{12}s_{23} - c_{12}c_{23}s_{13}e^{\delta_{13}} & c_{12}s_{23} - s_{12}c_{23}s_{13}e^{\delta_{13}} & c_{23}c_{13} \end{pmatrix}. \quad (1.2)$$

1.1.2 Quantum chromodynamics

QCD describes the strong interactions in the SM, being $SU(3)_C$ the underlying symmetry. There are three possible vertexes in QCD: quark-antiquark-gluon ($q\bar{q}g$), three-gluon and four-gluon, shown in the left, central and right panel of Figure 1.3, respectively. The self-interaction of gluons is possible due to the color charge that they carry.

In general, the use of QCD to describe a reaction such as those taking place at LHC, means the use of perturbative QCD (pQCD), which is well understood. The limit of applicability of perturbation theory relies on the strong coupling constant being small. It is actually not a constant, since its size varies with the size of the characteristic momentum transfer in a process (Q). To the leading order one has

$$\alpha_s(Q^2) = \frac{1}{\beta_0 \log\left(Q^2/\Lambda^2_{QCD}\right)}, \quad (1.3)$$

where Λ_{QCD} is an energy scale at which α_s diverges ($\mathcal{O}(200)$ MeV) and $\beta_0 = \frac{1}{12\pi}(33-2N_f)$ for N_f quark flavors. As a result, the coupling is small at high energies

and perturbation theory works as a good approximation. In contrast, at low energies the coupling is so strong that colored objects are only found in color-neutral composite states and pQCD is no longer valid (*confinement*). Therefore, quarks are always found in color-singlet (color-neutral) combinations named hadrons. There are two kinds of color-singlets, baryons (composed of three quarks, as protons or neutrons) and mesons (composed of a quark and an antiquark). There is an important consequence of confinement in particle colliders physics. Since colored partons cannot propagate freely after a collision, when they start to separate from each other the potential energy increases the point that spontaneously generates pairs of quark-antiquark. These quarks bond with the original ones, maintaining the color neutralness of the observable objects while reducing their kinematic energy. The process of formation of hadrons is called *hadronization*. The process repeats successively, transforming the initial kinematic energy of the disrupted quarks in a cascade of hadrons that moves along their initial direction, named *jets*.

1.1.3 Spontaneous symmetry breaking

The EW and QCD Lagrangians only contain massless fields (both, bosons and fermions) since adding mass terms would introduce a breaking of the gauge symmetry. On the other hand, there is experimental evidence of the masses of the fermions and of the $W$and Z bosons. This problem can be solved through a Spontaneous Symmetry Breaking (SSB), where the symmetry group $SU(2)_L \times U(1)_Y$ breaks down to $U(1)_{EM}$. This is known as the Brout-Englert-Higgs mechanism [12–14]. The Higgs mechanism introduces a complex scalar field, ϕ, that follows the SU(2) symmetry. The Lagrangian describing its kinematics is written as

$$\mathcal{L}_{Higgs} = (D_\mu \phi)^\dagger (D^\mu \phi) - V(\phi), \tag{1.4}$$

where $V(\phi) = \lambda(\phi^\dagger\phi)^2 - \mu^2\phi^\dagger\phi$ is the Higgs potential. If $\mu^2 > 0$, the field ϕ will acquire the value of minimum energy of the potential, known as the vacuum expectation value of $v = (\sqrt{2}G_F)^{-1/2} = 2M_W/g = 246$ GeV. When the field is situated at a minimum, the $SU(2)_L \times U(1)_Y$ symmetry is broken to form

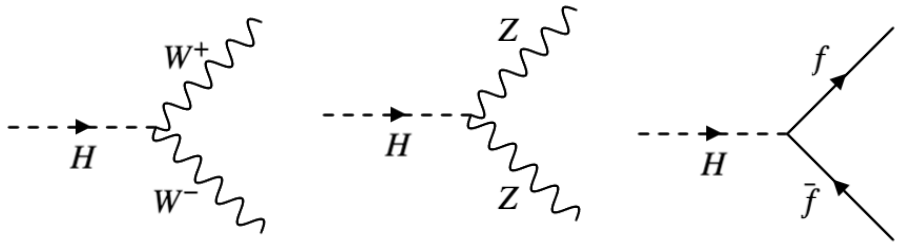

Figure 1.4: The three vertexes of Higgs interactions with $W^{\pm}$ bosons (*left*), Z bosons (*center*) and with fermions (*right*).

the $U(1)_{EM}$ symmetry, providing masses to the W and Z bosons and giving a non-complex field h which corresponds to the Higgs boson. The mass of the fermions is given by the interactions between the fermions of different chiralities and the Higgs field. This term is known as the Yukawa Lagrangian term. The strength of the coupling is proportional to the mass of the particle interacting with the Higgs boson, i.e. the heavier the particle, the stronger its coupling to the Higgs. The top quark has the largest Yukawa coupling, which makes it an important piece of the SM

$$\lambda_t = \frac{\sqrt{2}m_t}{v} = \frac{\sqrt{2} \times 173.1}{246} \sim 1. \tag{1.5}$$

The vertexes of the Higgs interaction with W and Z boson and to fermions are depicted in Figure 1.4.

Adding all the contributions mentioned in the previous subsections, the Lagrangian of the SM is composed by the following terms:

$$\mathcal{L}_{SM} = \mathcal{L}_{gauge} + \mathcal{L}_{Higgs} + \mathcal{L}_{matter} + \mathcal{L}_{Yukawa} + \mathcal{L}_{int}; \tag{1.6}$$

$\mathcal{L}_{gauge}$ and $\mathcal{L}_{matter}$ describe the gauge and fermion fields and $\mathcal{L}_{int}$, the interactions between them. $\mathcal{L}_{Higgs}$ stands for the contribution of the Higgs field, which triggers the spontaneous symmetry breaking of the electroweak group to the electromagnetic subgroup and gives masses to the W and Z bosons. Finally, the

$\mathcal{L}_{Yukawa}$ term accounts for the interaction of the fermions with the Higgs field, that gives rise to their masses (except the neutrinos).

1.1.4 Limitations of the SM

The SM as it stands now is a powerful theory tested by many experimental observations. Moreover, it was able to predict the existence of new particles as the charm and top quarks or the W, Z and Higgs bosons, previous to their observation at colliders. There are however some questions which cannot be answered within the SM framework and it is therefore thought that the SM is an effective field theory of a more complete description of the subatomic world. The main questions are:

Gravity The SM does not include a quantum field description of gravity, since none of the current attempts for it have been successful. Its inclusion is in particular difficult at high energies (close and above the Planck scale), where infinities due to quantum effects arise.

Neutrino oscillations The SM predicts that neutrinos are massless particles. However, the observation of neutrino oscillations implies non-zero masses. In addition, only left-handed neutrinos are observed, and thus, they cannot acquire their mass via the Yukawa interaction with scalars since that would imply the presence of right-handed neutrinos.

Matter-antimatter asymmetry Particles and antiparticles are created and annihilated in pairs, but the universe today contains mostly matter, while the Big Bang theory predicts equal quantity of matter and antimatter. The presence of a phase in the CKM matrix allows for CP violation, which provides a mechanism for the matter-antimatter asymmetry. However, the amount of CP-violation is too small to account for the asymmetry observed.

Strong CP problem It refers to the fact that, even if QCD does not forbid CP violation in strong interactions, it has not yet been observed in experiments.

Dark Matter and Dark Energy Dark Matter is a type of matter which does not interact via electromagnetic interactions and which existence has been inferred from gravitational effects in astrophysical and cosmological observations. While, according to the SM of cosmology, it should account for a $\approx 25\%$ of the energy content of the universe, the SM does not provide a proper candidate particle. On the other hand, about a 68% of the energy content of the universe is predicted to come from an even more intriguing Dark Energy; responsible of the accelerated expansion of the universe.

Naturalness The SM has 19 arbitrary parameters (including the fermion masses or the strong and electroweak couplings). The naturalness principle states that the dimensionless ratios of the parameters of a theory should be of order unity. This is in clear contradiction with, for example, the masses of the fermions, which range from ≈ 1 MeV for the first generation of fermions to about 173 GeV of the top quark. While this is not a problem of the theory itself, it is often considered as an indication of unknown principles underlying a more complete theory.

Hierarchy problem It arises from the huge gap between two fundamental scales of physics: the EW scale ($\sim 10^2$ GeV) and the Planck scale ($\sim 10^{19}$ GeV). The fact that the Higgs boson mass is well below the Planck scale seems to require new physics between the two scales. If the SM is valid up to the Planck scale instead, the Higgs mass need to be unnaturally fine tuned to cancel out the radiative corrections.

1.2 The top quark: a window for discovery of new physics

The SM top quark is the positively charged quark that forms part of the third generation of fermions together with the bottom quark. The existence of a third generation was predicted by Kobayashi and Maskawa in 1973 [11] in order to allow CP-violating interactions while preserving gauge invariance. While the top quark was inferred for the first time in 1977 [15], it wasn't until 1995 that D0 and CDF collaborations observed it in $\bar{p}p$ collisions at Tevatron [16, 17].

The importance of the top quark lies on its large mass, which translates in a very short lifetime ($\approx 0.5 \times 10^{-24}$ s) and thus the top quark decays rapidly through EW interactions before it has time to hadronize. As a result, it offers the possibility of studying its properties, in particular accessing to its spin information, through its decay products. In addition, since it is much heavier than the W boson, it can decay electroweakly to $t \to Wq$, having the mode $t \to Wb$ a branching ratio close to one (99.83%). Another consequence of its large mass is that the top quark is the only quark with a Yukawa coupling to the Higgs boson of the order of one; an accurate knowledge of its properties can therefore provide key information on fundamental interactions at the electroweak symmetry-breaking scale and beyond. Furthermore, there are many theories beyond the SM that predict the existence of new states that would preferentially couple to the top quarks due to its large mass. In addition, the top quark often constitutes an important background in searches of new physics at the LHC. Therefore, a detailed understanding of it will translate into improvements in those searches.

For all these reasons, performing precision measurements of the top quark properties and interactions as well as performing direct searches for new physics in the top quark sector are highly motivated. In this thesis, both approaches are considered in two different analysis. The first one presented aims at the precise study of the Wtb vertex using events in which the top quark is singly produced via electroweak interaction in the t-channel. The second analysis presents the direct search of new physics via the search of final states with a single top quark and a large amount of missing transverse momentum that would correspond to the unknown particle.

1.2.1 Top quark production at the LHC

In proton-proton collisions, top quarks are produced predominantly in pairs through the processes $q\bar{q} \to t\bar{t}$ and $gg \to t\bar{t}$ at leading order in QCD. The LO diagrams for $t\bar{t}$ production are depicted in Figure 1.5. The cross sections computed for these production mechanisms at next-to-next-to leading order (NNLO) with next-to-next-to-leading-log (NNLL) soft gluon resummation and

$\sqrt{s}$ [TeV]	Production cross section [pb]			
	QCD Pair production	EW Single-top production		
		t-channel	s-channel	Wt-production
7	$173.3^{+4.7}_{-6.1}$	$63.89^{+2.91}_{-2.52}$	$4.29^{+0.19}_{-0.17}$	$15.74^{+1.17}_{-1.21}$
8	$252.9^{+13.2}_{-14.4}$	$84.69^{+3.76}_{-3.23}$	$5.24^{+0.22}_{-0.20}$	22.37 ± 1.52
13	$831.8^{+40.3}_{45.7}$	$216.99^{+9.04}_{-7.71}$	$10.32^{+0.40}_{-0.36}$	71.7 ± 3.8
14	$984.5^{+47.4}_{-53.9}$	$248.09^{+10.30}_{-8.82}$	$11.39+^{+0.43}_{-0.39}$	$84.4^{+3.6}_{-5.2}$

Table 1.4: Summary of the predicted cross sections of the top pairs and single top productions calculated at NNLO (top pairs) and NLO (single top) in proton-proton collisions at different center-of-mass energies [18–22].

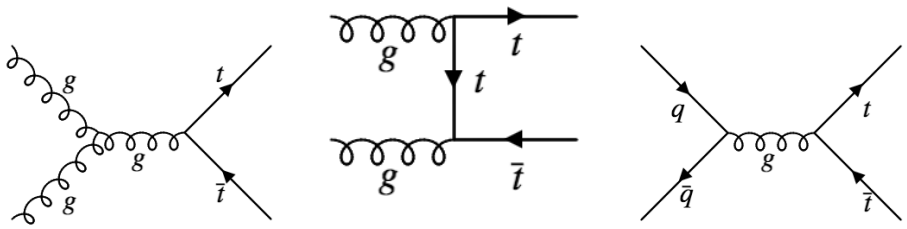

Figure 1.5: LO dominant production modes of top pairs at the LHC: gluon-gluon fusion (*left* and *center*) and quark-antiquark annihilation (*right*).

assuming a top-quark mass of $m_t = 172.5$ GeV/c^2 [18] are listed in Table 1.4. Top quarks can also be produced, with smaller cross sections, via electroweak interactions through the exchange of a virtual W boson in the s-channel ($q\bar{q}' \to t\bar{b}$) and the t-channel ($qb \to q't$) or in association with a W boson ($bg \to W^- t$) (see the LO diagrams in Figure 1.6). The predictions at NLO cross sections for the single top production (top plus antitop) in the t-channel [19, 20], s-channel [21] and in association with a W boson [22] are listed in Table 1.4. The top and bottom panels of Figure 1.7 show the values of the $t\bar{t}$ and single top production cross sections measured by ATLAS and CMS collaborations as a function of the center of mass energy.

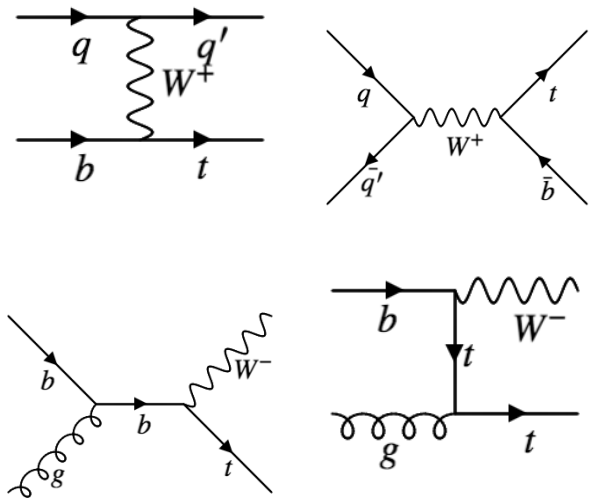

Figure 1.6: LO dominant production modes of single tops at the LHC: t-channel (*top-left*), s-channel (*top-right*) and Wt associated production (*bottom*).

1.2.1.1 Top quark polarization

At hadron colliders, the top quarks are predominantly produced in pairs. These top quarks have only a a small net polarization arising from electroweak corrections to the QCD-dominated production process. However, when produced singly via EW interaction in the t-channel, the top quark is expected to be highly polarized. For a final state with a top quark, the dominant production process (see the top-left panel of Figure 1.6) is $ub \to dt$. In the zero momentum frame (ZMF), the outgoing t and d quarks are back-to-back. The initial state u and b quarks couple to a W boson which has left handed chirality and thus they need to have left handed chirality as well. Since both quarks are ultrarelativistic, their masses are effectively zero and in this limit, chirality and helicity[3] are equivalent. Since the quarks are back-to-back and both have left-handed helicity, the spin projection in the initial state is zero. The final state d quarks (also referred to as spectator quark) is also massless and

[3]The helicity of a particle is the projection of its spin $\vec{s}$ along its momentum direction $\hat{p}$, $h = \vec{s} \cdot \hat{p}$. A particles has positive helicity if its spin is projected parallel to its momentum and negative in the projection is antiparallel to the direction of motion.

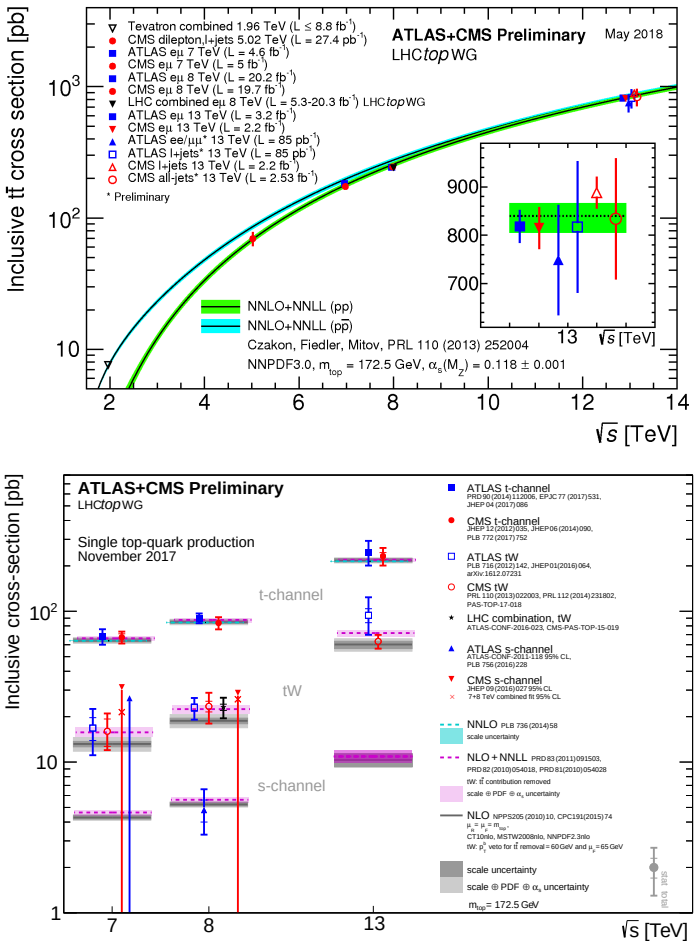

Figure 1.7: Top: Summary of LHC and Tevatron measurements of the top-pair production cross-section as a function of the centre-of-mass energy compared to the NNLO QCD calculation complemented with NNLL resummation (top++2.0) [23]. The theory band represents uncertainties due to renormalisation and factorisation scale, parton density functions and the strong coupling. The measurements and the theory calculation are quoted at m_t=172.5 GeV. Measurements made at the same centre-of-mass energy are slightly offset for clarity [24]. Bottom: Summary of ATLAS and CMS measurements of the single top production cross-sections in various channels as a function of the center of mass energy. The measurements are compared to theoretical calculations based on: NLO QCD, NLO QCD complemented with NNLL resummation and NNLO QCD (t-channel only) [25].

therefore its left-handed chirality implies left-handed helicity. The final state top quark is massive. However, conservation of angular momentum forces it to have left-handed helicity in this reference frame. Since the top quark is massive, boosting to another frame will, in general, introduce a right-handed helicity component. For instance, in the laboratory frame the top quark is left-handed only 66% of the time [26].

Because of its short lifetime, the spin information of the top quark is transferred to its decay products, which act as spin analyzers. As a results, the spin polarization of the top quark can be analyzed through the angular distributions of its decay products. The general form of the angular distribution of a spin analyzer with respect to the spin direction $\hat{z}$ is given by

$$\frac{1}{\Gamma}\frac{\mathrm{d}\Gamma}{\mathrm{d}\cos\theta^X} = \frac{1}{2}\left(1 + P_z\alpha_X\cos\theta^X\right), \tag{1.7}$$

where θ^X is the angle between the momentum direction of the decay particle $X = W, b, \ell, \nu$ in the top quark rest frame and the spin direction $\hat{z}$ chosen to quantize the top spin. P_z is the top quark polarization along the $\hat{z}$ direction and α_X is the spin analyzer power, which depends on the chosen particle [4]. When the top quark spin is decomposed along the direction of the d-type quarks, the spin down contribution is small and this is used to define the spectator basis by electing to use the direction of the spectator jet (defined as the light jet appearing in the final state) for the spin axis [27]. In this basis, the overall fraction of spin up quarks is 95%.

1.2.2 Top quark decay

As advanced in the previous Section 1.1, the top quark decays 99.83% of the time to a b quark and a W boson. The final state decays can be classified according to the subsequent decay mode of the W boson. W bosons can decay either leptonically or hadronically (left and right panels of Figure 1.8, respectively). In the leptonic decay, the $W^{+(-)}$ decays into a charged antilepton (lepton) and its corresponding (anti)neutrino. In the hadronic decay, the $W^{+(-)}$ boson decays into an up-type

[4] The splin analyzer power can range from -1 to 1. In the SM at the tree level, $\alpha_\ell = 1$, $\alpha_\nu = -0.32$ and $\alpha_b = -\alpha_W = -0.41$.

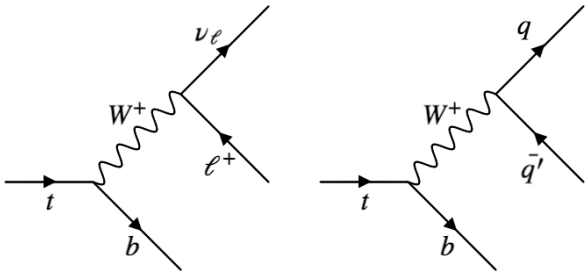

Figure 1.8: Top quark decays according to the decay modes of the W boson. Left: lepton channel. Right: hadron channel.

(anti)quark and a down-type antiquark (quark). Due to its high mass, it can decay into any quark except the top quark. The branching ratios of these decays are 32.6% for the leptonic and 67.4% for the hadronic modes.

When considering the $t\bar{t}$ production, the decay modes are classified according to the decays of the two W bosons. This leads to three decay modes:

- **All jets**: $t\bar{t} \to W^+bW^-\bar{b} \to q\bar{q}'bq''\bar{q}'''\bar{b}$ (45.7%)
- **Lepton+jets**: $t\bar{t} \to W^+bW^-\bar{b} \to q\bar{q}'b\ell^-\bar{\nu}_\ell\bar{b} + \ell^+\nu_\ell bq''\bar{q}'''\bar{b}$ (43.8%)
- **Dilepton**: $t\bar{t} \to W^+bW^-\bar{b} \to \ell^+\nu_\ell b\ell'^-\bar{\nu}_{\ell'}\bar{b}$ (10.5%)

1.2.2.1 Helicity of W bosons from top quark decays

The emitted W boson in a top quark decay, which has spin 1, is polarized with negative, positive or zero helicity. Each polarization state has a corresponding partial decay width (Γ_L, Γ_R and Γ_0) defined in relation to the total decay width $\Gamma(W \to tb) = \Gamma_L + \Gamma_R + \Gamma_0$. The W boson only couples to b quarks of left-handed chirality, which is equivalent to left-handed helicity in the limit of a massles b-quark. In the top quark rest frame, the W boson and the b quark are emitted back-to-back. Therefore, due to angular momentum conservation, the W boson can only be longitudinally or left-handed polarized, depending on the orientation of the top quark spin.

The different polarization states of the W boson determine the angular distribution of its decay products. In the leptonic decay, the helicity information is visible through the angle θ^*, which is defined as the angle between the momentum of the charged lepton in the W rest frame and the W momentum in the top quark rest frame. The normalized differential decay rate can be written as

$$\frac{1}{\Gamma}\frac{\mathrm{d}\Gamma}{\mathrm{d}\cos\theta^*} = \frac{3}{8}(1-\cos\theta^*)^2 F_\mathrm{L} + \frac{3}{4}\sin^2\theta^* F_0 + \frac{3}{8}(1+\cos\theta^*)^2 F_\mathrm{R}, \tag{1.8}$$

where $F_i = \Gamma_i/\Gamma$ are the W boson helicity fractions. Calculations at next-to-next-to-leading order (NNLO) in QCD predict the fractions to be $F_L = 0.311 \pm 0.005$, $F_R = 0.0017 \pm 0.0001$ and $F_0 = 0.687 \pm 0.005$ [28]. The most recent measurement from the ATLAS Collaboration is based on $t\bar{t}$ events in the lepton plus jets channel and yields the most precise values up to date: $F_L = 0.299 \pm 0.015$, $F_R = -0.008 \pm 0.014$ and $F_0 = 0.709 \pm 0.019$ [29]. From $t\bar{t}$ events in the same channel, CMS Colaboration obtains $F_L = 0.323 \pm 0.008(\mathrm{stat.}) \pm 0.014(\mathrm{syst.})$, $F_R = -0.004 \pm 0.005(\mathrm{stat.}) \pm 0.014(\mathrm{syst.})$ and $F_0 = 0.681 \pm 0.012(\mathrm{stat.}) \pm 0.023(\mathrm{syst.})$ [30].

1.3 Probing the structure of the Wtb vertex

The Wtb vertex appears both in the production and in the decay of the single-top t-channel process, and can be probed by either measuring the top-quark polarization or the W boson spin observables [31, 32].

In proton-proton (pp) collisions, the dominant production process of single top-quarks is the t-channel, depicted in fig. 1.9. In this process, the interaction of a light quark with a b-quark via the exchange of a space-like W boson produces a top quark and a forward light quark which is called the spectator quark. The produced top quark is predicted to be highly polarized, in particular along the direction of the spectator quark, due to the vector-axial-vector form of the Wtb vertex in the Standard Model [26, 33]. Moreover, due to its short lifetime, the top quark decays in a shorter timescale than that required for QCD interactions to randomize its

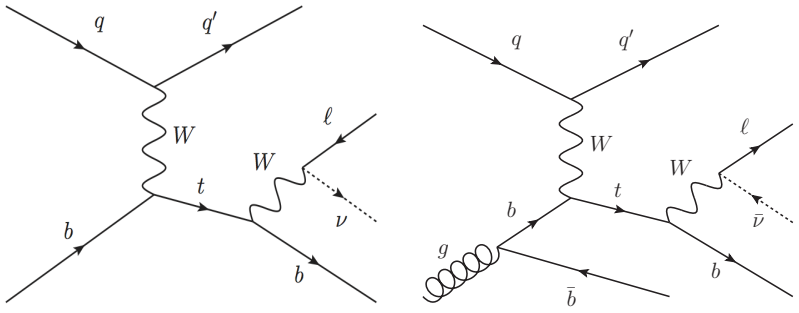

Figure 1.9: Leading-order Feynman diagrams for t-channel production of single top-quarks in pp collisions *(left)* $2\to2$ process (five-flavour scheme) and *(right)* $2\to3$ process (four-flavour scheme). The leptonic decay of the top-quark ($t\to Wb$ with $W\to\ell\nu$) is also displayed.

spin, allowing to access its spin orientation through the angular distribution of its decay products.

In this thesis, the observables related to the spin of the W boson are measured for decays of top quarks produced in the single top t-channel production, using pp collisions at a center-of-mass energy of 8 TeV, collected by the ATLAS detector. Therefore, the Wtb vertex is probed in the decay of the top-quark produced in the single-top t-channel process. The measurements are then interpreted in the context of an effective field theory (EFT). The measurement of the top-quark polarization observables, together with the measurements resulting from the work developed in this thesis, can be found in [1].

1.3.1 Effective field theory

As pointed out at the end of Section 1.1, in spite of the astonishing experimental success of the SM predictions, it can not be the ultimate theory. New physics can come as new particles and interactions appearing when higher energies are probed. These can appear at the Planck scale ($\sim 10^{19}$ GeV) or at intermediate scales, Λ. There exists in the literature a wide variety of models of physics beyond the SM. Effective field theories provide a way to enclose them in a model-independent approach [34–36]. The basic idea is the following: if the physics beyond the SM lies

at an energy scale Λ smaller than 1 TeV, we should be able to observe it at present hadron colliders. However, if it lies at much higher energy scales, its effect can be parametrized via higher-dimension operators, suppressed by inverse powers of the scale Λ. The effective Lagrangian then becomes:

$$\mathcal{L}_{eff} = L_0 + \frac{1}{\Lambda} L_1 + \frac{1}{\Lambda^2} L_2 + ..., \tag{1.9}$$

where L_0 is the order-4 SM Lagrangian, L_1 is the new interaction of order 5 and so on. The only constraint is that all the higher dimension Lagrangians are $SU(2)_L \times U(1)_Y \times SU(3)_C$ invariant.

Five order operators cannot fulfill the requirements of $SU(2)_L \times U(1)_Y \times SU(3)_C$ and conserve baryon and lepton number. Trunkating at higher terms, which are suppressed by higher powers of Λ, the effective Lagrangian at order six is written as

$$\mathcal{L}_{eff} = L_0 + \sum \frac{\mathcal{C}_x}{\Lambda^2} \mathcal{O}_x, \tag{1.10}$$

where $\mathcal{O}_x$ are dimension-six gauge invariant operators. The complex coeficients $\mathcal{C}_x$ are the so-called Wilson coefficients and correspond to the couplings of the SM fields to the new physics. These operators can induce corrections to the SM couplings. For instance, they may originate anomalous couplings of the top quarks to the gauge bosons.

1.3.2 Anomalous Wtb couplings

Among the possible 80 different independent operators [36], only fourteen contribute to top electroweak anomalous couplings [37] (either in the Wtb, Ztt or γtt vertexes or in FCNC top-up and top-charm interactions), and from these, only half of them are actually independent, while the rest can be written in terms of those. A generalized expression for the Wtb vertex is

$$\mathcal{L}_{Wtb} = -\frac{g}{\sqrt{2}} \bar{b} \gamma^\mu (V_L P_L + V_R P_R) t W^-_\mu - \frac{g}{\sqrt{2}} \frac{i\sigma^{\mu\nu}}{M_W} q_\nu (g_L P_L + g_R P_R) t W^-_\mu + \text{h.c.}, \tag{1.11}$$

where g is the weak coupling constant, m_W and q_ν are the mass and the four-momentum of the W boson, respectively, $P_{L,R} \equiv (1 \mp \gamma^5)/2$ are the left- and right-handed projection operators, and $\sigma^{\mu\nu} = [\gamma^\mu, \gamma^\nu]/2$. The constants $V_{\mathrm{L,R}}$ and $g_{\mathrm{L,R}}$ are the left- and right-handed vector and tensor couplings, respectively. In the Standard Model at tree level the coupling V_L is the V_{tb} element of the quark-mixing Cabibbo-Kobayashi-Maskawa (CKM) matrix that is close to one, while the rest of the couplings, referred to as ***anomalous couplings***, V_R and $g_{R,L}$ are all zero. Non-vanishing anomalous couplings would provide hints of physics beyond the Standard Model, and complex values would imply that the top-quark decay has a CP-violating component. The contribution to these couplings from the dimension-six operators are:

$$\delta V_L = \mathcal{C}_{\phi q}^{(3,33)*} \frac{v^2}{\Lambda^2}, \qquad \delta g_L = \sqrt{2}\mathcal{C}_{dW}^{33*} \frac{v^2}{\Lambda^2}, \tag{1.12}$$

$$\delta V_R = \frac{1}{2}\mathcal{C}_{\phi\phi}^{33*} \frac{v^2}{\Lambda^2}, \qquad \delta g_R = \sqrt{2}\mathcal{C}_{uW}^{33*} \frac{v^2}{\Lambda^2}. \tag{1.13}$$

$$\tag{1.14}$$

The involved operators can be classified in two types:

- The operators $\mathcal{O}_{\phi q}^{(3,33)}$ and $\mathcal{O}_{\phi\phi}^{33*}$ involve scalar fields carrying covariant derivative and are relevant in new physics models in which there are mixing effects between heavy particles (predicted by new physics models) and the SM particles [38–41]. It can be generated at tree level after integrating out the new heavy particles, such as a heavy charged vector boson ($W'^{\pm}$) that mixes with SM gauge boson ($W^{\pm}$) or a heavy quark that mixes with top quark or bottom quark.
- The operators $\mathcal{O}_{dW}^{33*}$ and $\mathcal{O}_{uW}^{33*}$ involve field strength tensors, and in this case, the new physics effects would appear at loop level (within models such as two Higgs doublet model or supersymmetric models).

The details of this computations are out of the scope of this thesis and can be read in [37] and [42].

Coupling	95% CL interval
Im g_{R}	$[-0.27, 0.27]$
Im g_{L}	$[-0.07, 0.07]$
Im V_{R}	$[-0.15, 0.15]$

Table 1.5: One dimension 95% CL limits on pure imaginary anomalous couplings from W-boson helicities and t-channel cross section combination of measurements at the LHC and Tevatron [46].

1.3.3 Constraints on *Wtb* anomalous couplings previous to this work

Limits on anomalous couplings haven been set in different experiments. The W boson helicity fractions, which can be measured in both top pairs (decay) and singly-produced top quarks (production and decay), are sensitive to the combinations of anomalous couplings. Assuming no imaginary part, ATLAS [29, 43] and CMS [30, 44, 45] collaborations have set limits on combinations of couplings. Figure 1.10 shows the two dimensional allowed regions obtained by both collaborations from $t\bar{t}$ events. A combination of the most precise values of helicity fractions from LHC and Tevatron results, leads to the more stringent limits shown in Table 1.5 [46].

The measurement of the t-channel single top cross section also allows to set precise limits on V_{L} by setting limits on the $|V_{tb}|$ element of the CKM matrix. Using results from 8 TeV data, ATLAS Collaboration sets the lower limits $|V_{tb}| > 0.92$ [47] while CMS Collaboration measures it to be $|V_{tb}| = 0.998 \pm 0.038(\mathrm{exp.}) \pm 0.016(\mathrm{theo.})$ [48].

Finally, direct searches for anomalous couplings in t-channel single top events have been carried out to set limits on combinations of couplings. In this analysis [49] the Wtb vertex is probed using the normalized double - differential (θ^*, ϕ^*) decay of top-quarks in single-top quark t-channel events. This is used to simultaneously determine the fraction of decays containing transversely polarized W bosons and the phase between amplitudes for transversely and longitudinally polarized W bosons recoiling against left-handed b-quarks. This analysis is based on of proton–proton collision data at a centre-of-mass energy of 7 TeV collected with

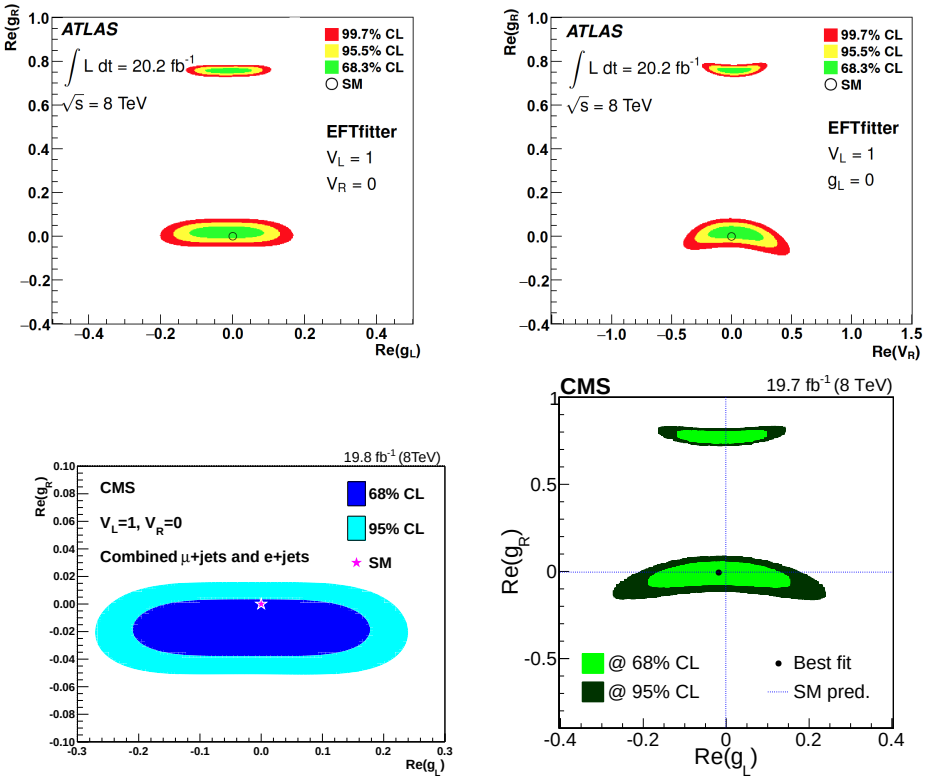

Figure 1.10: Top: Limits on the anomalous left- and right-handed tensor couplings (left) and on the right-handed vector and tensor couplings (right) of the Wtb decay vertex as obtained from the measured W boson helicity fractions in $t\bar{t}$ events at 8 TeV by ATLAS Collaboration [29]. Bottom-left: the corresponding allowed regions for the real components of the anomalous couplings g_{L} and g_{R} at 68% and 95% CL, for V_{L}= 1 and V_{R}= 0 as measured by CMS Collaboration from $t\bar{t}$ events at 8 TeV [30]. Bottom-right: Exclusion limits on the real part of g_{L} and g_{R} anomalous couplings, with V_{L}= 1 and V_{R}= 0, using the combined W boson helicity measurement in the single top quark event topology by the CMS Collaboration with 8 TeV data [45].

the ATLAS detector, yielding $\mathrm{Re}\ [g_R/V_L] \in [-0.36, 0.10]$ and $\mathrm{Im}\ [g_R/V_L] \in [-0.17, 0.23]$ with a correlation of 0.11 [49].

Apart from the measurements using events involving top quarks, it is interesting to take into account the effects of quantum corrections in processes that do not involve top quarks and which give complementary information to the direct searches. For example, measurements from electric dipole moments put very stringent limits in CP-violating couplings [50]. In addition, using precision measurements of B-meson decays, constraints from the FCNC processes where loops involving top quarks play a crucial role have been set to the anomalous couplings [51]

$$\begin{aligned} \delta V_L &\in [-0.13, 0.03], \\ V_R &\in [-0.0007, 0.0025], \\ g_L &\in [-0.0013, 0.0004], \\ g_R &\in [-0.15, 0.57]. \end{aligned}$$

1.3.4 W boson spin observables

In the analysis presented in this thesis, the Wtb vertex is studied at the decay of top quarks singly produced in the t-channel. The strategy followed is to measure the values of a set of observables which characterize the W boson spin state via the measurement of angular asymmetries of its decay products.

The spin state of the W boson coming from the decay of polarized top quarks can be described in the form of a 3×3 density matrix [32]. This can be parametrized in terms of expected values of observables which completely determine the angular distribution of the W boson decay products in $W^\pm \to \ell^\pm\nu$ with $\ell = e, \mu$. Denoting $(\theta^*_\ell, \phi^*_\ell)$ as the polar and azimuthal angles of the charged lepton momentum in the W boson rest frame, the fully differential decay width of a W^+ boson can be written as

$$\begin{aligned}\frac{1}{\Gamma}\frac{d\Gamma}{d(\cos\theta_\ell^*)d\phi_\ell^*} &= \frac{3}{8\pi}\left\{\frac{2}{3}-\frac{1}{\sqrt{6}}\langle T_0\rangle\left(1-3\cos^2\theta_\ell^*\right)+\langle S_3\rangle\cos\theta_\ell^*\right. \\ &+ \langle S_1\rangle\cos\phi_\ell^*\sin\theta_\ell^* \ +\langle S_2\rangle\sin\phi_\ell^*\sin\theta_\ell^* \\ &- \left.\langle A_1\rangle\cos\phi_\ell^*\sin 2\theta_\ell^* \ -\langle A_2\rangle\sin\phi_\ell^*\sin 2\theta_\ell^*\right\}, \end{aligned} \tag{1.15}$$

where $\langle T_0\rangle$, $\langle S_3\rangle$, $\langle S_1\rangle$, $\langle S_2\rangle$, $\langle A_1\rangle$ and $\langle A_2\rangle$ are the expected values of the W boson spin observables. They can be written in terms of eight form factors that depend on the *Wtb* anomalous couplings and that are defined in [31].

$$\begin{aligned}\langle S_1\rangle &= \tfrac{\pi}{2}\tfrac{m_t}{M_W}\mathrm{P}\tfrac{\mathcal{C}_0}{\mathcal{A}_0+2\mathcal{B}_0}, \\ \langle S_2\rangle &= -\tfrac{\pi}{2}\tfrac{q}{M_W}\mathrm{P}\tfrac{\mathcal{D}_1}{\mathcal{A}_0+2\mathcal{B}_0}, \\ \langle S_3\rangle &= 4\tfrac{q}{m_t}\tfrac{\mathcal{B}_1}{\mathcal{A}_0+2\mathcal{B}_0}, \\ \langle A_1\rangle &= -\tfrac{\pi}{4}\tfrac{q}{M_W}\mathrm{P}\tfrac{\mathcal{C}_1}{\mathcal{A}_0+2\mathcal{B}_0}, \\ \langle A_2\rangle &= \tfrac{\pi}{4}\tfrac{m_t}{M_W}\mathrm{P}\tfrac{\mathcal{D}_0}{\mathcal{A}_0+2\mathcal{B}_0}, \\ \langle T_0\rangle &= \sqrt{\tfrac{2}{3}}\tfrac{\mathcal{B}_0-\mathcal{A}_0}{\mathcal{A}_0+2\mathcal{B}_0}. \end{aligned} \tag{1.16}$$

The values of all the W boson spin observables can be obtained from an eight parameter fit of the distribution in 1.15. However, from an experimental point of view, it is simpler to project the distribution on certain directions to obtain one-dimensional distributions with less parameters. For example, the integral over the azimuthal angle leads to the polar angle distribution in which the off-diagonal terms of the W boson spin density matrix vanish and the three remaining parameters are the W boson polarization fractions, F_+, F_- and F_0

$$\frac{1}{\Gamma}\frac{d\Gamma}{d\cos\theta_\ell^*} = \frac{3}{8}F_+(1+\cos\theta_\ell^*)^2+\frac{3}{4}F_0\sin^2\theta_\ell^*+\frac{3}{8}F_-(1-\cos\theta_\ell^*)^2. \tag{1.17}$$

The polarization fractions, which must satisfy $F_+ + F_0 + F_- = 1$ correspond to the helicity fractions when the z axis is taken in the direction of the W momentum. The polarization fractions are related to the W boson spin observables via

$$\begin{aligned} F_+ &= \frac{1}{3} + \frac{1}{2}\langle S_3 \rangle + \frac{1}{\sqrt{6}}\langle T_0 \rangle, \\ F_0 &= \frac{1}{3} - \frac{2}{\sqrt{6}}\langle T_0 \rangle, \\ F_- &= \frac{1}{3} - \frac{1}{2}\langle S_3 \rangle + \frac{1}{\sqrt{6}}\langle T_0 \rangle, \end{aligned} \tag{1.18}$$

The explicit dependence of the diagonal elements on the W boson spin observables can be written in the fully differential decay with expression of the W boson, leading to a distribution which depends on only two observables which are in addition independent: $\langle S_3 \rangle$ and $\langle T_0 \rangle$. The integration of Eq. 1.15 over a function of ϕ^* that prevents cancellations of the total integral, but instead selects desired observables, allows the measurement of the off-diagonal elements. In this way, the six spin observables can be measured by fitting three distributions with two parameters each. Alternatively, they can be related to asymmetries in the angular distributions of the charged lepton momentum reconstructed in the W boson rest frame with respect to directions that can be defined in the top quark rest frame and in the W boson rest frame.

The coordinate system used and the defined angles are depicted in Fig. 1.11. Apart from the polar and azimuthal angles of the charged lepton momentum in the W boson rest frame, the normal and transverse directions, as proposed in Ref. [31] can be used to define new angular distributions. The normal axis is the orthogonal direction to the plane defined by the direction of the momentum of the W boson in the top-quark rest frame, $\vec{q}$, and the top-quark spin direction, $\hat{s}_t$, taken along the spectator quark momentum in the top-quark rest frame. The transverse axis is defined as the orthogonal direction to the plane defined by the normal direction and the W boson momentum in the top-quark rest frame. Table 1.6 summarizes the angles for the charged lepton reconstructed in the W boson rest frame in which the angular asymmetries are defined.

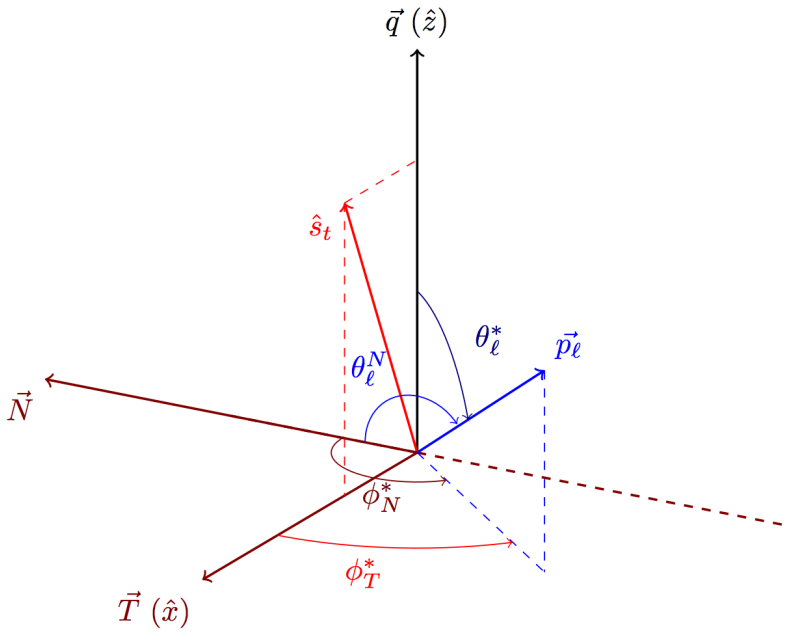

Figure 1.11: Right-handed coordinate system and angles used to define the W boson spin observables and their related angular asymmetries in the decay of polarized top-quarks. The W boson momentum $\vec{q}$ in the top-quark rest frame defines the $\hat{z}$ axis; the top-quark spin direction $\hat{s}_t$, taken along the spectator-quark momentum in the top-quark rest frame, is set in the $\hat{x} - \hat{z}$ plane. The polar and azimuthal angles of the charged lepton momentum $\vec{p}_\ell$ in the W boson rest frame are labeled θ^*_ℓ and ϕ^*_ℓ, respectively. The normal and transverse axes are defined with respect to $\vec{q}$ and $\hat{s}_t$ according to $\vec{N} = \hat{s}_t \times \vec{q}$ and $\vec{T} = \vec{q} \times \vec{N}$; they are along the $\hat{x}$ and $-\hat{y}$ axes of the coordinate system, respectively. The azimuthal angles ϕ^*_N and ϕ^*_T of the charged lepton in the W boson rest frame are defined with respect to the $\vec{N}$ and $\vec{T}$ axes, respectively ($\phi^*_T \equiv \phi^*_\ell$), while θ^N_ℓ and θ^T_ℓ (not shown in the figure) are the relative angles between $\vec{p}_\ell$ and the $\vec{N}$ and $\vec{T}$ axes, respectively.

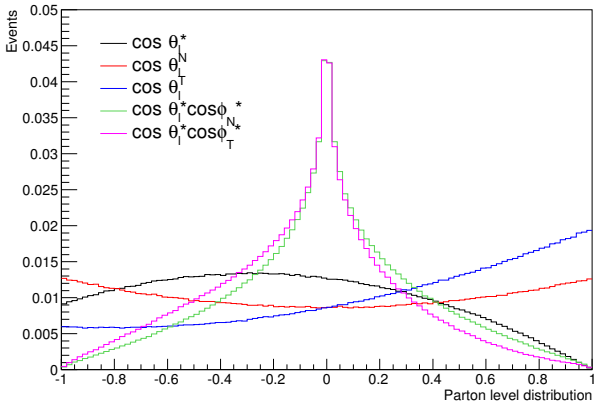

Figure 1.12: Angular distributions at parton level with SM couplings.

The shape of the above mentioned angular distributions at parton level are shown in Fig. 1.12 for top quarks produced in the t-channel at $\sqrt{s}$ = 13 TeV. These distributions are generated using PROTOS generator, assuming SM couplings, a top-quark mass of 172.5 GeV and a b-quark mass of 4.8 GeV.

Angle	Definition
θ^*_ℓ	Polar angle between $\vec{p}_l$ (W rest frame) and $\vec{q}$ (t rest frame)
θ^T_ℓ	Polar angle between $\vec{p}_l$ (W rest frame) and the transverse direction (t rest frame)
θ^N_ℓ	Polar angle between $\vec{p}_l$ (W rest frame) and the normal direction (t rest frame)
ϕ_T*	Azimuthal angle between $\vec{p}_l$ (W rest frame) and the transverse direction (t rest frame)
ϕ_N*	Azimuthal angle between $\vec{p}_l$ (W rest frame) and the normal direction (t rest frame)

Table 1.6: Summary of the angles used in the analysis.

Forward-backward angular asymmetries in an angular distribution, or a combination of them, are defined as

$$A_{\mathrm{FB}} = \frac{N(\cos\theta > 0) - N(\cos\theta < 0)}{N(\cos\theta > 0) + N(\cos\theta < 0)}, \tag{1.19}$$

while an edge-central asymmetry is defined as

$$A_{\mathrm{EC}} = \frac{N(|\cos\theta| > \frac{1}{2}) - N(|\cos\theta| < \frac{1}{2})}{N(|\cos\theta| > \frac{1}{2}) + N(|\cos\theta| < \frac{1}{2})}. \tag{1.20}$$

The SM predictions for the angular asymmetries and their related W boson spin observables are summarized in table 1.7.

Angular distribution	Spin observables		Asymmetries		
	Observable	SM pred.	Observable		SM pred.
$\cos\theta_{\ell}*$	$< S_3 >$	-0.30	A_{FB}	$= \frac{3}{4}\langle S_3\rangle$	-0.23
$\cos\theta_{\ell}*$	$< T_0 >$	-0.45	A_{EC}	$= \frac{3}{8}\sqrt{\frac{3}{2}}\langle T_0\rangle$	-0.20
$\cos\theta_{\ell}^{T}$	$< S_1 >$	0.46	A_{FB}^{T}	$= \frac{3}{4}\langle S_1\rangle$	0.34
$\cos\theta_{\ell}^{N}$	$< S_2 >$	0.00	A_{FB}^{N}	$= -\frac{3}{4}\langle S_2\rangle$	0.00
$\cos\theta_{\ell} * \cos\phi_{T}*$	$< A_1 >$	0.23	$A_{\mathrm{FB}}^{T,\phi}$	$= -\frac{2}{\pi}\langle A_1\rangle$	-0.14
$\cos\theta_{\ell} * \cos\phi_{N}*$	$< A_2 >$	0.00	$A_{\mathrm{FB}}^{N,\phi}$	$= -\frac{2}{\pi}\langle A_1\rangle$	0.00

Table 1.7: Summary of the angular asymmetries and their related spin observables with their SM prediction values.

The sensitivity of the asymmetries to the different Wtb couplings is depicted in Fig. 1.13. They are calculated assuming a top-quark mass of 172.5 GeV and a b-quark mass of 4.8 GeV; the top-quark and top-antiquark productions are combined using the predicted polarization values and the t-channel cross-sections calculated at NLO in QCD. The calculations are based on the `TopFit` code [52], in which the analytic expressions of the W boson spin observables, of the top-quark polarization and of the spin analyzing powers are implemented as a function of the Wtb coupling values. The asymmetries A_{FB}, A_{EC} and A_{FB}^{T} are mainly sensitive to $\mathrm{Re}\ g_{\mathrm{R}}$, while they exhibit a poor dependence on the rest of the couplings. On the other hand, the normal asymmetries, A_{FB}^{N} and $A_{\mathrm{FB}}^{N,\phi}$ are only sensitive to $\mathrm{Im}\ g_{\mathrm{R}}$.

In the SM, the asymmetries A_{FB}^{N} and $A_{\mathrm{FB}}^{N,\phi}$ are predicted to vanish at tree level. Therefore, a non-zero measurement would point to the presence of a complex phase in the Wtb vertex. Since A_{FB}^{N} is twice more sensitive to $\mathrm{Im}\ g_{\mathrm{R}}$ than $A_{\mathrm{FB}}^{N,\phi}$, this

asymmetry will be used to set limits on $\mathrm{Im}\ g_{\mathrm{R}}$. No limits will be set on $\mathrm{Re}\ g_{\mathrm{R}}$ since this coupling is better constrain in other measurements [29, 53].

1.4 Search for invisible particles produced in association with a top quark as evidence for Dark Matter

In the first half of the 20th century, the first observations of inconsistencies in the assumption that all the universe content is made up of ordinary, visible matter, were made. A proposed solution was the existence of a new type of matter that would interact only gravitationally and weakly at most with baryoric matter: Dark Matter. This elusive type of matter would account to up to $\sim 25\%$ of the energy content of the Universe, making it extremely relevant to detect it and understand its nature. This section gives an insight on the topic, from the observed evidence of its existence to targeted production modes in hadron colliders, in particular to the mono-top model that will be searched for in this thesis.

1.4.1 Evidence for Dark Matter

One of the main motivations of the presence of Dark Matter comes from the rotation curves of the galaxies, i.e., the distribution of the circular velocity of stars and gas inside a galaxy as a function of their distance to the center of the galaxy. Such a curve is depicted in Figure 1.14. The observed curve (points) has a characteristic flat shape at large distances which differs significantly from the expected curves given by the luminous matter in the form of stellar content (short dashed line) and gas (long dashed line). Indeed, according to Newtonian dynamics, the circular velocity of a star following a keplerian orbit inside the galaxy at a distance r from its center is expected to be

$$v = \sqrt{\frac{GM(r)}{r}}, \tag{1.21}$$

where $M(r) \equiv 4\pi \int \rho(r) r^2 \mathrm{d}r$. Outside the visible galaxy one would therefore expect $v(r) \propto 1/\sqrt{r}$. In order to have a constant velocity, a mass density $\rho(r) \propto 1/r^2$ is needed. A Dark Matter halo surrounding the galaxy could fulfill this condition.

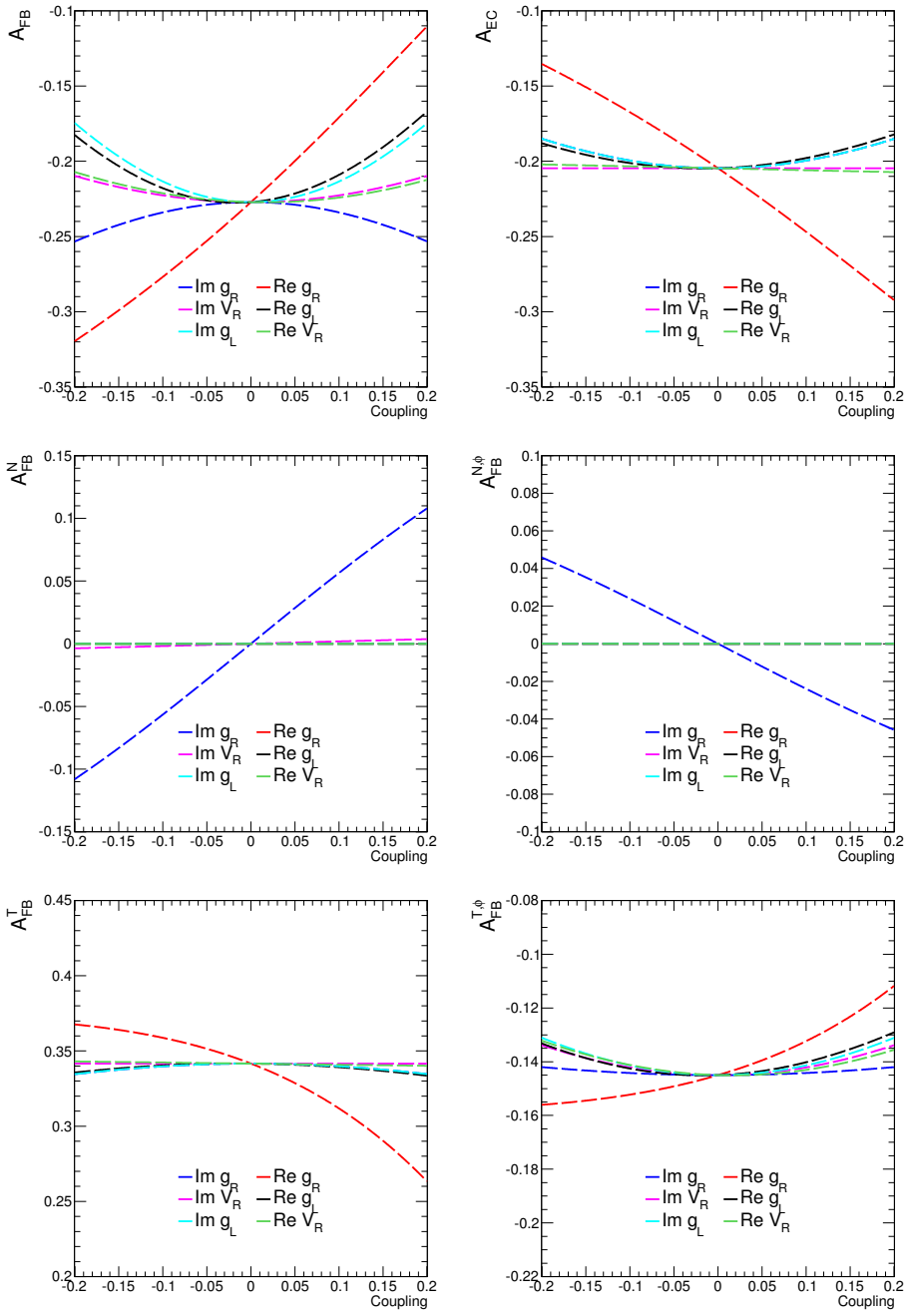

Figure 1.13: Dependence of the asymmetries on the *Wtb* couplings.

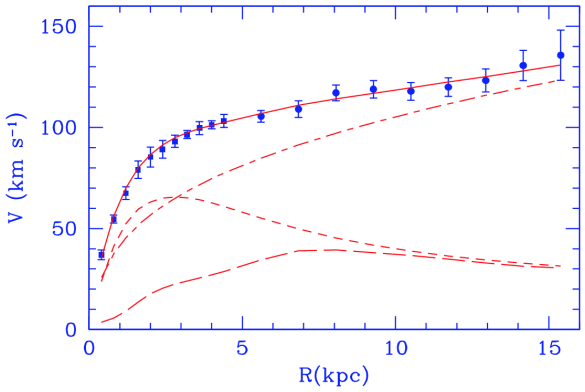

Figure 1.14: Rotation curve of M33 (points) compared with the best fit model (continuous line). The different components of the best fit model are shown as well: the DM halo (dashed dotted line), stellar disk (short dashed line), and gas contributions (long dashed line). Figure taken from from [54].

It was Fritz Zwicky, in 1933, who first noted that Dark Matter should be present in much greater amount than luminous matter from his studies of the rotational velocity of the Coma cluster [55]. In particular, he estimated that in order to obtain the observed redshift, the average density in the Coma system would have to be at least 400 times larger than that derived from observations of luminous matter. Similar observations with different conclusions were done by Horace W. Babcock, who attributed the discrepancies he observed in the mass-to-light ratio of light-emitting objects from Andromeda nebula (M31) to the additional light absorption mechanisms inside the galaxy not properly taken into account in the estimation of luminous matter [56]. It wasn't until 1970 that Zwicky's proposal was revisited, when the rotation of the Andromeda nebula was studied again using a spectroscopic survey from its emission regions and similar results were found [57]. More observations since then have reinforced the idea of a Dark Matter halo surrounding the galaxies and nowadays the focus is on the study of its profile density and distribution, as well as the nature of the matter that conforms it.

Another source of evidence of the existence of Dark Matter comes from the weak gravitational lensing [58, 59]. According to Einstein's general relativity, massive

gravitational objects curve the space itself. Thus, photons, which travel in straight lines in the space, are deflected when they pass near such an object. The weak gravitational lensing refers to the effect when the observations come from various sources which are stretched perpendicular to the lensing object, making the effect more difficult to observe. However, it can still be studied by means of a statistical analysis that combines a system of background sources. The mass of the lensing object, and in particular, the DM component present in it, can be obtained from the shape, size and orientation of the light-emitting source. An example of the application of the weak lensing effect to DM observation is the mapping of the Bullet cluster merger [60]. A spatial offset was observed between the center of the baryonic mass and the center of the total mass that cannot be explained with a modification of the gravity and which proves that the majority of the mass in the cluster cannot be seen.

There is also evidence of DM at cosmological scales. In the hot Big Bang Theory framework, the universe was dominated by radiation on its earliest stages. This radiation was fully ionized and electromagnetic radiation was scattered, allowing the universe to be in thermal equilibrium. As the universe expanded it also cooled down and, at some point, electrons started to recombine into atoms (recombination). The formation of neutral atoms lowered the rate of scattering, which eventually stopped when the process of recombination was complete. Therefore, photons could propagate freely through the universe, and they reach the observer today only affected by the redshift. This is what we know as the Cosmic Microwave Background (CMB). The fact that the photons have travelled freely through the universe is a powerful tool to understand the early stages of the universe, since they store in their power spectrum all the information about the cosmic plasma that filled the universe and the primordial perturbations at the time of recombination [61]. The CMB was observed for the first time by Penzias and Wilson [62] as a uniform background radiation corresponding to a temperature of 2.7 K. However, the temperature observed in different directions is not exactly the same. The origin of such anisotropies comes from different effects which need to be accounted for in the calculation of the power spectrum of the CMB. The Planck collaboration has mapped the power spectrum of the CMB and found that the best

fit to data corresponds to a ΛCDM model (the Standard Model of Cosmology), in which only 4.9% of the energy content of the universe is accounted for by ordinary matter, 26.8% by DM and 68.3% by so-called Dark Energy [63].

All the above evidences rely on descriptions that use classical Newtonian gravity or Einstein's general relativity. A different approach to tackle the observations would be to modify the theory of gravity. In this way, one would avoid to include so evasive kind of matter, which is sometimes perceived to be *ad hoc*. Indeed, many of the observations on galactic scales, in particular galactic rotation curves, can be reproduced within a purely non-relativistic Modified Newtonian Dynamics (MOND) without introducing DM [64]. There have been attempts to embed it into a relativistic field theory. Nevertheless, there are many issues with these theories, i.e., momentum conservation, and they require the existence of additional fields which are not needed in some models of DM [65].

1.4.2 Dark Matter candidates

Having not yet been directly detected, there is nowadays in the literature a wide variety of candidates for DM sources. There are some general conditions that a good candidate needs to fulfill. Firstly, they should have been non relativistic at the time of the galaxy formation to be consistent with analyses of structure formation in the Universe. This is what is usually referred to as "cold" or "cool". Moreover, they ought to be stable on cosmological time scales (otherwise they would have decayed by now), they must interact very weakly with electromagnetic radiation (otherwise they wouldn't qualify as dark matter), and they must have the right relic density [5]. Some, but not all, candidates include primordial black holes, axions, sterile neutrinos, and weakly interacting massive particles (WIMPs). They are outlined in the following lines. For a detailed review see [9].

- **Primordial black holes**, **PBH**: PBHs are those formed before the era of Big-Bang nucleosynthesis. Some cosmological models [66] predict the early

[5] The relic density of a particle is a measure of the present quantity of that particle remaining from the Big Bang.

creation of a large number of black holes. However, this kind of formation is very constrained from astrophysical observations [67].

- **Axions**: The existence of axions was first postulated to solve the strong CP problem of QCD [68]; they also occur naturally in superstring theories. Although very light, axions would constitute cold DM, since they were produced non-thermally.

- **Sterile neutrinos**: These hypothetical particles are similar to Standard Model neutrinos, but without Standard Model weak interactions, apart from mixing. Stringent cosmological and astrophysical constraints on sterile neutrinos come from the analysis of their cosmological abundance and the study of their decay products [69].

- **Weakly interacting massive particles**, **WIMPs**: commonly labeled as χ, are particles with masses between 10 GeV and a few TeV, and with cross sections of approximately weak strength. These particles would have been in thermal equilibrium with the hot soup of SM particles after inflation and dropped it out when the rate of the reactions that change SM particles into WIMPs became smaller than the Hubble expansion rate of the Universe (freeze out). After the freeze out, the WIMP density would remain constant and thus one can calculate it. Candidates of WIMPs are neutral lightest superparticles (LSP) in supersymmetric models with exact R-parity [70, 71]. Among the superpartners of ordinary particles, a sneutrino and a neutralino seem the most plausible. Also non-supersymmetric extensions of the SM offer good candidates. Examples are the lightest T−odd particle in "Little Higgs" models with conserved T−parity [72, 73], or "techni-baryons" in scenarios with an additional, strongly interacting ("technicolor" or similar) gauge group [74].

1.4.3 Searches for Dark Matter

All of the evidence reported in Section 1.4.1 derives from the gravitational interaction of DM with luminous matter. While this proves its existence, it does

not illuminate its nature. Experiments designed to detect it via non-gravitational interactions are categorized in three complementary approaches: direct searches, indirect searches, and production at particle colliders. Figure 1.15 depicts a schematic view of the three kinds of experiments. Each approach is sensitive to a specific DM scenario or WIMP mass range, and will not provide a complete description of DM. On the other hand, each type of experiment is subject to different systematic uncertainties. Therefore, it is the combination of measurements from all three approaches what will shed light to the nature of DM. A detailed explanation of the complementarity of the different methods can be read in [75] while here only a brief description is given.

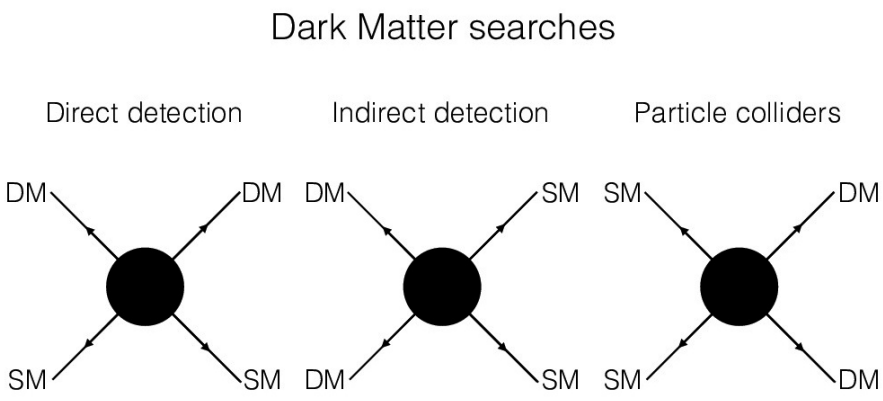

Figure 1.15: Summary of the three DM searches strategies.

1.4.3.1 Direct detection

This kind of searches target the processes in which a DM particle scatters off ordinary matter. Though rare, such events should be possible to detect, since the local density of DM on Earth is known to be $5 \times 10^{-25}\mathrm{g/cm}^3$ within a factor of 2. Depending on the target material, experiments can be sensitive to spin-dependent and spin-independent WIMP interactions with matter. Up to date, tightest constraints are given by LUX [76], PandaX-II [77] and XENON1T [78] experiments, whose results are in good agreement with the background-only

	Target	Fiducial Mass [kg]	Cross section [pb]	WIMP mass [GeV]	Ref.
Spin independent high mass (>10 GeV)					
Xenon1t	Xe	1042	7.7×10^{-11}	35	[78]
PANDAX II	Xe	364	8.6×10^{-11}	40	[77]
LUX	Xe	118	1.1×10^{-10}	50	[76]
Spin independent low mass (<10 GeV)					
LUX	Xe	118	2×10^{-9}	10	[76]
Xenon1t	Xe	1042	2×10^{-9}	10	[78]
PANDAX II	Xe	364	2×10^{-9}	10	[77]

Table 1.8: Summary of performances of the best direct detection experiments, for spin independent and spin dependent couplings. Adapted from [9].

hypothesis. The best experimental performances in therms of the upper limit on cross sections for spin-dependent and spin-independent couplings, at the optimized WIMP mass of each experiment, is summarized in Table 1.8, taken from [9], where a more extended review on the latest measurements can be read. These limits are expected to improve by one or two orders of magnitude in the future planned experiments LZ [79], DarkSide-20k [80] or Darwin [81].

1.4.3.2 Indirect detection

Indirect experiments do no aim to detect dark matter particles but the standard model particles that are produced in their annihilation or decay and thus modify the cosmic-rays fluxes. The targeted SM particles can be photons (gamma rays, X-rays, radio), neutrinos, protons and antiprotons. Fermi-LAT high-energy gamma-ray space-based telescope has placed strong constraints on WIMPs annihilating to $b\bar{b}$ and $\tau^+\tau^-$ channels and rules out DM masses below $\approx$ 100 GeV [82]. On the other hand, the ground-based telescope HESS [83] has less stringent limits and rules out DM masses above 2.5 TeV in the $\tau^+\tau^-$ channel. In spite of being abundantly produced in DM annihilations, neutrinos are very difficult to detect and thus, the limits placed by IceCube [84] and ANTARES [85] telescopes are not competitive with the ones cited above. Finally, the most stringent limits from positron measurements are derived from observations from AMS [86] telescope, which imposes stringent bounds on WIMPs with masses below 300 GeV [87].

1.4.3.3 DM production at hadron colliders

Dark matter may also be produced in high-energy particle collisions, as the ones taking place at the LHC. Once produced, Dark Matter particles are not expected to interact with the detector material and will not be directly detected. Nevertheless, their existence may be inferred from the imbalance in the visible momentum[6], just as in the case of neutrinos.

After the experience from Run-1, the ATLAS-CMS Dark Matter Forum agreed on a set of benchmark simplified models to use in the early Run-2 searches [88]. Several assumptions are made in order to harmonize the results from both experiments and different channels. In the first place, it is assumed that the DM particle is a single Dirac fermion WIMP, stable on collider timescales and non-interacting with the detector. It must, however, interact with SM hadrons. Another assumption of these models is that Minimal Flavor Violation (MFV) holds. That means that the flavor structure of the couplings between Dark Matter and ordinary particles follows the same structure as the Standard Model. Some of the models and the latest measurements are listed below.

Simplified models

Mono-X The usual production mechanism aimed at DM searches at the LHC produces a pair of DM particles from the decay of a s-channel mediator (which can be axial-vector, vector, scalar or pseudoscalar) along with additional radiation from the initial quarks or gluons participating in the reaction, resulting in missing momentum recoiling against a single energetic object such as a jet, a photon or a vector boson (and therefore known as mono-X):

$$pp \rightarrow \chi\bar{\chi} + jet/\gamma/W/Z... \tag{1.22}$$

Figure 1.16 shows an example of a Feynman diagram of one of these processes. The free parameters of the model are the masses of the mediator (M_{Med}) and of

[6]The observable in hadron colliders is the missing transverse momentum, $E_{\mathrm{T}}^{\mathrm{miss}}$.

the DM particle (m_χ) and the couplings of the mediator to quarks (g_q), to leptons (g_ℓ), and to the DM candidate (g_χ).

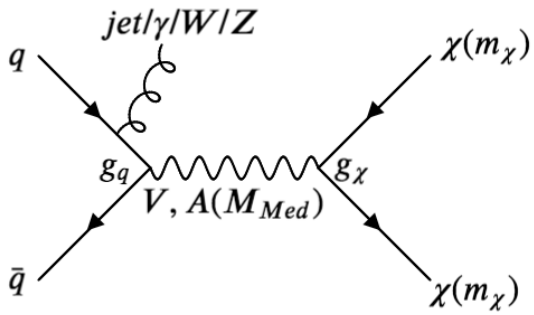

Figure 1.16: Feynman diagram for the pair production of WIMP particles, with a mediator A exchanged in the s-channel. The presence of an object from the ISR is also depicted.

ATLAS and CMS collaborations have studied these simplified models using 13 TeV and, while no excesses have been found, the results have been used to derive the limits on the mediator masses summarized in Table 1.9.

Resonances It is also possible that the mediator particle decays into a pair of SM particles, producing di-jets or di-lepton resonances. QCD dijet production predicts a smooth and monotonically decreasing distribution for the dijet invariant mass, m_{jj}, and small θ^* angles (polar angle with respect to the direction of the initial partons in the dijet center-of-mass frame). ATLAS (CMS) searches for dijet resonances [93]([94]) have placed lower limits on spin-1 mediators masses of $m_{Z'}$ < 2.1/2.9 TeV ($m_{Z'}$ < 2,9/2.1 TeV), depending on the coupling choice. Di-bjet searches [95]([96]), which target resonances in the dijet invariant mass spectrum with one or two jets identified as b-jets, exclude the Z' mass range between 1.1 and 1.5 TeV ($m_{Z'}$ < 1.5 TeV). Finally, $t\bar{t}$ resonances are also searched for in the lepton plus jets channel (combination of dilepton, lepton plus jets and all hadronic

Mediator type	Couplings g_q	Couplings g_χ	M_{Med} excluded up to (@95% CL) ATLAS	CMS	Ref.
Mono-jet + Mono-V					
Axial-vector	1/4	1	1.55 TeV (mono-jet)	1.95 TeV (mono-jet + Mono-V)	[89, 90]
Vector	1/4	1	1.55 TeV (mono-jet)	1.95 TeV (mono-jet + Mono-V)	[89, 90]
Pseudoscalar	1	1	Not sensitive	430 GeV (mono-jet)	[89, 90]
Scalar	1	1	1.67 TeV (mono-jet)	100 GeV (mono-jet + Mono-V)	[89, 90]
Mono-γ					
Axial-vector	1/4	1	1.2 TeV	700 GeV	[91, 92]
Axial-vector	0.1	1	750 GeV	—	[91]
Vector	1/4	1	1.2 TeV	700 GeV	[91, 92]
Vector	0.1	1	750 GeV	—	[91]

Table 1.9: Summary on excluded mediator masses from mono-X searches by ATLAS and CMS collaborations. They are derived assuming low DM particles masses.

chanels) [97] ([98]) and used to exclude Z' masses between 0.7 TeV and 2.0 TeV ($m_{Z'} < 2.4$ TeV).

Other Dark Matter searches by ATLAS Collaboration Other searches performed by the ATLAS Collaboration include extended Higgs sector DM models by involving an extended two-Higgs-doublet extended sector (2HDM), together with an additional mediator to DM that can be a vector or a pseudo-scalar [99–103].

1.4.4 Mono-top production at the LHC

The effort of this thesis is focused on the mono-top searches, i.e., final states with a single top and associated missing transverse momentum, and its interpretation in terms of DM. This model is different from the other mono-X searches outlined in the previous section since the final state top quark does not come from the ISR but from the decay of the mediator particle itself. A simplified model encompassing the processes leading to this phenomenology is described in Refs. [104–106], and is adopted as one of the benchmarks for Run-2 LHC searches.

Two mono-top production mechanisms are possible when it is imposed that the model Lagrangian respects the electroweak $SU(2)_L \times U(1)_\gamma$ gauge symmetry.

Another requirement demands minimality in terms of new states to supplement to the Standard Model fields.

The first production mechanism is the so-called *resonant model*. It is produced as shown in the left panel of Figure 1.17 where a colored resonance ϕ lying in the triplet representation of $SU(3)_C$ decays into a top quark and a DM particle. As examples, one finds supersymmetric models with R-parity violation in which a singly-produced top squark decays into a top quark and a long-lived neutralino [107–109], models with an extended gauge symmetry featuring leptoquarks that can decay into a particle pair constituted of a top quark and a right-handed neutrino [110] or hylogenesis scenarios for dark matter where the top quark is produced together with several dark matter candidates carrying missing momentum [111].

The second production mechanism is shown in the center and right diagrams of Figure 1.17. In this case, the mono-top state is made of a top quark and a vector state V connected to a hidden sector so that it could decay invisibly into, e.g., a pair of dark matter particles [106]. The production proceeds via flavor-changing neutral interactions of the top quark with a quark of the first or second generation and the invisibly decaying V boson.

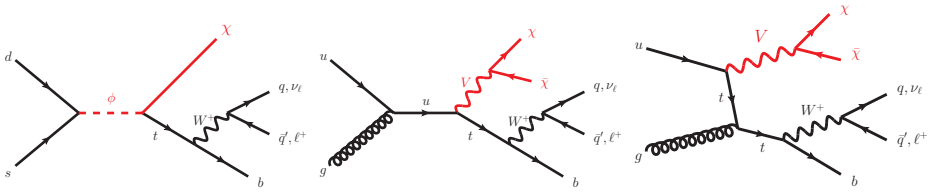

Figure 1.17: mono-top production in the context of an effective dark matter model: the leading order Feynman diagrams for the resonant (*left*) and non-resonant (s-(*center*)and t- channels(*right*)) cases are shown.

Mono-top final states can be classified in hadronic and leptonic channels, according to the decay channel of the W boson from the top quark decay. In this thesis, the leptonic decay is considered, in which the W boson decays into a lepton and its associated neutrino. This decay channel showed to be more sensitive to the non-resonant production, while the results obtained for the resonant production

mode where not competitive to those obtained in the hadronic channel. Therefore, only non-resonant models will be exploited in this thesis.

The Lagrangian describing the dynamics of this non-resonant mono-top production case is:

$$\mathcal{L}_{int} = [aV_\mu \bar{u}\gamma^\mu P_R t + g_\chi V_\mu \bar{\chi}\gamma^\mu \chi + h.c.]\,, \tag{1.23}$$

where a massive invisible vector boson V is coupled to a DM particle (represented by a Dirac fermion χ) whose strength can be controlled through a parameter g_χ. The parameter a stands for the coupling constant between the massive invisible vector boson V and top quark and γ^μ are the Dirac matrices. P_R stands for the right-handed chirality projector.

A feature of the non-resonant production that will be used later in the analysis comes from the fact that an initial state u quark is required for mono-t production, whereas mono-$\bar{t}$ production implies an initial state $\bar{u}$. Given that the LHC is an pp collider, we expect more t quarks than $\bar{t}$ quarks, since the protons contain more valence u quarks.

1.4.4.1 Complementary FCNC model

In the non-resonant production mentioned above, the mediator vector boson can decay visibly to a ut pair, as seen in Figure 1.18, leading to a final state containing two top quarks with the same electric charge tt. A combination of the results of this analysis [112] with the results presented in this thesis is ongoing at the moment.

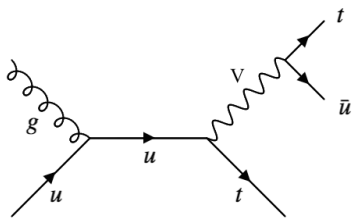

Figure 1.18: Diagram showing the FCNC production op a top quark in association with a mediator vector field which can decay to tu leading to a visible final state which contain same-sign top quarks.

2 | Experimental setup

The two analyses presented in this thesis use events which involve top quarks. Due to its large mass, the top quark requires high energy to be produced. Such high-energetic events happen in particle colliders, in which beams of particles are accelerated to high speeds and collide in specific points where the outcome of the collision is recorded. Nowadays, the world's largest and most powerful particle accelerator is the LHC at CERN, in which two beams of protons collide. The LHC was designed to both perform precision measurements of the SM predictions as well as to search for new physics. The analyses presented in this thesis use data provided by the LHC at center-of-mass energies of 8 TeV and 13 TeV, corresponding to the Run-1 data period (2012) and early Run-2 (2015 and 2016), and collected by the ATLAS detector.

This chapter introduces the experimental setup which is used to collect the data analyzed in this thesis. The basics of proton-proton (pp) collisions phenomenology, which need to be understood in order to obtain accurate results, are explained. The CERN accelerator complex and the ATLAS detector in which the collisions are recorded are also described. The quality of the final results rely on a good reconstruction of the events. The algorithms used in ATLAS to reconstruct the final state objects, which are essential in all the physics analysis, are also illustrated, including some highlights of their performance during Run-1 and Run-2.

2.1 The accelerator complex

The European Organization for Nuclear Research, CERN [113] (Conseil Européen pour la Recherche Nucléaire, in French) was founded in 1954 by the twelve founding Member States: Belgium, Denmark, France, the Federal Republic of Germany, Greece, Italy, the Netherlands, Norway, Sweden, Switzerland, the United Kingdom, and Yugoslavia. Its aim was to create a European laboratory, placed astride the Franco-Swiss border near Geneva, to study the inside of the atom. Today it is the world's largest particle physics laboratory with 22 European countries. There are also many non-European countries involved in different ways. Spain first joined CERN in 1961, left in 1969 and rejoined in 1983.

Since its foundation, the level of achievements has been remarkable. Among them, the first observation of a antinucleus was done in the Proton Synchrotron (PS), one of the first accelerators. The structure of the proton was probed in the Super Proton Synchrotron (SPS), but the major highlights of this accelerators came with the discovery of W and Z particles. At the end of 1989, the Large Electron-Positron collider (LEP) became the biggest particle accelerator, placed in a 27 km circumference underground tunnel that now hosts the LHC ring. During 11 years of research, LEP provided a detailed study of the electroweak interaction based on solid experimental foundations. Measurements performed at LEP also proved that there are three generations of particles of matter.

CERN has obtained important achievements outside particle physics, being the most remarkable the development of the Web. Info.cern.ch was the address of the world's first website and web server, running on a NeXT computer at CERN.

2.1.1 The Large Hadron Collider

The LHC [114,115] is currently the most powerful particle collider in the world. It consist of a beam injection complex in which two beams of protons acquire higher energies until they are finally injected in the 27 km LHC ring where they reach their final energy for the collisions. The accelerator complex is depicted in Figure 2.1. The source of protons in the LHC is a bottle of hydrogen gas. The hydrogen atoms are first stripped of their electrons with an electric field, and the resulting protons

are accelerated in Linac 2, the first of a chain of accelerators, up to 50 MeV. They are sent to the Proton Synchrotron Booster, which brings them up to 1.4 GeV, then to the Proton Synchrotron ring, and then to the Super Proton Synchrotron ring, accelerating to 25 GeV and 450 GeV respectively. Finally, they are injected into the LHC travelling in two opposite directions in two separated beam pipes. Acceleration of hadrons in the LHC is achieved through the use of radio frequency cavities that are tuned to a frequency and field orientation that gives the protons a push forward through each cavity.

Up to now, the LHC has delivered pp collisions at centre-of-mass energies of 7, 8 and 13 TeV. Pb–Pb collisions at centre-of-mass energies of 2.76 TeV and 5.02 TeV per nucleon and p–Pb collisions at 5.02 TeV centre-of-mass energy per nucleon have been delivered as well. The LHC's first run, Run-1, lasted from 2009 until March 2013. After a scheduled, long shutdown (LS1), the second run, Run-2 started in 2015 and will end in 2018.

Four large experiments are placed at interaction points of the LHC where the beams are brought to collision. ATLAS (A Toroidal LHC ApparatuS) [116] and CMS (Compact Muon Solenoid) [117] are multi-purpose detectors featuring extensive semi-conductor based tracking systems, large-coverage calorimeters and efficient muon detectors. They were optimized for the discovery and measurement of the Higgs boson and the search for new physics, but also pursue a considerable program of Standard Model measurements. ALICE (A Large Ion Collider Experiment) [118] focuses on the study of heavy-ion collisions. Since the decay products of B-hadrons are often expected to be found in the forward region, LHCb (LHC beauty) [119], an experiment designed for the precision study of flavour physics and CP violation, is built as a one-sided forward spectrometer. Three smaller experiments are also installed at the LHC: the TOTEM experiment [120] is devoted to measuring precisely the total proton-proton interaction cross-section as well as diffractive proton-proton physics, the LHCf experiment [121] studies large energy cosmic-rays physics; the MoEDAL experiment [122] searches for significant signals of magnetic monopoles.

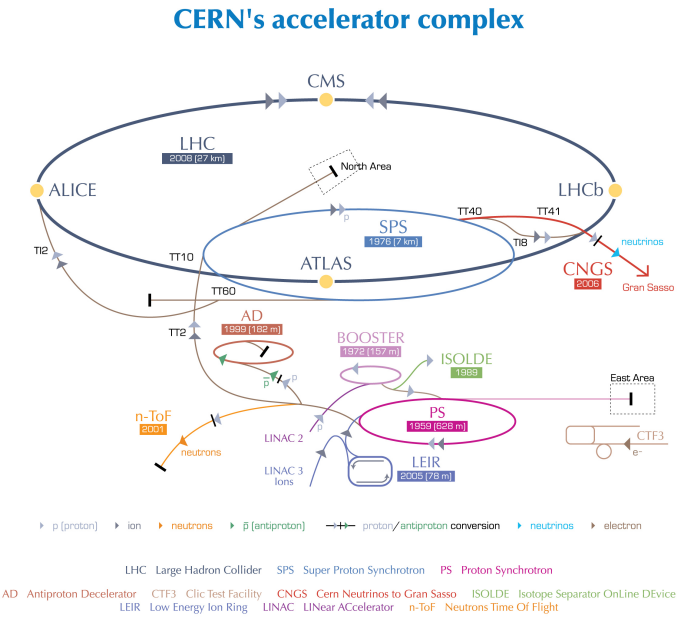

Figure 2.1: CERN accelerator complex.

2.2 Phenomenology of proton-proton collisions

At the LHC, beams of protons collide. To understand the outcome of the collisions, one first needs to understand the structure of the protons themselves. A proton is composed of three valence quarks, uud, and the sea quarks coming from gluon splitting into quark and antiquark pairs. At low energies, the momentum of the proton is mainly distributed among the three valence quarks. However, as the energy increases, gluons will also carry some of the momentum. The dynamics of the proton is therefore described by the fraction of its momentum distributed among its constituent partons (quarks and gluons) in the form of parton distribution functions, PDFs. Following subsections explain the basics to understand the hard scattering processes of interest in the proton-proton collisions as well as the accompanying interactions, with special emphasis on experimental effects such as the luminosity and pile-up.

2.2.1 Parton distribution functions

In hard proton-proton high-energy collisions, the scattering proceeds via the partonic constituents of the proton. To predict the rates of the various processes it is needed to know the distribution of the partons inside the proton. Parton distribution functions give the probability to find partons in a hadron as a function of the fraction x of the hadron momentum carried by the parton. These parton distribution functions can not be calculated due to the nonperturbative nature of QCD but rather are determined by global fits to data from deep inelastic scattering (DIS), Drell-Yan (DY), and jet measurements. The main experimental inputs come from fixed-target DIS experiments such as NMC, BCDMS, SLAC, HERA or ZEUS. Data from measurements of vector boson production in hadron-hadron colliders (Tevatron and LHC) are also used. The most common used sets of PDFs are provided by the MSTW [123], the NNPDF [124] and the CTE [125, 126] collaborations. As an example, Figure 2.2 shows parton distribution functions of a proton produced with the MSTW 2008 PDFs at NLO at two different scales [1],

[1] Q is the energy scale that characterizes the hard scattering, and typically corresponds to the momentum transfer in the given process.

$Q^2 = 10$ GeV^2 and $Q^2 = 10^4$ GeV^2, includind the associated 68% CL uncertainty bands.

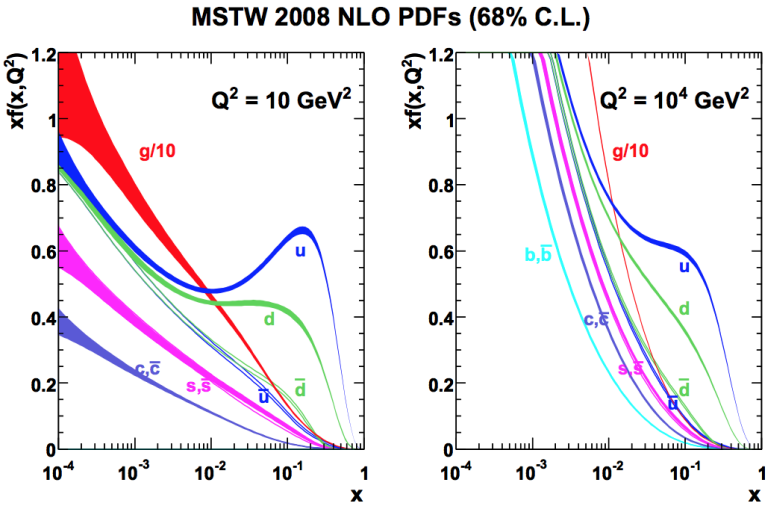

Figure 2.2: Parton distribution functions of a proton at two different values of Q^2 using the MSTW 2008 NLO PDF set [123].

2.2.2 The cross section for processes in hadron-hadron collisions

Within the QCD theory, the scattering processes at a hadron collider can be categorized in *hard* and *soft*. The hard processes are in general well understood and its properties can be predicted with good precision using perturbation theory. This is not the case for the soft processes in which non-perturbative QCD plays a major role.

The factorization theorem postulates that in hadronic collisions the cross section of a hard scattering process can be separated into a partonic cross section, which is process-dependent and calculable in pertubative QCD, and a universal part corresponding to the distribution of partons inside the colliding hadrons, given by the PDFs. The PDF for the parton a inside the hadron A carrying a fraction of the hadron momentum x_a ($f_{a/A}(x_a, Q^2)$) depends on the large momentum scale, Q^2,

which characterizes the hard scattering. The total cross section for X production in AB collision (see Figure 2.3), $\sigma_{AB\to X}$ can thus be written as

$$\sigma_{AB\to X} = \int \mathrm{d}x_a \mathrm{d}x_b f_{a/A}(x_a, \mu_F^2) f_{b/B}(x_b, \mu_F^2) \hat{\sigma}_{AB\to X}, \tag{2.1}$$

where Q^2 is chosen to be the factorization scale μ_F, which separates the long and short distance physics, i.e., above that scale one can rely on perturbation theory.

The partonic cross-section $\hat{\sigma}_{AB\to X}$ can be calculated in perturbative QCD giving rise to perturbative $\mathcal{O}(\alpha_s^n)$ corrections to the leading order cross section:

$$\hat{\sigma}_{AB\to X} = [\hat{\sigma}_{LO} + \alpha_s(\mu_R)\hat{\sigma}_{NLO} + \alpha_s^2(\mu_R)\hat{\sigma}_{NNLO} + ...]_{ab\to X}, \tag{2.2}$$

here, μ_R is the renormalization scale for the QCD running coupling. Formally, the cross section calculated to all orders is invariant under changes in μ_F and μ_R. However, when the series is truncated, a choice of the two scales is needed and the uncertainty on the prediction due to unknown higher order corrections becomes evident as different values of the scales yield to different numerical results. A standard choice is $\mu_F = \mu_R = m_X$.

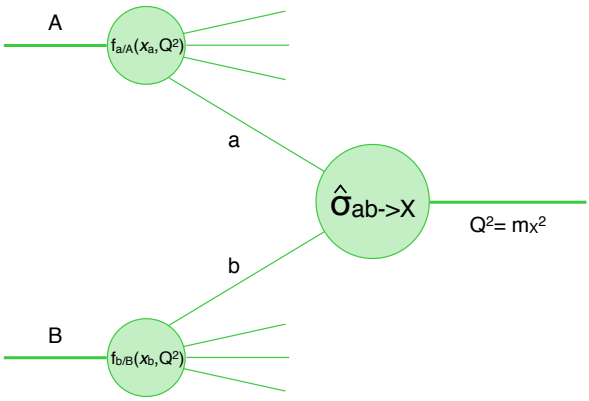

Figure 2.3: Schematic diagram of particle production in a proton-proton collision.

2.2.3 Underlying event

The underlying event, first introduced by the CDF collaboration [127], refers to all the activity accompanying the hard scattered process. As an illustrative example, Figure 2.4 depicts a proton-proton collision. The resulting event contains the particles that originate from the two outgoing partons product of the $2 \to 2$ hard scattering process (plus initial and final state radiation) and the beam-beam remnants (namely, the particles that come from the breakup of the protons). The underlying event is everything except the two outgoing hard scattered jets, i.e., consists of the beam-beam remnants plus initial and final state radiation. These residual particles may lead to multiple parton interactions within one collision which need to be modeled to properly account for its impact on the other high p_{T} measurements and the detector resolution. A common model to simulate the underlying event, including hard and soft interactions, parton distributions, initial- and final-state parton showers, multiparton interactions, fragmentation and decay, is implemented in PYTHIA [128] and assumes that multiple interactions take place in a substantially independent way so that Poisson statistics can be used, and that they can be described by perturbative QCD above a certain scale p_{T}^{min}, which becomes one of the main parameters of the model. An alternative model is implemented in HERWIG [129].

2.2.4 Luminosity and pile-up

In a proton-proton collider, the instantaneous luminosity, L, is the parameter thar relates the cross-section, σ, of the inelastic proton-proton process to the corresponding event rate, R (number of inelastic proton-proton collisions per second)

$$R = L \times \sigma, \tag{2.3}$$

which has units of $\mathrm{cm}^{-2}\mathrm{s}^{-1}$ or $\mathrm{fb}^{-2}\mathrm{s}^{-1}$.

Since the particle beams come in bunches, the event rate can be written in terms of the average number of inelastic interaction per bunch crossing (μ) and the bunch crossing frequency, f, so that

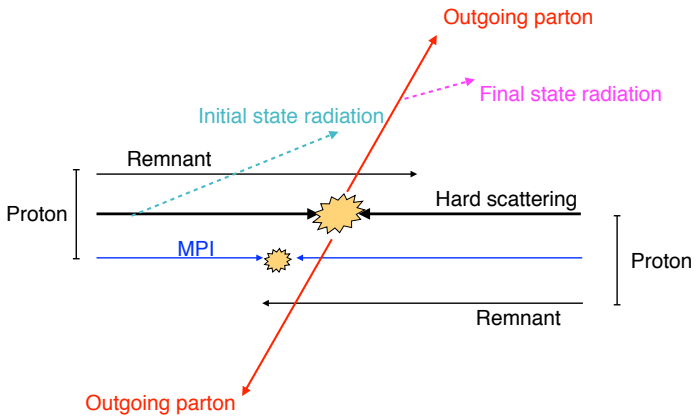

Figure 2.4: An example of a proton-proton collision: The resulting event contains particles that originate from the two outgoing partons and from the initial and final state radiation and particles that come from the break-up of the protons (beam-beam remnants). The underlying event is everything except the two outgoing hard scattered jets, i.e. consists of the beam-beam remnants plus initial and final state radiation.

$$L = \frac{R}{\sigma} = \frac{\mu f}{\sigma}. \tag{2.4}$$

In terms of the beam parameters, the above expression reads

$$L = \frac{N_1 N_2}{4\pi\sigma_x\sigma_y} f, \tag{2.5}$$

where N_1 and N_2 are the number of particles per bunch in each colliding beam and σ_x and σ_y are the Gaussian widths in the horizontal and vertical plane per bunch (it is assumed that the transverse particle bunch profile is Gaussian).

The integral of the instantaneous luminosity over time gives the integrated luminosity, $\mathcal{L}$, which is usually expressed in fb^{-1}. Figure 2.5 shows the cumulative luminosity delivered and recorded by ATLAS for the 2012 8 TeV data in Run-1 and 2015 and 2016 13 TeV data in Run-2, which correspond to the datasets analyzed in this thesis.

Another important ingredient to be taken into account is the concept of pile-up

$$\mu = \frac{N_1 N_2}{4\pi\sigma_x\sigma_y} \sigma, \tag{2.6}$$

which quantifies the fact that the detector can be affected by several events at the same time, i.e., that multiple independent interactions occur during one bunch crossing (*in time pile-up*). A similar effect appears when the spacing between the bunches is shorter than the response time of the detectors, so additional collisions from different bunches are recorded simultaneously (*out of time pile-up*). The average pile-up for the different data periods are shown in Table 2.1.

2.3 The ATLAS detector

The ATLAS detector [132] is a general-purpose detector designed to cover the widest range of physics produced by the LHC. Its design and operation is possible thanks to the collaborative effort among 38 nations and 3000 scientific authors. It is located 100 m underground in one of the LHC ring interaction points. As other general-purpose high-energy-physics experiments, it has a cylindrical shape,

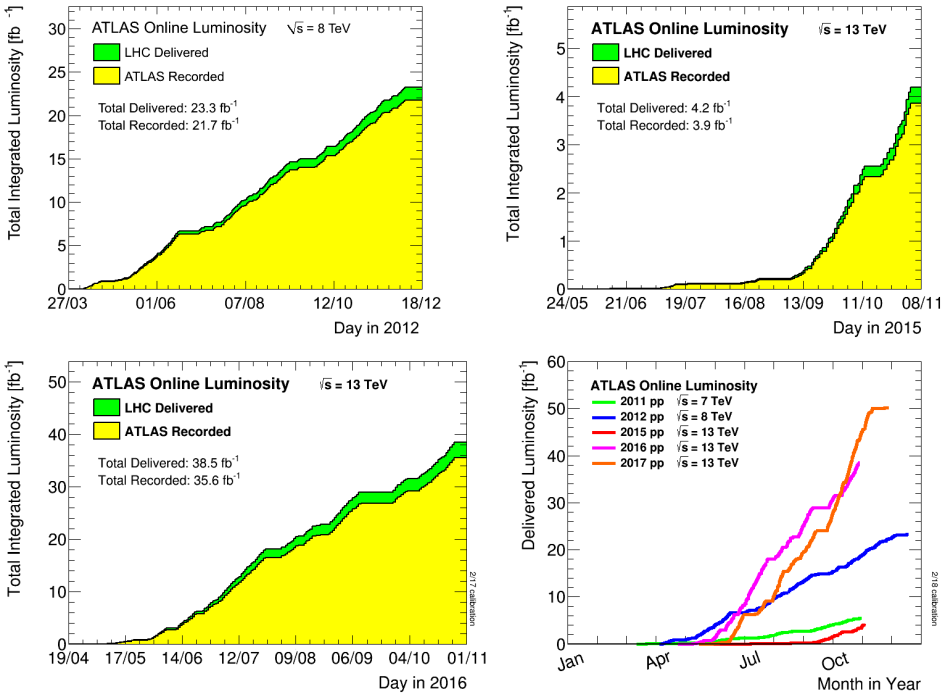

Figure 2.5: Cumulative luminosity versus time delivered to (green) and recorded by ATLAS (yellow) during stable beams for pp collisions for the data periods used in this thesis: 8 TeV in 2012 (*top-left*) and 13 TeV in 2015 (*top-right*) and 2016 (*bottom-left*). The delivered luminosity accounts for luminosity delivered from the start of stable beams until the LHC requests ATLAS to put the detector in a safe standby mode to allow for a beam dump or beam studies. The recorded luminosity reflects the data taking inefficiency. The *bottom-right* panel compares the cumulative luminosity versus day delivered to ATLAS during stable beams and for high energy pp collisions for all data-taking periods (2011, 2012, 2015, 2016 and 2017) [130,131].

Data period	$\sqrt{s}$	$\langle\mu\rangle$
2011	7 TeV	9.1
2012	8 TeV	20.7
2015	13 TeV	13.4
2016	13 TeV	25.1
2017	13 TeV	37.8
2018	13 TeV	38.3

Table 2.1: Average number of interactions per crossing for the different data periods collected by the ATLAS detector.

with dimensions of 44 m of length and a diameter of 25 m, and its different components, designed to measure a specific property of the particles emerging from the collisions, are arranged in layers. Figure 2.6 shows a cut-away view of the ATLAS detector; it is composed of three subsystems: the innermost of them is the tracking system, in which the charged particles are reconstructed. Surrounding the tracking system, the calorimeters determine the energy of the electromagnetic and strongly interacting particles. Finally, in the outermost part, the muon spectrometer measures the momentum of muons, the only charged particle that can propagate through the calorimeters. In addition to the subdetectors, the ATLAS experiment counts with a magnet system which bends the trajectories of the charged particles, aiding its reconstruction and momentum determination.

2.3.1 Inner detector

The innermost subsystem of the ATLAS experiment is the Inner Detector (ID) [133]. It is designed to provide a good reconstruction of the tracks of the charged particles, with excellent momentum resolution, as well as measurements of primary and secondary vertexes, covering a pseudorapidity range of $|\eta| < 2.5$ [2]. With expected ~ 1000 particles emerging from the interaction point, a fine

[2] ATLAS uses a right-handed coordinate system with its origin at the nominal interaction point (IP) in the centre of the detector and the z-axis along the beam pipe. The x-axis points from the IP to the centre of the LHC ring, and the y-axis points upwards. Cylindrical coordinates (r, ϕ) are used in the transverse plane, ϕ being the azimuthal angle around the z-axis. The pseudorapidity is

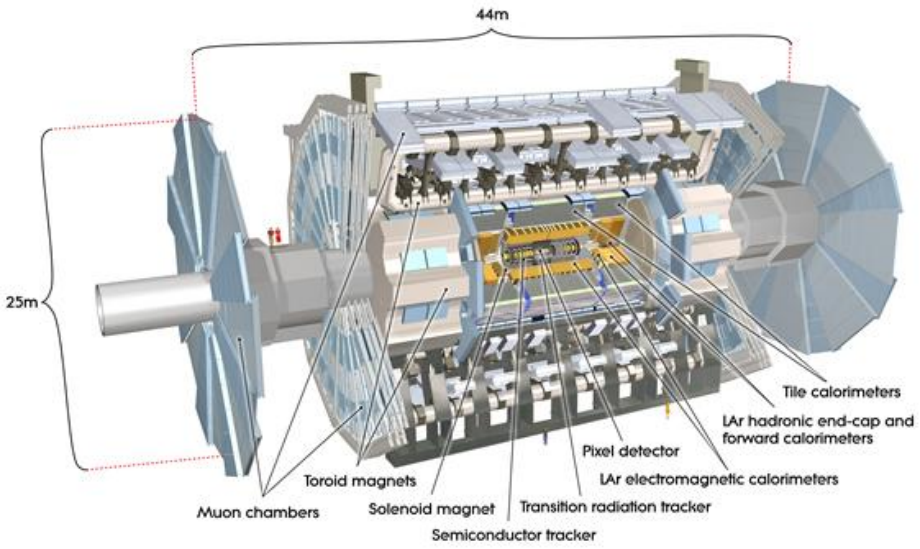

Figure 2.6: Schematic view of the ATLAS detector.

granularity is needed to accomplish its objectives. Its coverage range from 1082 mm of radius to 6.1 m of length, and it is embedded in a 2T solenoidal magnetic field that bends the trajectories of the charged particles, allowing for momentum and charge measurements. It is composed of three complementary subdetectors: the Pixel and the SemiConductor Tracker (SCT), which provide high-resolution pattern recognition via the usage of discrete space-points, and the Transition Radiation Tracker (TRT) that surrounds them and is made up of many layers of gaseous straw tube elements interleaved with transition radiation material. During LS1, the Insertable B-Layer (IBL) was inserted and commissioned to become an additional layer of the existing Pixel Detector [134]. Figure 2.7 depicts a 3D visualization of the sctructure of the barrel of the ID. Table 2.2 summarizes the main characteristics of the ID subdetectors. The excellent performance of the ID relies on a good alignment of all of its modules. Details on this procedure will be given in Chapter 3. In particular, a good vertex reconstruction is crucial to reconstruct the b-tagged

defined in terms of the polar angle θ as $\eta = -\ln\tan(\theta/2)$. Angular distance is measured in units of $\Delta R \equiv \sqrt{(\Delta\eta)^2 + (\Delta\phi)^2}$.

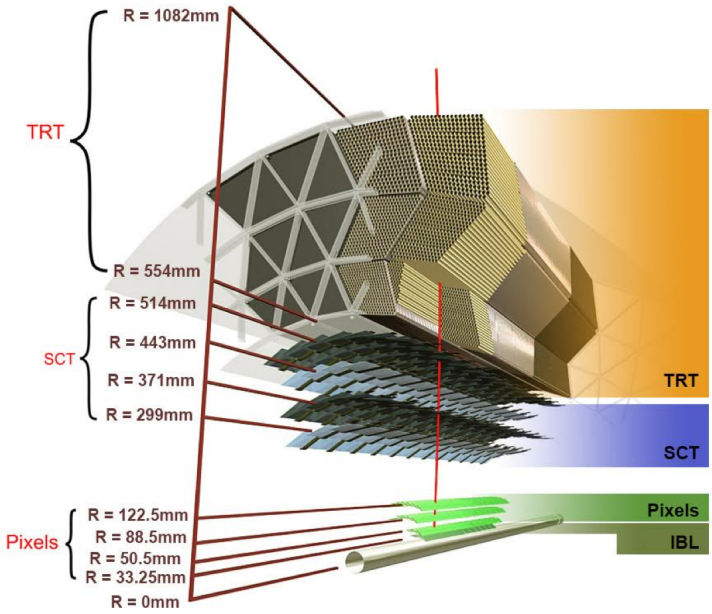

Figure 2.7: 3D visualisation of the structure of the barrel of the ID. In the picture are shown the beam pipe, the IBL, the Pixel layers, the four cylindrical layers of the SCT and the 72 straw layers of the TRT.

jets (jets likely to proceed from the hadronization of a b quark), which are a key ingredient of the two physics analysis presented in this thesis (Chapter 4 and 5). A brief description of the different components follows:

- **IBL**: the Insertable B-Layer is an additional layer added to the Pixel system as the closest layer to the interaction point [134]. This detector layer improves the tracking performance, specifically by enhancing the impact parameter resolution, which directly affects b-tagging and vertexing operation. It consists of 280 silicon pixel modules arranged on 14 azimuthal staves surrounding the beam pipe at a mean radius of 33.2 mm. Each stave comprises a 70 cm-long mechanical structure called the bare stave which holds a titanium cooling pipe. The staves have two types of sensors; there are 12 planar pixel sensors that are placed at the central region of the stave (covering the region of $|\eta| <$

2.7), each of which is connected to two front-end chips, and four 3D sensors, each of which is connected to a single front-end chip, and that are placed on the both extremities of the stave ($2.7 < |\eta| < 3$). Therefore, each stave mounts 32 pixel front-end chips in total, which are connected to the readout service bus, the Stave Flex, which is glued on the other side of the bare stave. The expected hit resolution is 8 μm in $r\phi$ and 40 μm in z.

- **Pixel**: the Pixel detector is composed of 1744 identical modules arranged in three concentric barrel layers around the beam axis and two end-caps perpendicular to the z axis with three disks each. The pixel elements have an intrinsic resolution of 10 μm in the $r\phi$ and 115 μm in the long pixel direction (along the beam pipes for the modules in the barrel and radial for the end-caps). Each track will create three hits on average on the Pixel detector.

- **SCT**: the SemiConductor Tracker is composed of 4088 modules arranged in four barrel layers around the Pixel detector and nine disks on each of the end-caps. Each module is composed by two silicon micro-strips sensors of 80 μm pitch in the barrel and of 85 μm on average in the end-caps that are glued back-to-back with a stereo angle of 40 mrad to provide a two dimensional measurement ($r\phi$ and z). The intrinsic accuracies per module are 17 μm across the strips, and 580 μm along the strips. Each track will create four hits on average on the SCT detector.

- **TRT**: the Transition Radiation Tracker is composed of $\sim$ 300.000 straw tubes arranged in parallel to the beam pipe in the barrel and radially in the end-caps. Each tube, with a diameter of 4 mm, is filled with gas, and the space between the tubes is filled with a different material where transition radiation photons are produced when a particle traverses it. The resolution of the tubes is 130 μm. Each track leaves around thirty hits in the TRT.

Subdetector	Element size	Intrinsic resolution [μm]
IBL	$50\mu\text{m} \times 250\mu\text{m}$	8×40
Pixel	$50\mu\text{m} \times 400\mu\text{m}$	10×115
SCT	$80\mu\text{m}$	17×580
TRT	$4\mu\text{m}$	130

Table 2.2: Summary of the main characteristics of the ID subdetectors. The intrinsic resolution of the IBL, the Pixel and the SCT detectors is reported along $r\phi$ and z, while only $r\phi$ is considered for the TRT.

2.3.2 Calorimeters

The ID is surrounded by an electromagnetic calorimeter (ECAL) covering the pseudorapidity region $|\eta| < 3.2$, a hadronic barrel calorimeter covering $|\eta| < 1.7$, hadronic end-cap calorimeters covering $1.5 < |\eta| < 3.2$, and forward calorimeters covering $3.1 < |\eta| < 4.9$. The task of the calorimeters is to identify and measure the energy of charged and neutral particles and jets by stopping them. The only known particles that escape the calorimeters material are neutrinos and muons. However, the missing transverse momentum, $E_{\text{T}}^{\text{miss}}$, associated to the neutrino is also measured in the calorimeters as the sum of all the measured energy deposits in the transverse plane. The ECAL has a fine granularity that ensures the precision measurement of electrons and photons, while the hadronic calorimeters (HCAL) have a coarser granularity, sufficient to reconstruct jets and $E_{\text{T}}^{\text{miss}}$.

Calorimeters are composed by a mixture of passive and active material. The passive material, also referred to as absorber, is a dense material which cause the particle to initiate a shower. The active material, which is interleaved with the absorbers, detects the particles created in the shower.

- **Electromagnetic calorimeter**: it is divided into a barrel part and two end-caps. The barrel part is split in two identical half-barrels separated by a smal gap at $z = 0$. Each end-cap calorimeter is mechanically divided into two coaxial wheels. In this subdetector, the passive material consists of lead arranged in an accordion shape to ensure a complete azimuthal coverage

without cracks. The active material is Liquid Argon and thus this subdetector is also known as LAr calorimeter. The total amount of material in the ECAL corresponds to 25-35 radiation lengths, X_0, [3] and to 2-4 nuclear interaction lenghts[4], λ, over the whole pseudorapidity range. It is surrounded by a cryostat to ensure the needed low temperatures to operate.

- **Hadronic calorimeter**: two different technologies are used in this sudbetector. For the barrel part, which covers the range $|\eta| < 1.7$, the iron scintillating-tile technique is used. This part is called thus, the Tile Calorimeter (TileCal). Liquid Argon is used again in the end-cap regions, covering the range $1.5 < |\eta| < 4.9$. In order to reduce the punch-through of the hadronic showers into the muon system, the hadronic calorimeter needs to be very thick. Its total thickness is 11 interaction lengths at $\eta = 0$. Together with the wide $|\eta|$ coverage, this will also guarantee a good $E_{\mathrm{T}}^{\mathrm{miss}}$ measurement, which is important for many physics signatures and in particular for the dark matter searches presented in this thesis (Chapter 5).

2.3.3 Muon spectrometer

The outermost ATLAS subsystem is designed to identify and reconstruct the trajectories of the muons. The muon spectrometer, MS, is based on the magnetic deflection of muon tracks in the large barrel toroid ($|\eta| < 1.0$) and end-cap magnets ($14 < |\eta| < 2.7$). Apart from the toroids, the muon spectrometer consists on trigger and high-precision tracking chambers. The chambers are arranged in three cylindrical layers (stations) that are situated around the beam axis in the barrel region and vertically in the end-caps. Four different technologies are used. Over most of the $|\eta|$ range, up to $|\eta| < 2.7$, the Monitored Drift Tubes provide a precision measurement of the track coordinates in the principal bending direction of the magnetic field. In the most forward regions, the Cathode Strip Chambers provide

[3] The radiation length, X_0, is both the mean distance over which a high-energy electron loses all but 1/e of its energy by bremsstrahlung, and 7/9 of the mean free path for pair production by a high-energy photon.

[4] Nuclear interaction length, λ, is the mean path length required to reduce the numbers of relativistic charged particles by the factor 1/e as they pass through matter.

a high granularity to withstand the demanding rate and background conditions. Resistive Plate Chambers in the barrel region and Thin Gap Chambers in the end-caps region are used for triggering and measuring the coordinate orthogonal to the bending direction.

2.3.4 Magnet system

The good momentum resolution measurements in the ID and MS reckon on the bending power of the magnet system. Its unusual configuration and large size make the magnet system a considerable challenge requiring careful engineering. The ATLAS superconducting magnet system is composed of a central solenoid (CS) that provides the ID with a magnetic field, surrounded by a system of three air-core toroids which generate a magnetic field for the MS. In total, the magnet system is 26 m in length and 20 m in diameter. Two end-cap toroids are inserted at each end of the barrel toroid, lining up with the CS. The CS provides a central field of 2 T. The toroids provide a peak magnetic field of 3.9 T at the barrel and 4.1 T a the end-caps.

2.3.5 Triggers

Given the limited computing resources for offline storage and data processing, not all the events delivered can be saved. The trigger system is in charge of deciding whether a given beam crossing is kept for later study or not. An efficient trigger system is of crucial importance since at its design luminosity, the LHC is expected to have 40 MHz bunch crossing rate, with an average of 25 interactions per bunch crossing.

During Run-1, the ATLAS trigger system [135] was split in three levels: the first level (L1) [136] and the High Level Trigger (HLT) [137] which consists of the second (L2) and third (Event Filter, EF) levels. Each level refines the decicions made at the previous level and, if needed, applies additional selection criteria. During the Run-1 operation at instantaneous luminosities of up to $8 \times 10^{33}\mathrm{cm}^{-2}\mathrm{s}^{-1}$ and $\sqrt{s}$ up to 8 TeV, the ATLAS trigger system collected more than 3 billion events. For the Run-2, the LHC has increased its energy to $\sqrt{s}$ = 13 TeV, and the nominal

bunch-spacing has decreased from 50 to 25 ns. Due to the higher energy, the trigger rates are on average 2.0 to 2.5 times larger for the same luminosity and with the same trigger criteria. Moreover, due to additional interactions from neighbouring bunch-crossings, certain trigger rates have increased as well. Therefore, several upgrades were introduce during the LS1 in preparation for Run-2 [138, 139]. In particular, L2 and EF were merged in a single HLT.

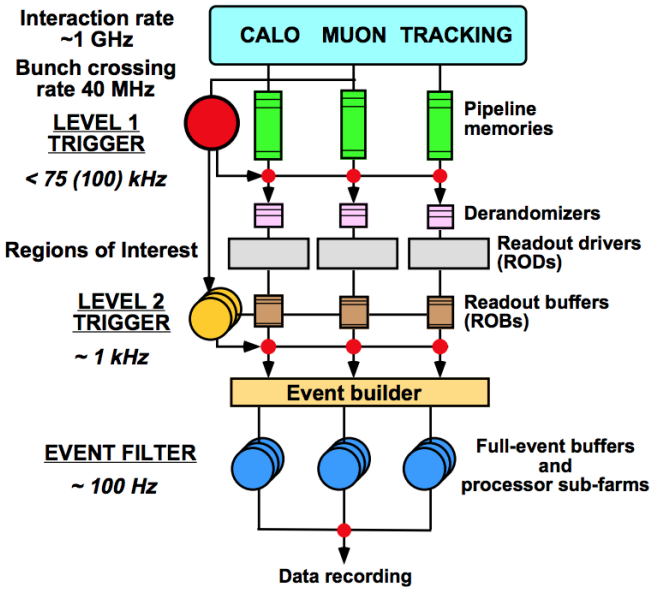

Figure 2.8: Diagram of the ATLAS trigger/DAQ system [136].

Figure 2.8 depicts an schematic view of the trigger and data acquisition (DAQ) systems of ATLAS experiment during Run-1. In a first step, the L1, which is implemented in fast custom electronics, reduces the rate of the detector signals to a maximum of 75 kHz with a latency of 2.5 μs. Besides, it identifies *Regions of Interest, RoI* within the detector to be further investigated by the HLT. These regions include information on the position (η and ϕ) and p_{T} range of the candidate objects. The next two levels are software-based. The L2 system has access to the full precision and granularity of the event data and it uses this information to reduce the rate to 3 kHz with an average processing time of 40 ms/event. Ultimately, the final

selection of the events that will be stored permanently is done in the EF, where the algorithms are based on offline code. The EF is designed to reduce the rate to ~ 200 Hz with an average processing time of ~ 4 s/event.

In the two analyses presented in this thesis, single-lepton (electron and muon) triggers are used.

The performance of electron triggers is studied using a tag-and-probe method in a sample of $Z \longrightarrow ee$ events (see the following sections for details on electrons identification and reconstruction) [139]. The method uses events triggered by a single-electron trigger and requires two offline reconstructed electrons with an invariant mass between 80 and 100 GeV. After identifying the electron that triggered the event (tag electron), the other electron (probe electron) is unbiased by the trigger selection, thus allowing its use to measure the electron trigger efficiency. HLT electrons (L1 EM objects) are matched to the probe electron if their separation is $\Delta R < 0.07(0.15)$. The trigger efficiency is calculated as the ratio of the number of probe electrons passing the trigger selection to the number of probe electrons. During Run-1, a different method, the orthogonal trigger method, was also used [135]. This method utilizes samples of $W \rightarrow e\nu$ decays and give results in agreement with those from the tag-and-probe method.

The top panel of Figure 2.9 compares the efficiencies of the e15_medium and e20_loose (loose and medium refer to identification requirements, see Section 2.4.2) triggers at the EF, measured for Run-1 data in W boson events with those measured in Z boson events as a function of the offline reconstructed electron transverse energy and pseudorapidity. The bottom panel of Figure 2.9 shows the efficiency of the combination of the lowest single-electron trigger e24_lhmedium_L1EM20VH and the high transverse momentum electron trigger e120_lhloose with respect to the offline objects as a function of the offline reconstructed electron transverse energy and pseudorapidity for 2015 data [139].

The L1 and HLT muon efficiencies are determined using a tag-and-probe method with $Z \rightarrow \mu\mu$ candidate events. Events are required to contain a pair of reference muons with opposite charge and an invariant mass within 10 GeV of the Z mass. Reference muons reconstructed offline using both ID and MS information are required to be inside the fiducial volume of the muon triggers ($|\eta| < 2.4$) and

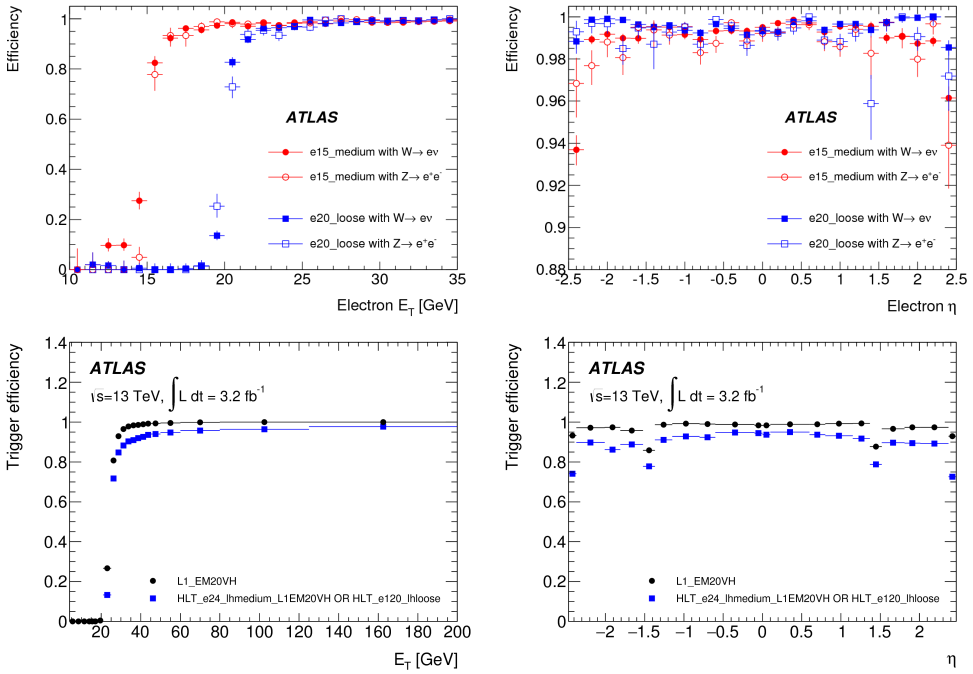

Figure 2.9: *Top:* Efficiencies for the e15_medium and e20_loose triggers, measured with respect to offline tight electrons in $W \to e\nu$ and $Z \to ee$ events as a function of E_{T} and η (Run-1 data) [135]. *Bottom:* efficiency of the combination of the lowest single-electron trigger e24_lhmedium_L1EM20VH and the high transverse momentum electron trigger e120_lhloose with respect to the offline objects as a function of the offline reconstructed electron transverse energy and pseudorapidity (Run-2 data) [139].

pass the medium identification requirements (see the following sections for details on muons identification and reconstruction). The left panel of Figure 2.10 shows the efficiencies in the barrel of the muon triggers with 13 GeV and 20 GeV thresholds and the MS-only trigger with a 40 GeV threshold for the Run-1 data [135]. The right panel shows the absolute efficiency of the L1_MU15 trigger and the absolute and relative efficiencies of the logical 'or' of mu20_iloose and mu50 as a function of the p_{T} of the offline muon track for the Run-2 data [139].

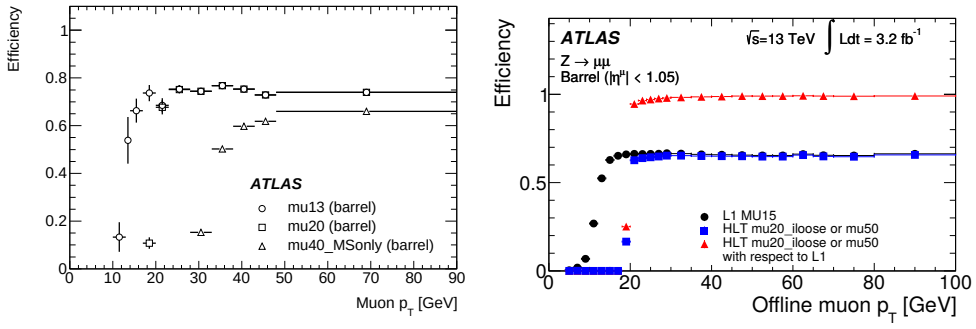

Figure 2.10: *Left:* efficiencies in the barrel of the muon triggers with 13 GeV and 20 GeV thresholds and the MS-only trigger with a 40 GeV threshold for the Run-1 data [135]. *Right:* absolute efficiency of the L1_MU15 trigger and the absolute and relative efficiencies of the logical 'or' of mu20_iloose and mu50 as a function of the p_{T} of the offline muon track for the Run-2 data [139].

Trigger selection Single lepton triggers are used in the two analysis presented in this thesis. For the Run-1 analysis, events in the electron channel are selected if the electron is isolated and its p_{T} is at least 24 GeV. Events are selected as well if their electron p_{T} is above 60 GeV, without any isolation requirement. Events with a muon are selected if the muon p_{T} is at least 24 GeV and are isolated or if their muon p_{T} is above 36 GeV with no isolation requirement.

For the Run-2 analysis, the trigger requires a p_{T} of at least 24 GeV (26 GeV) for electrons and 20 GeV (26 GeV) for muons for the 2015 (2016) dataset if they satisfy the isolation criteria. Events with relaxed isolation and identification requirements are also accepted if they have a p_{T} above 60 GeV (medium) or 120 GeV (loose)

for 2015 electrons, above 60 GeV (medium) or 140 GeV (loose) for 2016 electrons, and 50 GeV for muons (2015 and 2016).

2.4 Object reconstruction

The information from all the subdetectors is combined to transform the detector signals into reconstructed physics objects: electrons, muons, taus, photons or jets. The precision measurements involving top quarks require an excellent reconstruction of its decay products, namely electrons, muons, jets, b-jets and neutrinos (via the $E_{\mathrm{T}}^{\mathrm{miss}}$ reconstruction). An accurate identification of the $E_{\mathrm{T}}^{\mathrm{miss}}$ is also needed in searches for which a large amount of energy corresponding to undetected particles is expected to be unmeasured. The following subsections give a brief description of the methods used to reconstruct and identify these particles.

2.4.1 Tracking and vertexing

The trajectories of charged particles (tracks) are reconstructed in the ID. The *baseline* track reconstruction algorithm used during Run-1 [140] begins with the conversion of the raw data from the Pixel and SCT detectors into three-dimensional measurements referred to as space-points [141]. A space-point can come from a signal in a single pixel or from signal in a collection of neighboring pixels, forming a cluster. When the spatial separation of two or more charged particles traversing a module is only few pixels, their associated clusters can overlap and form merged clusters which are resolved using a neural network (NN). The merged clusters are then copied to create two or three *split* clusters.

The next step consists on iteratively finding tracks from combinations of three space-points from different detector layers. These combinations, known as seeds, can be composed of space-points purely from Pixel, from SCT or from one (two) points from the Pixel and two (one) from the SCT, leading to four types of seeds with varying purity (fraction of seeds that result in good quality tracks). To maximize purity, some quality criteria are applied.

Since all reasonable combinations of tracks have been made in the previous step, there are a number of track candidates with incorrectly assigned space-points.

To solve this, an ambiguity processor is used. The candidate tracks are scored in a reward–penalty schema with respect to one another with the following criteria. To favor fully reconstructed tracks over short track segments, each additional measurement associated with a track increases the track candidate score. The measurements from different sub-detectors are weighted differently, preferring the precision measurements (e.g. pixel clusters) and downgrading measurements from less precise detector parts. The concept of a hole on a track is introduced as a measure of the detector acceptance and efficiency. A hole represents a measurement on a detector module that is expected, given the trajectory predictions, but not observed. The presence of holes reduces the overall track score. The χ^2 of the track fit is also used to penalize poor-quality candidates. Finally, the logarithm of the track transverse momentum is considered as a criterion to promote energetic tracks and to suppress the larger number of tracks formed from incorrect combinations of clusters, which tend to have low measured p_{T}. After the reconstruction of tracks in the pixel and the SCT detectors, the successful candidates are extrapolated into the TRT volume and combined with measurements there.

The same procedure is used in Run-2 with some small modifications [142]. The major change is delaying the decision on how to use the information encapsulated within the NN. While in Run-1 it was used at the moment of cluster reconstruction to create the split clusters, in Run-2 this information is used in the track ambiguity solver. The other changes appear as a tuning of the existing cuts to optimize efficiency and rejection.

The correct reconstruction of hard-scatter interactions and full kinematics of the event relies on a good reconstruction of primary vertexes [143, 144], defined as the points in space where the hard interaction interactions occur. The reconstruction is carried out in two steps. The first stage consists on the association of reconstructed tracks to vertex candidates (vertex finding). In the second step, the position of vertex candidates is estimated via an iterative fit in which the less compatible tracks are down-weighted in each iteration. The output of the vertex reconstruction algorithm is a set of three dimensional vertex positions and their covariance matrices.

In the two analyses presented in this thesis, events are required to have at least one vertex candidate with at least five (two for the Run-2 analysis) tracks with $p_{\mathrm{T}} > 400$ MeV. From the available candidates, the primary vertex is taken to be the vertex candidate with the largest sum of squared transverse momenta of all associated tracks.

Secondary vertexes are also reconstructed and used to identify the flavor of jets, as it will be explained in the following. A good performance of the tracking system, which has a direct impact in the physics analyses, rely on a good alignment of the ATLAS ID. Some alignment basics and early Run-2 data results will be given in Chapter 3.

2.4.2 Electrons

Offline electron candidates in the central region of the detector ($|\eta_{cluster}| < 2.47$) are reconstructed from energy deposits in the electromagnetic calorimeter associated with a particle track from the inner detector [145–147] following a 4-steps procedure. First, a seed cluster is reconstructed from a longitudinal tower[5] with a total cluster energy above 2.5 GeV. Secondly, the ID track is reconstructed in two stages: pattern recognition and track fit. This is complemented with an electron-specific pattern recognition and track fit that are introduced to recover losses from bremsstrahlung. The obtained tracks are loosely matched to EM cluster using the distance in η and ϕ between the position of the track, after extrapolation in the calorimeter middle layer, and the cluster barycenter. The matching of the track candidate to the cluster seed completes the electron reconstruction procedure.

To determine whether the reconstructed electron candidates are prompt electrons [6], two different algorithms for electron identification are applied: cut-based and likelihood (LH) identifications, for the Run-1 and Run-2 analyses,

[5] The $\eta \times \phi$ space of the EM calorimeters is divided into a grid of $N_\eta \times N_\phi = 200 \times 256$ elements of size $\Delta\eta^{tower} \times \Delta\phi^{tower} = 0.025 \times 0.025$ called towers. Inside each of these elements, the energy of cells in all longitudinal layers is summed into the tower energy.

[6] Muons and electrons can be separated into two types. Prompt leptons are participants in the hard-scatter process, such as decay products of the W, Z and Higgs bosons. Non-prompt leptons are the weak decay products of b-jets and c-jets, whose lifetimes are relatively long. As a result, their decay products can be traced back to a vertex that is displaced from the hard-scatter process.

respectively. There are three quality categories with increasing background rejection power: Loose, Medium and Tight. The electrons selected with Tight are a subset of the electrons selected with Medium, which in turn are a subset of Loose electrons. In the cut-based identification, sequential cuts on discriminating variables are used: with increasing tightness more variables are added and requirements are tightened on the variables already used in the looser selections. The LH based method is a multivariate analysis (MVA) technique that simultaneously evaluates several properties of the electron candidates when making a selection decision.

Isolation criteria are in addition required in order to identify prompt leptons. Two isolation variables are used. The first one is a calorimetric isolation energy, $E_{\mathrm{T}}^{cone0.2}$, defined as the sum of transverse energies of topological clusters within a cone of $\Delta R = 0.2$ [7] around the candidate electron cluster. The second variable is a track isolation, $p_{\mathrm{T}}^{varcone0.2}$, defined as the sum of transverse momenta of all tracks, satisfying quality requirements, within a cone $\Delta R = \min(0.2, 10\,\mathrm{GeV})/E_{\mathrm{T}}$ around the candidate electron track and originating from the reconstructed primary vertex. The values of the cuts are chosen in order to have an isolation efficiency of 90% (99%) for electrons from $Z \to ee$ decays with $p_{\mathrm{T}} = 25(60)$ GeV.

Electron selection The electrons used in the two physics analyses presented in this thesis are required to be tight. Cuts on the impact parameter [8] are applied; for the Run-1 analysis, the electron candidates should have a longitudinal impact parameter z_0 from the primary vertex smaller than 2 mm, $z_0 < 0.5$ mm must be satisfied for the Run-2 analysis. Moreover, the transverse impact parameter significance of the candidate must be smaller than 5 in the latter. In addition, events with electrons falling in the calorimeter barrel-endcap transition region $1.37 < |\eta_{cluster}| < 1.52$, which contains a large amount of inactive material, are rejected.

[7] $\Delta R = \sqrt{(\Delta\eta)^2 + (\Delta\phi)^2}$

[8] The impact parameter determines the position of the track with respect to the closest point to the global Z axis.

Electron candidates with relaxed identification criteria (loose and medium) and with no isolation cuts applied, are also used in the analyses for the data-driven estimate of multijet backgrounds.

2.4.2.1 Electrons modeling uncertainty estimation

The efficiencies of the reconstruction and identification algorithms are measured in data and evaluated in simulated samples using the tag and probe method in electrons from $Z \rightarrow ee$, $Z \rightarrow ee\gamma$ and $J/\Psi \rightarrow ee$ decays. The efficiency to detect an electron is divided into different components, namely trigger, reconstruction and identification efficiencies and the efficiency to satisfy additional analysis criteria, like isolation. In order to achieve reliable results, the simulated MC samples need to be corrected to reproduce the measured data efficiencies as closely as possible. This is achieved by a multiplicative correction factor defined as the ratio of the efficiency measured in data to that in the simulation (escale factors, SFs). This ratios are applied as correction factors in the analyses and their uncertainties are propagated accordingly. The left and right panels of Figure 2.11 show the measured combined electron reconstruction and identification efficiencies for 2012 and 2015 datasets, respectively.

The electron energy scale and resolution are obtained from $Z \rightarrow ee$ events through an in-situ procedure [148,149]. The impact of its uncertainty on the selected sample is evaluated by scaling the p_{T} of all leptons up or down by 1σ and re-applying the event selection.

2.4.3 Muons

Offline muon candidates are reconstructed by combining independently reconstructed track segments in the inner detector and in the muon spectrometer [150–152]. Muon track candidates in the MS are built by fitting together hits from segments in the different layers. The combined ID-MS muon reconstruction is performed using various algorithms based on the information provided by the ID, the calorimeters and the MS. According to which subdetectors information is used, four types of muons are defined:

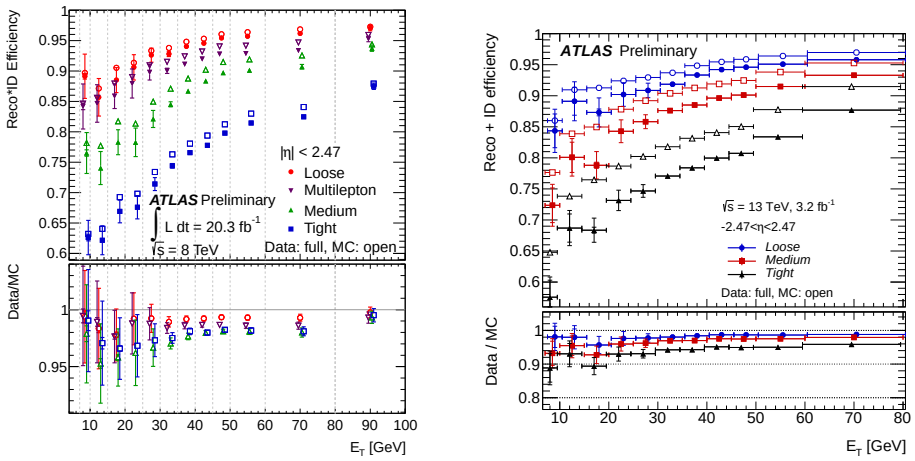

Figure 2.11: Combined electron reconstruction and identification efficiencies in $Z \to ee$ events as a function of the transverse energy $E_{\mathrm{T}}^{\mathrm{miss}}$, integrated over the full pseudorapidity range (left) for 2012 data at $\sqrt{s}$ = 8 TeV (*left*) and for 2015 data at $\sqrt{s}$ = 13 TeV (*right*). The data efficiencies are obtained from the data-to-MC efficiency ratios measured using $J\Psi$ and Z tag-and-probe, multiplied by the MC prediction for electrons from $Z \to ee$ decays. The uncertainties are obtained with pseudo-experiments, treating the statistical uncertainties from the different $(E_{\mathrm{T}}^{\mathrm{miss}}, \eta)$ bins as uncorrelated. Two sets of uncertainties are shown: the inner error bars show the statistical uncertainty, the outer error bars show the combined statistical and systematic uncertainty [146, 147].

- Combined (CB) muons: a combined track is formed with a global refit that uses the hits from the independent tracks reconstructed in the ID and MS.
- Segment-tagged (ST) muons: a combined track is formed via the combination of an extrapolated ID track to the MS and a local track segment in the MS. These muons are used when, due to their low p_{T} or regions with low MS acceptance, they only cross one MS layer.
- Calorimeter-tagged (CM) muons: a combined track is formed via the combination of an ID track and an energy deposit in the calorimeter compatible with a minimum-ionizing particle. These type of reconstructed muons recover acceptance in the region where the ATLAS muon spectrometer is only partially instrumented.
- Stand-Alone (SA) or extrapolated (ME) muons: the muon trajectory is reconstructed only in the MS. The parameters of the muon track at the interaction point are determined by extrapolating the track back to the point of closest approach to the beam line, taking into account the estimated energy loss of the muon in the calorimeters.

Four muon identification selections (Medium, Loose, Tight, and High-p_{T}) are provided to address the specific needs of different physics analyses. Loose, Medium, and Tight are inclusive categories in that muons identified with tighter requirements are also included in the looser categories.

Isolation criteria are applied in order to reduce contamination from events in which a muon is produced from a quark decay (for example heavy-flavour quarks that decay leptonically and result in a muon inside a jet). To that purpose, two isolation variables are used: a track-based isolation variable and a calorimeter-based isolation variable. The track-based isolation variable, $p_T^{varcone30}$, is defined as the scalar sum of the transverse momenta of the tracks with $p_{\mathrm{T}} > 1$ GeV in a cone of size $\Delta R = \min(10\ \mathrm{GeV}/p_T^{\mu}, 0.3)$ around the muon of transverse momentum p_T^{μ}, excluding the muon track itself. The calorimeter-based isolation variable, $E_T^{topocone20}$, is defined as the sum of the transverse energy of topological clusters in a cone of size $\Delta R = 0.2$ around the muon, after subtracting the contribution

from the energy deposit of the muon itself and correcting for pile-up effects. In the Run-1 analysis, the track-based isolation variable is used. For the Run-2 analysis, the information from the two isolation variables is used and the cuts are chosen such that an isolation efficiency of 95% for p_{T}=25 GeV and 99% for p_{T}=60 GeV is reached, corresponding to the Gradient Working point [152].

Muon selection To guarantee a good muon identification, the candidates must have a transverse momentum p_{T}> 25 GeV (26 GeV) for the Run-1 analysis (Run-2 analysis) and a pseudorapidity $|\eta|$ < 2.5. Selected muons must additionally satisfy a series of requirements on the number of track hits present in the various tracking sub-detectors. In addition, the longitudinal impact parameter z_0 of the muon candidates with respect to the primary vertex is required to be smaller than 2 mm (0.5 mm) for the Run-1 analysis (Run-2 analysis). In addition, the transverse impact parameter significance of the candidate must be <3 in the Run-2 analysis.

Muon candidates with relaxed identification criteria (loose and medium) and with no isolation cuts applied, are also used in the analyses for the data-driven estimate of fake backgrounds.

2.4.3.1 Muons modeling uncertainty estimation

For the muons lying in the central detector region, where both ID and MS tracks are used, a precise determination of the muon reconstruction efficiency is obtained with the tag-and-probe method using $Z \rightarrow \mu\mu$ and $J/\Psi \rightarrow \mu\mu$ events, with a similar procedure to that described for electrons [151,152]. As in the case of electrons reconstruction, SFs are obtained to correct a possible mismatch between the simulated MC samples and the measured data efficiencies. In the case of muons falling in the region $|\eta| > 2.5$ (forward region), where no ID tracks are available, a different method to estimate the efficiency is used. In this method, one of the muons from the Z decay is required to be in the central region and the other one in the forward region. The left and right panels of Figure 2.12 show the measured efficiencies for 2012 and 2015 datasets, respectively.

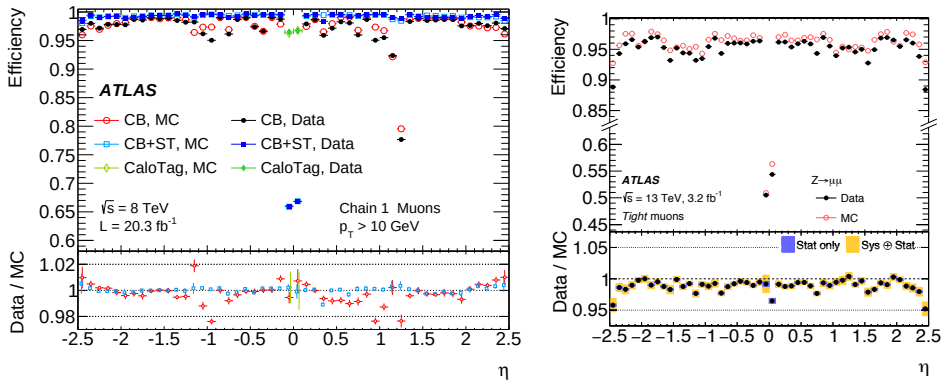

Figure 2.12: *Left*: Muon reconstruction efficiency as a function of η measured in $Z \to \mu\mu$ events (2012 dataset) for muons with p_{T} >10 GeV and different muon reconstruction types. Calo Tag muons are only shown in the region $|\eta| < 0.1$, where they are used in physics analyses. The error bars on the efficiencies indicate the statistical uncertainty. The panel at the bottom shows the ratio between the measured and predicted efficiencies. The error bars on the ratios are the combination of statistical and systematic uncertainties [151]. *Right*: Muon reconstruction efficiency as a function of η measured in $Z \to \mu\mu$ events (2015 dataset) for muons with p_{T}>10 GeV shown for the Tight muon selection. The error bars on the efficiencies indicate the statistical uncertainty. Panels at the bottom show the ratio of the measured to predicted efficiencies, with statistical and systematic uncertainties [152].

The muon energy scale and resolution are obtained from $Z \to \mu\mu$ and $J/\Psi \to \mu\mu$ decays. The impact of its uncertainty on the selected sample is evaluated by scaling the p_{T} of all muons up or down by 1σ and re-applying the event selection.

2.4.4 Jets

Jets are reconstructed from topological calorimeter clusters [153] using the anti-k_t algorithm [154] with a radius parameter of 0.4. This method relies on the definition of the distances d_{ij} between entities (particles, pseudojets) i and j and d_{iB} between entity i and the beam B

$$d_{ij} = \min(k_{ti}^{-2}, k_{tj}^{-1}) \frac{\Delta_{ij}^2}{R^2}, \tag{2.7}$$

$$d_{iB} = k_{ti}^{-2}, \tag{2.8}$$

where $\Delta_{ij}^2 = (y_i - y_j)^2 + (\phi_i - \phi_j)^2$ and k_{ti}, y_i and ϕ_i are respectively the transverse momentum, rapidity and azimuth of the particle i. The radius parameter, R is the radius of a cone which determines the size of the jets.

The clustering algorithm proceeds identifying the smallest of the distances with the following criteria: if it is a d_{ij}, the entities i and j are recombined; if it is a d_{iB}, the entity i is called a "jet" and it is removed from the list of entities. The distances are then recalculated and the procedure is repeated until there are no entities left. The inputs for the anti-k_t are three-dimensional, massless, positive-energy topological clusters (topo-clusters) made of calorimeter cell energies, which are built from neighbouring calorimeter cells that contain a significant energy above a noise threshold. These clusters are calibrated with the local cluster weighting method which partially corrects for detector response due to the non-compensating nature of the calorimeters [9] [155].

Figure 2.13 shows a schematic view of the jet energy scale (JES) calibration procedure. As a first step, the four-momentum of the jets is corrected so that they

[9] All calorimeters employed in ATLAS are non-compensating, meaning their signal for hadrons is smaller than the one for electrons and photons depositing the same energy ($e/h > 1$).

point to the hard-scatter primary vertex instead of to the center of the detector, which improves their η resolution. The procedure used in the Run-2 for this step is identical to the one used in the 2011 calibration [156]. Then, the excess energy due to in-time and out-of-time-pile-up is removed in two stages: an area-based p_{T} density subtraction, applied at the per-event level, followed by a residual correction derived from the MC simulation (same methods used in Run-1 and Run-2 [157]). Next, the absolute JES calibration corrects the jet four-momentum to the particle level energy scale, derived using dijet MC events, and accounts for biases in the jet η reconstruction. Such biases come from the transition between different calorimeter technologies and sudden changes in calorimeter granularity. The calorimeter response and the jet reconstruction are sensitive to fluctuations in the jet particle composition and the distribution of energy within the jet. The average particle composition and shower shape of a jet vary between initiating particles: a quark-initiated jet will often include hadrons with a higher fraction of the jet p_{T} that penetrate further into the calorimeter, while a gluon-initiated jet will typically contain more particles of softer p_{T}, leading to a lower calorimeter response and a wider transverse profile. To further account for these remaining dependencies of the JES on the longitudinal and transverse features of the jets, the global sequential calibration (GSC), a procedure explored in the 2011 [158] is used. This technique exploits the topology of the energy deposits in the calorimeter to characterize fluctuations in the jet particle content of the hadronic shower development. The correction uses several jet properties and each correction is applied sequentially. The last stages of the jet calibration account for differences in the jet response between data and MC simulation in the form of data-to-MC SFs. Such differences arise from the imperfect description of the detector response and detector material in MC simulation, as well as in the simulation of the hard scatter, underlying event, pile-up, jet formation, and electromagnetic and hadronic interactions with the detector. Differences between data and MC simulation are quantified by balancing the p_{T} of a jet against other well-measured reference objects. The η-intercalibration corrects the average response of forward jets to that of well-measured central jets using dijet events. The Z/γ+jet balance analyses use a well-calibrated photon or Z boson, the latter decaying into an electron or muon pair, to measure the p_{T}

response of the recoiling jet in the central region up to a p_{T} of about 950 GeV. Finally, the multijet balance analysis calibrates central high-p_{T} jets ($300 < pT < 2000$ GeV) recoiling against a collection of well-calibrated, lower-p_{T} jets.

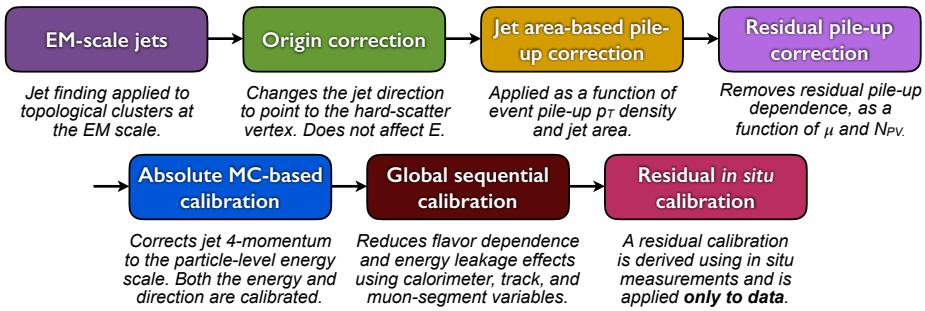

Figure 2.13: Calibration stages for EM-scale jets.

Jets selection

To suppress jets from in-time pile-up, two different methods are used. In the Run-1 analysis, a cleaning cut which only allows jets for which at least a 50% of the scalar p_{T} sum of its associated tracks (jet vertex fraction, JVF, variable) come from tracks compatible with the primary vertex is applied to low-p_{T} and central jets ($p_{\mathrm{T}} <$ 50 GeV and $|\eta| < 2.4$) [157]. In the Run-2 analysis, the jet-vertex-tagger discriminant (JVT) is used. It is based on a two dimensional likelihood method [159] and rejects jets with with $p_{\mathrm{T}} > 60$ GeV, $|\eta| < 2.4$ and JVT<0.59, leading to an effciency of 92% and a fake rate of 2%.

In order to avoid double counting of electron energy deposits as jets, the closest jet within a cone of radius $\Delta R < 0.2$ ($\Delta R_{y,\phi}$[10] < 0.2 for the Run-2) of a reconstructed electron is removed, since the jet and the electron are very likely to correspond to the same physics object. If the nearest jet is within ΔR ($\Delta R_{y,\phi}$) = 0.4 of the electron, the electron is discarded to ensure it is sufficiently separated from nearby jet activity.

Double counting of muons in the Run-1 analysis is avoided by rejecting any candidate muon within a distance of a cone of size $\Delta R = 0.4$ around a jet of $p_{\mathrm{T}} >$

[10] $\Delta R_{y,\phi} = \sqrt{(\Delta y)^2 + (\Delta\phi)^2}$

25 GeV and JVF > 0.5. In the Run-2 analysis, jets with less than 3 tracks and a distance $\Delta R_{y,\phi} < 0.2$ from a muon are removed. In addition, muons with a distance $\Delta R_{y,\phi} < 0.4$ from any of the surviving jets are removed to avoid contamination due to non-prompt muons from heavy-flavour hadron decays.

Furthermore, a jet cleaning is applied and events which contain at least one jet with a transverse momentum greater than 10 GeV (20 GeV) and reconstructed from noisy calorimeter cells are removed in the Run-1 (Run-2) analysis [158, 160, 161].

Finally, all jets considered should have a transverse momentum $p_{\mathrm{T}} > 30$ GeV (25 GeV) and a pseudo-rapidity of $|\eta| < 4.5$ (<2.5) for the Run-1 analysis (Run-2 analysis). In addition, for the Run-1 analysis, the p_{T} threshold is raised to 35 GeV for the jets having a pseudo-rapidity $2.7 < |\eta| < 3.5$, in order to remove some mis-modelling in the transition region between the central and forward hadronic calorimeters.

2.4.4.1 Jets modeling uncertainty estimation

- Jet energy scale: A precise knowledge of the JES is needed for various purposes like selections based on kinematic properties of jets and the reconstruction of other variables and objects based on jet properties. Systematic variations are derived from the JES calibration performed as explained above. In addition, the calorimeter response, the detector simulation, the jet flavor composition and the specific choice of parameters in the physics model implemented in the Monte Carlo (MC) event generator also contribute the JES uncertainty. Additional contributions due to pile-up effects are included. Also the effect of single high p_{T} particles is described. In total, a parametrization with 26 (18) uncorrelated components is considered in the Run-1 (Run-2) analysis. To evaluate the effect on the measurement of each of these uncertainty contributions, the energy of each simulated jet is re-scaled up and down by the corresponding 1σ before re-applying the object and event selections. The full combination of all uncertainties for the 2012 and 2015 datasets as a function of jet p_{T} at $\eta = 0$ is depicted in Figure 2.14.

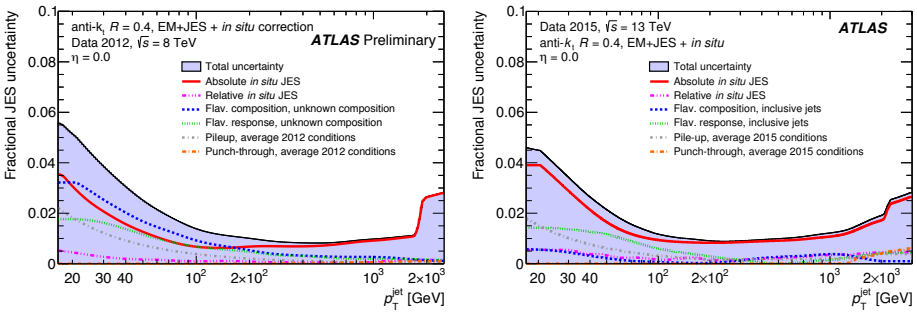

Figure 2.14: Combined uncertainty in the JES of fully calibrated jets as a function of of jet p_{T} at $\eta = 0$ for 2012 data at $\sqrt{s}$ = 8 TeV (*left*) and for 2015 data at $\sqrt{s}$ = 13 TeV (*right*). Systematic uncertainty components include pile-up, punch-through, flavour composition and response and uncertainties propagated from the in-situ JES calibration [155].

- Jet energy resolution (JER): It was measured in Run-1 data and simulation as a function of jet p_{T} and rapidity using dijet events [162]. Additional uncertainties considered in the Run-2 analysis come from the extrapolation from Run 1 to Run 2 conditions [163]. The combined uncertainty on the jet energy resolution is propagated by smearing the jet p_{T} in the simulation. The comparison of the nominal and smeared prediction defines a one-sided uncertainty which is then symmetrised.

- In-time pile-up suppresion: different uncertainties are considered depending on the method used in the analysis:

  - Jet vertex fraction: The systematic uncertainty associated to the efficiency of the cut on the jet vertex fraction is estimated via up and down variations by 1σ applied on the associated event weights.

  - Jet vertex tagger: Uncertainties on the JVT are provided as a two sided variation covering the differences in JVT efficiency measured in data and MC, based on scale factors derived in Z+jets events.

2.4.5 *b*-tagged jets

A b-hadron into which a b quark hadronizes, has a relatively long lifetime and thus it travels several millimeters before decaying in other particles. As a consequence, some of the charged particles from the b-hadron decay are significantly displaced from the primary vertex and have trajectories that come close together at a second point, called the secondary vertex. These charged particles can be identified by measuring the transverse and longitudinal impact paremeters. In addition, the presence of a muon inside a jet is another characteristic of a b-hadron decay, since $\sim 10\%$ of the b-hadron decays produce a muon. In spite of having a shorter lifetime and lower mass, jets with c-hadrons also produce the above signature. In order to identify b-jets, different methods have been developed exploiting the impact parameter or secondary vertices as well as the topology of b- and c-hadron decays.

- **Impact parameter-based algorithms**: the IP3D high-performance tagging algorithm uses a likelihood ratio technique in which input variables related to the impact parameter significance of all the tracks in a jet are compared to simulated distributions for both the b- and light-jet hypotheses (light jet refers to jets originating from light partons, i.e., u, d and s quarks and gluons).

- **Secondary vertex-based algorithms**: this type of algorithms use the information from the secondary vertex formed by the decay of the b-hadron. Different variables are used as discriminant depending on the algorithm: SV0 uses the decay length significance, while SV1 uses a combination of the invariant mass of all tracks associated to the vertex, the ratio of the sum of the energies of the tracks in the vertex to the sum of the energies of all tracks in the jet, and the number of two-track vertexes.

- **Decay chain reconstruction**: the JetFitter algorithm exploits the topology of the weak b- and c-hadron decays inside the jet. To do so, the flight path of the b-hadron is calculated as the distance between the primary and secondary vertex along a common line.

The output of these three basic taggers, IP3D, SV1 and JetFitter, are combined using multivariate analysis techniques in the two different algorithms used in the two analyses presented in this thesis.

2.4.5.1 MV1 algorithm

This algorithm used in the Run-1 analysis uses a neural network based on the most discriminant variables from the basic taggers [164]. The NN is trained with b-jets as signal and light-flavour jets as background, and computes a tag weight for each jet. The performance of the algorithm is characterized by the efficiency of tagging a b-jet and the "miss-tag rate", namely, the probabilities of mistakenly tagging as a b-jet a jet originating from a c quark or a light-flavor parton.

Working points are defined to obtain specified b-jet efficiencies in simulated samples of $t\bar{t}$ events. The calibration results are presented as scale factors defined as the ratio of the b-tag efficiency in data to that in simulation. The b-tagging efficiency in simulation is given by the fraction of jets tagged as b-jets compared to the generator level partons. The efficiency in data is measured with two different methods using semileptonic events, the p_{T}^{rel} and system8, described in [165]. Complementarily, four calibration methods based on $t\bar{t}$ events are also used: the tag counting method, the kinematic selection method, the kineamtic fit method and the combinatorial likelihood method [165]. The best overall precision of the b-jet tagging efficiency calibration measurements has been found for the combination of the di-jet based p_{T}^{rel} and system8 results with the $t\bar{t}$-based combinatorial likelihood results. The efficiencies to tag a c-jets as a b-jets (c-tagg efficiency) and the mistag rate are measured in samples with jets containing D^{*+} mesons and inclusive jet samples, respectively [164]. Figure 2.15 shows the b- and c-tagging efficiencies SFs and the mistag rate derived from 2011 and 2012 data and simulated samples

b-jets selection The threshold value applied to the MV1c (an improved version of the MV1 algorithm optimized to reject c-jets) output corresponds to a b-tagging efficiency of 50% measured in $t\bar{t}$ events. The corresponding mis-tagging rates for the charm-quark and light-flavour jets are 3.9% and 0.07%, respectively. A relaxed

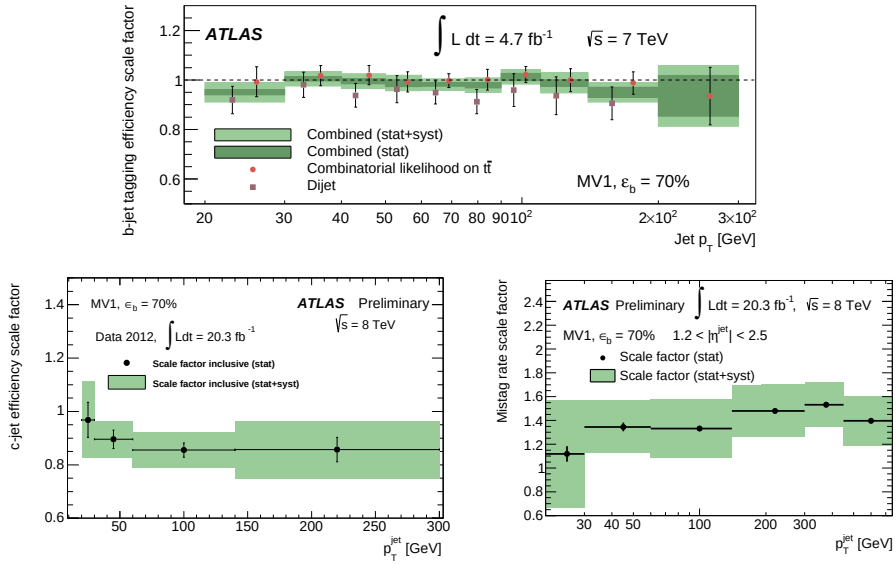

Figure 2.15: *Top:* The b-jet tagging efficiency data-to-simulation scale factors for the MV1 tagging algorithm at 70% efficiency, obtained by combining the di-jet based p_{T}^{rel} and system8 results with the $t\bar{t}$-based combinatorial likelihood results [165]. *Bottom-left:* data-to-simulation efficiency scale factor after extrapolation to inclusive charm jets, for the 70% working point of the MV1 tagger [164]. *Bottom-right:* the data-simulation mistag rate scale factor for the MV1 tagging algorithm at 70% efficiency obtained with the negative tag method, for jets with $1.2 < |\eta^{\mathrm{jet}}| < 2.5$ [164].

b-tagging requirement is used to define a control region enriched in W+jets events. The MV1 algorithm with a b-tagging efficiency of 80%, is applied in that case.

2.4.5.2 MV2 algorithms

In the Run-2 analysis, the MV2c10 multivariate tagging algorithm [166] is used. This algorithm benefits from a re-optimisation ahead of the 2016 Run-2 data taking, improving the b-jet identification as well as the c- and light-flavoured jet rejections. In this algorithm, the input variables obtained from the three basic algorithms are combined using a boosted decision tree (BDT) algorithm to discriminate b-jets from light- and c-jets. The training is performed on a set of approximately 5 million $t\bar{t}$ events. The MV2 algorithm constitutes a significant revision of the MV1 algorithm used in Run-1, which combined inputs from intermediate multivariate tools trained for each of the basic b-tagging algorithms. The new approach not only improves the performance but also significantly simplifies the algorithm by directly using the variables from the basic algorithms, omitting the additional intermediate multivariate tools. As in the case of MV1 algorithms, working points defined to obtain specified b-jet efficiencies in simulated samples of $t\bar{t}$ events are used.

The b-jet tagging efficiency is measured from a $t\bar{t}$ sample in which the number of non b-jets is reduced by requiring the W boson to decay leptonically. Two different methods are used: a new method which uses a tag-and-probe approach and a combinatorial likelihood approach based on the method used in Run-1. Figure 2.16 shows the data-to-simulation scale factors as a function of the jet p_{T} for both the tag-and-probe and likelihood methods, corresponding to the 70% b-jet tagging efficiency [167]. The misstag rate efficiency is measured using multijet events [168], while the b-tagging efficiency of c-jets is measured in $t\bar{t}$ events [169]. Data-to-simulation scale factors associated to both efficiencies are shown in the bottom panels of Figure 2.16.

b-jets selection In the Run-2 analysis, the MV2c10 algorithm is used. The suffix refers to the specific composition of the background sample used in the training: mixture of 90% light-flavour jets and 10% c-jets. A 70% b-jet efficiency operating point is used.

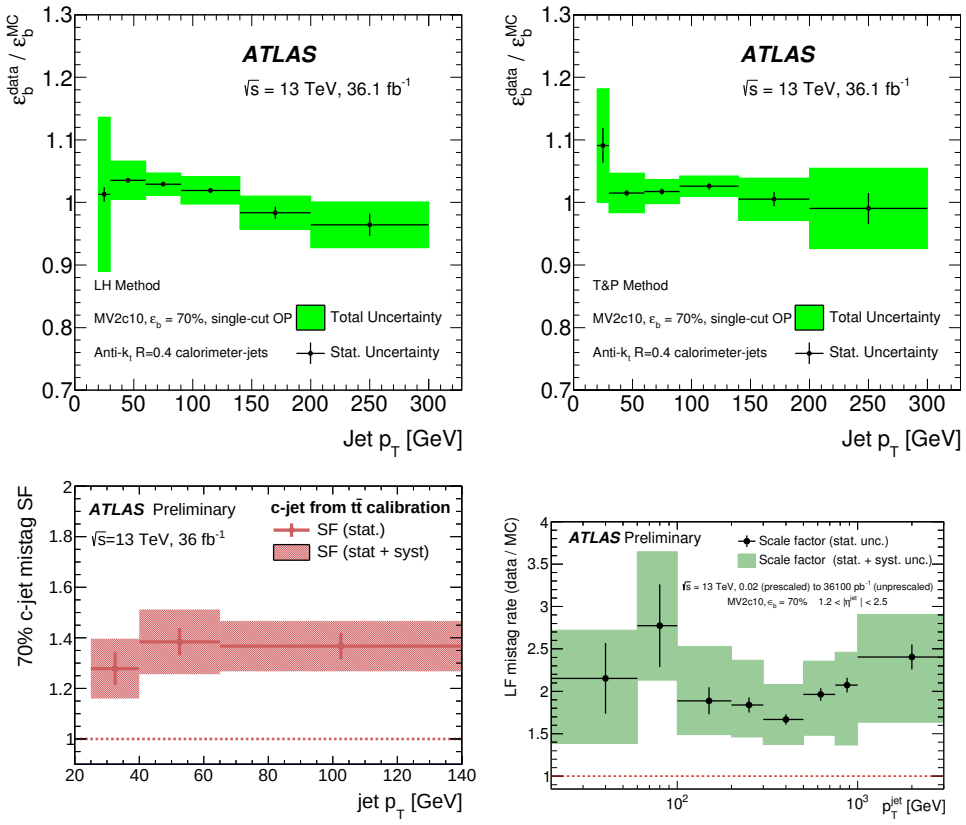

Figure 2.16: Top: data-to-simulation scale factors as a function of the jet p_{T} using (left) the likelihood method and (right) the tag-and-probe method [167]. Bottom-left: Result for the c-jet tagging efficiency scale factors determined for the 70% working point as a function of jet p_{T}. The red line represents the the statistical uncertainty while the shaded area represents the total uncertainty considering all systematic uncertainties [169]. Bottom-right: Ratio between the LF-jet mistag rate measured from data with the negative-tag method and as simulated using the Pythia 8 multijet sample for the 70% WP as a function of jet p_{T}. The negative-tag measurements include simulation-based corrections for HF-jet contamination and LF-jets with true secondary vertices. The statistical uncertainty represents the sum in quadrature of data and MC statistical uncertainties [168].

2.4.5.3 *b*-jets modeling uncertainty estimation

b-tagging efficiency scale factors, defined for b-quark, c-quark and light-flavor induced jets and depending on the jet tranverse momentum, are applied to the jets in the Monte Carlo simulations; this leads to three uncorrelated sources of systematic uncertainties: b-tagging efficiency, c-tagging efficiency (which also includes the τ-tagging efficiency) and mis-tagging rate. It is evaluated by varying the η, p_{T} and flavor-dependent scale factors applied to each jet in the simulation within a range that reflects the systematic uncertainty on the measured tagging efficiency and mistag rates. In the Run-2 analysis, the officially recommended eigenvector variations are used, leading to a set of six, three and sixteen independent scale factors for the different b-jets, c-jets and light-jets.

2.4.6 Missing transverse momentum

The sum of the vector transverse momenta of all the products of a collision should be zero due to the conservation of momentum in the plane transverse to the beam axis. An imbalance in the sum of visible transverse momenta is known as missing transverse momentum, $E_{\mathrm{T}}^{\mathrm{miss}}$, and indicates the presence of weakly-interacting stable particles in the final state. Within the SM, the $E_{\mathrm{T}}^{\mathrm{miss}}$ is a measure of the escaping neutrinos. In addition, a large $E_{\mathrm{T}}^{\mathrm{miss}}$ is a key signature for searches for new physics processes such as SUSY and extra dimensions. Therefore, a precise measurement of $E_{\mathrm{T}}^{\mathrm{miss}}$ has a direct impact in both, SM precision measurements and searches of new physics. Fake $E_{\mathrm{T}}^{\mathrm{miss}}$ can be produced via SM particles which escape the acceptance of the detector or are badly reconstructed, due to limited detector coverage, finite detector resolution, the presence of dead regions and different sources of noise.

The $E_{\mathrm{T}}^{\mathrm{miss}}$ is reconstructed as the negative vector sum of the transverse momenta of all detected particles [170–173]

$$E_{x(y)}^{\mathrm{miss}} = E_{x(y)}^{e} + E_{x(y)}^{\gamma} + E_{x(y)}^{\tau} + E_{x(y)}^{\mathrm{jets}} + E_{x(y)}^{\mu} + E_{x(y)}^{\mathrm{soft}}, \tag{2.9}$$

where the soft term is reconstructed from the transverse momentum deposited in the detector but not associated with any reconstructed hard object. It can be

reconstructed via calorimeter-based algorithms (Calorimeter Soft Term, CST [170]) or track-based methods (Track Soft Term, TST [173]).

The magnitude and azimuthal angle of the $E_{\mathrm{T}}^{\mathrm{miss}}$ are calculated from its x and y components as

$$E_{\mathrm{T}}^{\mathrm{miss}} = \sqrt{(E_x^{\mathrm{miss}})^2 + (E_y^{\mathrm{miss}})^2} \tag{2.10}$$

$$\phi^{\mathrm{miss}} = \arctan\left(\frac{E_x^{\mathrm{miss}}}{E_y^{\mathrm{miss}}}\right) \tag{2.11}$$

The objects contributing to the electron, muon, tau, photon and jets terms in Eq. 2.9 are selected as appropriate for a given analysis. In the particular case of the analyses presented in this thesis, electrons, muons and jets are used and selected as outlined in the previous subsections.

During Run-1, the soft term was reconstructed using the CST [170] method from the energy deposits in calorimeter cells, grouped into topoclusters, which are not associated with reconstructed hard objects. Only energy contributions from calorimeter cells belonging to a topocluster are included in the CST. This calorimeter-based approach is very sensitive to pile-up interactions (in-time and out-of-time) which can give an additional contribution to the calorimeter-based soft term and therefore different methods are applied to suppress the pile-up contribution. The most extensively used is based on scaling the $E_{\mathrm{T}}^{\mathrm{miss,SoftTerm}}$ with the soft term vertex fraction (STVF), i.e., the fraction of momenta of tracks matched to the soft term which are associated with the hard scattering vertex. The $E_{\mathrm{T}}^{\mathrm{miss,SoftTerm}}$ corrected with this method is called the STVF.

In Run-2 the soft term is reconstructed using the TST [173] method from tracks satisfying the selection criteria but not matched to any hard object. Only tracks associated to the primary vertex are used and tracks overlapping with calorimeter clusters associated to electrons are removed. An advantage of this method is that since tracks can be matched to a primary vertex, TST $E_{\mathrm{T}}^{\mathrm{miss}}$ is relatively insensitive to pile-up effects.

The quality of the $E_{\mathrm{T}}^{\mathrm{miss}}$ reconstruction is studied analyzing a number of data and simulated samples encompassing a variety of event topologies . This allows the the full exploitation of the detector capability in the reconstruction and calibration of different physics objects and optimization of the $E_{\mathrm{T}}^{\mathrm{miss}}$ calculation. The $Z \to \ell\ell$ process, with $\ell\ell$ being an electron-positron or muon-antimuon pair, is the standard for the evaluation of $E_{\mathrm{T}}^{\mathrm{miss}}$ performance owing to its clean detector signature. These events have very little genuine transverse missing momentum and therefore give information about the intrinsic resolution of the detector, of the algorithms involved and of the object reconstruction efficiencies. $W \to \ell\nu$ events provide a topology with high-p_{T} neutrinos, in which $E_{\mathrm{T}}^{\mathrm{miss}}$ is expected to be non-zero, giving information on the scale of $E_{\mathrm{T}}^{\mathrm{miss}}$. On its turn, $t\bar{t}$ events provide a tolopogy with many jets, and so are useful in investigation the robustness of $E_{\mathrm{T}}^{\mathrm{miss}}$ reconstruction in multijet environments [170, 171, 173]. The left (right) panel of Figure 2.17 shows the $E_{\mathrm{T}}^{\mathrm{miss,SoftTerm}}$ distribution for the $Z \to \mu\mu$ data corrected with STVF (TST) as corresponding to the Run-1 (Run-2) used method.

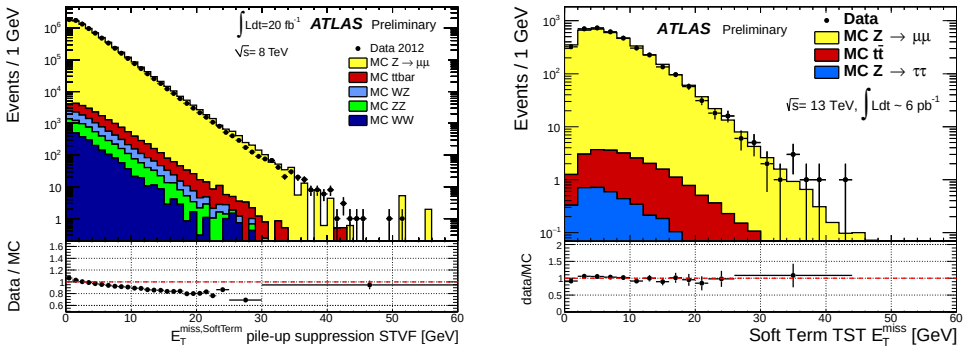

Figure 2.17: *Left:* Distribution of $E_{\mathrm{T}}^{\mathrm{miss,SoftTerm}}$ corrected with STVF for $Z \to \mu\mu$ data. The expectation from Monte Carlo simulation is superimposed and normalized to data, after each MC sample is weighted with its corresponding cross-section. The lower part of the figure shows the ratio of data over MC [171]. *Right:* Distribution of $E_{\mathrm{T}}^{\mathrm{miss,SoftTerm}}$ for TST $E_{\mathrm{T}}^{\mathrm{miss}}$ in $Z \to \mu\mu$ events. The expectation from MC simulation is superimposed and normalized to data, after each MC sample is weighted with its corresponding cross-section [173].

2.4.6.1 Missing transverse momentum modeling uncertainty estimation

Apart from the uncertainties associated with the reconstructed components used to calculate the $E_{\mathrm{T}}^{\mathrm{miss}}$, uncertainties related with soft terms are considered. Such effects include the modeling of the underlying event and in particular its impact on the p_{T} scale and resolution of unclustered energy. These are taken into account by including variations in the energy scale and smearing according to the resolution uncertainty in the parallel and perpendicular direction to the p_{T}-hard plane [171, 173] .

3 | Alignment of the Inner Detector

Accurate physics results rely on the good performance of the ATLAS Inner Detector (ID) when it comes to identify primary and secondary vertexes (necessary, among others, for a good identification of b-jets), and to reconstruct the trajectories of the charged particles and measure its charge and momentum with high precision. This is achieved thanks to its fine granularity and good resolution. However, after the detector assembly and installation, the position and orientation of each detector module is known in general with worse accuracy than its intrinsic resolution. Moreover, changes in the run conditions, such as magnetic field ramping or cooling changes, can alter the relative position of the detector modules or introduce deformations. The purpose of the ID alignment is the precise determination of the positions of the sensitive devices as well as their geometrical distortions relative to the ideal simulated geometry.

At the end of Run-1, the positions of the individual active detector modules in all three ID subsystems (Pixel, SCT, and TRT) were aligned to better than 1 μm [174]. During the Long Shutdown 1 [1] (LS1), a number of upgrades were done in the ATLAS ID. In particular, the Pixel detector was extracted and refurbished, and the IBL was installed as a new closest layer to the beam pipe. These changes are expected to affect the inherited knowledge from the end of Run-1.

After an introduction to the alignment procedure, this chapter presents the first results of the commissioning with cosmic-ray data taken in 2015 in preparation for Run-2 with special emphasis on the contributions of this thesis to this effort.

[1] The LS1 is the period during the end of the Run-1 and the beginning of the Run-2 in which the detector was updated in preparation for the new phase of operation.

3.1 Alignment basics

The ID alignment procedure uses the reconstructed tracks of the charged particles that cross the ID. The main ingredients for the algorithm are a common definition of a coordinate system, the track and alignment parameters as well as the track-to-hit residuals. All these concepts are explained in the following.

3.1.1 The ATLAS coordinate system

There are two relevant coordinate systems for the alignment procedure: the global coordinate frame which is used to specify the position of the individual modules or alignable structures and the the local frame, in which the hits on each module are reconstructed.

3.1.1.1 Global coordinate frame

The ATLAS global coordinate frame, X, Y, Z is a right-handed coordinate system with its origin at the nominal pp interaction point. As depicted in Figure 3.1, the Z axis lies along the beam direction and points in the direction of the solenoid magnetic field. The $X-Y$ plane is determined by the transverse plane to the beam direction. The positive X direction points towards the center of the LHC ring, while the the positive Y is taken along the center of the Earth, perpendicular to the X-Z plane.

Polar coordinates can be defined in the global frame. The azimuthal angle is measured in the $X-Y$ plane, $\phi \in [-\pi, \pi]$, where the positive X axis corresponds to $\phi = 0$ and the positive Y axis to $\phi = \pi/2$. The polar angle is measured with respect to the Z axis, $\theta \in [0, \pi]$, with $\theta = 0$ in the positive Z direction. From the polar angle, the pseudorapidity is defined as $\eta = -\log(\tan(\theta/2))$. These variables will be useful to characterize the kinematics of the events.

3.1.1.2 Local coordinate frame

The local coordinate frame, x', y', z' is a right-handed cartesian system defined for each module or alignable structure. It is shown in the right panel of Figure 3.1

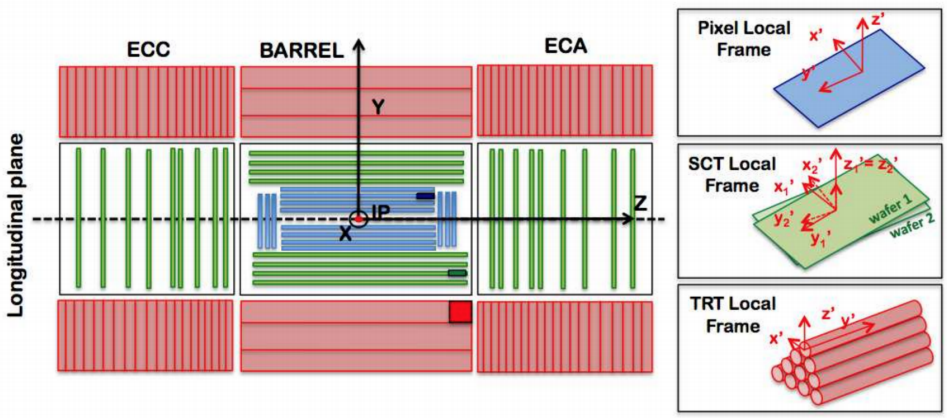

Figure 3.1: Left: Schematic representation of the longitudinal plane of the inner detector showing the Pixel and IBL (innermost layers, blue), the SCT (middle detection layer, green) and the TRT (outermost layers, red). The global system of coordinates is shown with the origin at the center of the detector. Right: Local system of coordinates on the corresponding devices.

for the pixel, SCT and TRT modules. The origin is located at the geometrical center of the device. The x' axis is taken along the most sensitive direction of the module. In the case of the pixel modules, it coincides with the short pitch side; and goes across the strips of the SCT and across the straws of the TRT. The y' axis is parallel to the long side of the modules. Finally, the z' axis is determined by the normal direction to the plane formed by the x' and y' directions. The hits are reconstructed in the local frame of each module.

3.1.2 Track and alignment parameters

Due to the solenoidal magnetic field, the charged particles describe helical trajectories inside the inner detector. These trajectories are represented via five *track parameters*, $\boldsymbol{\pi} = (d_0, z_0, \phi_0, \theta, q/p)$, which are shown in Figure 3.2. d_0 and z_0 represent the position of the track with respect the perigee (closest point to the global Z axis), while the other three parameters are used to characterize the momentum of the particle.

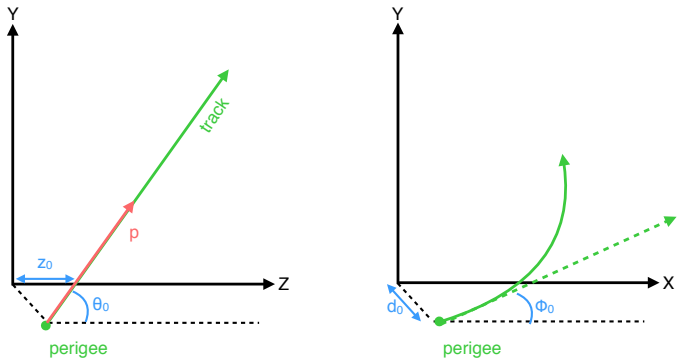

Figure 3.2: Graphical representation of the track parameters in the global reference frame.

- d_0: the transverse impact parameter is the distance of the perigee to the $X - Y$ plane. It is defined to be positive when the direction of the track is clockwise with respect to the origin.
- z_0: the longitudinal impact parameter is the z coordinate of the perigee.
- ϕ_0: azimuthal angle.
- θ: polar angle.
- **q/p**: the charge of the particle over its momentum and is related with the curvature of the tracks.

Another set of parameters is needed when aligning a detector module or structure. There are six degrees of freedom (DoF) that define uniquely the position and orientation in the space of a structure if we consider them as rigid bodies. These six DoF define the *alignment parameters*, and consist of three translations with respect to the origin of the reference frame and three rotations around the cartesian axes, $\boldsymbol{a} = (T_x, T_y, T_z, R_x, R_y, R_z)$.

3.1.3 Residuals

When a charged particle crosses the inner detector, it leaves a signal on each of the modules it crosses. These signals are called *hits*, and they consist of a cluster of pixels/strips in the Pixel and SCT, and of a drift circle in the TRT. If the track from a charged particle is well reconstructed, the distance between a hit in a module and the reconstructed track in that element will be small. This distance is named *residual* and is defined as:

$$r = (\boldsymbol{m} - \boldsymbol{e}(\boldsymbol{\pi}, \boldsymbol{a})) \cdot \boldsymbol{u}, \tag{3.1}$$

where $\boldsymbol{m}$ is the position of the hit in the sensor; $\boldsymbol{e}(\boldsymbol{\pi}, \boldsymbol{a})$ gives the extrapolated point of the track into the detector element, and depends both on the track and the alignment parameters of that element; finally, $\boldsymbol{u}$ is a vector that points along the sensing direction, which depends on the type of sensor in which the residual is measured. The residuals are calculated on the local reference frame of each alignable structure.

3.2 Track-based alignment

As outlined in the previous subsection, the good quality of a track implies small residuals. This is the basic idea underlying the track-based alignment methods. A schematic view is depicted in Figure 3.3. In the left panel, the real position of three detector layers is represented by the solid green boxes. One of the layers suffers from an initial misalignment a. In the absence of a magnetic field, a charged particle crossing the detector (solid arrow) will leave a hit on each module (yellow stars). From the hits information, the track of the particle is reconstructed (dashed arrow) using the apparent detector position (dashed blue boxes). Since the real and apparent layer positions are not the same, the track is incorrectly reconstructed. This is seen in the central panel of the figure. In order to recover the real position of the detector modules, an iterative algorithm that minimizes a χ^2 built from the residuals (blue arrows) is used. The result of the alignment procedure is depicted

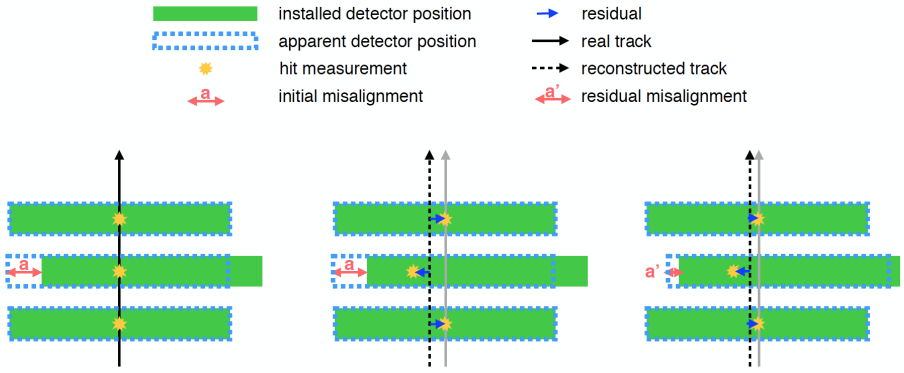

Figure 3.3: Schematic picture of the alignment procedure. The left panel shows the real track in the installed detector geometry. The central panel shows the reconstructed track using the apparent detector position. Finally, the right panel depicts the reconstructed track after the detector alignment.

in the right panel, in which one sees that the residuals and alignment corrections are much smaller, leading to a reconstructed track closer to the real one.

Each module or grouped collection of modules can be treated as an alignable structure. The alignment is done at different hierarchical levels which follow the assembly structure of the ID. In a first step, the Level 1, the detector subsystems are aligned separating into end-caps and barrel regions in order to correct possible global movements. The IBL layer, which was installed during the LS1, has an independent mechanical support and is therefore not expected to move in a correlated way with the rest of the Pixel system. For this reason, it is considered as an independent physical structure in the Level 1. The Level 2 alignment separates the individual barrel layers and end-cap disks. Finally, the Level 3 allows for a fine alignment at the module level (silicon module and TRT wire).

3.2.1 χ^2 minimization and alignment parameters

The ID detector alignment uses the *Global* χ^2 algorithm [175], an interative method which relies on the minimization of a χ^2 built from the residuals of all the hits in all tracks in the alignable structure considered:

$$\chi^2 = \sum_t \sum_h \left(\frac{r_{th}(\boldsymbol{\pi}, \boldsymbol{a})}{\sigma_h} \right)^2, \tag{3.2}$$

where t is the set of reconstructed tracks and h the set of hits associated to each track t. r_{th} is the residual of the hit h associated to the track t and σ_h is the hit error. This equation can be rewritten in a more compact form using the vector notation:

$$\chi^2 = \sum_t \boldsymbol{r_t}(\boldsymbol{\pi}, \boldsymbol{a})^T V^{-1} \boldsymbol{r_t}(\boldsymbol{\pi}, \boldsymbol{a}) \tag{3.3}$$

in this way, the hit errors are encoded in a covariance matrix, V.

The χ^2 built in this way has a minimum at the real detector geometry. Therefore, to find the correct position of the modules, one can minimize it with respect to $\boldsymbol{a}$:

$$\frac{\mathrm{d}\chi^2}{\mathrm{d}\boldsymbol{a}} = 0 \rightarrow \sum_t \left(\frac{\mathrm{d}\boldsymbol{r}_t(\boldsymbol{\pi}, \boldsymbol{a})}{\mathrm{d}\boldsymbol{a}} \right)^T V^{-1} \boldsymbol{r}_t(\boldsymbol{\pi}, \boldsymbol{a}) = 0. \tag{3.4}$$

We can write the explicit dependency of the residuals on the track and alignment parameters via its Taylor expansion up to first order, assuming that the residuals change linearly with $\delta\boldsymbol{a}$ and that the initial alignment parameters are already close to the real geometry of the detector:

$$\boldsymbol{r} = \boldsymbol{r_0} + \frac{\partial \boldsymbol{r}}{\partial \boldsymbol{\pi}} \delta\boldsymbol{\pi} + \frac{\partial \boldsymbol{r}}{\partial \boldsymbol{a}} \delta\boldsymbol{a} = \boldsymbol{r_0} + \left(\frac{\partial \boldsymbol{r}}{\partial \boldsymbol{\pi}} \frac{\partial \boldsymbol{\pi}}{\partial \boldsymbol{a}} + \frac{\partial \boldsymbol{r}}{\partial \boldsymbol{a}} \right) \delta\boldsymbol{a} = \boldsymbol{r_0} + \frac{\mathrm{d}\boldsymbol{r}}{\mathrm{d}\boldsymbol{a}} \delta\boldsymbol{a}. \tag{3.5}$$

Inserting Equation 3.5 into 3.4, we obtain

$$\left[\sum_t \left(\frac{\mathrm{d}\boldsymbol{r}}{\mathrm{d}\boldsymbol{a}} \right)^T V^{-1} \frac{\mathrm{d}\boldsymbol{r}}{\mathrm{d}\boldsymbol{a}} \right] \delta\boldsymbol{a} + \sum_t \frac{\mathrm{d}\boldsymbol{r}}{\mathrm{d}\boldsymbol{a}}^T V^{-1} \boldsymbol{r_0} = 0, \tag{3.6}$$

from which we can define the alignment matrix and vector:

$$\mathcal{M}_a = \sum_t \left(\frac{\mathrm{d}\boldsymbol{r}}{\mathrm{d}\boldsymbol{a}}\right)^T V^{-1} \frac{\mathrm{d}\boldsymbol{r}}{\mathrm{d}\boldsymbol{a}}; \tag{3.7}$$

$$v_a = \sum_t \frac{\mathrm{d}\boldsymbol{r}}{\mathrm{d}\boldsymbol{a}}^T V^{-1} \boldsymbol{r_0}. \tag{3.8}$$

With this definitions, Equation 3.6 can be written in a compact form

$$\mathcal{M}_a \delta\boldsymbol{a} + v_a = 0 \rightarrow \delta\boldsymbol{a} = -\mathcal{M}_a^{-1} v_a, \tag{3.9}$$

so that the alignment parameters become:

$$\boldsymbol{a} = \boldsymbol{a_0} + \delta\boldsymbol{a} = \boldsymbol{a_0} - \mathcal{M}_a^{-1} v_a. \tag{3.10}$$

To obtain the alignment corrections, $\delta\boldsymbol{a}$, to the initial parameters $\boldsymbol{a_0}$, one needs to invert the alignment matrix. The approximation made in Equation 3.5 is not usually true and the solution will not be exact. In order to get an accurate result, the alignment procedure is run iteratively until converge is reached, so that the final alignment parameters become

$$\boldsymbol{a}_{\mathrm{Iter(N)}} = \boldsymbol{a}_{\mathrm{Iter(N-1)}} + \delta\boldsymbol{a}_{\mathrm{Iter(N)}}. \tag{3.11}$$

The Global χ^2 algorithm correlates all the alignable structures crossed by the same track, which makes the alignment matrix non-diagonal. Moreover, when going to higher alignment levels, the size of the matrix will increase ($\sim$35.000 DoF for the silicon detectors). With all this, solving the linear system in Equation 3.9 becomes challenging from the computational point of view.

This section has presented a very brief description of the Global χ^2 algorithm, and more details can be read in [176].

3.3 Calibration loop during data taking

The data delivered by the LHC is recorded in different streams defined with dedicated trigger setups. The physics stream is the one used for physics analyses and the trigger setup depends on the required final state objects required for the specific analyses. As an example, in the case of the two analyses presented in this thesis, the single-lepton triggers need to be fired. The express stream contains a reduced fraction of the data ($\sim 4\%$) and is used for data quality purposes. Finally, the calibration stream contains specific events for several detectors and is used to compute the alignment and calibration constants for them. The express and calibration streams are quickly processed at Tier-0 facility at CERN [2] to ensure a good quality assessment and reconstruction of the physics data. The streams are processed and used to calibrate the detectors within 48 hours in the so-called Calibration Loop. After the calibration loop, the full dataset is reprocessed in the bulk, taking into account the outcome of the calibration loop. In order to correct any possible movement or deformation prior to the bulk reconstruction, a run-by-run [3] alignment was implemented in the calibration loop in Run-1.

3.4 Alignment commissioning in 2015 with cosmic rays

During the LS1 the ID was upgraded. In particular, the Pixel detector was extracted and refurbished, and the IBL was installed as a new closest layer to the beam pipe. These changes moved the detector elements from their positions at the end of Run-1. In preparation for Run-2, an alignment using cosmic rays data collected in February 2015 was performed, with the objective of confirming the position of all the previously installed systems and determining the position of the new IBL [2].

[2] The Tier-0 facility at CERN is responsible for the first-pass processing of the raw data received from the ATLAS detector and the archival of raw and derived data on the Tier-0 mass storage system [177].

[3] Data at the LHC is delivered and recorded in in bunches named runs, which typically last between few minutes and some hours.

Cosmic rays consist on atmospheric muons that are created in cosmic ray interactions in the Earth's atmosphere. Thus, they cross the detector from top to bottom, providing a non-uniform illumination of all ID modules. Figure 3.4 shows the distributions of the track parameters for the tracks used in alignment. The top-left panel depics the distribution of the signed track transverse momentum ($q \cdot p_{\mathrm{T}}$). The asymmetry observed in this distribution is due to the predominantly positively charged primary cosmic ray spectrum. The top-right panel shows the nearly-flat distribution of the longitudinal impact parameter z_0 in which the sharp drop at $z_0 = \pm 400$ mm corresponds to the edges of the Pixel barrel. In the bottom-left of the figure, the pseudorapidity η is depicted. The double-peack structure at $\eta \approx -0.4$ and $\eta \approx 0.3$ is due to the construction shafts through which the ATLAS detector components were lowered into the cavern and reflects the fact that particles could enter into the ATLAS cavern through the access of shafts more easily than through the rock. Finally, the bottom-right panel shows the azimuthal angle ϕ_0. The peak at $\frac{3\pi}{2}$ reflects the down-going flux of atmospheric muon events.

Previous to the results from February data, preliminary aligment chains were run on data collected in the so-called Milestone weeks. In the following, the alignment run on data from M7 Milestone week, corresponding to data taking during the first week of December 2014 is shown.

To account for the non-uniform illumination of the ID modules, some DoFs are fixed when it is expected a poor resolution in this direction due to low number of hits. Table 3.1 details the alignment chain, including the number of iterations of the *Global* χ^2 algorithm for each alignment level and the DoFs considered for the Run-2 commissioning with cosmic-ray data.

The data sample used contains 3.5×10^5 tracks. To ensure a good quality of the alignment, the tracks are required to have measurements from all the subdetectors and to satisfy the following cuts on the number of hits on each structure:

- $N^{Pixel} \geq 1$: at least one hit in the Pixel detector.
- $N^{SCT} \geq 10$: at least ten hits in the SCT detector.
- $N^{silicon} \geq 12$: at least twelve hits in the silicon detector.

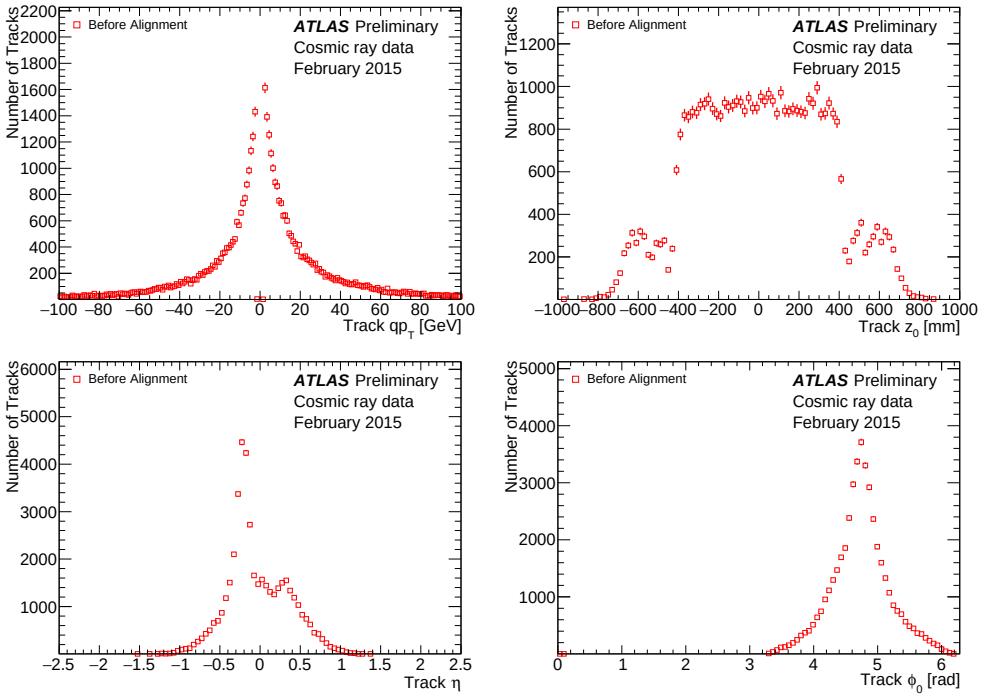

Figure 3.4: Track parameters for tracks used in alignment using cosmic-ray data collected in February 2015. The distribution of the charge signed track transverse momentum (p_{T}) is shown on the top-left, the longitudinal impact parameter z_0 on the top-right, the pseudorapidity η on the bottom-left, and the track azimuthal (ϕ_0) angle at the bottom-right [2].

Level	Description	Structures	DOF
1	IBL	1	All except R_x
5 iterations	Pixel detector	1	All except R_x
	SCT barrel (end-caps fixed)	1	All except R_x
2	IBL and Pixel barrel split into layers	4	All except R_x
5 iterations	Pixel end-caps split into disks	6	T_x, T_y, R_z
	SCT barrel split into layers	4	T_x, R_y, R_z
	SCT end-caps split into 2	2	T_x, T_y, R_z
3 (only for Pixel)	IBL and Pixel barrel modules	1736	T_x, T_y, R_y, R_z
3 iterations	Pixel end-caps split into disks	6	T_x, T_y, R_z
	SCT barrel split into layers	4	T_x, R_y, R_z
	SCT end-caps split into 2	2	T_x, T_y, R_z

Table 3.1: Alignment levels used during Run II cosmic-ray data commissioning. The TRT detector was kept fixed in all levels.

  - $N^{silicon,top} \geq 4$: at least two hits in the top half shells of the silicon detector.
  - $N^{silicon,bottom} \geq 4$: at least two hits in the bottom half shells of the silicon detector.
- $N^{TRT} \geq 25$: at least twenty-five hits in the TRT detector.

Moreover, a minimum p_{T} of 2 GeV is applied to the tracks in order to reduce the impact of multiple coulomb scattering in the traversed material [4]. After applying the selection criteria, 43500 tracks were used for the alignment.

Figure 3.5 shows the evolution of the alignment corrections as a function of the number of iterations for the Level 1. The six degrees of freedom are displayed. The red line corresponds to the IBL layer, which has the biggest initial misalignment. The grey and light blue lines correspond to the Pixel and SCT subdetectors, respectively. The corrections for all DoFs aligned converge after few iterations. The corrections after the fifth iteration will be the starting point for the Level 2

[4] A charged particle traversing a medium is deflected by many small-angle scatters. Most of this deflection is due to Coulomb scattering from nuclei, and hence the effect is called multiple Coulomb scattering.

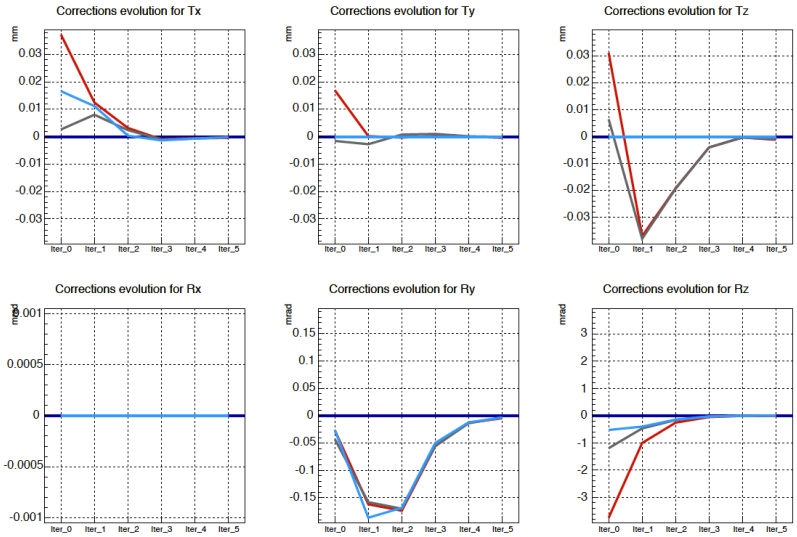

Figure 3.5: Evolution of the alignment corrections as a function of the number of iterations for the Level 1. The six degrees of freedom are displayed. The red, grey and light blue lines correspond to the IBL, Pixel and SCT subdetectors, respectively.

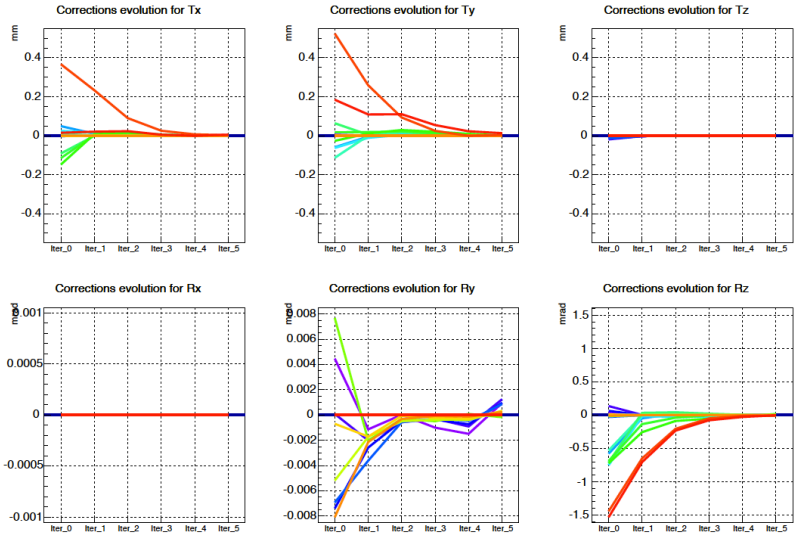

Figure 3.6: Evolution of the alignment corrections as a function of the number of iterations for the Level 2. The six degrees of freedom are displayed. Each line represents an alignable structure and the legend follows a rainbow palette, from purple (IBL layer) to red (SCT end-cap C).

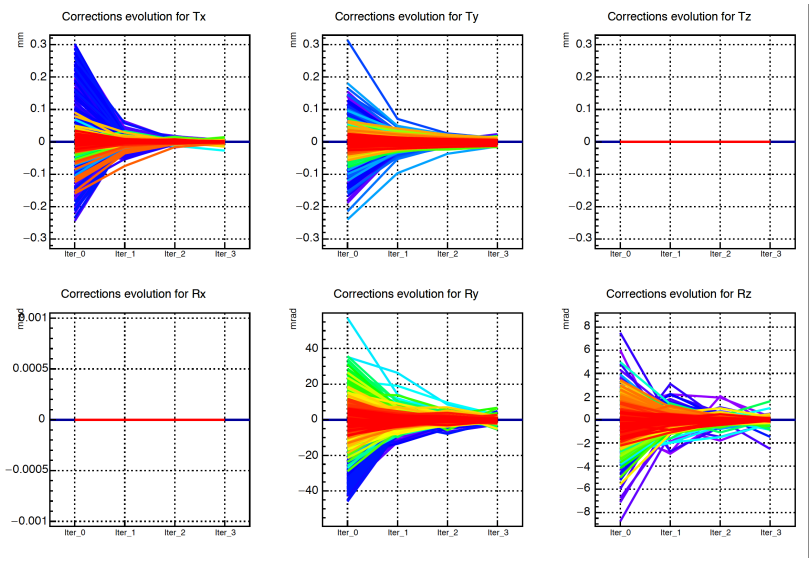

Figure 3.7: Evolution of the alignment corrections as a function of the number of iterations for the Level 3. The six degrees of freedom are displayed. Each line represents an alignable structure and the legend follows a rainbow palette, from purple (first IBL module) to red (SCT end-cap C).

alignment, and subsequently for Level 3. The evolution of the corrections at these levels are shown in Figures 3.6 and 3.7.

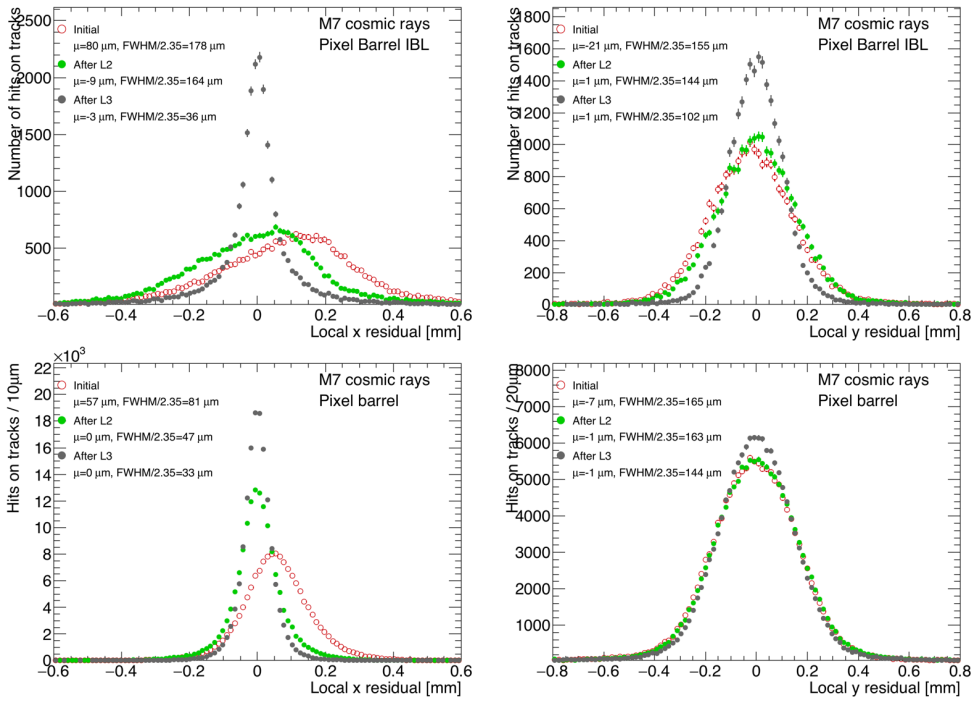

Figure 3.8: Local $x\prime$ (*left*) and local $y\prime$ (*right*) residual distributions for all hits-on-track in the IBL (*top*) and in the Pixel barrel (*bottom*) for the cosmic-ray data sample reconstructed before (red) and after Level 2 (green) and Level 3 (grey) alignment. The parameter μ represents the mean of the distributions.

The alignment procedure is based on the residuals minimization. The local $x\prime$ (*left*) and local $y\prime$ (*right*) residual distributions for all hits-on-track in the IBL (*top*) and in the Pixel barrel (*bottom*) are shown in Figure 3.8. The improvement between before and after alignment is quantified in terms of the Full Width Half Maximum (FWHM) of the distributions. A misalignment of 80 (-21) μm in the $x\prime$ ($y\prime$) direction of the IBL is corrected, with the FWHM/2.35 [5] being reduced from 178 (155) μm to 36 (102) μm respectively. Similarly, a bias of 57 (7) μm in the Pixel barrel local

[5] In a Gaussian distribution, the FWHM is related to the standard deviation via FWHM = 2.35σ.

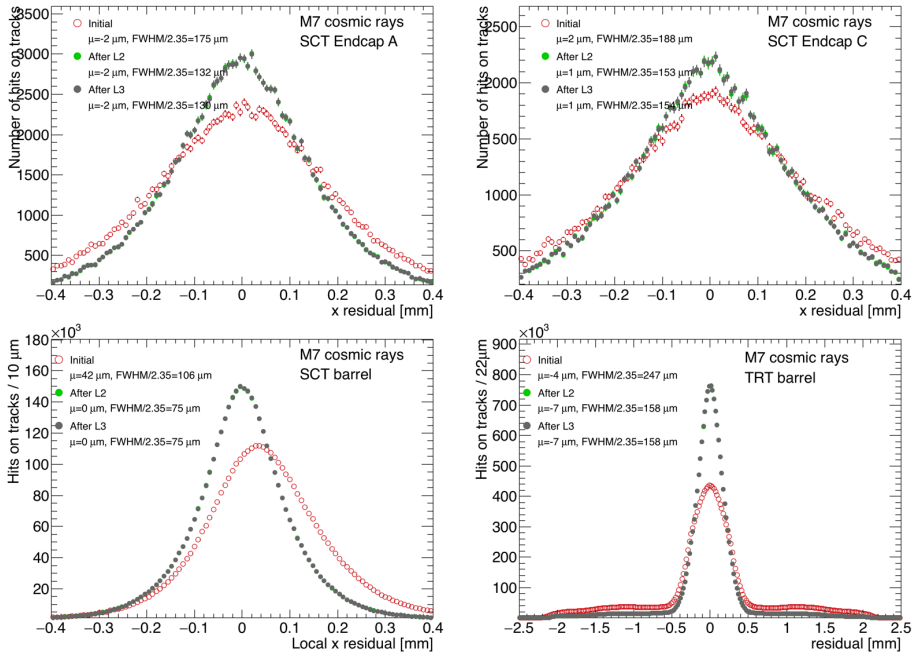

Figure 3.9: Local $x\prime$ and local $y\prime$ residual distributions in the SCT end-caps (*top*), the SCT barrel (*bottom-left*) and TRT barrel (*bottom-right*) for the cosmic-ray data sample reconstructed before (red) and after Level 2 (green) and Level 3 (grey) alignment. The parameter μ represents the mean of the distributions.

$x\prime$ and local $y\prime$ direction has been corrected. The width of the distribution has been reduced from 81 (165) μm to 33 (144) μm in $x\prime$ and $y\prime$, respectively. Figure 3.9 shows the local $x\prime$ and local $y\prime$ residual distributions in the SCT end-caps (*top*), the SCT barrel (*bottom-left*) and TRT barrel (*bottom-right*). The residual mean of the SCT barrel is corrected by 42 μm and the FWHM/2.35 is reduced from 106 μm to 75 μm. This value is far from the SCT intrinsic resolution because SCT alignment still needs to be refined by using higher alignment levels. The slight improvement observed in the TRT barrel, which is fixed in all the alignment procedure, comes from the corrections in the reconstructed tracks. Finally, the end-caps distributions do not show a significant improvement since cosmic-ray events do not provide high

enough statistics and incident angles within end-caps are very large, not allowing for a proper alignment.

3.4.1 IBL distortion

During the period of commissioning, it was observed that the IBL staves exhibit a temperature dependent bowing shape distortion from the flat designed shape. The observed distortion is the consequence of a mismatch in the coefficient of thermal expansion between the bare stave and the Stave Flex glued on it. This effect is estudied in detail in [3], and only a brief summary is given here.

Cosmic-ray events were collected in March 2015 at different IBL operating temperature set points (+15 ºC, +7 ºC, 0 ºC, -10 ºC, -15 ºC and -20 ºC) with the purpose of studying the correlation between the temperature and the size of the IBL distortion. The top panel in Figure 3.10 shows the observed local x-residual averaged over all modules of the same global z position in different staves. The staves distortion is negligible at IBL temperatures close to room temperature (20 ºC), as can be seen in the distribution at 15 ºC, which is flat within a few tens of micrometers. The maximum displacement with respect to the nominal position is observed at a temperature of -20 ºC, for which the deviation is of more than 300 μm.

The bottom panel of the Figure shows the same distribution after a Level 3 alignment (module level). The corrections are derived for the dataset collected at a temperature of 20 ºC, starting from initial corrections corresponding to a flat stave. After the correction, the observed residuals for the 20 ºC dataset are consistent with zero, showing that a module level alignment is able to correct the distortion.

From studies using a Finite Element Analysis [6], the distortion is expected to be parabolic. Therefore, the following parabolic function can be used to describe the averaged local-x residual, Δx_L:

$$\Delta x_L(z) = B - \frac{M}{z_0^2}(z^2 - z_0^2) \tag{3.12}$$

[6]The Finite Element Analysis is the simulation of any given physical phenomenon using a numerical technique which cuts the structure into several elements and then reconnects them at nodes, resulting in a set of algebraic equations.

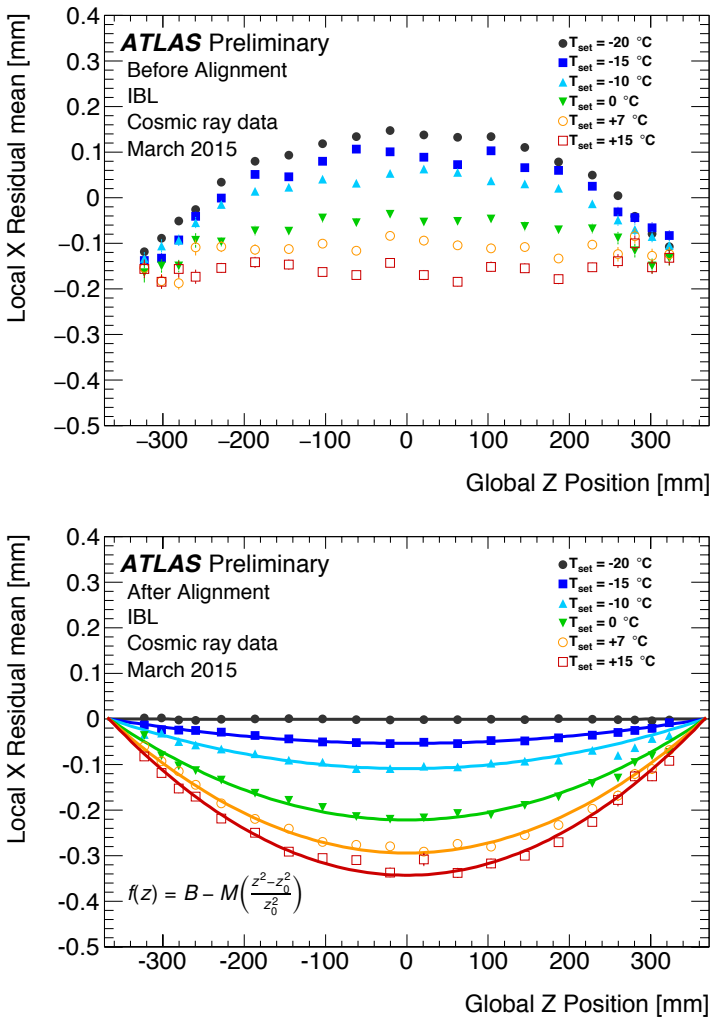

Figure 3.10: *Top*: The track-to-hit residual mean in the local-x direction. The residual mean is averaged over all hits of modules at the same global-z positon. There are no alignment corrections applied to the local positions in the IBL module frame during the track reconstruction. *Bottom*: The same distributions after applying the alignment corrections derived at -20 ºC. Each data set is fitted to a parabola which is constrained to match to the baseline B = 0 at $z = \pm z_0 = \pm 366.5\text{mm}$(see Eq. 3.12).

where z is the global z position of the module and z_0 = 366.5 mm is the fixing point of the stave at both ends. B is the baseline which describes the overall translation of the whole stave and is set to a common constant for all temperature points because the end-blocks of each stave are fixed mechanically. M, the free parameter in the fit, is the magnitude of the distortion at the center of the stave and quantifies the size of the distortion. The parameterization function describes the distortion shape of each temperature point as presented in the bottom panel of Figure 3.10. The dependence between the set temperature and the size of the distortion is linear and is fit as

$$\frac{\mathrm{d}M}{\mathrm{d}T} = -10.6 \pm 0.7 \mu\mathrm{m/K}. \tag{3.13}$$

The instability of the IBL temperature can be due to the intrinsic stability of the cooling system and the ambient environment or to module power consumption variations. Using data collected from the temperature sensors of the IBL during the stable cosmic-ray data taking, the size of the temperature variation of the IBL staves is measured to be less than 0.2 K, leading to negligible biases in the impact track parameters.

3.4.2 Run-by-run alignment

As mentioned in the previous section, in order to correct any possible movement or deformation prior to the bulk reconstruction, a run-by-run alignment was implemented in the 48 hours calibration loop at Tier0 in Run-1. After the end of each run, two iterations at Level 1 were run. To facilitate the task of monitoring the ouput from the calibration loop, a web monitoring [7] was also developed, using the web framework *CherryPy* [178] and PyROOT [179].

The web application automatically searches for new runs and keeps the outputs on a database. Then, it creates plots on demand by the user, with an intuitive interface. The tool allows to produce residual distributions, hit maps and alignment correction plots for individual runs, as well as plots of evolution of the alignment constants for a range of runs.

[7] https://atlasalignment.cern.ch/

In preparation for Run-2 both, the calibration loop and the web display were updated to accommodate the changes during the LS1. With the introduction of the IBL, the alignment levels had to be updated to include this structure. The geometry of the detector changed and the scripts were modified to accommodate the new needs that appeared during Run-2. The new alignment at the calibration loop includes four iterations, two at Level 1 followed by two at Level 2 [8].

The top panel of Figure 3.11 shows a screenshot of the web display taken in 2015. As an example of the kind of plots that can be done, the bottom panel shows the evolution of the T_x correction after Level 1 alignment for a range of runs.

[8]This thesis reflects the work done in ID alignment during 2015. The calibration loop has been further updated and the configuration is quite different at present. Among other changes, the alignment levels have changed and it includes a time-dependent alignment to correct the bowing of the IBL, which has a more sizable effect during collisions, due to the increased luminosity.

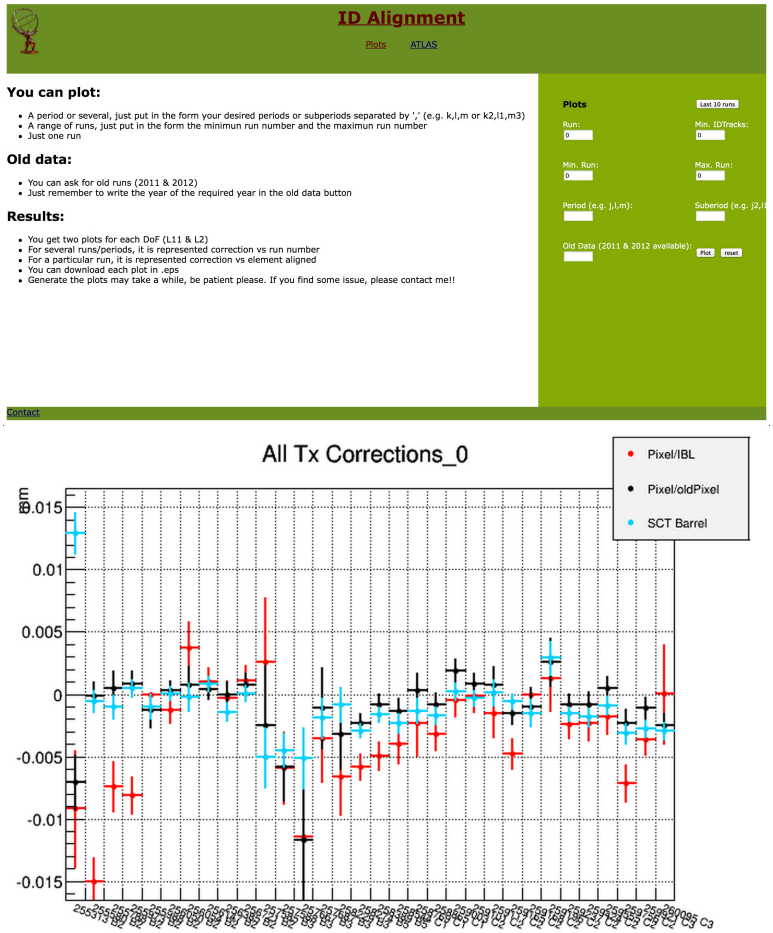

Figure 3.11: *Top*: screenshot of the web display as it was seen in 2015. The available plotting options are listed. *Bottom*: evolution of the T_x corrections for a range of runs after Level 1 alignment.

4 | Wtb vertex at single-top-quark decay in pp collisions at 8 TeV

With a mass close to the electroweak symmetry breaking scale, the top-quark is the heaviest fundamental constituent of the SM. Due to its large mass, the top quark can be used to probe the electroweak symmetry breaking mechanism, opening a gate to discovery of new physics phenomena. By taking advantage of the high production rate of top quarks at the LHC, this chapter presents the measurement of a set of observables which probe the structure of the Wtb vertex and can provide a hint of the presence of new physics in this vertex in the form of anomalous couplings.

The Wtb vertex appears in the production and decay of the top quark when it is produced singly in the t-channel, and the produced top quarks are highly polarized. Moreover, due to its short lifetime, the information on the top-quark spin can be obtained from its decay products. The observables presented in this thesis consist on asymmetries of angular distributions of the decay products of the W boson, thus probing the vertex at the decay of the top quark. These asymmetries are related to observables that completely describe the polarization of the W boson. Both, the angular asymmetries and their related W boson spin observables are listed in Table 4.1 and discussed in detail in Chapter 1.3.

This chapter is based on the results publised in [1]. The data analyzed is from pp collisions at a center of mass energy of $\sqrt{s}$ = 8 TeV collected by the ATLAS detector. The first step of the analysis consists on defining a signal region enriched in t-channel events. The signal and background processes are estimated via MC simulations or data-driven techniques and control regions are defined to check the

Angular distribution	Spin observables		Asymmetries			
	Observable	SM pred.	Observable			SM pred.
$\cos\theta_\ell*$	$< S_3 >$	-0.30	A_{FB}	=	$\frac{3}{4}\langle S_3\rangle$	-0.23
$\cos\theta_\ell*$	$< T_0 >$	-0.45	A_{EC}	=	$\frac{3}{8}\sqrt{\frac{3}{2}}\langle T_0\rangle$	-0.20
$\cos\theta_\ell^T$	$< S_1 >$	0.46	$A_{\rm FB}^T$	=	$\frac{3}{4}\langle S_1\rangle$	0.34
$\cos\theta_\ell^N$	$< S_2 >$	0.00	$A_{\rm FB}^N$	=	$-\frac{3}{4}\langle S_2\rangle$	0.00
$\cos\theta_\ell * \cos\phi_T*$	$< A_1 >$	0.23	$A_{\rm FB}^{T,\phi}$	=	$-\frac{2}{\pi}\langle A_1\rangle$	-0.14
$\cos\theta_\ell * \cos\phi_N*$	$< A_2 >$	0.00	$A_{\rm FB}^{N,\phi}$	=	$-\frac{2}{\pi}\langle A_1\rangle$	0.00

Table 4.1: Summary of the angular asymmetries measured in this analysis and their related spin observables with their SM prediction values.

modeling of background events. In particular, a maximum likelihood fit of the expected event yields to data is performed in the signal and control regions in order to constrain the normalization of the background processes. Signal is extracted by subtracting backgrounds to data in the signal region. These distributions are then corrected to parton level to correct for physics and detector effects using an unfolding method. From these distributions, the W boson spin observables are determined. The measurement of the W boson spin observables is performed assuming SM couplings and therefore these results are used as a consistency test of the SM predictions. In addition, one of the asymmetries is measured in an independent manner and the result is used to set limits on the imaginary part of the anomalous coupling $g_{\rm R}$. Complex values of this couplings would imply that the top-quark decay has a CP-violating component.

4.1 Signal production and background contamination

The top quark is produced in the t-channel at leading order when a valence quark interacts with a bottom quark from the sea through the exchange of a W boson, which results in the production of a light quark and a top quark. There are two different schemes at LO depending on the origin of the initial-state b quark. The $2 \to 2$ process $b+q \to q'+t$ (Figure 4.1 (a)) that occurs when the b-quark is one of the initial partons is called the five-flavor scheme, considering presences of five

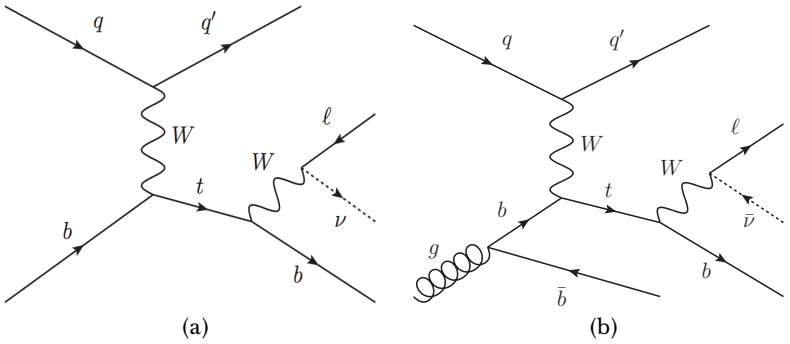

Figure 4.1: Leading-order Feynman diagrams for t-channel production of single top-quarks in pp collisions: (a) $2\to2$ process (five-flavour scheme) and (b) $2\to3$ process (four-flavour scheme). The leptonic decay of the top-quark ($t \to Wb$ with $W \to \ell\nu$) is also displayed.

flavor quarks inside the proton (u, d, c, s or b). The $2 \to 3$ process $g + q \to q' + t + \bar{b}$ (Figure 4.1 (b)), is the so-called 4-flavor scheme where the proton is considered to be composed of only four light quarks (u, d, c and s) and the b quarks arise from the splitting of a virtual gluon into nearly collinear $b\bar{b}$. In this scheme, the $\bar{b}$ quark in the final state is characterized by its soft transverse momentum spectrum, being most of the time outside the kinematic acceptance. The singly-produced top quark decays into a bottom quark and a W boson. The W can decay into either two quarks or a charged lepton and a neutrino. Despite having a larger branching ratio, the hadronic decay suffers from a large multijet background and consequently the leptonic one is preferred. In addition, the spin analyzer power of the charged lepton is $\approx$ 1 and the observables measured in this analysis are defined in the leptonic decay channel. Therefore, those events in which the W boson decays giving an electron or a muon, together with its corresponding neutrino, are considered in this analysis. The tau lepton is difficult to identify and therefore events in which the W decays to a τ lepton are included only if the τ lepton decays subsequently to an electron or a muon

$$t \to Wb; \quad W \to \ell\nu_\ell$$
$$t \to Wb; \quad W \to \tau\nu_\tau; \quad \tau \to \ell\nu_\ell$$

where $\ell = e$ or μ.

As a result, signal events with a single-top quark produced in the t-channel with a leptonic W boson decay leave a signature characterized by the presence of two jets, one of them being identified as a b-jet, exactly one lepton and missing transverse momentum corresponding to the neutrino, as shown in Fig. 4.1.

There are several processes in the SM which have a similar signature to the one just described and can pass the selection requirements; the main background contributions are listed below.

- **Top processes**: these include single-top quarks created via electroweak interaction in the s-channel or via Wt associated production as well as strong production of $t\bar{t}$ pairs. These processes, which were discussed in detail in Chapter 1.2, are difficult to distinguish from the signal since they contain real top quarks in the final state.

- W**+jets production**: production of a real W boson in association with heavy flavor ($W + b\bar{b}$ and $W + c\bar{c}$) or light flavor quark jets. An example of a W+jets process is depicted in Figure 4.2 (a).

- Z**+jets production**: electroweak production of a single Z boson in association with heavy flavor ($Z + b\bar{b}$ and $Z + c\bar{c}$) or light flavor quark jets. An example of a Z+jets process is depicted Figure 4.2 (b).

- **Diboson production**: electroweak production of diboson (WW, ZZ or ZW). An example of a WW production process is depicted in Figure 4.2 (c).

- **Multijet production**: events originating from QCD multijet production in which one of the jets is misidentified as an isolated lepton, or in which a

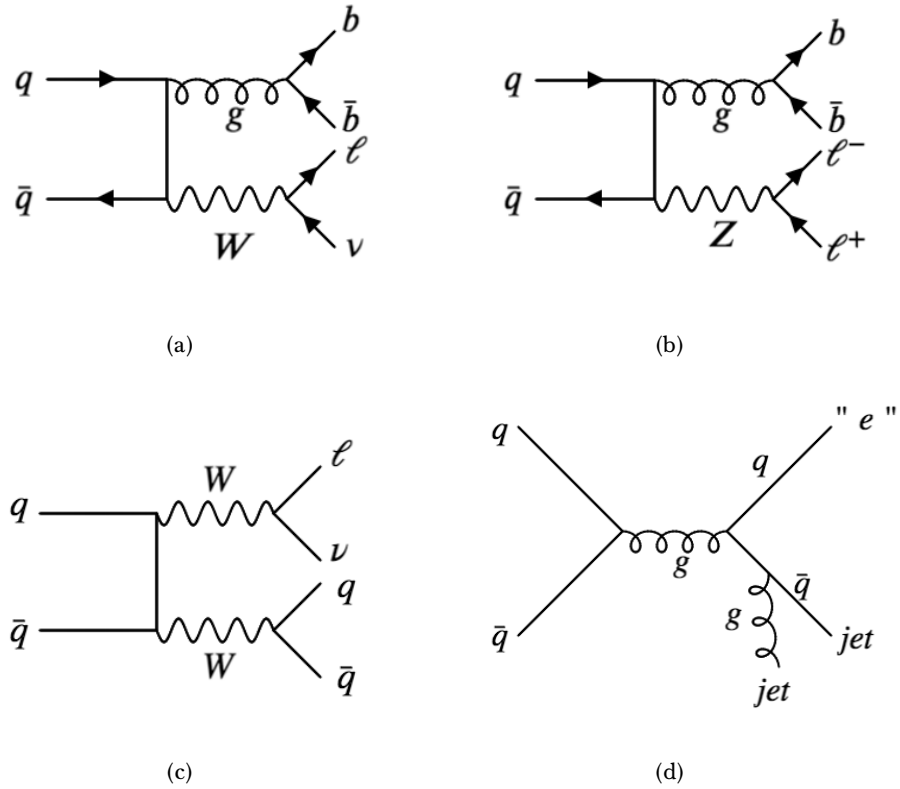

Figure 4.2: Example Feynman diagrams of the main backgrounds (besides other top production) faking single-top t-channel signatures: (a) W+jets, (b) Z+jets, (c) diboson and (d) multijet production from left to right and top to bottom.

non-prompt lepton appears to be isolated (both referred to as fake leptons). An example of a multijet process is depicted in Figure 4.2 (d).

4.2 Data and simulation samples

The analysis is performed using pp collision data collected in 2012 by the ATLAS detector at a center-of-mass energy of 8 TeV. The events are required to pass single-electron or single-muon triggers [135, 180], resulting, after detector

and data-quality requirements, in a data sample corresponding to an integrated luminosity of $20.2\ \mathrm{fb}^{-1}$. The electron and muon triggers impose a threshold of 24 GeV on the transverse momentum (p_{T}), along with isolation requirements. To recover efficiency for higher-p_{T} leptons, the isolated lepton triggers are complemented by triggers without isolation requirements, but with a threshold raised to 60 GeV for electrons and to 36 GeV for muons.

Simulated samples

Samples of signal and background events are simulated using various Monte Carlo generators. The generated events are passed through a simulation of the ATLAS detector [181] based on the GEANT4 framework [182]. For some samples a faster simulation (ATLFAST-II [183]), making use of a parametrized response of the electromagnetic and hadronic calorimeters, is used instead. Minimum-bias events [1] simulated with the PYTHIA (8.1) [184] generator are overlaid to model the pile-up effects from additional pp collisions in the same and nearby bunch crossings. All simulated events are then processed using the same reconstruction and analysis chain as for data events.

Signal samples

Signal t-channel single-top-quark events are generated with the NLO POWHEG-BOX (r2556) [185–187] generator, which uses the four-flavour scheme (Figure 4.1 (b)) for the matrix-element calculations [188]. Events are generated with the CT10f4 [125] parton distribution functions (PDFs), and the renormalization and factorization scales are set to $\mu_{\mathrm{R}}^2 = \mu_{\mathrm{F}}^2 = 16\left(m_b^2 + p_{\mathrm{T},b}^2\right)$, where m_b is the mass of the b-quark and $p_{\mathrm{T},b}$ is the transverse momentum of the b-quark from the initial gluon splitting (called the spectator b-quark) [188]. Additional t-channel samples are produced with the LO PROTOS (2.2) [42] generator using the CTEQ6L1 PDFs [126]. PROTOS events are generated using the four-flavor scheme, as well, and anomalous couplings are enabled in both the production and the decay vertices, varying Re V_{L}

[1] Min-bias is a generic term which refers to events that are selected with a loose trigger that accepts a large fraction of the overall inelastic cross section.

and $\mathrm{Im}\, g_\mathrm{R}$ simultaneously to keep the top-quark width invariant. The factorization scale is set to $\mu_\mathrm{F}^2 = -p_W^2$ for the light quark, where p_W is the four-momentum of the exchanged W boson, and to $\mu_\mathrm{F}^2 = m_b^2 + p_{\mathrm{T},b}^2$ for the gluon. Five PROTOS samples generated with $\mathrm{Im}\, g_\mathrm{R}$ in the range $[-0.144, 0.144]$ and $\mathrm{Re}\, V_\mathrm{L}$ in the range [0.982, 1] are used, including the Standard Model configuration $\mathrm{Im}\, g_\mathrm{R} = 0$ and $\mathrm{Re}\, V_\mathrm{L} = 1$. For each non-standard configuration, the two couplings are varied in such a way to keep the total top-quark decay width invariant. These PROTOS samples are used to compute the parton-level unfolding corrections and to check the reliability of the unfolding method, while the POWHEG-BOX sample is used to determine the expected event yields and template distributions. The reason behind the choice of a LO generator over a NLO one to compute the migration matrix comes from the fact that the light quark is not unambiguously defined at NLO, making it impossible to properly define the distributions at parton level. Tables 4.2 and 4.3 show the predicted values of the W boson spin observables and the angular asymmetries for the different PROTOS Wtb anomalous couplings settings used in the analysis. Table A.2 in Appendix A.1 lists the LO PROTOS configurations used in the analysis.

Img_R	$\langle S_3 \rangle$	$\langle T_0 \rangle$	$\langle S_2 \rangle$	$\langle S_1 \rangle$	$\langle A_2 \rangle$	$\langle A_1 \rangle$
SM	-0.303	-0.446	0	0.455	0	0.228
0.094	-0.311	-0.436	-0.071	0.453	-0.035	0.227
-0.094	-0.311	-0.436	0.071	0.453	0.035	0.227
0.23	-0.348	6 -0.390	-0.163	0.443	-0.081	0.222
-0.23	-0.348	-0.390	0.163	0.443	0.081	0.222

Table 4.2: W boson spin observables for the different Wtb anomalous couplings settings used in the analysis to test the unfolding performance.

Background samples

$t\bar{t}$ [189], s-channel single-top-quark and Wt [190] processes are produced using the POWHEG-BOX (r2819, r3026) generator with the CT10 PDFs. To generate the $t\bar{t}$ sample, the model parameter h_damp, which effectively regulates the high-p_T

Im g_R	$A_{FB}^{T,\phi}$	A_{FB}^{N}	A_{FB}	A_{EC}	$A_{FB}^{N,\phi}$	A_{FB}^{T}
SM	-0.145	0.0	-0.227	-0.205	0.0	0.342
0.094	-0.144	0.053	-0.233	-0.200	-0.023	0.339
-0.094	-0.144	-0.053	-0.233	-0.200	0.023	0.339
0.23	-0.141	0.122	-0.261	-0.179	-0.052	0.332
-0.23	-0.141	-0.122	-0.261	-0.179	0.052	0.332

Table 4.3: Angular asymmetries for the different Wtb anomalous couplings settings used in the analysis to test the unfolding performance.

gluon radiation, is set to the top-quark mass m_t [191]. The parton showering, hadronization and the underlying event of these samples are simulated with PYTHIA (6.426) [192] using parameter values set to the Perugia 2011C tune [193], and the CTEQ6L1 PDFs. All top-quark processes are simulated assuming a top-quark mass of 172.5 GeV, and the top-quark decay is assumed to proceed exclusively through $t \to Wb$.

Vector-boson production in association with jets is simulated using the multileg LO SHERPA (1.4.1) [194] generator with its own parameter tune and the CT10 PDFs. SHERPA is used not only to generate the hard process, but also for the parton shower and the modeling of the underlying event. W+jets and Z+jets events with up to four additional partons are generated. The CKKW method [195] is used to remove overlaps between the partonic configurations generated by the matrix element and by the parton showering. Diboson samples of WW, WZ and ZZ events are also produced, using the SHERPA (1.4.1) generator with the CT10 PDFs. All the generated SHERPA single-boson and diboson events are passed through the ATLFAST-II simulation of the detector.

The full list of the baseline simulated samples is available in Appendix A.1.

Samples to evaluate signal and background modeling

To study the modeling uncertainties of all processes involving top quarks, either alternative generators or parameter variations in the POWHEG-BOX and PYTHIA settings are used. For the estimation of the uncertainty in

the t-channel matrix-element calculation, a sample is produced using the MadGraph5_aMC@NLO (2.0) [196] generator, interfaced to Herwig (6.52) [197, 198] for parton showering and to Jimmy (4.31) [199] for the underlying-event modeling with the ATLAS AUET2 tuned parameter settings [200] and the CT10f4 PDFs. The events are generated using the four-flavor scheme. For the $t\bar{t}$, s-channel and Wt processes, alternative samples are produced using the MC@NLO (4.03) [201–204] generator interfaced to Herwig (6.52) for parton showering and Jimmy (4.31) for the underlying-event modeling with the ATLAS AUET2 tune and the CT10 PDFs. To specifically study the impact of the parton-shower modeling, a t-channel sample and a Wt sample both generated with Powheg-Box and coupled to Herwig (6.52) and Jimmy (4.31) with the AUET2 tune are used. For the $t\bar{t}$ process, samples generated using Powheg-Box with the CT10 PDFs, interfaced to Herwig (6.52) with the AUET2 tune or to Pythia (6.426) with the AUET2B tune, are used. Effects of varying the amount of radiation are studied by changing the hard-process and parton-shower scales simultaneously in the Powheg-Box and Pythia (6.426, 6.427) simulations. In the single-top-quark samples the factorization and renormalization scales are increased or decreased by a factor of two or one-half, respectively, in combination with the Perugia 2012 radLo and radHi tunes [193]. In the $t\bar{t}$ samples, h_{damp} is set to m_t or $2m_t$ in combination with the radLo and radHi parameterizations, respectively.

4.3 Event reconstruction and selection

The candidate events that match the signal topology explained in Section 4.1 at the level of the basic physics objects defined in Chapter 2.4 are preselected. From these events, the W boson and the top quark are reconstructed. Finally, a set of selection requirements defined in order to enhance the presence of the signal over the background events is applied to define the signal region. Additional requirements that increase the presence of the different background processes are also used to define control regions that are used for normalizing the backgrounds in the signal region and validating the background modeling, as it will be explained later in this chapter.

4.3.1 Objects selection

The object reconstruction was explained in detail in Section 2.4 and only a summary is given in the following.

Electron candidates are reconstructed from isolated energy deposits in the electromagnetic calorimeter which are associated with inner-detector tracks fulfilling strict quality requirements [145]. They are required to satisfy $p_{\mathrm{T}} > 25\,\mathrm{GeV}$ and $|\eta| < 2.47$, excluding the barrel–endcap transition region, corresponding to $1.37 < |\eta| < 1.52$. Muon candidates are reconstructed using combined tracking information from the inner detector and the muon spectrometer [151]. They are required to have $p_{\mathrm{T}} > 25\,\mathrm{GeV}$ and $|\eta| < 2.5$. The electron and muon candidates must fulfill additional isolation requirements, as described in Ref. [205], in order to reduce contributions from misidentified jets, non-prompt leptons from the decay of heavy-flavor quarks and electrons from photon conversions.

Jets are reconstructed using the anti-k_t algorithm [154] with a radius parameter of 0.4, from topological clusters [153], calibrated with a local cluster weighting method [158]. Jets are calibrated using an energy- and η-dependent simulation-based scheme, with in situ corrections based on data. The jet energy is further corrected for the effect of multiple pp interactions. To reject jets from pile-up events, a so-called jet-vertex-fraction criterion [157] is applied to the jets with $p_{\mathrm{T}} < 50\,\mathrm{GeV}$ and $|\eta| < 2.4$: at least 50% of the scalar sum of the p_{T} of the tracks associated with a jet is required to be from tracks compatible with the primary vertex. Only events containing two reconstructed jets with $p_{\mathrm{T}} > 30\,\mathrm{GeV}$ are selected. In addition, one of them must be b-tagged with $|\eta| < 2.5$, while the second jet is required to be untagged and to have $|\eta| < 4.5$. The b-tagging is performed using a neural network which combines three different algorithms exploiting the properties of a b-hadron decay in a jet [164]. The b-tagging algorithm is optimized to improve the rejection of c-quark jets, since W-boson production in association with c-quarks is a major background for the selected final state. The requirement applied to the neural-network discriminant corresponds to a b-tagging efficiency of 50%, and mistagging rates of 3.9% and 0.07% for c-quark jets and light-flavor jets, respectively, as predicted in simulated $t\bar{t}$ events [206, 207].

The missing transverse momentum, with magnitude $E_{\mathrm{T}}^{\mathrm{miss}}$, is reconstructed from the vector sum of energy deposits in the calorimeter projected onto the transverse plane [170]. All cluster energies are corrected using the local cluster weighting method. Clusters associated with high-p_{T} jets and electrons are further calibrated using their respective energy corrections. Contributions from the p_{T} of the selected muons are also included in the calculation.

4.3.2 Signal preselection

The signal event candidates are selected by requiring a single isolated electron or muon, significant missing transverse momentum, and exactly two jets with one of them identified as likely to contain a b-hadron (b-tagged jet). The presence of a third jet is not required since the additional jet resulting from the spectator b-quark originating from the gluon splitting (as shown in Figure 4.1 (b)) is expected to have a softer p_{T} spectrum and a broader $|\eta|$ distribution than the b-tagged jet produced in the top-quark decay, and, therefore, is in general not detected.

In addition, events are required to contain at least one good primary-vertex candidate, and no jets failing to satisfy reconstruction quality criteria. The magnitude of the missing transverse momentum is required to be larger than 30 GeV. In addition, the transverse mass of the lepton–$E_{\mathrm{T}}^{\mathrm{miss}}$ system must be greater than 50 GeV in order to reduce the multijet background contribution. [2] Further reduction of this background is achieved by imposing an additional requirement on events where the lepton and the leading jet in p_{T} have opposite directions in the transverse plane [208]

$$\frac{p_{\mathrm{T}}(\ell)}{1-\frac{\pi-|\Delta\phi(\ell,\mathrm{j})|}{\pi-1}} > 40\,\mathrm{GeV} \tag{4.1}$$

where $|\Delta\phi(\ell,\mathrm{j})|$ is the difference in azimuthal angle between the lepton momentum and the leading jet in p_{T}. To reduce the $t\bar{t}$ dilepton background, events containing

[2] The transverse mass of the lepton–$E_{\mathrm{T}}^{\mathrm{miss}}$ system is defined as $m_{\mathrm{T}}(\ell, E_{\mathrm{T}}^{\mathrm{miss}}) = \sqrt{2p_{\mathrm{T}}(\ell)E_{\mathrm{T}}^{\mathrm{miss}}\,(1-\cos\Delta\phi(\ell, E_{\mathrm{T}}^{\mathrm{miss}}))}$, where $\Delta\phi(\ell, E_{\mathrm{T}}^{\mathrm{miss}})$ is the difference in azimuthal angle between the lepton transverse momentum and the missing transverse momentum.

an additional lepton, identified with less stringent criteria (referred to as a loose lepton) and with a p_{T} threshold lowered to 10 GeV, are rejected.

Table 4.4 shows the predicted and observed event yields for electron and muon channels after applying the preselection requirements. The expected signal-to-background ratio is also given. The main background contributions come from the $t\bar{t}$ production and the W+jets processes.

Process	e-channel	μ-channel	e+μ
t-channel	8702 ± 26	10926 ± 30	19628 ± 39
$t\bar{t}$, Wt, s-channel	22372 ± 55	27761 ± 62	50133 ± 82
W+heavy-jets	$18\,450 \pm 120$	$25\,120 \pm 130$	44008 ± 180
W+light-jets	1196 ± 80	1600 ± 110	2800 ± 140
Z+jets, Diboson	2902 ± 45	2206 ± 37	5108 ± 58
Multijet	4300 ± 2200	5500 ± 2700	9800 ± 3500
Total expected	$57\,900 \pm 2200$	$73\,100 \pm 2700$	$131\,000 \pm 3500$
Data	58956	73246	132202
S/B	0.18	0.18	0.18

Table 4.4: Signal and background event yields in the preselected signal region. The quoted uncertainties correspond to the uncertainties due to the limited size of the simulation samples, except for the data-driven multijet contribution to which a normalization uncertainty of 70% is applied. The total expectation is compared to the observed number of events.

4.3.3 W boson and top quark reconstruction

The definition of the angular asymmetries, as well as the signal region definition, rely on the kinematics of the W boson and the top quark. They are reconstructed from the identified and selected objects.

The W boson four-momentum is reconstructed from the lepton and neutrino four-momenta

$$
\begin{aligned}
W \to \ell\nu_\ell \longrightarrow (p^W)^2 &= (p^\ell + p^{\nu_\ell})^2 \longrightarrow \\
m_W^2 &= m_\ell^2 + 2(E^\ell, \vec{p}^{\,\ell})(E^\nu, \vec{p}^{\,\nu}) \\
&= m_\ell^2 + 2(E^\ell E^\nu - \vec{p}^{\,\ell}\vec{p}^{\,\nu}) \\
&= m_\ell^2 + 2(E^\ell E^\nu - p_x^\ell p_x^\nu - p_y^\ell p_y^\nu - p_z^\ell p_z^\nu). \qquad (4.2)
\end{aligned}
$$

Since the neutrino escapes undetected, its transverse momentum is assumed to correspond to the x- and y- components of the transverse missing momentum

$$
\begin{aligned}
E^\nu &= \sqrt{(E_{\mathrm{T}}^{\mathrm{miss}})^2 + (p_z^\nu)^2}, \\
p_x^\nu &= E_{\mathrm{T}}^{\mathrm{miss}} \cos\phi_{E_{\mathrm{T}}^{\mathrm{miss}}}, \\
p_y^\nu &= E_{\mathrm{T}}^{\mathrm{miss}} \sin\phi_{E_{\mathrm{T}}^{\mathrm{miss}}},
\end{aligned}
$$

where $\phi_{E_{\mathrm{T}}^{\mathrm{miss}}}$ is the azimuthal angle associated with the missing transverse momentum.

The longitudinal component of the neutrino momentum is calculated by imposing a constrain on the lepton-neutrino system of the W boson pole mass ($m_W = 80.4$ GeV)

$$
\begin{aligned}
m_W^2 &= m_\ell^2 + 2(E^\ell E^\nu - p_x^\ell p_x^\nu - p_y^\ell p_y^\nu - p_z^\ell p_z^\nu) \\
&= m_\ell^2 + 2E^\ell \sqrt{(E_{\mathrm{T}}^{\mathrm{miss}})^2 + (p_z^\nu)^2} - 2\left[E_{\mathrm{T}}^{\mathrm{miss}}(p_x^\ell \cos\phi_{E_{\mathrm{T}}^{\mathrm{miss}}} + p_y^\ell \sin\phi_{E_{\mathrm{T}}^{\mathrm{miss}}}) + p_z^\ell p_z^\nu\right].
\end{aligned}
$$

Reordering the terms and squaring both sides leads to

$$
4(E^\ell)^2\left[(E_{\mathrm{T}}^{\mathrm{miss}})^2 + (p_z^\nu)^2\right] = \left[m_W^2 - m_\ell^2 + 2E_{\mathrm{T}}^{\mathrm{miss}}(p_x^\ell \cos\phi_{E_{\mathrm{T}}^{\mathrm{miss}}} + 2p_y^\ell \sin\phi_{E_{\mathrm{T}}^{\mathrm{miss}}})\right]^2.
$$

The only unknown term is the longitudinal component of the neutrino momentum that is obtained solving the second order equation

$$a(p_z^\nu)^2 + bp_z^\nu + c = 0 \tag{4.3}$$

with

$$\begin{aligned}
a &= (E^\ell)^2 - (p_z^\ell)^2, \\
b &= -p_z^\ell \left[m_W^2 - m_\ell^2 + 2E_{\mathrm{T}}^{\mathrm{miss}}(p_x^\ell \cos\phi_{E_{\mathrm{T}}^{\mathrm{miss}}} + p_y^\ell \sin\phi_{E_{\mathrm{T}}^{\mathrm{miss}}}) \right] \\
&= -p_z^\ell \left[m_W^2 - m_\ell^2 + 2(p_x^\ell p_x^\nu + p_y^\ell p_y^\nu) \right], \\
c &= (E^\ell)^2 (E_{\mathrm{T}}^{\mathrm{miss}})^2 - \frac{1}{4}\left[\frac{1}{2}(m_W^2 - m_\ell^2) + 2(p_x^\ell p_x^\nu + p_y^\ell p_y^\nu) \right]^2 .
\end{aligned}$$

The solution of the above equation is

$$p_z^\nu = \frac{1}{4\left[(E^\ell)^2 - (p_z^\ell)^2\right]} \left\{ p_z^\ell \left[m_W^2 - m_\ell^2 + 2(p_x^\ell p_x^\nu + p_y^\ell p_y^\nu) \right] \pm \sqrt{\Delta} \right\} \tag{4.4}$$

where

$$\Delta = (E^\ell)^2 \left[\left(m_W^2 - m_\ell^2 + 2(p_x^\ell p_x^\nu + p_y^\ell p_y^\nu) \right)^2 - 4(E_{\mathrm{T}}^{\mathrm{miss}})^2 ((E^\ell)^2 - (p_z^\ell)^2) \right]. \tag{4.5}$$

There are three possible cases depending on the value of the discriminant Δ:

- $\Delta = 0$: there is only one solution that is chosen as p_z^ν
- $\Delta > 0$: among the two possible solutions, the one giving the lower p_z^ν is chosen
- $\Delta < 0$: non-real solutions occur when the $E_{\mathrm{T}}^{\mathrm{miss}}$ is not well determined due to the non-perfect resolution and calibration of $E_{\mathrm{T}}^{\mathrm{miss}}$ measurement or when there are other contributions to it apart from the neutrino momentum itself (for example, extra neutrinos from B-hadron or τ-decays or contributions from the ISR/FSR). The strategy followed in this case is to modify the magnitude of the $E_{\mathrm{T}}^{\mathrm{miss}}$ while preserving the azimuthal angle, imposing that

the reconstructed $m_{\mathrm{T}}(W)$ matches the pole mass. This is equivalent to solving the equation $\Delta = 0$

$$\alpha(E_{\mathrm{T}}^{\mathrm{miss}})^2 + \beta E_{\mathrm{T}}^{\mathrm{miss}} + \gamma = 0 \tag{4.6}$$

with

$$\begin{aligned}
\alpha &= (p_x^\ell \cos\phi + p_y^\ell \sin\phi) - \left[(E^\ell)^2 - (p_z^\ell)^2)\right], \\
\beta &= (m_W^2 - m_\ell^2)(p_x^\ell \cos\phi + p_y^\ell \sin\phi), \\
\gamma &= \frac{1}{4}(m_W^2 - m_\ell^2)^2.
\end{aligned}$$

The solution of this equation is

$$E_{\mathrm{T}}^{\mathrm{miss}\prime} = \frac{(m_W^2 - m_\ell^2)(p_x^\ell \cos\phi + p_y^\ell \sin\phi) \pm (m_W^2 - m_\ell^2)\sqrt{(E^\ell)^2 - (p_z^\ell)^2}}{2(p_x^\ell \cos\phi + p_y^\ell \sin\phi) - 2\left[(E^\ell)^2 - (p_z^\ell)^2)\right]}. \tag{4.7}$$

The solution providing closer $E_{\mathrm{T}}^{\mathrm{miss}\prime}$ to the original $E_{\mathrm{T}}^{\mathrm{miss}}$ is chosen and increased by few eV to make $\Delta > 0$. This new $E_{\mathrm{T}}^{\mathrm{miss}}$ is applied in Equation 4.4 to obtain the final value of p_z^ν.

Once the four-momenta of the W boson is reconstructed, it is used to compute the four-momenta of the of the top quark candidate:

$$t \to Wb \longrightarrow p^t = p^W + p^b. \tag{4.8}$$

4.3.4 Signal selection

As seen in Table 4.4, background processes contribute to a big fraction of the events if a selection based only on the final signal topology is applied. In order to further separate signal from background, additional requirements that exploit the topology of t-channel single top quark events are applied to the events that fulfill the preselection criteria. The choice of the four selection variables is based on the studies performed for the 7 TeV cut-based t-channel analysis published in Ref [209] and is optimized with respect to the expected signal-to-background ratio, taking into consideration the expected statistical and systematic uncertainties. Figure 4.3

shows the shape comparison for these variables between the t-channel signal and the main backgrounds at preselection level. The dashed vertical lines represent the requirements that define the signal region:

- The pseudorapidity of the untagged jet must satisfy $|\eta| > 2.0$, since the spectator quark tends to be produced in the forward direction in the t-channel process.
- The separation in η between the untagged jet and the b-tagged jet must be larger than 1.5, to reduce the contribution from $t\bar{t}$ background events.
- The mass of the reconstructed top quark is required to be between 130 GeV and 200 GeV, to reject background events from processes not involving top quarks.
- The scalar sum (H_{T}) of the p_{T} of the lepton, the p_{T} of the jets and $E_{\mathrm{T}}^{\mathrm{miss}}$ must be larger than 195 GeV, to further reduce the number of background events, in particular the W+jets contribution.

Figure 4.4 shows the distributions of the four variables relevant for these requirements, comparing data to the predicted signal and background distributions normalized to the results of the maximum-likelihood fit described in Section 4.5. The cuts that define the signal region are indicated for each of the variables. The multijet background estimate shown in the figure is discussed in Section 4.4.

4.4 Background normalization and modeling

As seen in Table 4.4, the largest background contributions to t-channel single top-quark production arise from $t\bar{t}$ and W+jets production. Other minor backgrounds originate from Wt, s-channel single top-quark, Z+jets and diboson production.

For all processes, except multijet production, the normalization is initially estimated by using the Monte Carlo simulation scaled to the theoretical cross-section predictions, and the event distribution modeling is taken from simulation.

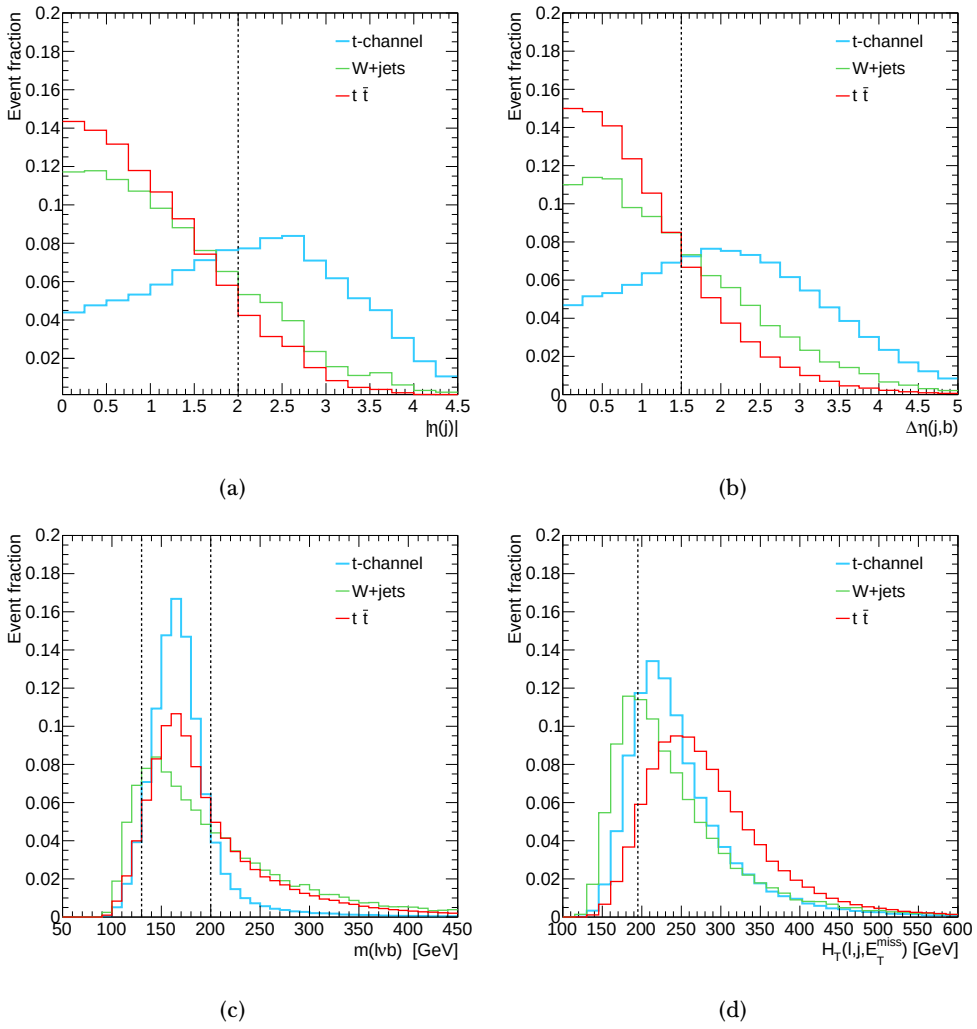

Figure 4.3: Shape distributions of the selection variables in the preselected signal region for the signal and main backgrounds: (a) the $|\eta|$ of the untagged jet, (b) the separation in η between the untagged and b-tagged jets, (c) the mass of the reconstructed top quark and (d) the scalar sum of the p_{T} of the lepton, the p_{T} of the jets and the $E_{\mathrm{T}}^{\mathrm{miss}}$. The distributions are normalized to one and the dashed vertical lines represent the values of the cuts that define the signal region.

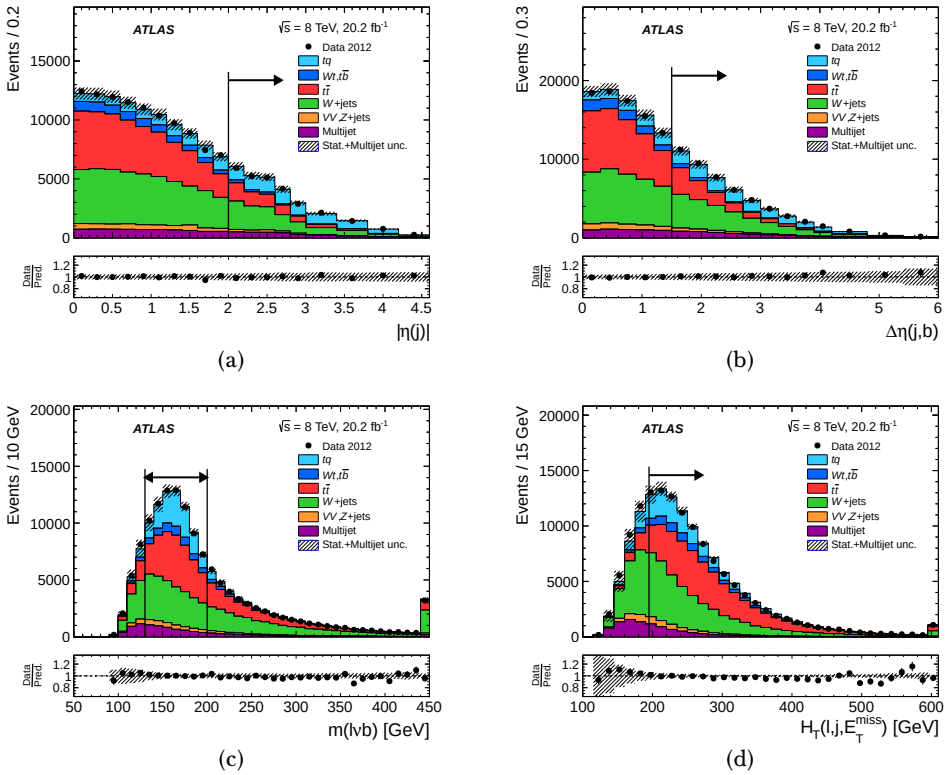

Figure 4.4: Distributions of the selection variables in the preselected signal region: (a) $|\eta|$ of the untagged jet, (b) separation in η between the untagged and b-tagged jets, (c) reconstructed top-quark mass, and (d) scalar sum of the p_{T} of the lepton, the p_{T} of the jets and $E_{\mathrm{T}}^{\mathrm{miss}}$. The observed distributions are compared to the predicted signal and background distributions, normalized to the results of the maximum-likelihood fit. The labels tq and $t\bar{b}$ refer to the t-channel and s-channel single-top-quark processes, respectively, and VV to diboson production. The vertical lines and the arrows define the signal region. The uncertainty bands include the statistical post-fit uncertainty, the uncertainty due to the limited size of the simulation samples and the uncertainty in the normalization of the multijet background, added in quadrature. The last bin of the histograms includes overflows. The lower panels show the ratio of data to prediction.

The $t\bar{t}$ production cross-section is calculated at NNLO in QCD including resummation of next-to-next-to-leading-logarithm (NNLL) soft gluon terms with Top++2.0 [18, 23, 210–213]. Its predicted value is 253^{+13}_{-15} pb [210]. The quoted uncertainties include the PDF and α_{s} uncertainties calculated according to the PDF4LHC prescription [214] with the MSTW2008 NNLO [123, 215], CT10 NNLO [125, 216] and NNPDF2.3 5f FFN [217] PDF sets, and the QCD scale uncertainty. The t-channel, Wt and s-channel single-top-quark production cross-sections are calculated at NLO precision in QCD through NNLL resummation, leading to $87.7^{+3.4}_{-1.9}$ pb [218], 22.4 ± 1.5 pb [219] and 5.6 ± 0.2 pb [21], respectively. The calculations assume a top-quark mass of 172.5 GeV and use the MSTW2008 NNLO [123] PDFs. The quoted uncertainties include those due to the QCD scale uncertainty and the correlated PDF–α_{s} uncertainty.

The cross-sections for inclusive W- and Z-boson production are estimated with NNLO precision using the FEWZ program [220, 221] and the MSTW2008 NNLO PDFs. The diboson samples are normalised to the NLO cross-section predictions calculated with MCFM [222]. A normalization uncertainty of 20% is assigned to the W+jets background. This uncertainty is estimated from parameter variations of the SHERPA generator covering the measured W+jets cross-sections [223]. A normalization uncertainty of 20% is also assumed for the Z+jets and diboson processes.

4.4.1 Data-driven multijet estimate

Multijet events can pass the signal selection if in addition to two reconstructed jets a fake lepton is selected. A fake lepton is a jet misidentified as an isolated lepton, or a non-prompt lepton that appears to be isolated. This non-negligible source of background is estimated with the data-driven matrix method [224]. This method relies on the solution of a set of equations which relate the observed sample composition in terms of tight (signal selection) and loose leptons (see Section 2.4 for details on tight and loose selection), to its true composition in terms of prompt (real) and fake leptons. An overview of this technique is given in the following.

The number of events with one tight lepton (N^{tight}) and the number of events with one loose lepton (N^{loose}) in a given data sample containing events with a single lepton can be expressed as a linear combination of the number of events with a real or a non-prompt or fake lepton passing the tight or the loose selection:

$$\begin{aligned} N^{loose} &= N^{loose}_{real} + N^{loose}_{fake}, \\ N^{tight} &= \epsilon_{real} N^{loose}_{real} + \epsilon_{fake} N^{loose}_{fake}, \end{aligned} \tag{4.9}$$

where ϵ_{real} is the fraction of real leptons passing the loose selection that also pass the tight one, and ϵ_{fake} is the fraction of non-prompt and fake lepton backgrounds passing the loose selection that also pass the tight one.

The real and fake efficiencies are measured in data in control samples which are enriched in either real or non-prompt or fake lepton. As explained in Section 2.4, one of the two triggers used to select events has an isolation requirement, while loose leptons are defined without any isolation cut. Efficiencies are thus derived and applied depending on the trigger being fired by the lepton and on the lepton p_{T} being below or above the high-p_{T} trigger threshold. In addition, several kinematic information can be used to parametrize the efficiencies of the events. As an example, Figure 4.5 shows the real and fake efficiencies for electrons firing the trigger with isolation requirement, as a function of different variables, in the selected sample of events using the tight lepton requirement.

The real and fake efficiencies are used to calculate the number of events with a non-prompt or fake lepton given the measured N^{loose} and N^{tight}. Therefore, the number of tight events coming from non-prompt or fake lepton backgrounds can be expressed as:

$$N^{tight}_{fake} = \frac{\epsilon_{fake}}{\epsilon_{real} - \epsilon_{fake}} (\epsilon_{real} N^{loose} - N^{tight}). \tag{4.10}$$

The real and fake efficiencies measured as a function of different variables are convoluted in different combinations to compute a global efficiency for the event

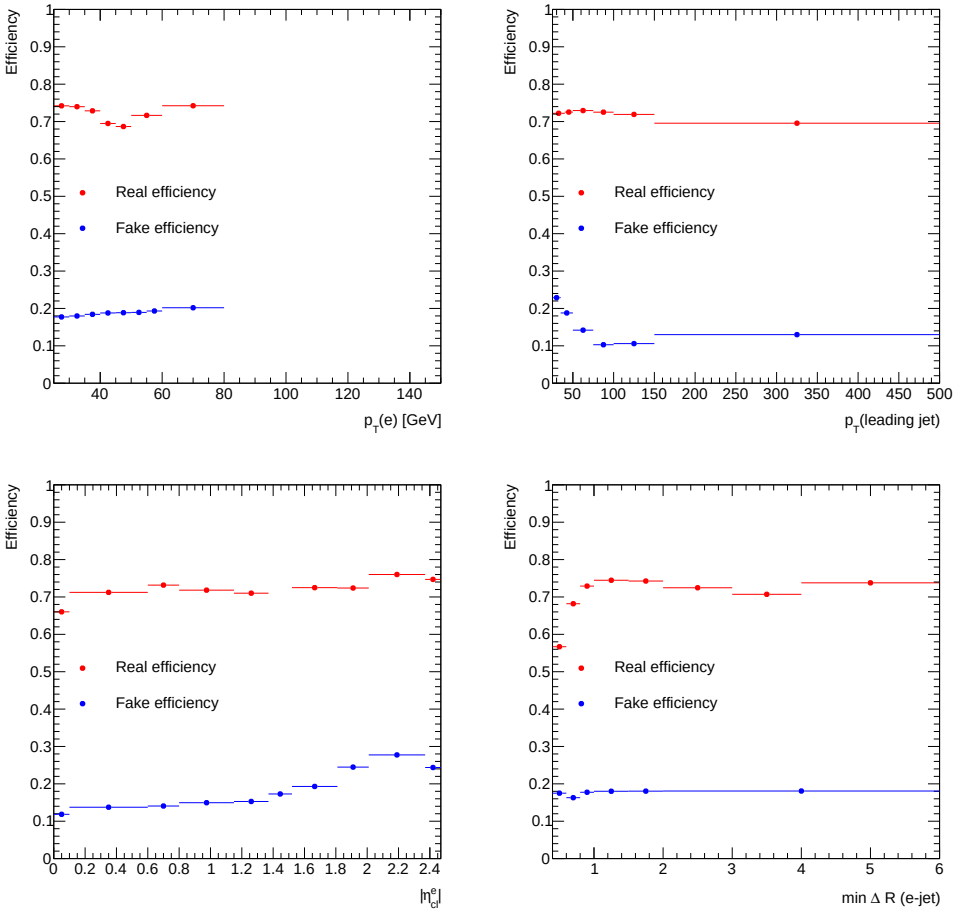

Figure 4.5: Real and fake efficiencies for electrons firing the trigger with isolation requirement, as a function of the different variables used for the parametrization: the lepton p_{T}, leading jet p_{T}, lepton $|\eta|$, and angular distance between the lepton and the closest jet.

$$\epsilon_k(x_1, ..., x_N; y_1, ..., y_M) = \frac{1}{\epsilon_k(x_1, ..., x_N)^{M-1}} \cdot \prod_{j=1}^{M} \epsilon_k(x_1, ..., x_N; y_j) \tag{4.11}$$

where $\epsilon_k(x_1, ..., x_N)$ is the efficiency measured as a function of all the x variables, while $\epsilon_k(x_1, ..., x_N$ represents the efficiency measured as a function of all the x variables and of the y_j variable.

Different variables and combinations of them were tested to find the optimal parametrization, summarized in Table 4.5. The real efficiencies for both electrons and muons are extracted as a function of the lepton pseudorapidity and p_{T} and the distance of the lepton to the closest jet (ΔR_{min}). The fake efficiencies are parametrized in terms of the electrons pseudorapidity, the leading jet p_{T} and the ratio of the leading jet p_{T} to ΔR_{min} in the case of the electron channel. For the muon channel, the fake efficiency is derived as a function of the muon pseudorapidity and p_{T}, the distance ΔR_{min}, and the significance of the d_0 parameter.

	Real efficiency	Fake efficiency
el-channel	$\lvert\eta^e_{cl}\rvert$, $p_{\mathrm{T}}(e)$, min ΔR(e,jet)	$\lvert\eta^e_{cl}\rvert$, p_{T}(leading jet), $\frac{p_{\mathrm{T}}(\text{leading jet})}{\min \Delta R(\text{e,jet})}$
μ-channel	$\lvert\eta^\mu_{cl}\rvert$, $p_{\mathrm{T}}(\mu)$, min $\Delta R(\mu, \text{jet})$	$\lvert\eta^\mu_{cl}\rvert$, $p_{\mathrm{T}}(\mu)$, min $\Delta R(\mu, \text{jet})$, $< d_0 >$

Table 4.5: Real and fake parametrizations chosen for the electron and muon channels.

Finally, an event-by-event weight is computed from the efficiencies, taking into account the kinematics of the event:

$$w_i = \frac{\epsilon_{fake}}{\epsilon_{real} - \epsilon_{fake}}(\epsilon_{real} - \delta_i), \tag{4.12}$$

where δ_i equals unity if the loose event i passes the tight event selection and 0 otherwise. These are the weights applied to the loose electrons sample, which are electrons satisfying medium likelihood-based selection criteria and on which no requests on the isolation criteria are made.

Comparison with alternative procedures (Jet-Electron/Antimuon models) and alternative parametrizations to select the real and fake efficiencies leads to non-negligible differences. An overall normalization uncertainty of 70% is assigned on the estimate of the multijet background contribution. A systematic uncertainty is also considered to take into account the differences in the shape modeling found between the matrix method and the jet-electron/antimuon models [205].

4.4.2 Control selections

To check the modeling of the $t\bar{t}$ and W+jets background contributions, the simulated events are compared to the data in two dedicated background-dominated regions.

- $t\bar{t}$ **control region**: Samples enriched in $t\bar{t}$ events are defined by considering events preselected as explained in Section 4.3, but containing two additional jets that are required to be untagged. The dilepton rejection and the four final selection cuts are not applied. This control region is also used in the normalization fit described in Section 4.5.

- W**+jets control region**: Samples enriched in W+jets events are selected by applying a relaxed b-tagging requirement corresponding to an efficiency of 80%. In addition, all events satisfying the signal b-tagging requirement are excluded. The dilepton rejection and the final selection cuts are not applied.

- **Anti-signal region**: An additional category of events is defined by selecting all events not passing the final signal selection cuts. This region is only used in the normalization fit, in combination with the $t\bar{t}$ control region. It is preferred to the W+jets control region to constrain the W+jets normalization because it has a flavor composition more similar to that of the signal region.

Tables 4.6 and 4.7 summarize the requirements criteria that define all the regions used in the analysis.

Tables 4.8 and 4.9 show the predicted and observed event yields for electron and muon channels, respectively, in the three control regions. In the anti-signal control

Preselected signal region	Signal region
Dilepton veto	$\|\eta(\mathrm{j})\| > 2.0$
1 isolated lepton candidate ($p_{\mathrm{T}}(\ell) > 25\mathrm{GeV}$)	$\|\Delta\eta(\mathrm{j},\mathrm{b})\| > 1.5$
2 jets ($p_{\mathrm{T}}(\mathrm{j}) > 30\mathrm{GeV}$, $\|\eta(\mathrm{j})\| < 4.5$) one of them b-tagged (MV1c, eff: 50%)	130 GeV$< m(\ell,\nu,\mathrm{b}) <$ 200 GeV
$E_{\mathrm{T}}^{\mathrm{miss}} > 30\mathrm{GeV}$ and $m_{\mathrm{T}}(W) > 50\mathrm{GeV}$	$H_{\mathrm{T}}(\ell,\mathrm{j},E_{\mathrm{T}}^{\mathrm{miss}})$ >195 GeV
$p_{\mathrm{T}}(\ell)/\left(1-\frac{\pi-\|\Delta\phi(\ell,\mathrm{j})\|}{\pi-1}\right)$ > 40 GeV	

Table 4.6: Summary of the requirements criteria that define the preselected and signal regions.

W+ jets control region	$t\bar{t}$ control region	Anti-signal control region
Preselection requirements, except: b-tagging efficiency: 80% Reject events that satisfy signal preselection	Preselection requirements 2 extra untagged jets	Satisfy preselection requirements Not satisfy selection requirements

Table 4.7: Summary of the requirements criteria that define the control and validation regions.

region the main contributions come from the top-quark backgrounds, representing a 40% of the total yield, and the W+jets production, with a contribution of 35% in the electron channel and 38% in the muon channel. The composition of the W+jets background is this region is a 2% of W+light jets and 33%-35% of W+heavy flavor, which is very similar to the signal region, that has 1% of W+light and 17% of W+heavy flavor. This control region has a expected signal to background ratio of $\sim$ 13%. In the $t\bar{t}$ control region the top backgrounds are expected to represent a 85% of the total yields and to have a signal to background ratio of $\sim$ 3%. Finally, the contribution of the W+jets production in the W+jets validation region is expected to represent 77% (83%) of the events, with a 34% (37%) coming from W+light jets and 43% (45%) from W+heavy flavor in the electron (muon) channel. The flavor composition of the W+jets production differs significantly from that of the signal region, and that's why the anti-signal region is preferred to constrain the

normalization of the backgrounds with the procedure explained in the following subsection. Figure 4.6 depicts the expected composition of the signal and control regions.

Process	Anti-signal CR	$t\bar{t}$ CR	W+jets CR
t-channel	6035 ± 22	842 ± 9	4631 ± 19
$t\bar{t}$, Wt, s-channel	21396 ± 54	27926 ± 51	10792 ± 41
W+heavy-jets	$17\,720 \pm 120$	2701 ± 38	$71\,010 \pm 310$
W+light-jets	1148 ± 79	121 ± 27	$56\,090 \pm 520$
Z+jets, Diboson	2822 ± 44	649 ± 31	$10\,630 \pm 150$
Multijet	4100 ± 2900	430 ± 300	$11\,000 \pm 7700$
Total expected	$53\,300 \pm 2900$	$32\,670 \pm 310$	$164\,100 \pm 7700$
Data	54342	32586	164112
S/B	0.13	0.03	0.03

Table 4.8: Predicted and observed event yields in the three control regions for the electron channel. The quoted uncertainties correspond to the uncertainties due to the limited size of the simulation samples, except for the data-driven multijet contribution to which the normalization uncertainty of 70% is applied. The total expectation is compared to the observed number of events.

Good overall data–prediction agreement is found in the $t\bar{t}$ W+jets and anti-signal control regions for the relevant kinematic observables, as well as for the various angular observables used in the measurements. Figure 4.7 shows the distributions in the $t\bar{t}$ control region of the four variables used to define the final selections. The distributions obtained in the W+jets control region are displayed in Figure 4.8.The distributions in both figures are normalized to the results of the maximum likelihood fit explained in the following subsection.

4.5 Signal and background event yields

The signal and background event yields are estimated through a simultaneous maximum-likelihood fit to the numbers of data events observed in the signal and anti-signal regions, and in the $t\bar{t}$ control region.

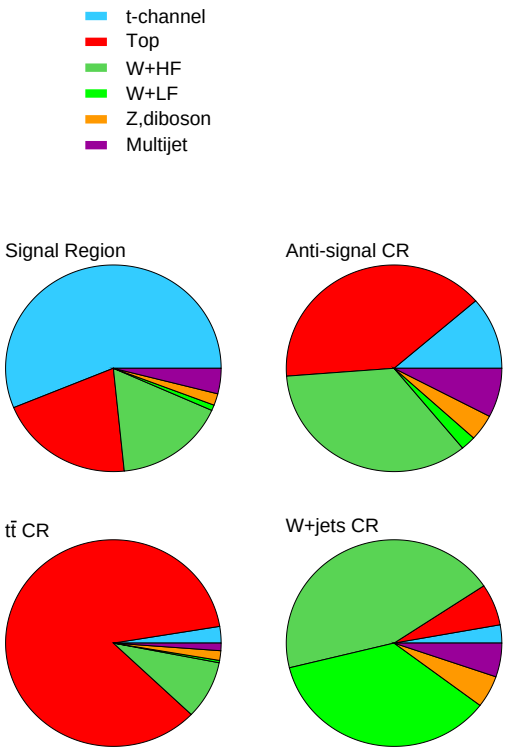

Figure 4.6: Comparison of the expected composition in the different control and signal regions. The contribution of W+jets is split in heavy flavor (W+HF) and light flavor (W+LF) contributions.

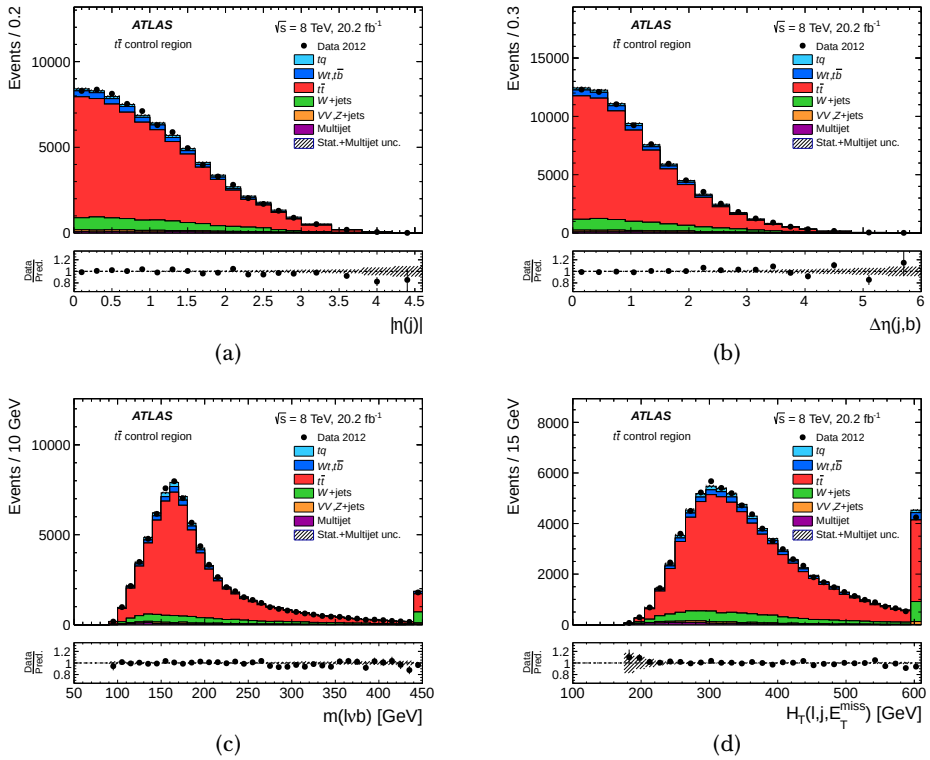

Figure 4.7: Distributions of the selection variables in the $t\bar{t}$ control region: (a) $|\eta|$ of the untagged jet, (b) separation in η between the untagged and b-tagged jets, (c) reconstructed top-quark mass, and (d) scalar sum of the p_{T} of the lepton, the p_{T} of the jets and $E_{\mathrm{T}}^{\mathrm{miss}}$. The observed distributions are compared to the predicted signal and background distributions, normalized to the results of the maximum-likelihood fit. The labels tq and $t\bar{b}$ refer to the t-channel and s-channel single-top-quark processes, respectively, and VV to diboson production. The uncertainty bands include the statistical post-fit uncertainty, the uncertainty due to the limited size of the simulation samples and the uncertainty in the normalization of the multijet background, added in quadrature. The last bin of the histograms includes overflows. The lower panels show the ratio of data to prediction.

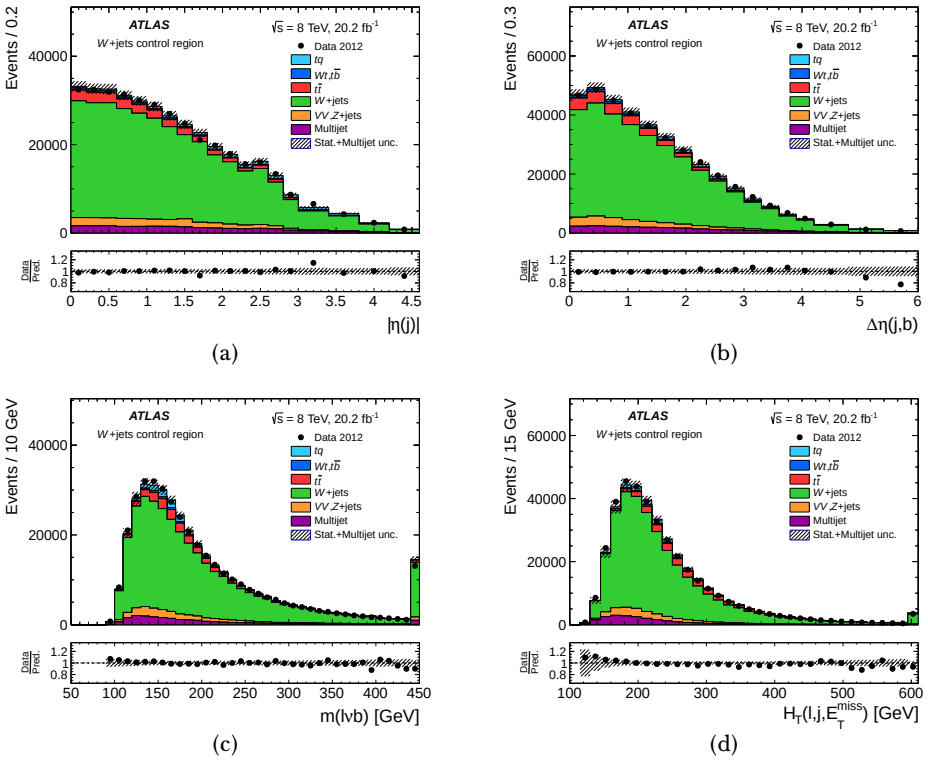

Figure 4.8: Distributions of the selection variables in the W+jets control region: (a) $|\eta|$ of the untagged jet, (b) separation in η between the untagged and b-tagged jets, (c) reconstructed top-quark mass, and (d) scalar sum of the p_{T} of the lepton, the p_{T} of the jets and $E_{\mathrm{T}}^{\mathrm{miss}}$. The observed distributions are compared to the predicted signal and background distributions. The W+jets distributions are normalized to match the observed number of events. The labels tq and $t\bar{b}$ refer to the t-channel and s-channel single-top-quark processes, respectively, and VV to diboson production. The uncertainty bands include the uncertainty due to the limited size of the simulation samples and the uncertainty in the normalization of the multijet background, added in quadrature. The last bin of the histograms includes overflows. The lower panels show the ratio of data to prediction.

Process	Anti-signal CR	$t\bar{t}$ CR	W+jets CR
t-channel	7596 ± 25	1082 ± 10	5917 ± 22
$t\bar{t}$, Wt, s-channel	26578 ± 61	35461 ± 59	13413 ± 47
W+heavy-jets	$24\,090 \pm 130$	4052 ± 51	$94\,310 \pm 350$
W+light-jets	1560 ± 110	144 ± 25	$77\,080 \pm 610$
Z+jets, Diboson	2093 ± 37	471 ± 15	7970 ± 110
Multijet	5100 ± 3600	450 ± 310	8700 ± 6100
Total expected	$67\,000 \pm 3600$	$41\,660 \pm 330$	$207\,000 \pm 6100$
Data	70125	41535	208735
S/B	0.13	0.03	0.03

Table 4.9: Predicted and observed event yields in the three control regions for the muon channel.The quoted uncertainties correspond to the uncertainties due to the limited size of the simulation samples, except for the data-driven multijet contribution to which the normalization uncertainty of 70% is applied. The total expectation is compared to the observed number of events.

The likelihood function [208] is given by the product of Poisson probability terms associated with the fitted regions, combined with the product of Gaussian priors to constrain the background rates to their predictions within the associated uncertainties. In the fit the t-channel single-top-quark contribution is treated as unconstrained. The top-quark background contributions ($t\bar{t}$, Wt and s-channel single top-quark production) are merged with their relative fractions taken from simulation, and the applied constraint is derived from the combination of their cross-section uncertainties presented in Section 4.4. The flavor composition of the W+jets contribution is taken from simulation. In all fitted regions the production of a W boson in association with heavy-flavor jets is the dominant contribution to the W+jets background, predicted to be around 95% in the three regions. The Z+jets and diboson contributions, which are very low in the signal region (2% of the total expectation), are merged and fixed to the predictions. The multijet contribution is kept fixed to its data-driven estimate. The likelihood function is therefore written as

$$L(\beta^s;\beta_j^b) = \prod_{i=1}^{N_{selections}} \frac{e^{-\mu_i}\cdot\mu_i^{n_i}}{n_i!} \cdot \prod_{j=1}^{N_{backgrounds}} G\left(\beta_j^b;1,\Delta_j\right) \tag{4.13}$$

$$\text{with} \quad \mu_i = \mu_i^s + \sum_{j=1}^{N_{backgrounds}} \mu_{ij}^b \quad , \quad \mu_i^s = \beta^s\cdot\tilde{\nu}_i^s \;\; and \;\; \mu_{ij}^b = \beta_j^b\cdot\tilde{\nu}_{ij}^b \tag{4.14}$$

where β^s is the scale factor associated to the signal process and β_j^b is the scale factor associated to the background process j. The index i runs over the regions used in the fit and n_i is the observed number of events. The j term represents the constrain applied to the normalization of the background process j used in the Gaussian term.

The results of the maximum-likelihood fit together with the associated statistical uncertainties (referred to as statistical post-fit uncertainties) are shown in Table 4.10. They are presented as scale factors to be applied to the predicted event yields. The results are found to be stable when the constraints imposed on the top-quark and W+jets backgrounds are significantly relaxed. Table 4.11 provides the signal and background event yields in the signal region after scaling to the results of the fit to the data. The signal-to-background ratio is 1.2, the t-channel single top-quark production representing 54% of the total expectation. The two main background contributions come from W+jets (19%) and $t\bar{t}$ production (18%).

Process	Scale factor
t-channel	0.95 ± 0.02
$t\bar{t}$, Wt, s-channel	1.01 ± 0.01
W+jets	1.10 ± 0.01

Table 4.10: Scale factors and uncertainties extracted for the signal and background processes from the simultaneous maximum-likelihood fit of the event yields in the signal, anti-signal and $t\bar{t}$ regions. The quoted uncertainties are statistical only.

Process	e-channel	μ-channel	$e + \mu$
t-channel	2560 ± 81	3160 ± 101	5700 ± 110
$t\bar{t}$, Wt, s-channel	988 ± 15	1195 ± 17	2179 ± 12
W+heavy-jets	780 ± 33	1167 ± 42	1947 ± 53
W+light-jets	51 ± 14	50 ± 17	101 ± 22
Z+jets, Diboson	80 ± 5	108 ± 8	188 ± 9
Multijet	176 ± 88	250 ± 120	420 ± 290
Total expected	4640 ± 130	5940 ± 160	$10\,530 \pm 320$
Data	4614	5702	10316
S/B	1.2	1.1	1.2

Table 4.11: Signal and background event yields in the signal region after scaling to the results of the maximum-likelihood fit. The quoted uncertainties add in quadrature the post-fit uncertainties and the uncertainties due to the limited size of the simulation samples, except for the data-driven multijet contribution to which the normalization uncertainty of 70% is applied. The total expectation is compared to the observed number of events.

4.6 Angular distributions

The distributions observed at reconstruction level for the angular observables used to measure the various asymmetries are shown in Figures 4.9 and 4.10. They are compared to the predicted signal and background distributions, normalized to the results of the maximum-likelihood fit. To minimize the unfolding corrections that are applied after background subtraction, two bins are chosen for the angular distributions from which forward-backward asymmetries are extracted, while four bins are used for the angular distribution from which the A_{EC} asymmetry is determined.

4.7 Measurement of the W boson spin observables

In order to compare the extracted asymmetries directly to the theoretical predictions and to the results from other experiments, the angular distributions

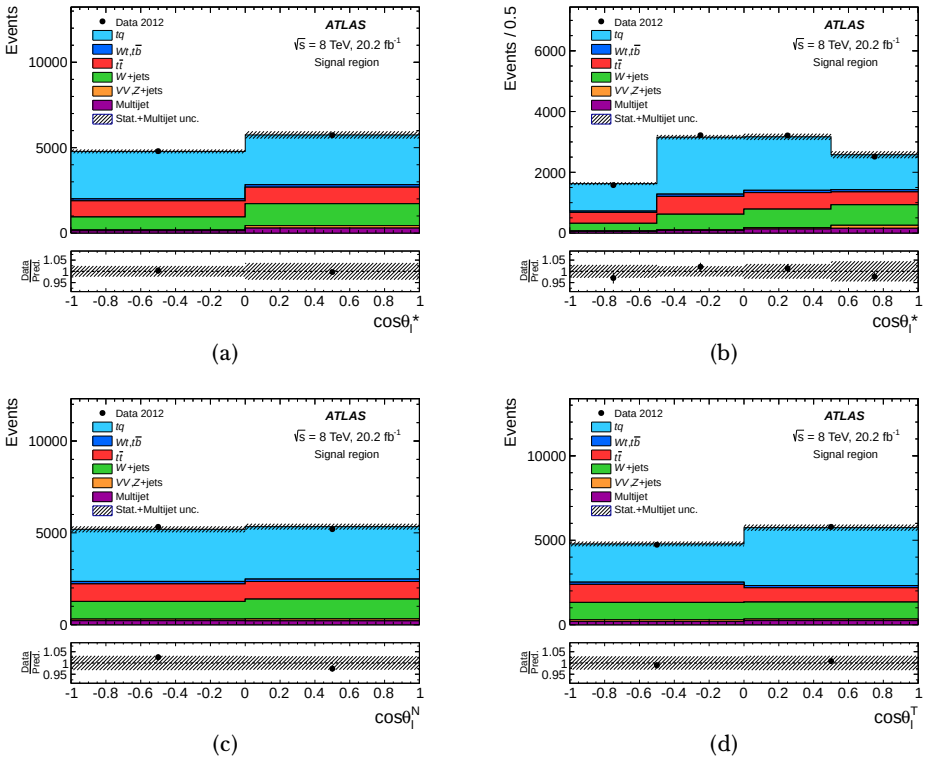

Figure 4.9: Distributions in the signal region of the angular observables used to measure the various asymmetries: (a) $\cos\theta_\ell^*$ with two bins for A_{FB}, (b) $\cos\theta_\ell^*$ with four bins for A_{EC}, (c) $\cos\theta_\ell^N$ for A_{FB}^N and (d) $\cos\theta_\ell^T$ for A_{FB}^T. The observed distributions are compared to the predicted signal and background distributions, normalized to the results of the maximum-likelihood fit. The template t-channel distributions are taken from the baseline POWHEG-BOX sample. The labels tq and $t\bar{b}$ refer to the t-channel and s-channel single-top-quark processes, respectively, and VV to diboson production. The uncertainty bands include the statistical post-fit uncertainty, the uncertainty due to the limited size of the simulation samples and the uncertainty in the normalization of the multijet background, added in quadrature. The lower panels show the ratio of data to prediction.

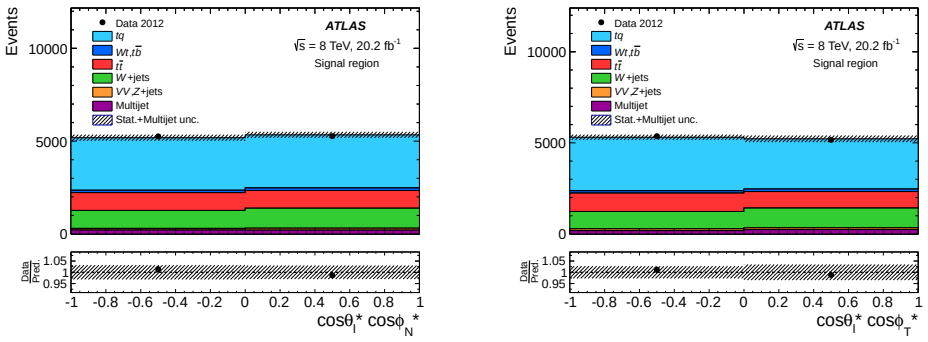

(a) (b)

Figure 4.10: Distributions in the signal region of the angular observables used to measure the various asymmetries: (a) $\cos\theta^*_\ell \cos\phi^*_N$ for $A_{\mathrm{FB}}^{N,\phi}$, and (b) $\cos\theta^*_\ell \cos\phi^*_T$ for $A_{\mathrm{FB}}^{T,\phi}$. The observed distributions are compared to the predicted signal and background distributions, normalized to the results of the maximum-likelihood fit. The template t-channel distributions are taken from the baseline POWHEG-BOX sample. The labels tq and $t\bar{b}$ refer to the t-channel and s-channel single-top-quark processes, respectively, and VV to diboson production. The uncertainty bands include the statistical post-fit uncertainty, the uncertainty due to the limited size of the simulation samples and the uncertainty in the normalization of the multijet background, added in quadrature. The lower panels show the ratio of data to prediction.

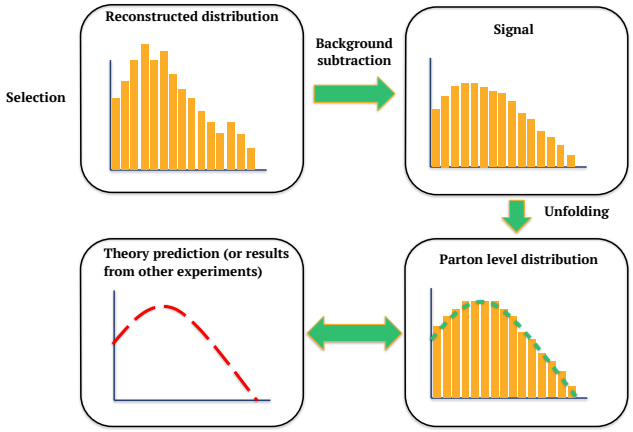

Figure 4.11: Schematic representation of the unfolding procedure: the simulated background is subtracted to the measured data distribution. The unfolding corrections allow to compare the measurement to theory predictions or to results from different experiments.

are unfolded to parton level [3]. The process of unfolding corrects for the distortions due to detector effects, such as the finite resolution of the detector, the triggering and the reconstruction and selection efficiencies, in addition to the physics effects, such as parton hadronization and showering processes. The unfolding procedure is applied to the angular distributions after subtracting the background contributions. A schematic representation of the unfolding procedure is depicted in Figure 4.11.

The unfolding corrections are calculated from simulated events of the signal process through the generation of a migration matrix and an efficiency curve for each angular distribution.

With the aim of testing their compatibility with the Standard Model predictions, all asymmetries, except A_{FB}^{N}, are extracted using the PROTOS simulation generated with the Standard Model values of the Wtb couplings to determine the migration

[3] Partons are defined from the matrix-element hard process and immediate decays.

matrix and the selection efficiency. For all the asymmetry measurements, the Standard Model Wtb couplings are considered for the subtracted top-quark backgrounds.

To constrain Im g_{R}, A_{FB}^{N} must be measured without any assumption about Im g_{R}. It is observed that the presence of anomalous couplings in general modifies the kinematics in such a way that the efficiency corrections are dependent on the Wtb couplings. Thus the measurement of A_{FB}^{N} is found to depend on the unfolding corrections used. By applying an interpolation technique it is possible to unfold the $\cos\theta_{\ell}^{N}$ angular distribution independently of any assumption about Im g_{R}, so that the extracted A_{FB}^{N} asymmetry can be used to constrain this coupling.

The unfolding method used in this analysis is the iterative bayesian unfolding, as proposed in [225] and implemented in the `RooUnfold` package [226]. The validation of the Bayes unfolding procedure [227] includes a convergence test used to define the optimal number of iterations of the algorithm and tests to check the closure and linearity of the method.

4.7.1 Bayesian unfolding

In order to compare measured observables to theory predictions and to measurements from other experiments, the reconstructed distribution, $E(r)$ needs to be corrected to obtain the truth distribution, $C(t)$ [227].

If the reconstructed (truth) distribution has E_r (C_t) bins of a width Δr (Δt) and bin centers r_j (t_i); then the probability to reconstruct truth values from the interval $(\Delta t)_i$ to the interval $(\Delta r)_j$ is summarized in the ***response matrix*** R

$$R_{ij} = p(r \in (\Delta r)_j | t \in (\Delta t)_i). \tag{4.15}$$

The response matrix connects the number of reconstructed events in the bin j, ν_j to the number of truth events in the bin i, μ_i

$$\nu_j = \sum_i R_{ij}\mu_i. \tag{4.16}$$

Monte Carlo events which contain both, truth and reconstructed, information are used to build the response matrix by filling a two-dimensional histogram with all the events which contain both values. The resulting matrix is the migration matrix, that represents the probability to observe r inside an interval $(\Delta r)_j$ and for which the truth value t is found inside the interval $(\Delta t)_i$

$$M_{ij} = P(r \in (\Delta r)_j, t \in \Delta t)_i). \tag{4.17}$$

The reconstruction efficiency, given by the sum of all the possible outcomes, represents the probability of reconstructing a truth value at all

$$\epsilon_i = \sum_{j=1}^{N_r} P(r \in (\Delta r)_j, t \in \Delta t)_i), \tag{4.18}$$

where N_R stands for the total number of reconstructed events.

The combination of the reconstructed efficiency and the migration matrix gives the response matrix

$$R_{ij} = \frac{M_{ji}}{\epsilon_i^{-1} \sum_{k=1}^{N_r} M_{ki}}. \tag{4.19}$$

Unfolding a distribution implies the inversion of the response matrix, $R \cdot R^{-1} = I$, which has in general no exact solution. Therefore, approximations are needed to perform the matrix inversion to acceptable accuracy.

An extensively used method is based upon the iteratively application of the Bayes theorem, proposed by d'Agostini [225]. The idea is the following: if the problem is described in terms of an *effect*, E_j (the reconstructed measured angular distribution, being j the bin number), and a *cause*, C_i (the angular distribution at truth level, being i the bin number), the expected number of events assignable to each of the causes is given by:

$$\hat{n}(C_i) = \sum_{j=1}^{n_E} P(C_i|E_j) \cdot n(E_j), \tag{4.20}$$

where $n(E_j)$ is the j bin content of the measured distribution and $P(C_i|E_j)$ is the probability that the ***effect*** has been due to the i-th ***cause***.

Using the Bayes' formula, one can write the conditional probability of the i-th cause to produce the effect E_j as

$$P(C_i|E_j) = \frac{P(E_j|C_i) \cdot P_0(C_i)}{\sum_{l=1}^{n_C} P(E_j|C_l) \cdot n_0(C_l)}, \tag{4.21}$$

where the probability for an effect to be originated from a cause, $P(E_j|C_i)$, correspond to the $n_E \times n_C$ response matrix, that is determined with Monte Carlo simulation.

The final result for $\hat{n}(C_i)$ is derived from an iterative procedure starting from the initial distribution $n_0(C_l)$. The number of iterations N_{iter} is the regularization parameter of the unfolding method and depends on the angular distribution. The simulated signal distribution at parton level is used as initial prior in Eq. 4.21. After each iteration, this prior is updated with the $\hat{n}(C_j)$ obtained from Eq. 4.20.

4.7.2 SM based unfolding

In this analysis, we call SM based unfolding to that carried out using the corrections computed from a simulated sample implementing SM couplings. The migration matrix translates the true parton-level values into the corresponding reconstruction values for a given angular observable. The number of bins is chosen so that the fraction of simulated events belonging to the diagonal matrix elements lies between 68% and 90%, which leads to a stable unfolding. Besides, the statistical and systematic precision are taken into account in the choice. The baseline migration matrices and efficiency corrections for the SM based unfolding are shown in figures 4.12 and 4.13. The selection efficiencies are between 0.6% and 1.6%.

Unfolding validation

Several tests are done aiming to test the performance of the unfolding algorithm. The first step is to choose an appropriate number of iterations for the algorithm.

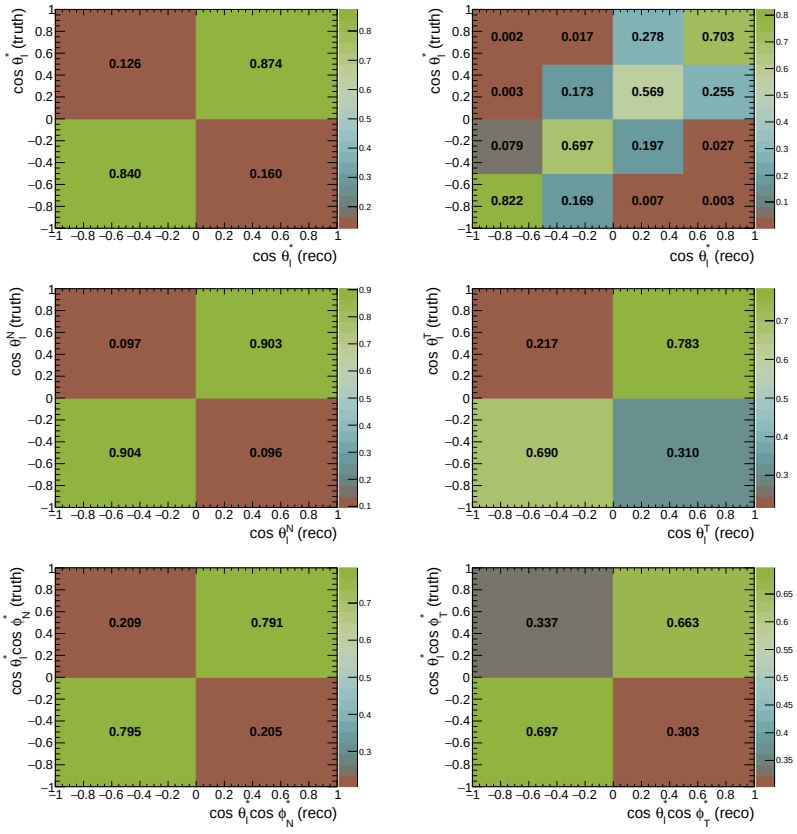

Figure 4.12: Migration probability matrices calculated from the PROTOS SM sample.

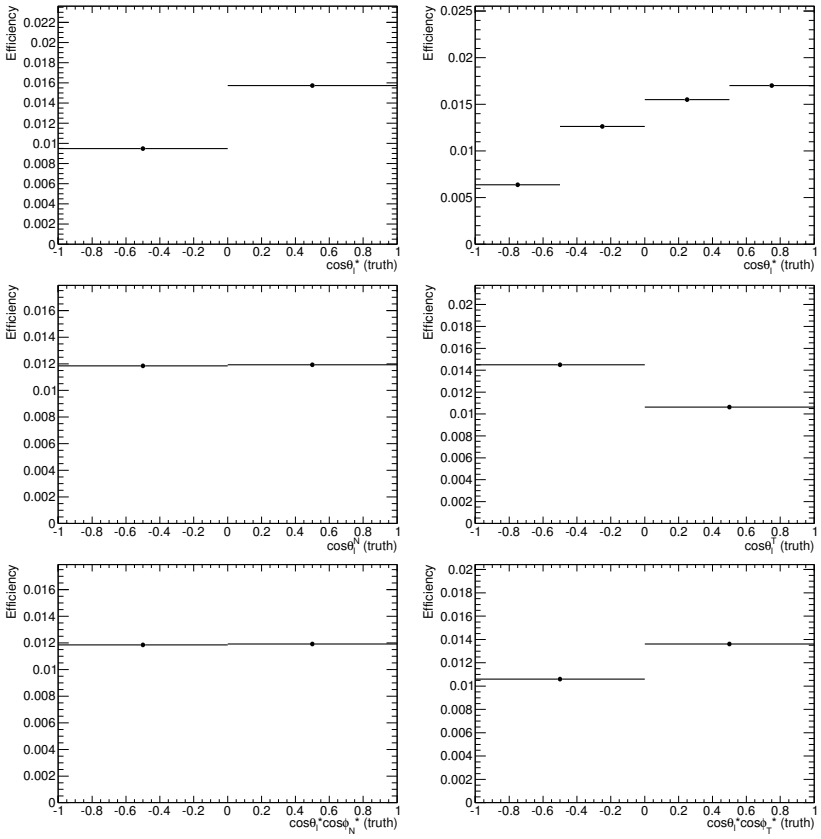

Figure 4.13: Efficiency probability matrices calculated from the PROTOS SM sample.

After this, the performance is validated through closure and linearity tests, for which several t-channel events samples are generated using the MC generators POWHEG-BOX and PROTOS, all of them interfaced to PYTHIA for the parton showering. The LO generator PROTOS is used to determine the detector and physics corrections needed for the unfolding algorithm, while the other samples are used as signal inputs. The electron and muon channels are combined for the validation tests, as they will be for the rest of the analysis, since no different behavior is observed for both channels.

Convergence test

Figure 4.14 shows the evolution of the asymmetries extracted from the unfolded distributions as a function of the number of iterations. The unfolding procedure is considered to have converged when the absolute difference between two steps is smaller than 0.0005. The test is done using as input the baseline PROTOS sample as well as several POWHEG-BOX samples (the nominal POWHEG-BOX used to estimate the expected signal process, the POWHEG-BOX sample passed trough the ATLFAST-II simulation of the detector and POWHEG-BOX simulation interfaced to PYTHIA with the Perugia 2012 tune). The convergence for the PROTOS sample is fast since the same sample is used to unfold and to calculate the correction. However, for the POWHEG-BOX samples, the convergence is slower and a higher number of iterations is needed in order to reach a plateau. From this figure it is also seen that, even when the convergence is reached, there is a difference between the unfolded values of each of the samples. This means that the unfolding response is very sensitive to the generator modeling (LO *vs* NLO), to the parton shower tune (P2011c *vs* P2012) and to the detector simulation (full *vs* fast). A systematic uncertainty from the comparison of the unfolded asymmetry obtained with PROTOS sample and the various POWHEG samples will be used to account for the unfolding response. Table 4.12 summarizes the chosen number of iterations for each asymmetry, based on the results from the convergence test.

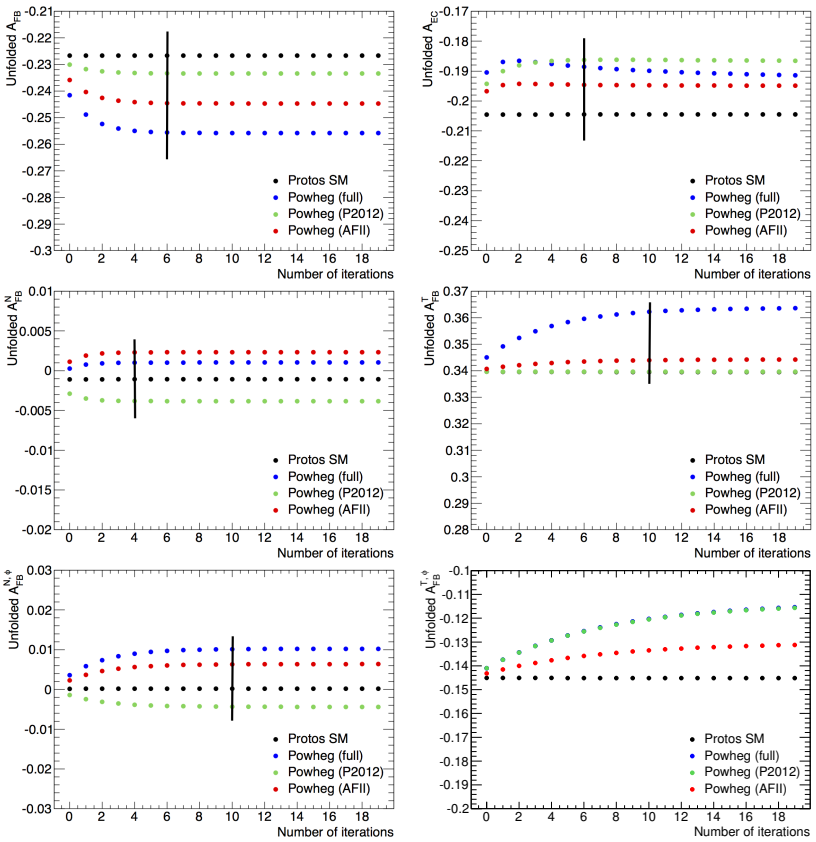

Figure 4.14: Unfolded values of the asymmetries as a function of the number of iterations of the Bayes algorithm.

Asymmetry	Number of iterations
A_{FB}	6
A_{EC}	6
A_{FB}^{N}	4
A_{FB}^{T}	10
$A_{\mathrm{FB}}^{N,\phi}$	10
$A_{\mathrm{FB}}^{T,\phi}$	25

Table 4.12: Numbers of Bayes iterations chosen for the unfolding measurements of the asymmetries.

Closure test

The closure test is used to check the intrinsic bias of the unfolding algorithm. The baseline PROTOS samples is split in two statistically independent subsets with the same number of events each. Then, one of them is unfolded using the migration and efficiency corrections from the other. The extracted asymmetries are compared with the parton level values. The statistical uncertainties due to the limited size of each of the subsets used is taken into account in the comparison. The result of the closure test is shown in Figure 4.15. From this figure one can see that all the measured asymmetries are compatible with their parton-level value within statistical uncertainties. Therefore, no bias will be considered in the measurement of the asymmetries.

Linearity test

The linearity test checks the response of the unfolding on samples with non vanishing anomalous couplings. The unfolding method is said to have a linear response if it allows to recover a parton-level measurement compatible with the truth value with which the sample was generated. The unfolding response will not be linear if the unfolding corrections depend on the anomalous couplings assumptions. The chosen configurations to run the linearity test have non standard values for

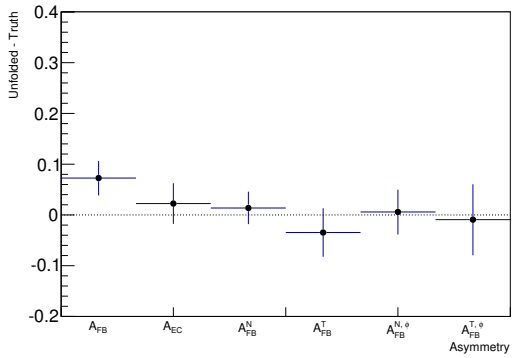

Figure 4.15: Difference between the unfolded asymmetry and its value at parton level when the PROTOS sample is divided in two statistically independent subsets from which the unfolding corrections and unfolded distributions are derived.

Im g_{R}, while the rest of the anomalous couplings are fixed to their SM prediction (see Table A.2). The choice of the anomalous coupling varied is motivated based on the sensitivity studies presented in Section 1.3.4 and on the existing limits.

Figure 4.16 shows the unfolded values for each sample as a function of their parton-level value for the different observables. The lines corresponding to a perfect response (linearity, slope = 1, offset = 0) are displayed. The error bars correspond to the statistical uncertainties due to the limited size of the unfolded PROTOS samples.

The black dots, which correspond to the baseline PROTOS samples with SM couplings, exhibit always a perfect response. For the rest of the points, in which anomalous couplings are implemented, one observes a scattering around the perfect linearity with varying degrees of disagreement depending on the observables. A_{FB}, A_{EC} and A^{T}_{FB} show a good linearity within statistical uncertainties. The asymmetries with respect to the normal direction, A^{N}_{FB} and $A^{N,\phi}_{\mathrm{FB}}$ evidence a linear response with a slope different from 1.

The non-linearities observed with the various PROTOS samples come from the significant changes in the event kinematics when the Wtb couplings are varied, resulting in different efficiency corrections. It was checked that processing more iterations of the Bayes algorithm does not allow to recover a linear response with respect to the various anomalous couplings. In addition, unfolding the

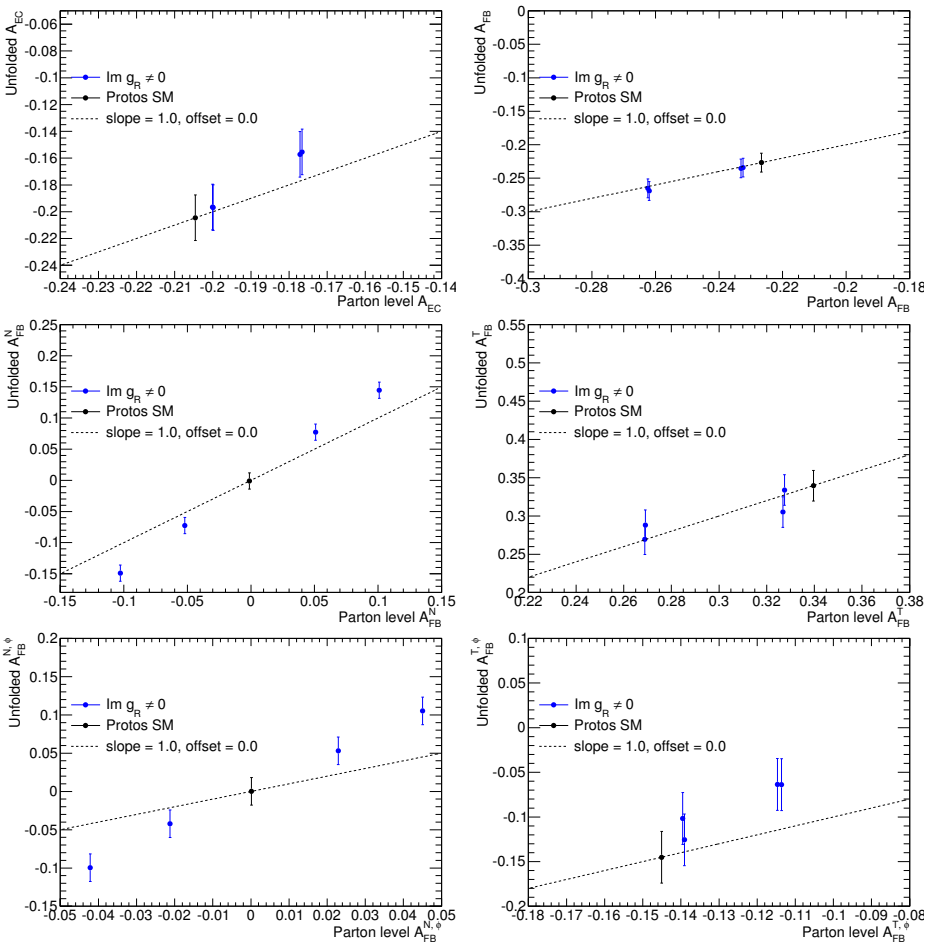

Figure 4.16: Unfolded asymmetries as a function of their parton level value. The error bars cover simulation statistical uncertainties. The dashed line corresponds to the perfect linearity response.

distributions with the migration matrix and efficiency corrections calculated using the same PROTOS sample than that used to build the distributions gives a perfect linear response. This fact motivated the development of an iterative interpolation technique which uses the information from the varied PROTOS in order to recover a linear response of the unfolding method.

4.7.3 Interpolation-based unfolding

The main motivation to probe the Wtb vertex in t-channel single-top production is to search for a complex phase of the g_{R} coupling ($\mathrm{Im}\ g_{\mathrm{R}}$), to which the A_{FB}^{N} asymmetry is very sensitive. As it was seen in the previous section, using the SM-based unfolding leads to a non-linear response for this observable. To resolve these non-linearities, an iterative interpolation technique, based on Lagrange polynomials, was developed. Within this approach the migration and efficiency matrices obtained from PROTOS samples implementing different values of $\mathrm{Im}\, g_{\mathrm{R}}$ are linearly combined in order to correct from the expected changes in the event kinematics. This method provides a measurement independent of any assumption on $\mathrm{Im}\ g_{\mathrm{R}}$ (the rest of the couplings are assumed to be SM) and is applied to the A_{FB}^{N}.

The method works as follows. The unfolding corrections corresponding to a value x of the forward-backward asymmetry A_{FB}^{N} extracted from the normal angular distribution provided by a given sample (data or simulation) are obtained using the following linear interpolation based on Lagrange polynomials:

$$L(x) = f_1 \cdot p_1(x) + f_2 \cdot p_2(x) + f_3 \cdot p_3(x) + f_4 \cdot p_4(x) + f_5 \cdot p_5(x) \qquad (4.22)$$

with the weights $p_i(x)$ defined as:

$$
\begin{aligned}
p_1(x) &= \frac{(x-x_2)(x-x_3)(x-x_4)(x-x_5)}{(x_1-x_2)(x_1-x_3)(x_1-x_4)(x_1-x_5)},\\
p_2(x) &= \frac{(x-x_1)(x-x_3)(x-x_4)(x-x_5)}{(x_2-x_1)(x_2-x_3)(x_2-x_4)(x_2-x_5)},\\
p_3(x) &= \frac{(x-x_1)(x-x_2)(x-x_4)(x-x_5)}{(x_3-x_1)(x_3-x_2)(x_3-x_4)(x_3-x_5)},\\
p_4(x) &= \frac{(x-x_1)(x-x_2)(x-x_3)(x-x_5)}{(x_4-x_1)(x_4-x_2)(x_4-x_3)(x_4-x_5)},\\
p_5(x) &= \frac{(x-x_1)(x-x_2)(x-x_3)(x-x_4)}{(x_5-x_1)(x_5-x_2)(x_5-x_3)(x_5-x_4)}
\end{aligned}
\tag{4.23}
$$

being f_i the sets of migration and efficiency corrections, and x_i the values of A_{FB}^N at parton level corresponding to the five samples i with different $\mathrm{Im}\, g_{\mathrm{R}}$ values. The five used PROTOS samples always include the Standard Model one. The weights $p_i(x)$ are obtained using an iterative procedure. The iteration process is the following: an initial value of x is extracted by using the PROTOS Standard Model based unfolding. This value is used to compute the weights, using Eq. 4.23, which are then used to compute new efficiency and migration unfolding corrections, using Eq. 4.22 to obtain a new value of x after unfolding the normal angular distribution. The iterative procedure is stopped when convergence is reached; the chosen convergence criterion requires that the difference on the unfolded asymmetry values from two successive steps is smaller than 0.0001. The interpolation is expected to work for values of x within the range covered by the various PROTOS new physics samples. The initial seed is forced to be within this range. If after the iterations, x ends up to be outside this range, the unfolding provided by the new physics PROTOS sample with the truth A_{FB}^N closest to x is used. The available range is however quite reasonable given the current constraints on $\mathrm{Im}\, g_{\mathrm{R}}$. The used samples to derive the interpolated corrections correspond to $\mathrm{Im}\, g_{\mathrm{R}}$= ± 0.094 and ± 0.23, together with the nominal PROTOS sample ($\mathrm{Im}\, g_{\mathrm{R}}$= 0); these samples correspond to parton-level values of A_{FB}^Nequal to ± 0.05, ± 0.10 and 0.0, respectively. This particular set is chosen because it allows to cover the full available range with equidistant working points, making the interpolation method more robust and reliable.

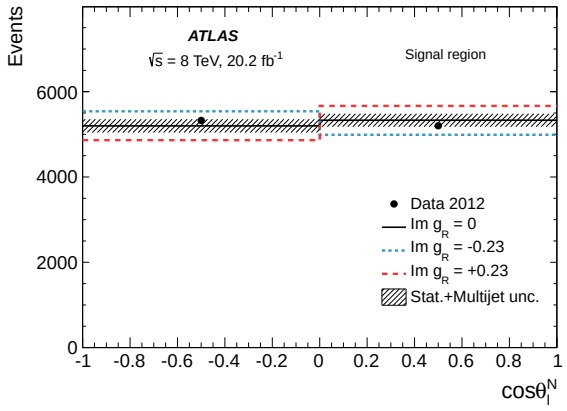

Figure 4.17: Comparison of the distribution observed in the signal region with the distribution predicted as a function of $\mathrm{Im}\, g_{\mathrm{R}}$ for the angular observable from which the asymmetry used to set limits on this coupling is measured, $\cos\theta_{\ell}^{N}$ for A_{FB}^{N}. The predicted distribution is determined by adding the signal and background contributions normalized to the results of the maximum-likelihood fit. The template signal distribution is taken from the PROTOS samples generated with $\mathrm{Im}\, g_{\mathrm{R}} = 0$ (Standard Model parametrization) and $\mathrm{Im}\, g_{\mathrm{R}} = \pm 0.23$. The corresponding parton-level values for the A_{FB}^{N} asymmetry are 0 and ± 0.10, respectively. The uncertainty bands include the statistical post-fit uncertainty, the uncertainty due to the limited size of the simulation samples and the uncertainty in the normalization of the multijet background, added in quadrature.

The sensitivity to $\mathrm{Im}\, g_{\mathrm{R}}$ of $\cos\theta_{\ell}^{N}$ distribution, which is used to set limits on this coupling, is illustrated in Figure 4.17. In this figure the observed distribution is compared to the signal-plus-background predictions built by adding the signal templates given by the PROTOS samples generated with $\mathrm{Im}\, g_{\mathrm{R}} = 0$ (Standard Model parametrization) and $\mathrm{Im}\, g_{\mathrm{R}} = \pm 0.23$, the latter corresponding to the maximum values considered in the interpolation method described above.

Unfolding validation

Samples with intermediate values of $\mathrm{Im}\ g_{\mathrm{R}}$ are generated to test the performance of the method. These samples are only used as signal inputs and their parton-level information is not used in the corrections. The appropriate

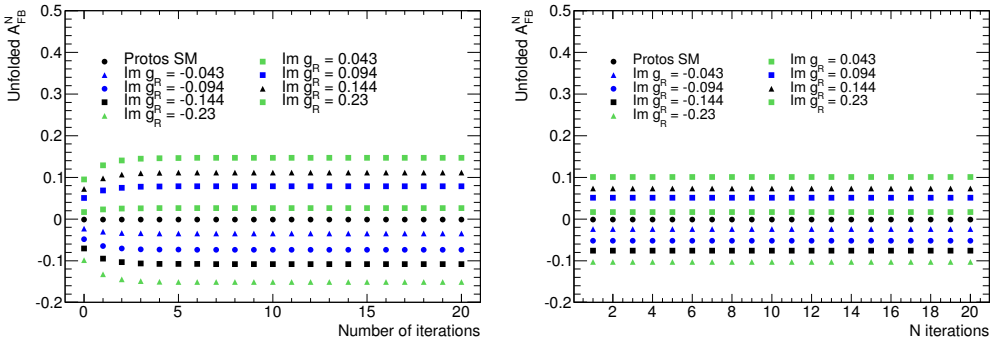

Figure 4.18: Unfolded values of the asymmetry A_{FB}^Nas a function of the number of iterations of the Bayes algorithm obtained with the Standard Model-based unfolding (*left*) and the interpolation method (*right*).

number of iterations for the method is chosen after studying the convergence of the interpolation method. After this test, the linearity of the technique is also studied and compared to the SM-based unfolding method.

Convergence test

The seed for the interpolation technique is obtained from the SM-based unfolding. The left panel on Figure 4.18 illustrates the evolution of the A_{FB}^N initial point as a function of the number of iterations. As it was the case in the previous section, all samples have converged after 4 iterations, and this is therefore the number chosen to obtain the seed.

Once the initial value is determined, only 1 iteration of the Bayes unfolding is processed in each iteration of the interpolation method, since the measured values of the asymmetry A_{FB}^N become independent of the number of iterations of the Bayes unfolding, as shown in the right panel of Figure 4.18.

Linearity test

The linearity of the response provided by the interpolation method is tested; this linearity test is also based on the PROTOS sample with the Standard Model Wtb couplings and all those with non-vanishing values of the anomalous coupling

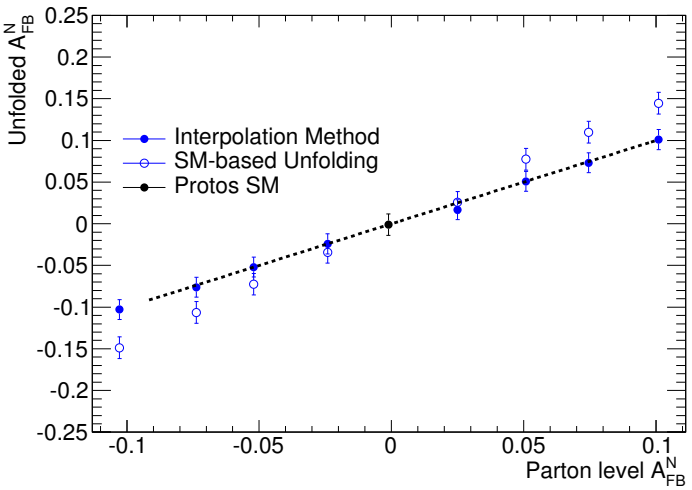

Figure 4.19: Unfolded asymmetries as a function of their parton level value. It compares the results from the interpolation technique (full points) with the results from the SM-based unfolding (open points). The error bars cover simulation statistical uncertainties. The dashed line corresponds to the closure test.

$\mathrm{Im}\ g_{\mathrm{R}}$. Figure 4.19 compares the results of the linearity test using the iterative interpolation technique (full points) with the results using the SM-based unfolding (open points). It is verified that with this method, the good linearity is recovered, also for the points that are not used in the interpolation step.

4.8 Systematic uncertainties

Different sources of systematic uncertainties affect the normalization and shape of the angular distributions that will be used to extract the angular asymmetries. Two categories group all the sources of uncertainties: the signal and background modeling and normalization, and the detector modeling. The effect due to the limited size of the data and MC samples is also take into account. The influence of each type of systematic uncertainty is evaluated separately and they are propagated in a correlated way to the signal and background regions. The total impact on each observable of systematic uncertainties is evaluated by adding in quadrature the individual contributions.

The sources of systematic uncertainty are split into the following categories:

Background normalization

The uncertainties in the normalization of the top-quark and W+jets background processes are determined from the maximum-likelihood fit. For the merged Z+jets and diboson processes the normalization uncertainty of 20% introduced in Section 4.4 is applied to the predictions. For the data-driven normalization of the multijet background the uncertainty of 70% estimated from the comparison of the matrix-method estimates with those given by the jet-electron and anti-muon methods is used.

The uncertainty in the integrated luminosity is 1.9% [228]. It is propagated to the asymmetry measurements through the normalization of the simulated backgrounds.

Signal and background modeling

Systematic uncertainties associated with the signal and background modeling are estimated by comparing event samples from different generators and by varying parameters in the event generation.

The uncertainty in the matrix-element calculation in the simulation of the t-channel single-top-quark process is estimated by comparing MadGraph5_aMC@NLO+Herwig with Powheg-Box+Herwig. For the $t\bar{t}$ and Wt processes, MC@NLO is compared with Powheg-Box, both generators interfaced to Herwig. The uncertainty in the parton shower is estimated by comparing Powheg-Box interfaced with Pythia and Herwig for the t-channel, $t\bar{t}$ and Wt processes. For the s-channel single-top-quark contribution the uncertainty due to the choice of generator and parton shower is estimated in a combined way by comparing MC@NLO+Herwig with Powheg-Box+Pythia.

An additional modeling uncertainty is considered for the signal process by comparing the NLO Powheg-Box+Pythia sample to the LO Protos sample implementing the Standard Model parameterisation of the Wtb couplings. To

estimate this uncertainty, only the shapes of the distributions are varied in order to assess the impact of using a LO generator to determine the unfolding corrections.

The uncertainty in the amount of QCD radiation is evaluated for all top-quark processes by comparing the POWHEG-BOX samples generated with the varied hard-process and parton-shower scales presented in Section 4.2. The largest shift in the measured asymmetries is taken as uncertainty.

The dependence of the measured asymmetries on the top-quark mass is estimated using POWHEG-BOX samples generated with different top-quark masses (165, 167.5, 170, 175, 177.5 and 180 GeV). Variations lower than 0.01 per GeV are found for the measured asymmetry values. Therefore, these variations are not included in the total systematic uncertainty.

The impact of the flavour composition on the modeling of the W+jets distributions is determined by propagating an uncertainty of 50% in the ratio of W+$b\bar{b}$ to W+$c\bar{c}$ events. As reported in Section 4.5, W+light-flavour jets events give a small contribution in the signal region and no associated modeling uncertainty is taken into account.

An additional shape-modeling uncertainty is considered for the W+jets distributions. Indeed, in the W+jets control region a few kinematic variables are slightly mismodeled, and the impact of this mismodeling is evaluated by reweighting the W+jets angular distributions in the signal region. The applied event weights are derived from matching to data (after subtraction of all processes other than W+jets) the mismodeled kinematic variables in the W+jets control region. This procedure leads to a conservative estimate since it also accounts for mismodeling of the W+light-flavour jets events, which have a much more important contribution in the W+jets control region than in the signal region.

The systematic uncertainty associated with the data-driven shape modeling of the multijet events is estimated by comparing the shapes provided by the baseline matrix method and the alternative modeling given by the jet-electron and anti-muon methods.

All the signal and background modeling uncertainties, except that associated with the W+jets flavour composition, are symmetrised by taking the difference

between the nominal and varied measurements as positive and negative uncertainties.

Systematic uncertainties related to the parton distribution functions are estimated for all processes, except for the multijet contribution. The uncertainty is estimated, following the PDF4LHC prescription [214], by calculating the envelope of the uncertainties at 68% confidence level of the CT10 [125], MSTW2008NLO [123] and NNPDF2.3 [217] sets.

Detector modeling

Systematic uncertainties in the reconstruction and energy calibration of jets, electrons and muons are propagated in the analysis through variations in the modeling of the detector response. All these sources of uncertainty are discussed in detail in Section 2.4. For the jets, the main source of uncertainty is the energy scale, evaluated using a combination of in situ techniques [229]. Other jet-related uncertainty sources are the modeling of the energy resolution [230] and reconstruction efficiency [229] (both referred to as jet reconstruction uncertainties), and the modeling of the tagging efficiencies of b-quark jets, c-quark jets and light-flavour jets [164, 207]. Uncertainties related to leptons come from trigger, identification and isolation efficiencies, as well as from the energy scale and resolution [145, 151] (all referred to as lepton reconstruction uncertainties). The uncertainties in the energy scale and resolution corrections applied to leptons and jets are propagated to the computation of the missing transverse momentum. The scale and resolution uncertainties due to soft jets and to contributions of calorimeter energy deposits not associated with any reconstructed objects are also considered and evaluated independently (they are labelled $E_{\mathrm{T}}^{\mathrm{miss}}$ reconstruction uncertainties). For all detector modeling uncertainties, positive and negative uncertainties are estimated separately from the corresponding shifts.

Limited size of simulation samples

The statistical uncertainties associated to the limited size of the simulated samples are evaluated through pseudo-experiments. For each process in each

pseudo-experiment the bins are varied by a random number drawn according to a Gaussian distribution of width equal to the statistical error associated with the bin content. The whole analysis chain is carried out and all the observables are obtained. The final statistical uncertainty is assigned to the standard deviation associated with the distribution of the measured asymmetries provided by the ensemble of pseudo-experiments.

The uncertainties due to the limited sizes of the data samples are estimated from pseudo-experiments by varying the rates and the shapes through bin-per-bin Poissonian fluctuations on the expected signal and background angular distributions (the data-driven multijet contribution is not fluctuated) and the final statistical uncertainty is obtained in the same way as the simulation uncertainty. As an example, Figure 4.20 shows the distribution of A_{FB} using 100000 pseudo-experiments to evaluate the data statistics uncertainty of this observable. From this result, the associated uncertainty is 0.02. All the statistical uncertainties reported in this thesis are evaluated by running 10000 pseudo-experiments.

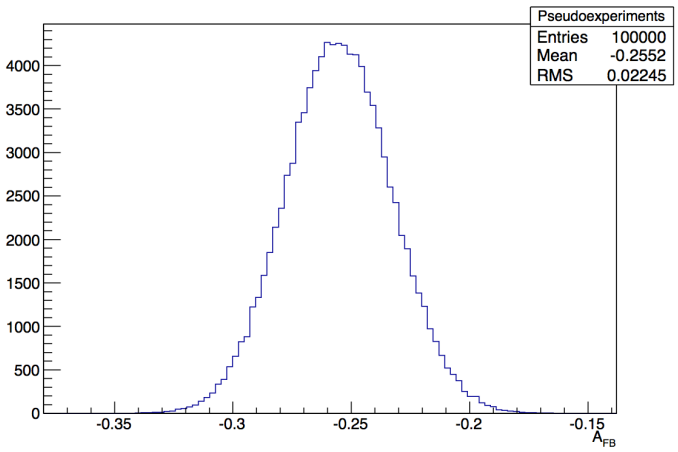

Figure 4.20: Pseudoexperiments distribution to compute statistical uncertainty of A_{FB}.

Estimation of uncertainties

The varied samples obtained as described in the previous subsection are used to estimate the effect of each source of uncertainty in the expected and observed asymmetries measured.

Expected uncertainties

For each source of systematic uncertainty, once the up and down varied samples are build as explained in the previous section, they are used to simulate the signal and backgrounds, instead of the nominal samples. The expected uncertainty on each asymmetry is computed with the following procedure:

- A pseudo-data sample is created by adding all the varied background and signal samples.
- The nominal simulated samples are fitted to the pseudo-data sample with the procedure explained in Section 4.5, to account for the correlations of the varied samples in the different regions.
- The obtained scale factors are applied to the nominal backgrounds and those scaled backgrounds are subtracted to the pseudo-data to obtain a pseudo-signal distribution.
- This signal distribution, on which the effect of the systematic source has been propagated, is unfolded using the nominal migration matrices and efficiency corrections.
- The final effect of the uncertainty source on the asymmetry is given by the difference between the nominal asymmetry and the value from the varied samples; the up uncertainty is given as $A^{up} - A^{nominal}$ while the down uncertainty is $A^{nominal} - A^{down}$.

Observed uncertainties

A similar procedure is used to evaluate the observed systematics.

- First, the nominal samples need to be scaled with the scale factors obtained from the fit to data explained in Section 4.5, SF^{data}. Then, a pseudo-data sample is created by adding all the varied background and signal samples.

- To accommodate the fact that the shape of the simulated signal sample is not the same as the shape of the signal obtained from data, bin-by-bin scale factors are derived for the t-channel simulated samples by comparing the shapes of the nominal simulated signal sample and the distribution obtained from the nominal background subtracted to data.

- This re-scaled t-channel sample is now fitted, together with the nominal simulated background samples scaled with SF^{data}, to the pseudo-data sample to obtain a set of scale factor, SF^{syst}.

- Now, the following procedure as for the expected systematics is applied: the nominal simulated backgrounds are scaled with SF^{syst} and subtracted to the pseudo-data sample and the resulting pseudo-signal distribution is unfolded. The final effect of the uncertainty source on the asymmetry is given by the difference between the nominal asymmetry and the value from the varied samples; the up uncertainty is given as $A^{up} - A^{nominal}$ while the down uncertainty is $A^{nominal} - A^{down}$.

Table 4.13 shows the contribution of each source of systematic uncertainty to the measured asymmetries. The systematic contributions are grouped according to the type of reconstructed object for the detector-related uncertainties and to the type of process for the normalization and modeling uncertainties. For all asymmetries, the main uncertainty contribution comes from the limited size of the data sample. The second source of uncertainties is due to the modeling of the t-channel and $t\bar{t}$ processes. The third contribution comes from the jet energy scale uncertainty.

4.9 Results

The measured asymmetries are listed in the following. The input information are the angular distributions presented in Section 4.6. After a simultaneous

Uncertainty source	$\Delta A_{\mathrm{FB}} * 10^2$	$\Delta A_{\mathrm{EC}} * 10^2$	$\Delta A_{\mathrm{FB}}^{N} * 10^2$	$\Delta A_{\mathrm{FB}}^{T} * 10^2$	$\Delta A_{\mathrm{FB}}^{N,\phi} * 10^2$	$\Delta A_{\mathrm{FB}}^{T,\phi} * 10^2$
Statistical uncertainty	± 2.3	± 2.8	± 2.2	± 3.1	± 3.0	± 4.6
Simulation statistics	± 1.4	± 1.7	± 1.3	± 2.0	± 1.8	± 2.9
Luminosity	<0.1	<0.1	<0.1	<0.1	<0.1	<0.1
Background normalization	± 0.9	± 0.7	± 0.4	± 1.1	± 0.6	± 1.1
E_T^{miss} reconstruction	$^{+1.1}_{-0.7}$	$^{+0.8}_{-0.2}$	$^{+0.3}_{-0.4}$	$^{+0.5}_{-0.3}$	$^{+0.5}_{-0.8}$	$^{+0.4}_{-1.3}$
Lepton reconstruction	± 1.4	$^{+0.6}_{-0.3}$	$^{+0.1}_{-0.2}$	$^{+1.3}_{-1.5}$	$^{+0.6}_{-0.5}$	$^{+1.6}_{-0.6}$
Jet reconstruction	± 1.2	± 1.8	± 0.8	± 0.5	± 1.6	± 1.3
Jet energy scale	$^{+3.4}_{-2.7}$	$^{+2.0}_{-0.7}$	$^{+0.9}_{-0.8}$	$^{+3.9}_{-4.6}$	$^{+0.6}_{-2.5}$	$^{+4.5}_{-2.5}$
Jet flavor tagging	± 0.6	± 0.4	± 0.2	± 0.6	± 0.3	± 0.6
PDF	<0.1	± 0.2	± 0.1	± 0.1	± 0.1	± 0.4
$t\bar{t}$ generator	± 0.2	± 1.2	± 0.2	± 3.5	± 1.7	± 1.3
$t\bar{t}$ parton shower	± 2.7	± 0.3	± 1.5	± 1.0	± 0.9	± 1.6
$t\bar{t}$ scales	± 1.2	± 0.3	± 0.3	± 0.8	± 0.3	± 1.3
Wt,s-channel generator	± 0.4	± 0.3	± 0.2	± 0.8	± 0.3	± 1.4
Wt,s-channel scales	± 0.3	± 0.3	± 0.6	± 0.5	± 0.4	± 0.9
t-channel NLO generator	± 0.6	± 2.7	± 0.3	± 4.5	± 2.6	± 7.2
t-channel LO-NLO generator	± 2.6	± 1.8	± 0.5	± 1.9	± 1.3	± 3.2
t-channel parton shower	± 3.5	± 0.2	± 0.7	± 0.9	<0.1	± 1.1
t-channel scales	± 0.6	± 1.6	± 0.9	± 2.2	± 1.4	± 2.6
W+jets, multijet modeling	$^{+2.2}_{-2.1}$	$^{+1.3}_{-1.2}$	$^{+0.7}_{-0.6}$	$^{+1.3}_{-1.7}$	± 0.6	$^{+2.3}_{-1.7}$
Systematic uncertainty	$^{+7.3}_{-6.9}$	$^{+5.3}_{-4.8}$	$^{+2.9}_{-2.9}$	$^{+8.3}_{-8.8}$	$^{+4.8}_{-5.4}$	$^{+10.9}_{-10.1}$

Table 4.13: Uncertainties contributing to the measurements of the angular asymmetries. For a better readability the uncertainties are multiplied by 10^2.

likelihood fit in the signal and control regions ($t\bar{t}$ and anti-selection, see Section 4.5), the normalized backgrounds are subtracted from data in the signal region and the resulting signal distributions are unfolded to parton level using the iterative Bayesian unfolding procedure explained in Section 4.7. From the unfolded distribution, the asymmetries are measured and presented in following subsections. The W boson spin observables derived from the measured asymmetries are also written.

For all the asymmetries, except A_{FB}^{N}, the SM-based unfolding, which provides a consistency test of the SM, is used. A_{FB}^{N} is unfolded using the iterative interpolation unfolding method, which allows to extract a value independent from

any assumption on Im g_{R} coupling. This value will be used together with the asymmetry A_{FB}^{ℓ}= $0.487^{+0.060}_{-0.060}$ presented in [1], to set limits on Im g_{R}.

4.9.1 Asymmetries and spin observables

The measured values of the asymmetries related to the W boson spin observables are

$$
\begin{aligned}
A_{\mathrm{FB}} &= -0.26 \pm 0.02(\mathrm{stat.}) \pm 0.07(\mathrm{syst.}) = -0.26 \pm 0.08\,, \\
A_{\mathrm{EC}} &= -0.25 \pm 0.03(\mathrm{stat.}) \pm 0.05(\mathrm{syst.}) = -0.25 \pm 0.06\,, \\
A_{\mathrm{FB}}^{N} &= -0.04 \pm 0.02(\mathrm{stat.}) \pm 0.03(\mathrm{syst.}) = -0.04 \pm 0.04\,, \\
A_{\mathrm{FB}}^{T} &= 0.39 \pm 0.03(\mathrm{stat.}) \pm 0.09(\mathrm{syst.}) = 0.39 \pm 0.09\,, \\
A_{\mathrm{FB}}^{N,\phi} &= -0.03 \pm 0.03(\mathrm{stat.}) \pm 0.05(\mathrm{syst.}) = -0.03 \pm 0.06\,, \\
A_{\mathrm{FB}}^{T,\phi} &= -0.17 \pm 0.05(\mathrm{stat.})^{+0.11}_{-0.10}(\mathrm{syst.}) = -0.17^{+0.12}_{-0.11}\,.
\end{aligned}
$$

The values of the W boson spin observables derived from the measured A_{FB}, A_{EC}, A_{FB}^{T}, A_{FB}^{N}, $A_{\mathrm{FB}}^{N,\phi}$ and $A_{\mathrm{FB}}^{T,\phi}$ asymmetries through the relations given in Table 4.1 are

$$
\begin{aligned}
\langle S_3 \rangle &= -0.35 \pm 0.03(\mathrm{stat.}) \pm 0.10(\mathrm{syst.}) = -0.35 \pm 0.10\,, \\
\langle T_0 \rangle &= -0.55 \pm 0.06(\mathrm{stat.}) \pm 0.12(\mathrm{syst.}) = -0.55 \pm 0.13\,, \\
\langle S_1 \rangle &= 0.52 \pm 0.04(\mathrm{stat.}) \pm 0.12(\mathrm{syst.}) = 0.52 \pm 0.12\,, \\
\langle S_2 \rangle &= 0.06 \pm 0.03(\mathrm{stat.}) \pm 0.04(\mathrm{syst.}) = 0.06 \pm 0.05\,, \\
\langle A_2 \rangle &= -0.05 \pm 0.05(\mathrm{stat.}) \pm 0.09(\mathrm{syst.}) = -0.05 \pm 0.10\,, \\
\langle A_1 \rangle &= 0.27 \pm 0.07(\mathrm{stat.})^{+0.16}_{-0.17}(\mathrm{syst.}) = 0.27^{+0.17}_{-0.19}\,.
\end{aligned}
$$

These results are displayed in Figure 4.21, in which the top panel shows the summary of the measured asymmetries and the the bottom panel, the derived W boson spin observables, all compared to SM predictions.

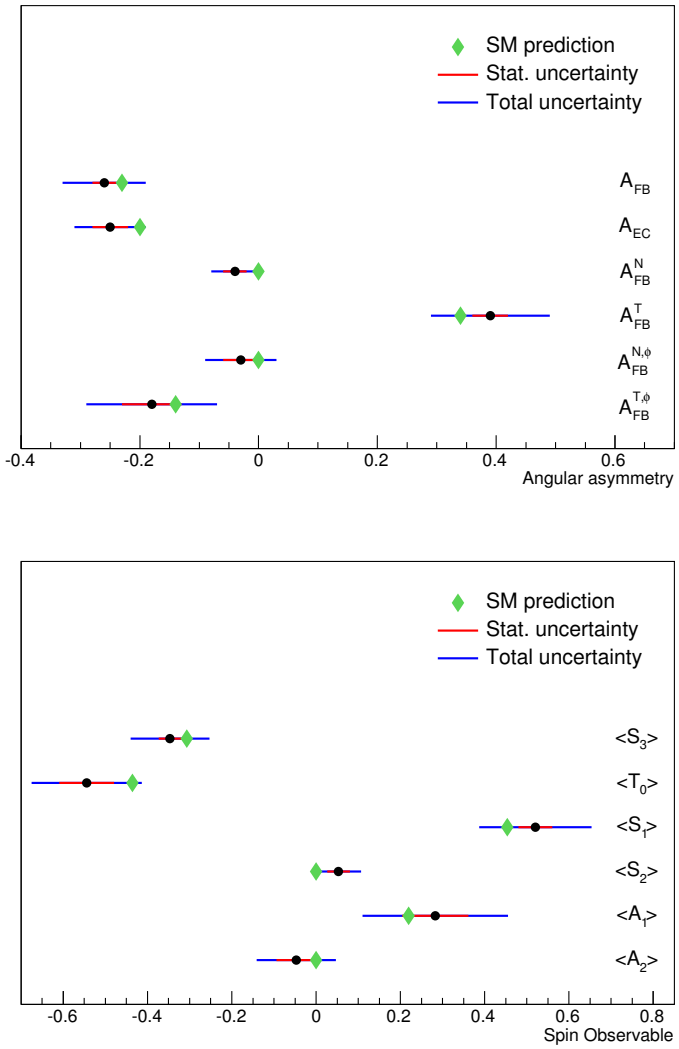

Figure 4.21: Sumary of the measured asymmetries and the derived W boson spin observables, and the comparison with SM predictions.

4.9.2 Compatibility of the measurements with the SM

The p-value is a function that quantifies how often, if an experiment was repeated many times, one would obtain data as far away (or more) from the null hypothesis as the observed data, assuming the null hypothesis to be true. In this case, the null hypothesis correspond to the SM predictions. Therefore, the smaller the p-value, the greater the incompatibility of the measurement with the SM predictions. The p-value is computed from the cumulative distribution function of the χ^2 statistic

$$\chi^2 = \sum_{i,j}(A_i^{\text{measured}} - A_i^{\text{theory}})(A_j^{\text{measured}} - A_j^{\text{theory}})\text{Cov}(A_i, A_j)^{-1}, \tag{4.24}$$

where A_i^{measured} is the measured central value of the asymmetry, A_i^{theory} is the SM prediction for the asymmetry and $\text{Cov}(A_i, A_i)^{-1}$ stands for the element of the inverted covariance matrix.

The p-value is given by

$$p - \text{value} = \int_{\chi^2}^{+\infty} \frac{1}{\Gamma(4)2^{ndf}/2} x^{ndf/2-1} \exp\{-x/2\}\text{d}x, \tag{4.25}$$

where ndf is the number of degrees of freedom, *i.e.*, the number of measured asymmetries.

The p-value for the combination of the decay observables measurements is

$$p - value = \int_{2.986}^{+\infty} \frac{1}{\Gamma(4)2^6/2} x^{6/2-1} \exp\{-x/2\}\text{d}x = 81\%. \tag{4.26}$$

Given this result, the measured asymmetries are in agreement with the predictions of the SM.

4.9.3 Limits on $\text{Im}\ g_{\text{R}}$

The asymmetry A_{FB}^N, which has the highest sensitivity to $\text{Im}\ g_{\text{R}}$ is used, together with the asymmetry A_{FB}^ℓ, to extract limits on the anomalous coupling $\text{Im}\ g_{\text{R}}$. In

addition, the overall compatibility of the measurements with the Standard Model predictions is evaluated through the extraction of a p-value. The limit extraction is done with the `TopFit` code [52], through the generation of pseudo-experiments. All the analytical expressions which encode the dependence of the asymmetries on the anomalous couplings are implemented in `TopFit`. Random points are generated within a reasonably specified range following a uniform distribution. Then, an acceptance-rejection method is used. The events are accepted or rejected based on the χ^2 constructed as in Eq. 4.24 with i and j running over A_{FB}^{N} and A_{FB}^{ℓ} .

The covariance matrix is computed from the complete systematic breakdown for each asymmetry as follows. A correlation ± 1 is assigned for each systematic looking at the sign of the uncertainty variation on each asymmetry. The plus (minus) correlation is assigned when both uncertainties have the same (opposite) sign. In the case of the statistical uncertainties, the bootstrap method is used in order to find the statistical correlation among the two observable and a correlation $\rho = 0$ is found. The bootstrap method consists on generating of pseudoexperiments from the data sample by assigning each event a weight pulled from a Poissonian distribution with unit mean. The angular distributions in $\cos\theta_{\ell}^{N}$ and $\cos\theta_{\ell}$ are then reconstructed using the weighted events. The procedure is repeated with statistically independent weights and 10000 ensembles of pseudoexperiments are generated.

The covariance matrix is computed from the individual correlation coefficients and the symmetrized uncertainties as follows:

$$\begin{aligned} \mathrm{Cov}(\mathrm{A_i}, \mathrm{A_i}) &= \sigma^2(A_i), \\ \mathrm{Cov}(\mathrm{A_i}, \mathrm{A_j}) &= \sum_k \rho_k^{i,j} \sigma_k(A_i)\sigma_k(A_j). \end{aligned} \tag{4.27}$$

in the above expressions, the index k runs over all the systematic uncertainty, and the total uncertainties $\sigma^2(A_i)$, are the quadratic sum of the symmetrized uncertainties.

Acceptance-rejection method The basic idea of this method is to find an ensemble of points distributed according to the unknown probability distribution function of the measured asymmetries from which to find the maximum and minimum values of $\mathrm{Im}\ g_{\mathrm{R}}$ compatible with the target confidence level (CL) of 95%. The points used to describe the measurements are accepted or rejected from a pool of random points uniformly distributed in the range $\mathrm{Im}\ g_{\mathrm{R}} \in [-0.5, 0.5]$, which is a reasonable range given the current constraints is this anomalous coupling. For each pseudoexperiment, A_{FB}^{N} and A_{FB}^{ℓ} are computed as a function of the random $\mathrm{Im}\ g_{\mathrm{R}}$ (the rest of the couplings are assumed to have SM values), and the computed pseudo-asymmetries values are set as A_i^{theory} in Eq. 4.24. A probability for this point is computed as $P = e^{-\chi^2/2}$. Now, this value of $\mathrm{Im}\ g_{\mathrm{R}}$ is sampled uniformly from 0 to the maximum of the probability density function, 1. If the sampled value is greater than the value of the desired distribution at this $\mathrm{Im}\ g_{\mathrm{R}}$, P, this pseudo-experiment is not kept. This process is repeated until 5000000 points are kept. These points will be distributed according to the probability distribution function of the measured asymmetries. The CL of the ensemble of pseudoexperiements can be calculated as

$$CL = \frac{N(\chi^2 - \chi^2_{test})}{5000000} \tag{4.28}$$

where $N(\chi^2 - \chi^2_{test})$ is the number of pseudoexperiments whose χ^2 is smaller than an arbitrary initial test χ^2_{test}. The value of χ^2_{test} is increased or decreased until CL = 0.95 is found. Finally, from all the pseudoexperiments with $\chi^2 < \chi^2_{final}$, the two that have the minimum and maximum $\mathrm{Im}\ g_{\mathrm{R}}$ are kept.

Using this method, the limits on $\mathrm{Im}\ g_{\mathrm{R}}$ set at 95% CL are:

$$\mathrm{Im}\ g_{\mathrm{R}} \in [-0.18, 0.06]$$

4.10 Conclusion

This chapter presents the measurement of the W boson polarization observables in t-channel single top-quark production at $\sqrt{s} = 8$ TeV with 20.2 fb^{-1} of pp collision data recorded with the ATLAS detector at the LHC. The observables

are obtained from the measurement of asymmetries of the angular distributions of the top quark decay products. The selected events contain one isolated electron or muon, large missing transverse momentum and exactly two jets, of which one is tagged as a b-jet. The electron and muon channels are combined. A cut-based analysis is used to discriminate the signal events from background. The asymmetries are measured on the angular distributions unfolded to parton level. Two different approaches are used to compute the unfolding corrections. The first one is based on a Standard Model simulation of the t-channel process and is used to test the compatibility of the measurements with the SM predictions. The measured asymmetries are in agreement with the predictions of the SM with a p-value of 81%. The second approach allows to obtain model-independent corrections using an interpolation technique. It is used to set limits on the imaginary part of the anomalous coupling g_{R} of $\mathrm{Im}\, g_{\mathrm{R}} \in [-0.18, 0.06]$ at the 95% confidence level. The extracted values improve on the most recently published limits for this coupling.

5 | Mono-top searches in pp collisions at 13 TeV

Although there is strong evidence for the presence of Dark Matter filling our universe, all of it comes from astrophysical probes of its gravitational interaction with ordinary matter. There is yet no evidence of non-gravitational interactions that could shed light on its true nature. This allows for a wide variety of models. Dark Matter searches at LHC are signature-based, focusing on the final state particles, regardless of the theory model behind. A more detailed description of the current status of DM was given in Section 1.4.

This chapter describes the DM search carried out by the ATLAS experiment targeting events with one top quark and a large amount of missing transverse momentum $E_{\mathrm{T}}^{\mathrm{miss}}$, which would partially correspond to the undetected DM particle. Such production, known as mono-top, has been previously searched by ATLAS and CMS collaborations using Run-1 data at 8 TeV [231, 232] and Run-2 data at 13 TeV [233], and by the CDF collaboration using 1.96 TeV data from Tevatron [234]. There are two DM production mechanisms that may lead to a final signature with one top and large $E_{\mathrm{T}}^{\mathrm{miss}}$, the resonant and non-resonant production discussed in Section 1.4. The effort of this thesis is focused on the non-resonant production. The considered channel is the leptonic decay of the W boson produced in the top quark decay. The data analyzed is from pp collisions at a center of mass energy of $\sqrt{s}$ = 13 TeV collected by the ATLAS detector. First, a signal region is defined to maximize the discovery potential. Then, the signal and background processes are estimated via MC simulations or data-driven techniques and control regions are

defined to estimate the modeling of background events. In particular, a maximum likelihood fit of the expected background events to data is performed in the control regions in order to ensure a good modeling of the background processes in regions where the presence of the signal process is expected to be negligible. Once the backgrounds are well modeled, the signal region is fitted together with the control regions under a signal-plus-background hypothesis for a variety of signal processes. The fit is performed to the shape of the $E_{\mathrm{T}}^{\mathrm{miss}}$ distribution, which is the most discriminant observable. In the absence of evidence for these signals, 95% CL upper limits on the corresponding production cross-sections are obtained and these limits are translated into constraints on the parameter space of the considered models. Finally, the results presented in this thesis, which consider only the leptonic decay of the W boson, are combined with the results from the hadronic decay channel.

5.1 Signal production and background contamination

The targeted process of this analysis is the non-resonant mono-top production, whose final state is characterized by the presence of a top quark and a vector state V that decays invisibly to a pair of DM particles. This production mechanism proceeds via flavor-changing neutral interactions of the top quark with a quark of the first or second generation and the invisible V boson. The produced top quark decays into a b-quark and a W boson, which can subsequently decay into either two quarks or a charged lepton and a neutrino. This thesis presents the leptonic channel analysis of the non-resonant mono-top production.

As a result, signal events leave a signature characterized by the presence one jet identified as a b-tagged jet, exactly one lepton and missing transverse energy corresponding to the neutrino and the invisible DM particles, as shown in Figure 5.1.

There are several processes in the SM that can mimic the final state just described and thus pass the selection requirements. Background contributions come from other top quark processes ($t\bar{t}$ production, t-channel, s-channel and Wt production), W+jets, Z+jets, diboson and multijet processes.

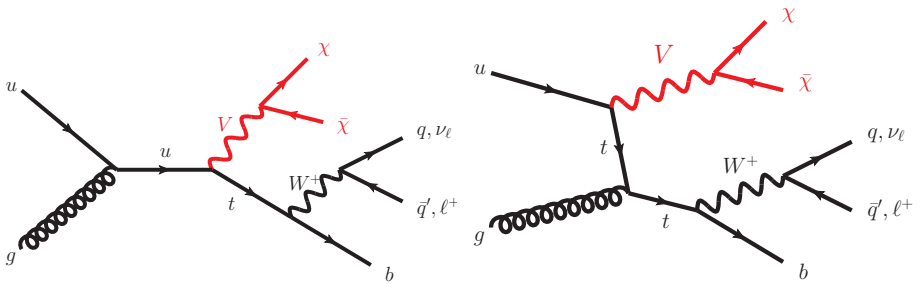

Figure 5.1: Mono-top production in the context of an effective dark matter model: the leading order Feynman diagrams for the non-resonant s- (*center*) and t-channels(*right*) cases are shown.

5.2 Data and simulation samples

This analysis is performed using pp collision data recorded at a center-of-mass energy of $\sqrt{s} = 13\,\text{TeV}$ with the ATLAS detector during 2015 and 2016 in the periods when the LHC was operating with 25 ns bunch spacing and with an average number of collisions per bunch crossing $\langle\mu\rangle$ of around 23. Only periods in which all detector components were functional are considered, resulting in a data sample with a total integrated luminosity 36.1 fb^{-1}.

Events are required to pass at least one of the single-muon or single-electron triggers [139]. The triggers require a p_{T} of at least 20 GeV (26 GeV) for muons and 24 GeV (26 GeV) for electrons for the 2015 (2016) data set, and also have requirements on the lepton reconstruction and isolation. These are complemented by triggers with higher p_{T} thresholds and relaxed isolation and identification requirements to ensure maximum efficiency at higher lepton p_{T}.

Simulation samples

Samples of signal and background events are simulated using various Monte Carlo generators. All MC samples are normalized using the highest-order inclusive cross-sections available at $\sqrt{s} = 13\,\text{TeV}$. The dominant backgrounds $t\bar{t}$ and W+jets are available at NNLO in QCD [23, 235]. The EvtGen v1.2.0 program [236] was

used to simulate properties of the bottom and charmed hadron decays except for samples generated with SHERPA. All simulated background samples are processed with the full simulation of the ATLAS detector [181] using GEANT4 [182]. Additional samples used in the estimation of systematic uncertainties, as well as the signal samples, are instead produced using a faster simulation ATLFAST2 [183]. All samples are simulated with a varying number of minimum-bias interactions generated with PYTHIA8.186 using a set of tuned parameters called the A2 tune [237], overlaid on the hard-scattering event to account for the multiple pp interactions in the same or nearby bunch crossings (pile-up). The average number of interactions per bunch crossing in simulation is reweighed to match the distribution in data.

Signal samples

Signal events for non-resonant DM scenario are generated according to the generic model [106] described in Section 1.4.4, interfaced to MADGRAPH5_aMC@NLO [196] through FeynRules 2.0 [238, 239]. Such generation is done at LO in QCD using the NNPDF3.0LO [124] PDF set. Parton showering and hadronization are handled using the PYTHIA 8.212 [184] event generator with the A14 [240] set of tuned parameters, using the NNPDF2.3LO PDF set [217]. Several signal samples are generated for ranges of the invisible mediator mass between $m_V = 25$ GeV and 2.5 TeV, and DM mass $m_\chi = 1$ GeV corresponding to the expected sensitivity of the analysis. The kinematic distributions predicted by the model only have a small dependency on the coupling parameters and therefore all samples are generated using $a = 0.5$ and $g_\chi = 1.0$. The samples are normalized considering the LO values for the corresponding cross-sections, computed with MADGRAPH5_aMC@NLO.

In addition to the generated samples, a reweighing procedure is used estimate the discovery potential for the full range of parameters. Such procedure is validated with dedicated samples and allows to reproduce the correct event kinematics for the masses and couplings required for the multi-dimensional scans performed in the current analysis.

Background samples

The $t\bar{t}$ background is simulated using POWHEG-BOX v2 [185–190,241] interfaced to PYTHIA8.210 using the A14 set of tunable parameters.

The single-top quark production in the t-, Wt- and s-channels are generated with POWHEG-BOX v1 interfaced to PYTHIA6.428 [192]. The CT10 PDF set [125] is used in the matrix element calculations while CTEQ6L1 PDF set [126] and the corresponding Perugia 2012 tune [193] is used in the parton shower, hadronization, and underlying event simulation.

The tZq MC samples are generated at LO using MADGRAPH5_aMC@NLO in the four-flavor scheme, treating the b-quark as massive, with the CTEQ6L1 PDF set, and interfaced to PYTHIA6.428 with Perugia 2012 parameters. This negligible background is included as part of the single-top production.

To model the W+jets and Z+jets background the SHERPA v2.2.1 [194] generator is used. Matrix elements are calculated for up to two partons at NLO and up to four partons at LO using COMIX [242] and OPENLOOPS [243] ME generators, and merged with the SHERPA parton shower [244] using the ME+PS@NLO prescription [245]. The NNPDF3.0 NNLO PDF set [124] is used in conjunction with a dedicated SHERPA parton shower tuning.

Diboson processes are simulated with POWHEG-BOX v2 interfaced to PYTHIA8.186. The CT10nlo PDF set is used for the hard-process while the CTEQ6L1 PDF set is used for the parton shower.

The full list of the baseline simulated samples is available in Appendix A.2.

5.3 Event reconstruction and selection

The experimental signature of the leptonic mono-top events is one isolated lepton from the W boson decay, large missing transverse momentum, and one jet identified as likely to have originated from a b-quark. In a first step, candidate events are preselected if they match the signal topology at the level of the basic objects defined in Section 2.4. The final selection is done in a second step by applying cuts in the most discriminant variables. These cuts are optimized for various signal

benchmarks using simulated data. The following subsections describe the applied preselection and selection criteria.

5.3.1 Objects selection

The object reconstruction was explained in detail in Section 2.4 and only a summary is given in the following.

Electron candidates are reconstructed from an isolated electromagnetic calorimeter energy deposit matched to a track in the inner detector passing tight likelihood-based requirements [147]. They are required to have a transverse energy $E_{\mathrm{T}} > 30\,\mathrm{GeV}$ and pseudorapidity $|\eta| < 2.47$, with the transition region between the barrel and endcap electromagnetic calorimeters, $1.37 < |\eta| < 1.52$, excluded. The electron candidates must satisfy requirements on the transverse impact parameter significance with respect to the beamline of $|d_0|/\sigma_{d_0} < 5$ and on the longitudinal impact parameter calculated with respect to the primary vertex of $|\Delta z_0 \sin\theta| < 0.5\,\mathrm{mm}$. Muon candidates are reconstructed by combining matching tracks reconstructed in both the inner detector and muon spectrometer, and are required to satisfy $p_{\mathrm{T}} > 30\,\mathrm{GeV}$ and $|\eta| < 2.5$ [152]. The muon candidates must satisfy the requirements on the transverse impact parameter significance and on the longitudinal impact parameter of $|d_0|/\sigma_{d_0} < 3$ and $|\Delta z_0 \sin\theta| < 0.5\,\mathrm{mm}$, respectively. Both electrons and muons must satisfy isolation requirements based on inner detector tracks and topological clusters in the calorimeter [246], with an isolation efficiency of 90% (99%) for electrons and muons from $Z \to ee$ and $Z \to \mu\mu$ decays with $p_{\mathrm{T}} = 25(60)\,\mathrm{GeV}$.

Jets are reconstructed from topological clusters of energy deposited in the calorimeter [246] using the anti-k_t algorithm [154] with a radius parameter of 0.4, as implemented in the FastJet package [247]. Jets are calibrated using an energy- and η-dependent simulation-based calibration scheme with corrections derived from data [163]. Jets are accepted within the fiducial region $|\eta| < 2.5$ and $p_{\mathrm{T}} > 30\,\mathrm{GeV}$. Quality criteria are imposed to reject events that contain any jets arising from non-collision sources or detector noise [161]. To reduce the contribution from jets associated with pile-up, jets with $p_{\mathrm{T}} < 60\,\mathrm{GeV}$ and $|\eta| < 2.4$ are required to pass a

criterion that associates them to the hard scatter event using information from tracks reconstructed in the inner tracking detector [159]. To prevent double counting of electron energy jets, the closest jet with $\Delta R_{y,\phi} \equiv \sqrt{(\Delta y)^2 + (\Delta\phi)^2} < 0.2$ of a reconstructed electron is removed. If the nearest jet is within $\Delta R_{y,\phi} = 0.4$ of the electron, the electron is discarded to ensure it is sufficiently separated from nearby jet activity. Jets with fewer than three tracks and distance $\Delta R_{y,\phi} < 0.2$ from a muon are removed to reduce the number of jet fakes from muons depositing energy in the calorimeters. Muons with a distance $\Delta R_{y,\phi} < 0.4$ from any of the surviving jets are removed to avoid contamination due to non-prompt muons from heavy-flavor hadron decays.

Jets are b-tagged as likely containing b-hadrons using multivariate techniques which exploit the long lifetime of b-hadrons and large invariant mass of their decay products relative to c-hadrons and unstable light hadrons [165, 166]. The working point used provides an average tagging efficiency of 70% for b-jets and a rejection factor of 12.2 against jets initiated by c-quarks and 381 against jets initiated by light-flavour quarks, in simulated $t\bar{t}$ events [165, 168, 169].

The missing transverse momentum $E_{\mathrm{T}}^{\mathrm{miss}}$ is calculated as the negative vector sum of the transverse momenta of particles in the event. In addition to the identified jets, electrons, muons, hadronically decaying τ-leptons and photons, a track-based soft term is included in the $E_{\mathrm{T}}^{\mathrm{miss}}$ calculation by considering tracks associated with the hard-scattering vertex in the event which are not also associated with an identified jet, electron, muon, hadronically decaying τ-lepton, or photon [172, 173].

5.3.2 Signal preselection

Events are required to have at least one vertex candidate with at least two tracks with p_{T}> 400 MeV. The primary vertex is taken to be the vertex candidate with the largest sum of squared transverse momenta of all associated tracks.

Preselected candidate events are required to contain exactly one tight lepton with $p_{\mathrm{T}} > 30$ GeV, exactly one jet with $p_{\mathrm{T}} > 30$ GeV and required to be b-tagged and a large amount of missing transverse momentum, $E_{\mathrm{T}}^{\mathrm{miss}} > 50$ GeV. Multijet events are characterized by low $E_{\mathrm{T}}^{\mathrm{miss}}$ and low $m_{\mathrm{T}}(W)$, and therefore a lower cut

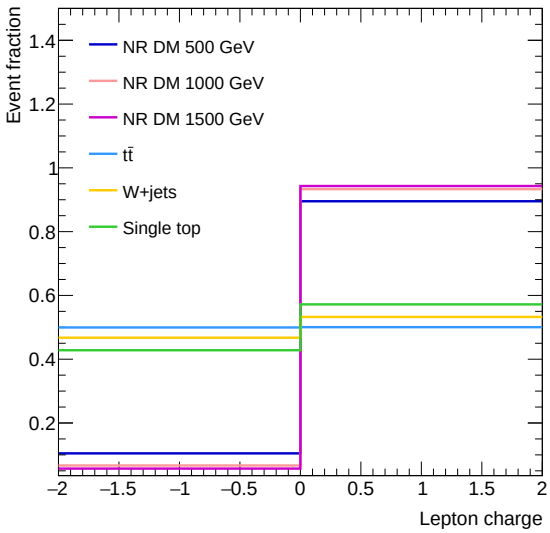

Figure 5.2: Event fraction of expected signal for various mediator masses and main background events with positive and negative lepton charge.

in the sum of these two variables is applied to reject the contribution from such events, $m_{\mathrm{T}}(W) + E_{\mathrm{T}}^{\mathrm{miss}} > 60$ GeV. In addition, as discussed in Section 1.4.4, in the non-resonant production the up-type quark initiated production of top quarks is favored with respect to the anti-top quark production, due the PDF structure of the proton. Therefore, positively charged leptons are favored. This is seen in Figure 5.2, in which the expected fraction of events with positive and negative lepton charge of various mediator masses and of the most contributing backgrounds is displayed. The lines representing the $t\bar{t}$, W+jets and single-top background contributions, are predominantly flat. In contrast, more than 90% of the signal events contain a positive lepton. Thus, only events with a positive lepton are selected.

Figure 5.3 shows the comparison of data and SM predictions for the $E_{\mathrm{T}}^{\mathrm{miss}}$ distribution, which is the variable used as discriminant in the likelihood fit explained in the following sections, for events satisfying the preselection criteria. The expected distributions for the non-resonant model are shown for the mediator mass $m_V = 500$ GeV and $m_V = 1.5$ TeV hypothesis normalized to the SM background

predicted yield. The uncertainty bands cover the Monte Carlo simulation statistics contribution and a 50% normalization uncertainty for the data-driven multijet background.

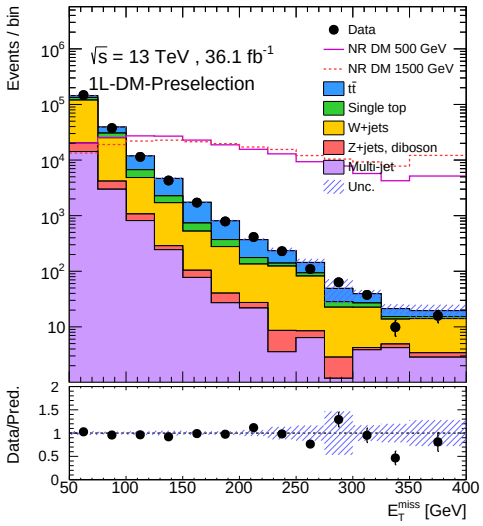

Figure 5.3: Comparison of data and SM prediction for the $E_{\mathrm{T}}^{\mathrm{miss}}$ distribution for events satisfying the preselection criteria. The expected distributions for the non-resonant model are shown for the mediator mass $m_V = 500$ GeV and $m_V = 1.5$ TeV hypothesis normalized to the SM background predicted yield. The SM backgrounds correspond to the simulation predictions normalized to the theoretical predictions, except the multijet background that is estimated from data. The error bands include statistical uncertainties. The last bin contains the overflow events.

Apart from the $E_{\mathrm{T}}^{\mathrm{miss}}$ distribution, there are two variables that have more power to discriminate the shape of signal versus the background. These variables are the transverse mass of the reconstructed W boson and the azimuthal separation $|\Delta\phi(\ell, b)|$ between the lepton and the b-tagged jet. Hence, these two variables, which from now on are called selection variables, will be used to define the final selection as well as the control and validation regions. Figure 5.4 shows the distributions agreement of data and SM predictions for the selection variables in the preselected signal region. Two non-resonant signal models with m_V = 500 and 1500 GeV are

also displayed, normalized to the total expected background yields. The uncertainty bands cover statistical and systematic uncertainties. As seen in the figure, the reconstructed b-tagged jet and the lepton are closer to each other when arising from the decay of a top quark -as signal events- compared to the case of W+jets, Z+jets, diboson production and multijet background events. In addition, the presence of signal is enriched in regions with higher $m_{\mathrm{T}}(W)$, while the background decreases significantly.

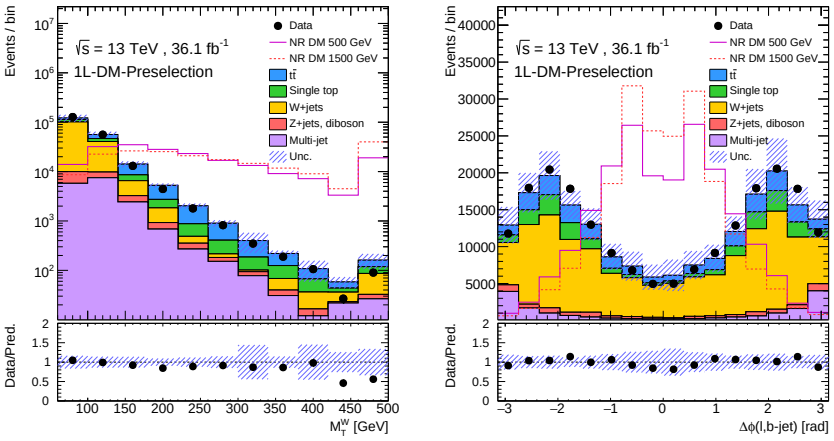

Figure 5.4: Comparison of data and SM prediction for the $m_{\mathrm{T}}(W)$ (left) and $|\Delta\phi(\ell, b)|$ (right) distributions for events satisfying the preselection criteria. The expected distributions for the non-resonant model are shown for the mediator mass $m_V = 500$ GeV and $m_V = 1.5$ TeV hypothesis normalized to the SM background predicted yield. The SM backgrounds correspond to the simulation predictions normalized to the theoretical predictions, except the multijet background that is estimated from data. The error bands include statistical and systematic uncertainties. The last bin contains the overflow events.

5.3.3 Signal region definition

Besides applying preselection criteria, an optimization of the $|\Delta\phi(\ell, b)|, m_{\mathrm{T}}(W)$- space is performed. The signal region selection is optimized for several benchmarks with simulated data. In the optimization the sensitivity is

estimated by performing a fit to the shape of the $E_{\mathrm{T}}^{\mathrm{miss}}$, the most discriminating observable, including systematic uncertainties (see Section 5.6 for details). To do the optimization, the discriminating power of the azimuthal separation $|\Delta\phi(\ell, b)|$ between the lepton and the b-tagged jet is exploited by imposing a criterion that rejects events at high $|\Delta\phi(\ell, b)|$ values, with thresholds varied between 2.8 and 1.0 in steps of 0.2. In addition, the $m_{\mathrm{T}}(W)$ range between 160 and 300 GeV is explored, in steps of 20 GeV. For each of the considered regions, the expected upper limit on the signal strength, μ [1], is computed under the background-only hypothesis. The aim is to find the region that gives the smaller μ, provided there is no such signal process. After this optimization, the signal region 1L-DM-SR is defined by requiring

- $m_{\mathrm{T}}(W) > 260\,\mathrm{GeV}$
- $|\Delta\phi(\ell, b)| < 1.2$

The optimization based on maximizing the signal significance (discovery potential) leads to equivalent results. The signal region requirements are summarized in Table 5.1 and in Figure 5.5.

5.4 Background normalization and modeling

The dominant background in the signal regions comes from $t\bar{t}$ production, representing 78% of the total background in the signal region. This is followed by a 13% contribution from single top processes and 6.8% from W+jets production. A minor background in the signal region with a non-negligible contribution in the control regions is the multijet production. Additional small backgrounds considered in the analysis are Z+jets and diboson production. The multijet production background is estimated from data while the rest of background processes are taken from simulation. Dedicated control regions enriched in the dominant backgrounds are included in the fit to constrain these backgrounds from data. In addition,

[1] The μ parameter determines the strength of the signal process, with $\mu = 0$ corresponding to the background-only hypothesis and $\mu = 1$ being the nominal signal hypothesis.

Selections	1L-DM-SR	1L-TCR	1L-WCR	1L-TVR	1L-WVR	MCR (μ-channel)
N(tight leptons)	1	1	1	1	1	1
$p_T(\ell)$ [GeV]	> 30	> 30	> 30	> 30	> 30	> 30
charge sign	> 0	> 0	> 0	> 0	> 0	> 0
N (b-jets)	1	2	1	2	1	1
$p_T(b-\text{jets})$ [GeV]	> 30	> 30	> 30	> 30	> 30	> 30
$E_{\mathrm{T}}^{\mathrm{miss}}$ [GeV]	> 50	> 50	> 50	> 50	> 50	
$m_{\mathrm{T}}(W) + E_{\mathrm{T}}^{\mathrm{miss}}$ [GeV]	> 60	> 60	> 60	> 60	> 60	
$m_{\mathrm{T}}(W)$ range [GeV]	> 260	[60,100]	[60,100]	[100,180]	[100,180]	[0,60]
$\lvert\Delta\phi(\ell, b)\rvert$	< 1.2			< 1.8	< 1.8	

Table 5.1: Summary of the definion of the signal (1L-DM-SR),top and W+jets control (1L-TCR, 1L-WCR), and top and W+jets validation (1L-TVR, 1L-WVR) regions.

intermediate validation regions are defined in order to validate the background normalization. Table 5.1 and Figure 5.5 summarize the definitions of the signal, control and validation regions used in the analysis. Figure 5.6 depicts the expected background composition in each of the regions.

The multijet shape, normalization and related systematic uncertainties are estimated with two different methods. In the electron channel the matrix method already introduced in Chapter 4.4.1, is used. The prompt lepton efficiencies are measured in terms of the p_{T} of the leading jet and the angular distance between the lepton and its nearest jet, while the non-prompt or fake efficiencies are parametrized in terms of the p_{T} of the leading jet, the angle in the transverse plane between the lepton and the $E_{\mathrm{T}}^{\mathrm{miss}}$ and the b-tagged jet multiplicity. From the comparison of different combinations of parametrizations, a 50% normalization uncertainty is assessed to the multijet background [205, 248].

In the muon channel the antimuon method [205] is used. This method gives a model for the shape of the multijet backgrounds in μ+jets events which can be later fitted to data to estimate the normalization. To obtain a data sample highly enriched in non-prompt muons, the cuts on the isolation variables defined in 2.4 are changed or inverted in a way that non-isolated muons pass the requirements but its kinematic properties are still similar to those fulfilling the standard requirements.

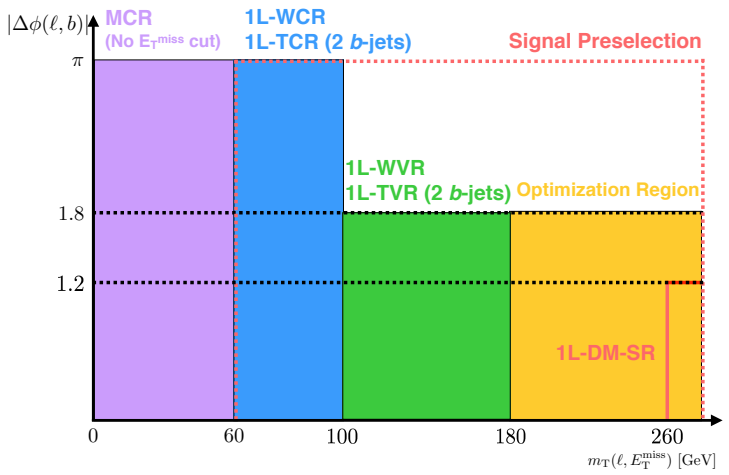

Figure 5.5: Sketch depicting the control, signal and validation regions in the $|\Delta\phi(\ell, b)|, m_{\mathrm{T}}(W)$- space.

Once the shape of the multijet background is given by the antimuon model, the $E_{\mathrm{T}}^{\mathrm{miss}}$ distribution is fitted in a dedicated control region MCR. This region is defined with the preselection criteria removing the requirement on $E_{\mathrm{T}}^{\mathrm{miss}}$and requiring $m_{\mathrm{T}}(W) < 60\,\mathrm{GeV}$ (see Table 5.1 and Figure 5.5). The results of the fit are depicted in Figure 5.7. The uncertainty bands cover the statistical uncertainties of the simulated samples.

5.4.1 Background only fit in the control regions

The control regions used to constrain from data the $t\bar{t}$ (1L-TCR) and W+jets (1L-WCR) backgrounds are defined after requiring the preselection criteria by modifying the requirement on $m_{\mathrm{T}}(W)$ to a window around the W boson mass, $60\,\mathrm{GeV} < m_{\mathrm{T}}(W) < 100\,\mathrm{GeV}$, and removing the requirement on $|\Delta\phi(\ell, b)|$. For the 1L-TCR, events are also required to contain a second b-tagged jet. These definitions ensure orthogonality between the control and signal regions (see Table 5.1 and Figure 5.5). The expected relative composition of the control regions in comparison to that of the signal region is shown in Figure 5.6. The signal contribution is

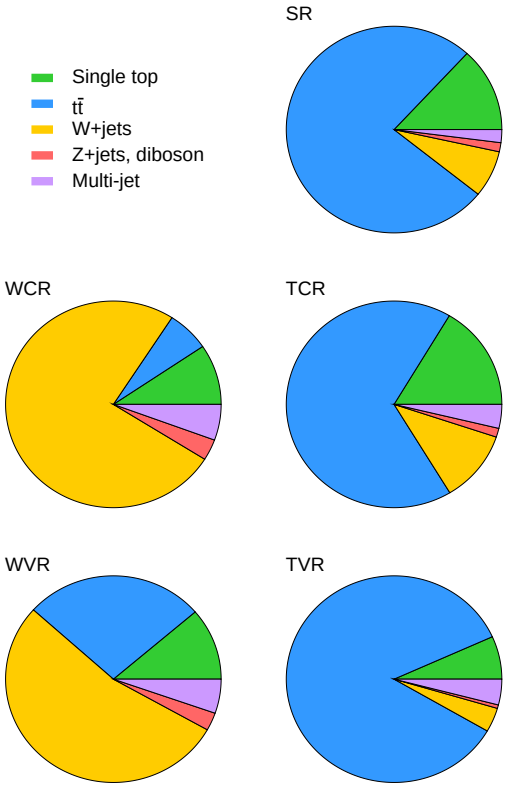

Figure 5.6: Comparison of the expected composition of the signal, control and validation regions. The electron and muon channels are merged.

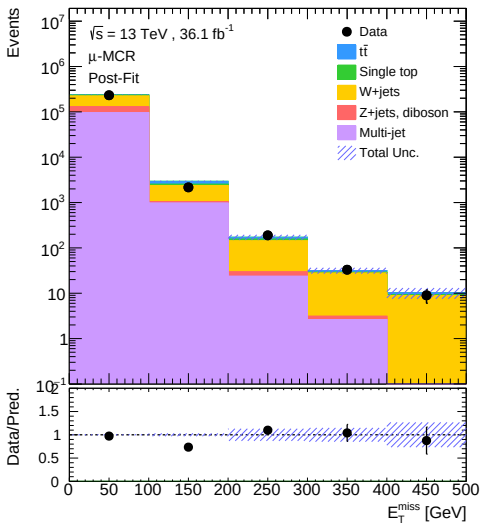

Figure 5.7: $E_{\mathrm{T}}^{\mathrm{miss}}$ distribution in the MCR in the muon channel after the likelihood fit to calculate the normalization of the multijet contributions estimated with the antimuon method.

expected to be negligible in the control regions, representing less than a 0.02% of the expected total yield.

A maximum-likelihood fit of the background expectations to the data is applied in the two control regions to constrain simultaneously the normalization of the W+jets and $t\bar{t}$ contributions (free parameters of the fit), while the rest of the backgrounds are fixed to their predictions. In the fitting procedure the background rates are constrained with gaussian priors. A normalization constrain of $^{+5.58}_{-6.11}\%$, corresponding to its cross-section theoretical uncertainty, is set to the $t\bar{t}$ process, while a $\pm 5\%$ is assessed to the W+jets. The obtained scale factors are shown in Table 5.2.

Since the scale factors obtained for both background processes are compatible with unity, it is preferred to not apply them and treat the normalization of these backgrounds as nuisance parameters (NP) constrained to their theoretical cross-section uncertainties.

Process	Scale Factor
W+jets	1.01 ± 0.04
$t\bar{t}$	0.97 ± 0.07

Table 5.2: Scale factors extracted for the W+jets and $t\bar{t}$ background processes from the simultaneous maximum-likelihood fit to the number of data events observed in the WCR and TCR control regions. The uncertainties come from the likelihood fit; they are related to the Poissonian and Gaussian terms of the likelihood function.

One of the challenges of this analysis is the limited simulation statistics of the background samples in the signal region, which can lead to non-convergences in the fit procedure and nonphysical results. The way to solve this is to merge all the minor backgrounds (single-top production, W+jets, Z+jets, diboson and multi-jet processes) in a non-$t\bar{t}$ background. Since the normalization scale factors obtained for W+jets processes are compatible with unity, the different contribution of this background in the signal and control regions does not compromise the validity of the fit if only the normalization is included in the control regions for the final fit to data in the signal and control regions. The fit procedure used when including the signal region is explained in detail in Section 5.6.

A comparison of data and expectation in the control regions for the $E_{\mathrm{T}}^{\mathrm{miss}}$ distribution is shown in Figure 5.8 for the 1L-TCR and 1L-WCR regions. The expectations are obtained from a fit of the background-only hypothesis to data in the control regions, where the normlizations of the $t\bar{t}$ and W+jets processes are treated as nuisance parameters in the fit (see Section 5.6 for details on the fit). There is a good agreement between data and MC expectation.

5.4.2 Background validation

In order to validate the background normalization, intermediate validation regions are defined. These regions are not included in the fit, but are used to validate the agreement of data and expectation after applying the results of the fit in the control regions. Two validation regions, one for each of the dominant backgrounds, are defined and referred to as 1L-TVR and 1L-WVR. Both validation

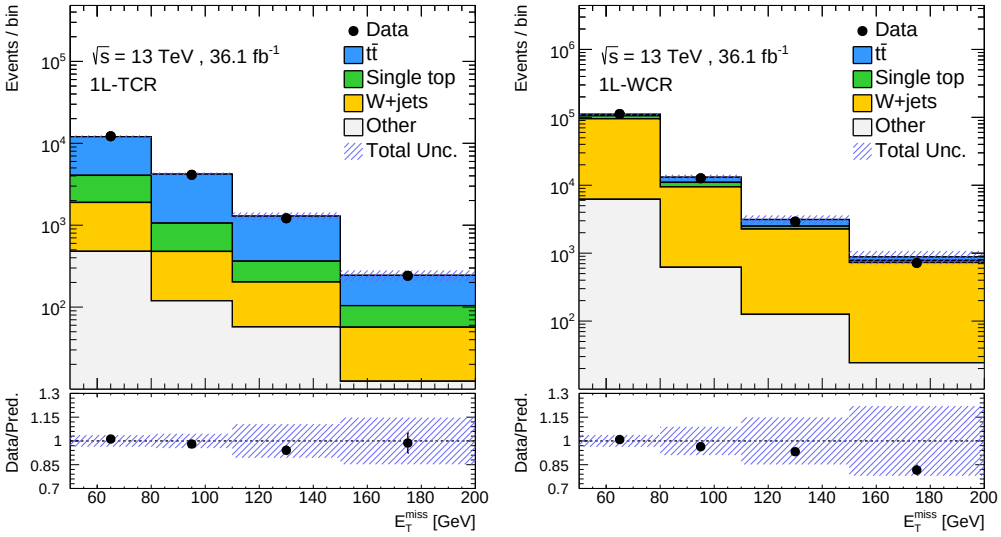

Figure 5.8: Comparison of data and SM prediction for the $E_{\mathrm{T}}^{\mathrm{miss}}$ distribution in the 1L-TCR (left) and 1L-WCR (right) control regions. The expectations are obtained from a fit of the background-only hypothesis to data in the the two control regions, where the noramlizations of the $t\bar{t}$ and W+jets processes are treated as nuisance parameters in the fit. Other backgrounds include multijet, Z+jets and diboson contributions. The error bands include statistical and systematic uncertainties. The last bin contains the overflow events.

regions are defined after applying the same preselection as to the signal region, but changing the cuts in the $|\Delta\phi(\ell, b)|$, $m_{\mathrm{T}}(W)$- space, as seen in Figure 5.5 and Table 5.1. In the case of the $t\bar{t}$ validation region, an additional b-jet is required. The cuts applied in the validation regions are $|\Delta\phi(\ell, b)| < 1.8$ and 100 GeV < $m_{\mathrm{T}}(W)$< 180 GeV. The expected relative composition of the validation regions in comparison to that of the signal and control regions is shown in Figure 5.6.

A comparison of data and expectation in the validation regions for the $E_{\mathrm{T}}^{\mathrm{miss}}$ distribution is shown in Figure 5.9 for the 1L-TVR and 1L-WCR regions. The expectations are obtained from a fit of the background-only hypothesis to data in the control regions, where the normalizations of the $t\bar{t}$ and W+jets processes are treated as nuisance parameters in the fit. The agreement is good within statistical uncertainties.

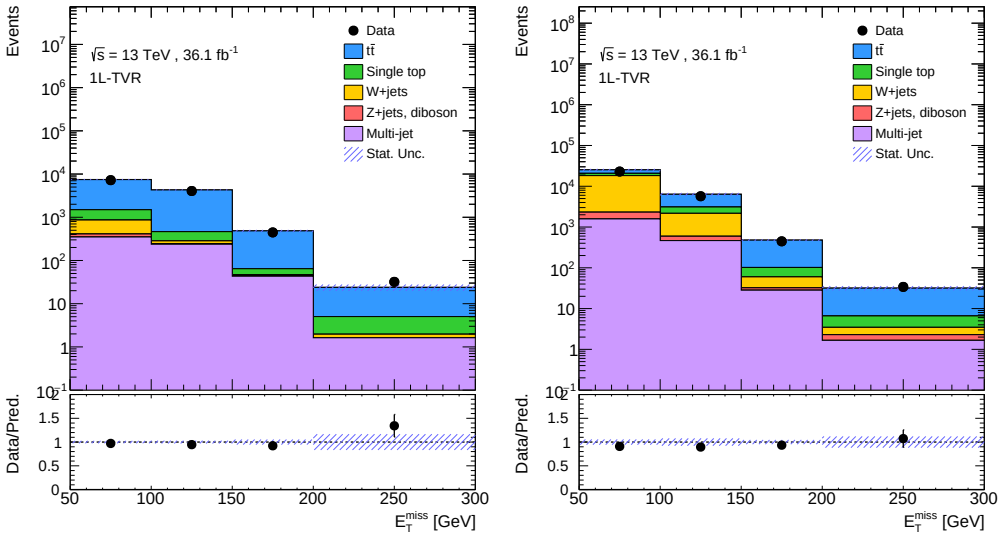

Figure 5.9: Comparison of data and SM prediction for the $E_{\mathrm{T}}^{\mathrm{miss}}$ distribution in the 1L-TVR (left) and 1L-WVR (right) validation regions. The expectations are obtained from a fit of the background-only hypothesis to data in the the two control regions, where the noramlizations of the $t\bar{t}$ and W+jets processes are treated as nuisance parameters in the fit. The error bands include statistical uncertainties and a 50% normalization uncertainty on the multijet background. The last bin contains the overflow events.

5.5 Systematic uncertainties

Different sources of systematic uncertainties from experimental sources and from theoretical predictions can affect both the overall yield and shape of the observables used in the fit for the statistical analysis. Despite being limited by statistical uncertainties, each source of uncertainty is considered in the analysis and included as a nuisance parameter in the likelihood fit that determines the possible signal contribution.

- **Experimental uncertainties**: The experimental sources of uncertainty include the uncertainty in the lepton trigger, identification and isolation efficiencies, the lepton energy scale and resolution [147, 152, 246], the $E_{\mathrm{T}}^{\mathrm{miss}}$ track-based soft term scale and resolution [172, 173], the jet pile-up rejection requirement, energy scale and resolution [155], the b-tagging efficiency [165, 166] and the pile-up reweighing. For a detailed discussion on these uncertainties, see Section 2.4.

- **Luminosity**: A 2.1% uncertainty is assigned to the integrated luminosity. It is derived, following a methodology similar to that detailed in Ref. [228], from a calibration of the luminosity scale using x–y beam-separation scans. This systematic uncertainty is applied to all background and signals that are estimated using MC events, which are normalized to the measured integrated luminosity.

- **Modeling uncertainties**: Theoretical cross-section uncertainties are applied to the normalization of the simulated processes. Additional shape uncertainties stemming from theoretical estimations are calculated by comparing simulated samples with different assumptions and are estimated for the dominant backgrounds.

  The uncertainties in the modeling of the $t\bar{t}$ and t-channel single top background come from the choice of the NLO-matching method, parton shower and hadronization modeling, and the amount of additional gluon radiation. The NLO-matching uncertainty is estimated by comparing

events produced with POWHEG-BOX and MADGRAPH5_aMC@NLO [196], both interfaced with Herwig++ [129]. The parton shower, hadronization, and underlying-event model uncertainty is estimated by comparing two parton shower models, PYTHIA and Herwig++, while keeping the same hard-scatter matrix element generator. Variations of the amount of additional gluon radiation are estimated by comparing simulated samples with enhanced or reduced radiation and different values of tunable parameters related to additional radiation [191]. The choice of scheme to account for the interference between the Wt and $t\bar{t}$ processes constitutes another source of systematic uncertainty, and it is estimated by comparing samples using either the diagram removal scheme or the diagram subtraction scheme [204].

The effect of the uncertainties on PDF on the acceptance of the $t\bar{t}$ are estimated following the PDF4LHC prescription [249].

Based on comparisons of the rates obtained using alternative methods described in previous analyses [205, 248], an uncertainty of 50% is considered for the normalization of the multijet background.

A breakdown of the effect from the various sources of systematic uncertainties in the background prediction is summarized in Table 5.3. The relative effect on the background yields in the signal region after the simultaneous fit to data is shown. These uncertainties are computed individually for each source of systematic uncertainty as the relative difference between the nominal process integral and the post-fitted symmetrized systematic variation, and give an estimate of the effect of the systematic in the process yield. Individual sources of uncertainties are grouped in categories by adding them in quadrature taking into account the correlations between them.

5.6 Results

Assuming that no significant excess of data is observed with respect to the expected SM backgrounds, the event yields in the electron and muon channels are combined in an statistical analysis to calculate exclusion limits on the production

	1L-DM-SR		1L-TCR		1L-WCR	
	non-$t\bar{t}$	$t\bar{t}$	non-$t\bar{t}$	$t\bar{t}$	non-$t\bar{t}$	$t\bar{t}$
Background modelling	15	15	12	8.0	6.4	6.9
Jets	11	7.2	10	8.7	7.3	11
Lepton	1.2	0.7	3.6	0.4	2.0	0.4
Luminosity	2.1	2.0	2.1	2.1	2.0	2.1
MET reconstruction	12	1.1	13	0.2	8.3	0.5
Pile-up	5.5	1.4	0.4	1.2	1.6	1.4
b-tagging	5.0	4.4	10	8.1	11	4.1

Table 5.3: Relative effect (in %) on the background predicted yields in the signal and control regions used for the dark matter search, obtained after the fit to data in the 1L-TCR, 1L-WCR and 1L-DM-SR regions, under the background-only hypothesis.

cross-section of each signal scenario. The signal process and the backgrounds ($t\bar{t}$ and non-$t\bar{t}$) are fitted simultaneously in the signal, 1L-WCR and 1L-TCR regions to data with the procedure described in Subsection 5.6.1. Finally, the results of the fit are interpreted in terms of the non-resonant DM signal model.

5.6.1 Likelihood fit

Hypothesis testing is performed using a frequentist approach implemented in the `TRexFitter` package (within the `RooStats` framework [250]), which uses the asymptotic approximation described in [251]. The shape of the $E_{\mathrm{T}}^{\mathrm{miss}}$ distribution with three bins is used in the fit, as it was seen to be the most sensitive to the presence of new physics. Several binning configurations were tested and, while a noticeable improvement was achieved from a cut-and-count analysis to the three bins used, no difference was seen when changing to a finer binning. The chosen binning allows to improve sensitivity while keeping reasonable statistics in all the bins, specially in the highest $E_{\mathrm{T}}^{\mathrm{miss}}$ region, assisting the robustness of the fitting procedure. The distributions in the control regions are not binned.

The expected number of events in the ith bin of the $E_{\mathrm{T}}^{\mathrm{miss}}$ distribution is given by

$$N_i^{exp}(\mu, \boldsymbol{\theta}) = \mu s_i(\boldsymbol{\theta}) + b_i(\boldsymbol{\theta}), \tag{5.1}$$

where s_i and b_i represent the expected signal and background yields in the ith bin, and μ is a scaling parameter applied to the signal to test the sensitivity of the search, named signal strength. The null hypothesis (background-only hypothesis) corresponds to $\mu = 0$ while the test hypothesis (signal-plus-background hypothesis) corresponds to $\mu = 1$. Both signal and background yields are functions of nuisance parameters $\boldsymbol{\theta}$ which parametrize the effect of the systematic uncertainties.

On the other hand, the observed number of events in the i-th bin is denoted by n_i.

In addition to the $E_{\mathrm{T}}^{\mathrm{miss}}$ distribution corresponding to the expected and observed events in the signal region, subsidiary measurements in control regions are also taken into account to help to constrain the nuisance parameters. These are considered as two additional bins (there are two control regions with unbinned distributions), k, with expected number of events u_k and observed number of events m_k. The likelihood function is the product of Poisson probabilities for all bins:

$$L(\mu, \boldsymbol{\theta}) = \prod_{i=1}^{N} \frac{(\mu s_i + b_i)^{n_i}}{n_i!} e^{-(\mu s_i + b_i)} \prod_{k=1}^{M} \frac{u_k^{m_k}}{m_k!} e^{-u_k}, \tag{5.2}$$

where i runs over the bins in the signal region ($N = 3$) and k runs over the bins in the control regions ($M = 2$).

A common way to introduce the effect of the different sources of systematic uncertainties ($\boldsymbol{\theta}$ nuisance parameters) in the likelihood is through the addition of gaussian terms, $\mathrm{Gauss}(0|\alpha, 1)$, where the scale of the parameter α of a given systematic is chosen such that values ± 1 correspond to the nominal uncertainty. When the result of the likelihood fit leads to $\alpha \neq 0 \pm 1$ the systematic is said to be pulled (if its central value differs from 0) or constrained (if its uncertainty is smaller than 1) by the fit.

To test a given signal hypothesis, a test statistic is needed. It is a variable constructed from the measurements alone used to determine the level of agreement of a hypothesis with the observation. There is a relative freedom in the choice of

the test statistic, but it should result in a clear separation of its distributions for the background-only and signal-plus-background hypothesis. A useful test statistic to set upper limits in the signal strength of a signal hypothesis is:

$$q_\mu = \begin{cases} -2\ln\frac{L(\mu,\hat{\hat{\boldsymbol{\theta}}})}{L(\hat{\mu},\hat{\boldsymbol{\theta}})} & \hat{\mu} \leq \mu, \\ 0 & \hat{\mu} > \mu, \end{cases}$$

where $\hat{\hat{\boldsymbol{\theta}}}$ denotes the value of $\boldsymbol{\theta}$ that maximizes the likelihood for the specified μ (conditional maximum-likelihood estimator of $\boldsymbol{\theta}$) and the denominator is the maximized (unconditional) likelihood function ($\hat{\mu}$ and $\hat{\boldsymbol{\theta}}$ are their maximum-likelihood estimators). Setting $q_\mu = 0$ for $\hat{\mu} > \mu$ is useful when setting upper limits since one would not regard data with $\hat{\mu} > \mu$ as representing less compatibility with μ than the data obtained, and therefore is it not taken as part of the rejection region of the test.

The level of agreement between the data and the hypothesized μ is quantified with a p-value

$$p_\mu = \int_{q_{\mu,\mathrm{obs}}}^{\infty} f(q_\mu|\mu)\mathrm{d}q_\mu, \tag{5.3}$$

where $f(q_\mu|\mu)$ is the probability density function (pdf) of q_μ assuming the hypothesis μ. In general, to estimate the pdf of a test statistic, numerical methods through MC simulations are needed. However, when using a likelihood-ratio test statistic such as the one written above, an asymptotic distribution can be resorted as an approximation of the true distribution. Within this approximation (the detailed derivation can be found in [251]), the p-value for a hypothesized μ is given by:

$$p_\mu = \int_{q_{\mu,\mathrm{obs}}}^{\infty} f(q_\mu|\mu)\mathrm{d}q_\mu = 1 - F(q_\mu|\mu) = 1 - \Phi(\sqrt{q_\mu}) \tag{5.4}$$

If the p-value is found below a specified threshold $\alpha = 0.05$, then the value is said to be excluded at a confidence level (CL) of 95%. The upper limit on μ is the largest μ with $p_\mu \leq 0.05$

$$\mu_{up} = \hat{\mu} + \sigma\Phi^{-1}(1 - 0.05), \tag{5.5}$$

where σ is the standard deviation of $\hat{\mu}$.

Likelihood fit to data

For the final signal plus background fit in the signal and control regions, the distribution of the $E_{\mathrm{T}}^{\mathrm{miss}}$ is used in the signal region and the number of events is used instead in the control regions. The binning of the $E_{\mathrm{T}}^{\mathrm{miss}}$ distribution is optimized to get the highest expected sensitivity.

Uncertainties due to the limited size of the simulated samples are taken into account in each bin of the fitted distributions as nuisance parameters. Figure 5.10 shows the post-fit values of the nuisance parameters associated to the limited statistics of each bin that enters into the fit. From this figure it is seen that the simulation statistics in the last bin of the $E_{\mathrm{T}}^{\mathrm{miss}}$ distribution in the signal region has a big contribution to the total uncertainty.

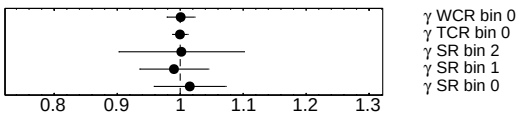

Figure 5.10: Pull plot of the MC statistical uncertainties after a background-only fit of expected backgrounds to data in the signal and control regions.

The different sources of systematic uncertainties are treated as nuisance parameters in the fit. They are symmetrized and also smoothed if the bin-to-bin statistical variation is significant. In case of one-sided systematics (for example the modeling ones), the given variation is defined to be the up variation. The effect of the down systematic variation is then symmetrized by inverting the up variation

$$\text{down} \rightarrow \text{nominal} - (\text{up} - \text{nominal}).$$

The rest of systematics are also symmetrized to avoid bad behavior of the fit due to asymmetric errors. The symmetrization in this case is done as

$$\begin{aligned} \text{up} &\rightarrow \text{nominal} + (\text{up} - \text{down})/2 \\ \text{down} &\rightarrow \text{nominal} - (\text{up} - \text{down})/2 \end{aligned}$$

.

A pruning process to reject systematic uncertainties which have an impact smaller than 1% on either normalization or shape is applied. The outcome of this process is shown in Figure 5.11, where each source of systematic uncertainty listed in Section 2.4 is considered individually. Systematic contributions marked as red are not included in the analysis and only the normalization is considered for those marked in yellow.

The constrain on the nuisance parameters that enter into the fit to data is shown in Figure 5.12. Most uncertainties are not found to be significantly constrained or pulled from their initial values. Small variations are observed in the $t\bar{t}$ modeling uncertainties due to the mis-modeling observed in the shape of the transverse momentum distribution of top quarks [252, 253].

Figure 5.13 shows the influence of the main systematics on the fitted value of the signal strength parameter μ (top axis values), before the systematics are fitted to the data (empty rectangles) and after (full rectangles). The black points, bars and the bottom axis correspond exactly to those of the pull plots. For each nuisance parameter the shift in the signal strength is obtained for a fit with the NP fixed to its pre-fit or post-fit ($\pm 1\sigma$) values, respectively. The leading sources of systematic uncertainties come from the simulation statistics in the last bin of the $E_{\mathrm{T}}^{\mathrm{miss}}$ distribution in the SR, the modeling of the $t\bar{t}$ and t-channel processes and the energy scale of the b-tagged jets.

The number of events observed in the signal and control regions is presented in Table 5.4, together with the background estimated previous to the simultaneous fit. Figure 5.14 shows the three input distributions after the fit under the background-only hypothesis, *i.e.*, the yields in the 1L-TCR and 1L-WCR and the

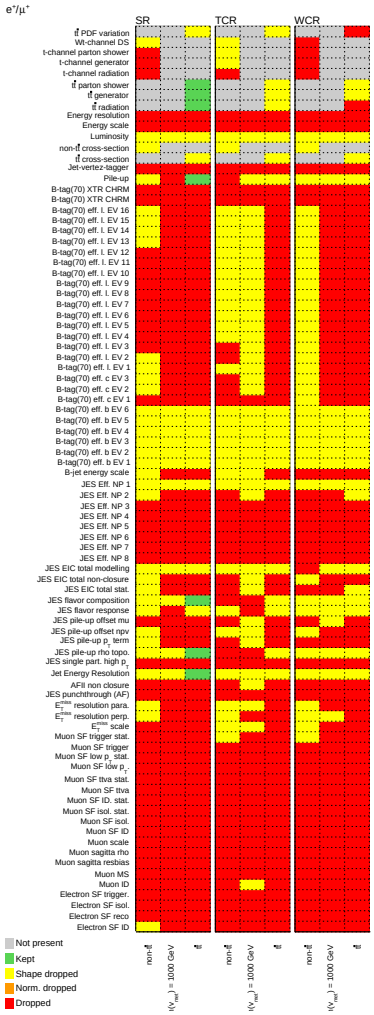

Figure 5.11: Output list of systematic treatment after pruning procedure. Each source of systematic uncertainty listed in Section 2.4 is considered individually.

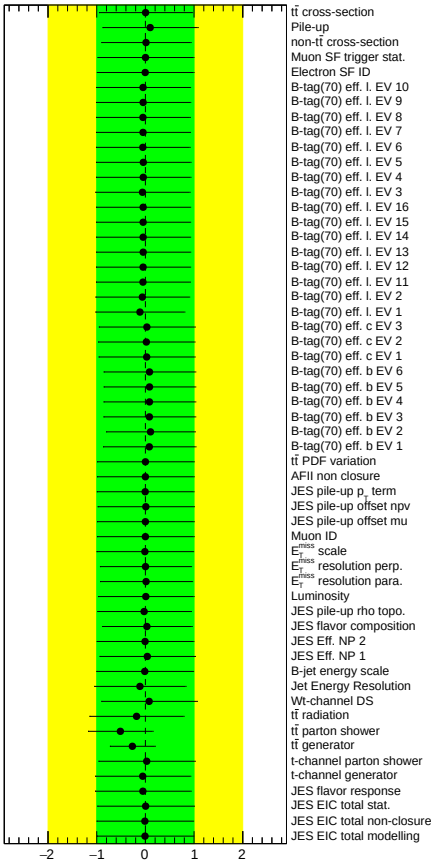

Figure 5.12: Pull plot of the nuisance parameters after a background-only fit of expected backgrounds to data in the signal and control regions.

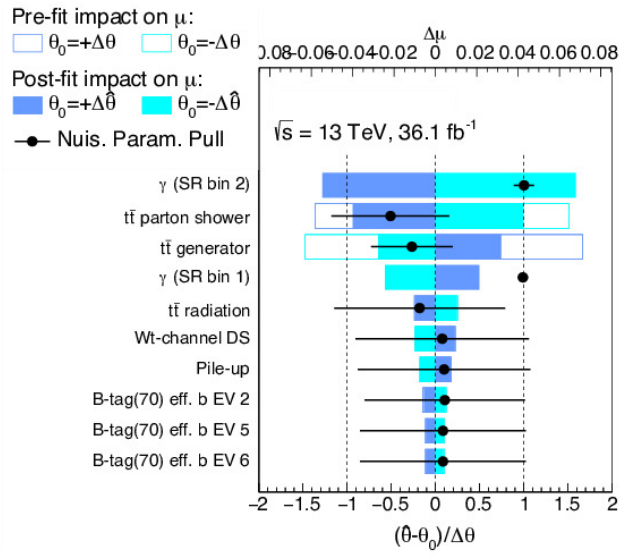

Figure 5.13: Ordered list of the 10 NPs with the highest impact on the signal strength μ.

binned $E_{\mathrm{T}}^{\mathrm{miss}}$ in the 1L-DM-SR, with the electron and muon channels merged and the backgrounds grouped in $t\bar{t}$ and non-$t\bar{t}$ processes. The figures show that no significant excess above the SM is found in the signal region.

	1L-DM-SR	1L-TCR	1L-WCR
$t\bar{t}$	390 ± 140	$12\,300 \pm 3100$	8400 ± 1700
Single top	66 ± 21	2930 ± 760	$12\,200 \pm 1700$
W+jets	34.2 ± 8.4	1890 ± 640	$92\,000 \pm 24\,000$
Z+jets	0.40 ± 0.86	112 ± 49	3410 ± 990
Other	14 ± 15	640 ± 880	$7000 \pm 10\,000$
Total	501 ± 140	$17\,900 \pm 3400$	$123\,000 \pm 26\,000$
Data	511	17662	127286
NR DM $m_V = 1$ TeV	165 ± 23	1.02 ± 0.47	20.2 ± 2.8
NR DM $m_V = 2$ TeV	6.5 ± 2.7	0.027 ± 0.013	0.50 ± 0.097

Table 5.4: Number of events observed in the signal and control regions, together with the estimated SM backgrounds previous to the fit to data. The uncertainties include statistical and systematic uncertainties.

5.6.2 Dark Matter interpretation

In the absence of an evidence for a signal, expected and observed upper limits on the signal cross-section as a function of the mass of the mediator for the non-resonant model are set.This is done by performing the signal-plus-background fit for a variety of signal hypothesis with varying m_V between 0 and 2500 GeV. The excluded cross-section is calculated as

$$\sigma_{95\%\mathrm{CL}}^{\mathrm{obs}} = \mu_{up} \times \sigma_{\mathrm{theory}}, \tag{5.6}$$

where μ_{up} is the upper limit on the signal strength, calculated as described in Section 5.6.1.

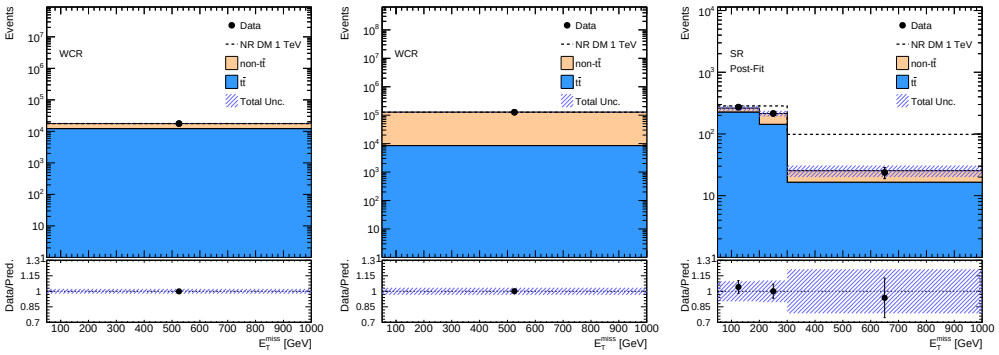

Figure 5.14: Comparison of data and fitted expectations for the event yields in the 1L-TCR (left) and 1L-WCR (center) control regions and the $E_{\mathrm{T}}^{\mathrm{miss}}$ distributions in the signal region. The background only hypothesis is used in the fit. The error bands include statistical and systematic uncertainties. The expected shape for a benchmark signal normalised to the theoretical prediction is added on top of the SM prediction. The benchmark signal corresponds to: the non-resonant (NR) DM model with $m_V = 1$ TeV.

Figure 5.15 shows the expected and observed [2] 95% CL excluded cross-section as a function of the mass of the invisible state for the non-resonant model. The black line corresponds to the maximum cross-section allowed by the observations while the red line depicts the theoretical predictions. Therefore, mediator masses for which maximum observed cross-section is below the theory prediction, are excluded by these observations. The corresponding values are shown in table 5.5. From these results, mediator masses are excluded up to 1450 GeV.

5.6.3 Statistical combination of the lepton+hadron channels

The expected sensitivity of the lepton channel for the non-resonant DM model presented in this thesis is comparable to the expected sensitivity for the same search in the hadron channel. Therefore, the inputs in the signal and control regions used for this model in both channels are combined in a single likelihood to do a combined fit to data.

[2] Expected means fitted to an Asimov dataset built from MC only, while observed refers to the results fitted to the actual data.

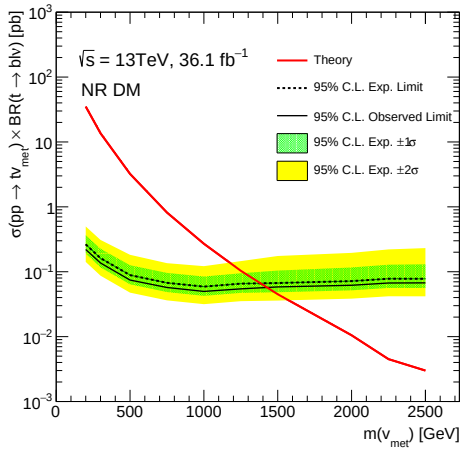

Figure 5.15: Expected 95% CL upper limits on the production cross-section for the non-resonant model in the leptonic channel. The mass of the DM particle is m_χ = 1 GeV while the coupling constant between the massive invisible vector boson and the top quark is a = 0.5 and the coupling constant betwen the mediator and the dark matter particles is g_χ = 1.0.

m_V [GeV]	Theory, $\sigma(pp \to tV)$ $\times BR(t \to tl\nu)$ [pb]	Expected 95%CL limit [pb]	Observed $95\%CL$ limit [pb]
200	23.405	0.265	0.221
300	9.084	0.163	0.137
500	2.147	0.090	0.075
750	0.545	0.070	0.059
1000	0.18	0.062	0.052
1250	0.069	0.068	0.058
1500	0.03	0.071	0.061
2000	0.007	0.073	0.063
2250	0.003	0.078	0.068
2500	0.002	0.078	0.068

Table 5.5: Expected and observed %95 CL upper limits on the production cross-section of the non-resonant model as a function of the mass of the invisible state, compared to LO theoretical predictions for the leptonic channel.

In the hadronic channel, due to large expected Lorentz boost of the top quarks produced in the signal events, the top-quark decay products are collimated into a large-R jet [254]. Preselected events are then required to contain zero leptons and one large-R jet with $p_{\mathrm{T}} > 250$ GeV and $|\eta| < 2.0$. In order to suppress the multijet background contribution $E_{\mathrm{T}}^{\mathrm{miss}} > 200$ GeV is also required. As in the lepton channel, two control regions are defined in addition to the signal region. These two regions are enriched in the two main background processes, namely $t\bar{t}$ and W/Z+jets. Table 5.6 shows a summary of all the regions included in the combined fit: three for the leptonic channel and three for the hadronic channel. The selection of the two channels is orthogonal by definition and therefore there is no statistical overlap in the different regions used in the combined fit.

The most discriminant observable in the hadronic channel, that is used in the fit is the transverse mass of the top-tagged large-R jet (J) and the $E_{\mathrm{T}}^{\mathrm{miss}}$ system, $m_{\mathrm{T}}(E_{\mathrm{T}}^{\mathrm{miss}}, J)$. A comparison of data and expectation in the control regions for the $m_{\mathrm{T}}(E_{\mathrm{T}}^{\mathrm{miss}}, J)$ distribution is shown in Figure 5.16 for the hadronic channel. The expectations are obtained from a fit of the background-only hypothesis to data in the the 0L control regions, where the noramlizations of the $t\bar{t}$ and W/Z+jets processes are treated as nuisance parameters in the fit. The agreement is good within statistical and systematic uncertainties.

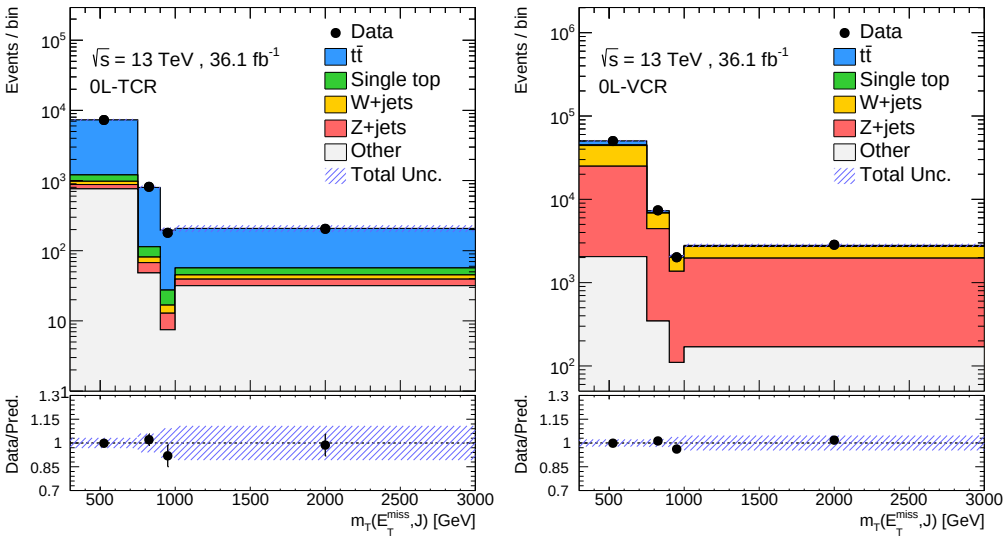

Figure 5.16: Comparison of data and SM prediction for the the transverse mass of the top-tagged large-R jet and the $E_{\mathrm{T}}^{\mathrm{miss}}$ system, $m_{\mathrm{T}}(E_{\mathrm{T}}^{\mathrm{miss}}, J)$, distribution in the $t\bar{t}$ (left) and W/Z+jets (right) control regions used for the dark matter searches. The expectations channel are obtained from a fit of the background-only hypothesis to data in the the 0L control regions, where the normalizations of the $t\bar{t}$ and W/Z+jets processes are treated as nuisance parameters in the fit. The error bands include statistical and systematic uncertainties. The last bin contains the overflow events.

Selections (leptonic channel)	1L-DM-SR	1L-TCR	1L-WCR
number of leptons	= 1	= 1	= 1
$p_{\mathrm{T}}(\ell)$ [GeV]	> 30	> 30	> 30
lepton charge	> 0	> 0	> 0
number of jets	=1	=2	=1
number of b-tagged jets	=1	=2	=1
p_{T}(b-tagged jet)[GeV]	> 30	> 30	> 30
$E_{\mathrm{T}}^{\mathrm{miss}}$[GeV]	> 50	> 50	> 50
$m_{\mathrm{T}}(W) + E_{\mathrm{T}}^{\mathrm{miss}}$ [GeV]	> 60	> 60	> 60
$m_{\mathrm{T}}(W)$ [GeV]	> 260	$60 < m_{\mathrm{T}}(W) < 100$	$60 < m_{\mathrm{T}}(W) < 100$
$\lvert\Delta\phi(\ell, b)\rvert$	< 1.2	-	-

Selections (hadronic channel)	0L-DM-SR	0L-VLT-SR	0L-TCR	0L-VCR
number of forwards jets	= 0	≥ 1	-	-
number of leptons	= 0		= 0	= 0
$E_{\mathrm{T}}^{\mathrm{miss}}$[GeV]	> 200		> 200	> 200
number of large-R jets	≥ 1		≥ 1	≥ 1
number of top-tagged jets	≥ 1		≥ 1	≥ 1
$\Delta\Phi(E_{\mathrm{T}}^{\mathrm{miss}}, J)$	$> \frac{\pi}{2}$		$> \frac{\pi}{2}$	$> \frac{\pi}{2}$
number of track-jets	≥ 1		≥ 1	≥ 1
number of b-tagged track-jets	= 1		≥ 2	= 0
Veto jet (masked tile-calo)	-		applied	-
$\Omega = \frac{E_{\mathrm{T}}^{\mathrm{miss}} - p_T(J)}{E_{\mathrm{T}}^{\mathrm{miss}} + p_T(J)}$	> -0.3		> -0.3	> -0.3
$\Delta\Phi_{\mathrm{min}}(E_{\mathrm{T}}^{\mathrm{miss}}, \mathrm{calo\,jets})$	> 1.0		$0.2 < \Delta\Phi_{\mathrm{min}} < 1.0$	> 1.0

Table 5.6: Overview of the event selections used to define the signal and control regions.

After the combined fit, the breakdown of the effect from the various sources of systematic uncertainties in the background prediction is summarized in Table 5.7. The relative effect on the background yields in the signal region after the simultaneous fit to data is shown. These uncertainties are computed individually for each source of systematic uncertainty as the relative difference between the nominal process integral and the post-fitted symmetrized systematic variation, and give an estimate of the effect of the systematic in the process yield. Individual sources of uncertainties are grouped in categories by adding them in quadrature taking into account the correlations between them.

The distribution of the observable used in the fit ($E_{\mathrm{T}}^{\mathrm{miss}}$ or $m_{\mathrm{T}}(E_{\mathrm{T}}^{\mathrm{miss}}, J)$) in the signal regions for data and the fitted SM expectation under the background only hypothesis is shown in Figure 5.17. In these plots, the expected contribution from

	1L-DM-SR		0L-DM-SR					
	non-$t\bar{t}$	$t\bar{t}$	$t\bar{t}$	Single top	W+jets	Z+jets	Multi-jet	Other
b-tagging	4.8	4.6	4.1	2.9	9.2	7.7	-	8.0
$E_{\mathrm{T}}^{\mathrm{miss}}$	12	1.1	2.2	2.1	2.2	2.2	3.0	2.0
Large-R jets	-	-	9.0	9.5	13	13	-	12
Small R-jets	9.9	7.0	1.3	2.9	1.0	0.5	-	1.0
Lepton	1.2	0.8	< 0.1	< 0.1	< 0.1	< 0.1	-	< 0.1
Luminosity	2.0	2.1	2.1	2.1	2.3	2.2	-	2.1
Pile-up	5.3	1.4	0.3	0.3	0.8	1.2	-	1.4
Background modelling	15	14	8.9	5.3	27	27	111	1.0

Table 5.7: Relative effect (in %) of the systematic uncertainties in the background prediction in the signal regions used for the dark matter search, obtained after the fit to data.

two benchmark signal hypotheses is also shown for comparison. The number of events observed in the signal and control regions is presented in Table 5.8, together with the background estimated in the simultaneous fit to data in the corresponding regions under the background only hypothesis. No significant excess above the SM is found in the signal regions.

In the absence of an evidence for a signal, expected and observed upper limits on the signal cross-section as a function of the mass of the mediator for the non-resonant model are derived at 95% CL and are shown in Figure 5.18.

The LO values for cross-section of the non-resonant DM production are evaluated using MadGraph5_aMC@NLO, as detailed in Section 5.2, assuming $m_\chi = 1$ GeV, $a = 0.5$ and $g_\chi = 1$. The observed (expected) mass limits at 95% CL are 2.0 (1.9) TeV and 3.4 (3.3) TeV.

The observed (expected) 95% CL upper limit contours in different parameter spaces for the signal strength $\sigma/\sigma^{\text{theory}}$ are shown in Figures 5.19 the non-resonant model, in which σ is the observed (expected) limit on the model cross section at a given point of the parameter space and σ_{theory} is the predicted cross section in the model at the same point. The planes showed are the mass of the mediator V vs. a, the mass of the mediator V vs. g_χ and the mass of the mediator V vs mass of the DM candidate χ. Since a reweighing procedure was used to obtain the required

Leptonic channel	1L-DM-SR	1L-TCR	1L-WCR
$t\bar{t}$	385 ± 41	$12\,100 \pm 2000$	8470 ± 800
non-$t\bar{t}$	117 ± 17	5540 ± 960	$119\,000 \pm 26\,000$
Total Background	502 ± 62	$17\,700 \pm 3100$	$127\,000 \pm 26\,000$
Data	511	17662	127286
NR DM $m_V = 1$ TeV	165 ± 23	1.02 ± 0.47	20.2 ± 2.8
NR DM $m_V = 2$ TeV	6.5 ± 2.7	0.027 ± 0.013	0.50 ± 0.097
Hadronic channel	0L-DM-SR	0L-TCR	0L-VCR
$t\bar{t}$	9900 ± 870	7160 ± 620	5900 ± 250
Single top	990 ± 110	273 ± 36	879 ± 98
W+jets	2050 ± 520	119 ± 65	$23\,100 \pm 4900$
Z+jets	2460 ± 460	135 ± 61	$29\,900 \pm 4600$
Multi-jet	87 ± 90	760 ± 350	0 ± 0
Other	328 ± 41	50.1 ± 5.6	2670 ± 310
Total	$15\,800 \pm 1200$	8490 ± 760	$62\,400 \pm 1500$
Data	15781	8493	62304

Table 5.8: Number of events observed in the signal and control regions used for the non-resonant dark matter search, together with the estimated SM backgrounds in the the fit to data, under the background only hypothesis. The uncertainties include statistical and systematic uncertainties. The uncertainties in the individual backgrounds are correlated, and do not necessarily add in quadrature to the total background uncertainty. The expected number of events for benchmark signals corresponding to the non-resonant (NR) DM model with $m_V = 1$ TeV and $m_V = 2$ TeV, assuming in both cases $m_\chi = 1$ GeV, $a = 0.5$ and $g_\chi = 1$, are also shown.

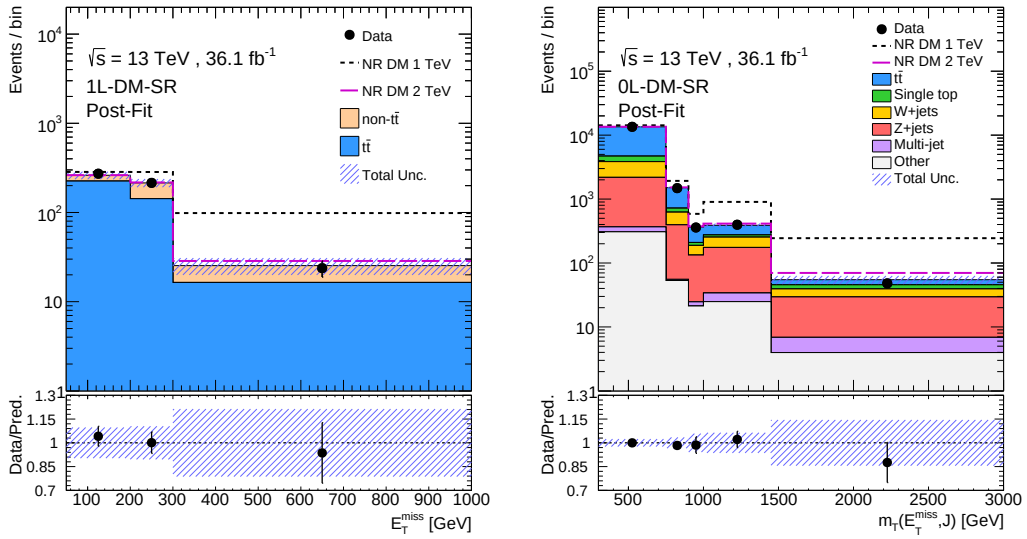

Figure 5.17: Comparison of data and fitted expectations for the $E_{\mathrm{T}}^{\mathrm{miss}}$ and the transverse mass of the top-tagged large-R jet and the $E_{\mathrm{T}}^{\mathrm{miss}}$ system, $m_{\mathrm{T}}(E_{\mathrm{T}}^{\mathrm{miss}}, J)$, distributions in the signal regions. The background only hypothesis is used in the fit including the 1L and 0L DM signal regions as well as the 1L and 0L control regions. The error bands include statistical and systematic uncertainties. The expected shape for a benchmark signal normalized to the theoretical prediction is added on top of the SM prediction. The benchmark signals correspond to the non-resonant DM model with $m_V = 1$ TeV and 2 TeV, $m_\chi = 1$ GeV, $a = 0.5$ and $g_\chi = 1$

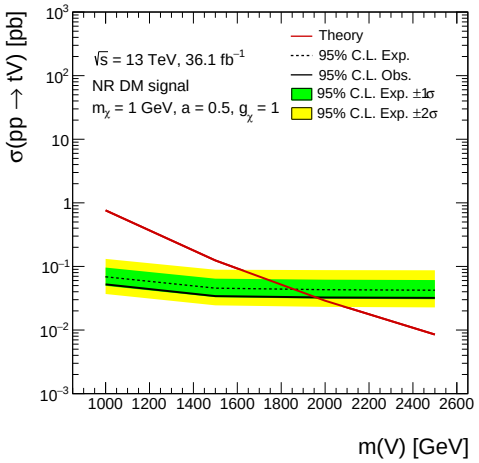

Figure 5.18: 95% CL upper limits on the signal cross-section as a function of the mass of the mediator for the non-resonant (NR) model. LO values for the production cross-section were computed for the non-resonant DM production modes assuming $m_\chi = 1$ GeV, $a = 0.5$ and $g_\chi = 1$.

signal points, the results shown in Figure 5.19 include a systematic uncertainty on the signal normalization associated to this procedure. Such uncertainty is estimated from dedicated MC samples to be 10%, by comparing reweighed samples with those generated with the corresponding signal masses and couplings.

5.7 Conclusions

Mono-top events were searched for in LHC pp data at $\sqrt{s} = 13$ TeV collected by the ATLAS detector in 2015 and 2016 and corresponding to an integrated luminosity of 36.1 fb^{-1}. No evidence for beyond SM (BSM) phenomena was observed and 95% CL upper limits on the production cross-section of the BSM non-resonant DM production in association with single top quarks. These limits were also interpreted in terms of the excluded regions on the parameter space of the considered BSM scenarios.

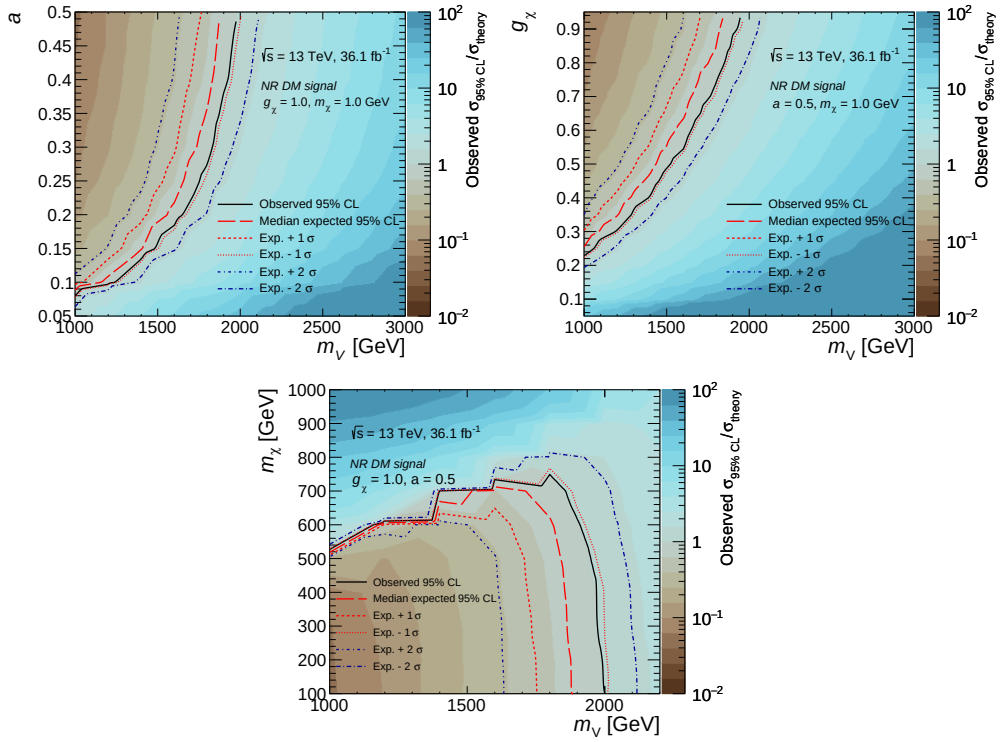

Figure 5.19: Ratios of the observed and expected 95% C.L. upper limits on the signal cross section to the predicted signal cross sections for the non-resonant DM production models: (top-left) mass of the mediator V vs. a; (top-right) mass of the mediator V vs. g_χ and (bottom) mass of the mediator V vs mass of the DM candidate χ. The predicted cross-sections were computed with MadGraph5_aMC@NLO.

6 | Conclusions

The Standard Model of particles physics provides the most accurate description of the subatomic world so far. It has been thorough tested up to the TeV scale giving satisfactory results in a wide variety of phenomena. However, it is believed not to be the final theory since there remain questions the SM fails to explain. A particle widely used in new physics searches is the top quark. One of the properties that makes this quark useful is its large mass, which translates in a very short lifetime. One consequence is that its properties are accesible via its decay products. Moreover, its Yukawa coupling to the Higgs bosson is of the order of one, giving access to information on fundamental interactions at the electroweak symmetry-breaking scale and beyond. The work presented in this thesis is devoted to the search for new physics in the top sector via two different analyses.

The first analyses has been carried out using data from proton-proton interactions at center of mass energy of 8 TeV delivered by the LHC and collected by the ATLAS detector in 2012, corresponding to a total integrated luminosity of 20.2 fb^{-1}. Its main target is the precise study of the Wtb vertex in the decay of single top quarks electroweackly produced in the t-channel, which are predicted to be highly polarized. The Wtb vertex, which is expected to be very sensitive to the presence of new physics, is studied within the framework of an effective field theory. The basic idea of effective field theories relies on considering that physics beyond the SM lies at an energy scale, Λ much higher than 1 TeV and its effects can therefore be parametrized via higher-dimension operators, supressed by inverse powers of the scale Λ. The effective Lagrangian that describes it is

$$\mathcal{L}_{Wtb} = -\frac{g}{\sqrt{2}}\bar{b}\gamma^{\mu}(V_L P_L + V_R P_R)tW^{-}_{\mu} - \frac{g}{\sqrt{2}}\frac{i\sigma^{\mu\nu}}{M_W}q_{\nu}(g_L P_L + g_R P_R)tW^{-}_{\mu} + \text{h.c.}, \tag{6.1}$$

where g is the weak coupling constant, m_W and q_ν are the mass and the four-momentum of the W boson, respectively, $P_{L,R} \equiv (1 \mp \gamma^5)/2$ are the left- and right-handed projection operators, and $\sigma^{\mu\nu} = [\gamma^\mu, \gamma^\nu]/2$. The constants $V_{\rm L,R}$ and $g_{\rm L,R}$ are the left- and right-handed vector and tensor couplings, respectively. In the Standard Model at tree level the coupling V_L is the V_{tb} element of the quark-mixing Cabibbo-Kobayashi-Maskawa (CKM) matrix that is close to one, while the rest of the couplings, referred to as ***anomalous couplings***, V_R and $g_{R,L}$ are all zero. Non-vanishing anomalous couplings would provide hints of physics beyond the Standard Model, and complex values would imply that the top-quark decay has a CP-violating component.

The chosen strategy to study the vertex consists on the measurement of asymmetries in the angular distributions of the decay products of polarized top quarks produced in the t-channel. For polarized top quarks there are two meaningful directions in the top quark rest frame: the momentum $\vec{q}$ of the W and the spin direction of the top quark $\vec{s_t}$, taken along the direction of the momentum of the spectator quark. From these, further directions can be defined normal $\vec{N}$ and transverse $\vec{T}$ to the plane formed by $\vec{q}$ and $\vec{s_t}$. With these definitions, one can measure asymmetries in the distributions of the polar and azimuthal angles formed by the momentum of the charged lepton in the W boson rest frame and the directions $\vec{q}$, $\vec{N}$ and $\vec{T}$. These asymmetries are related to a set of six W boson spin observables which characterize the spin state of the W boson. There is one asymmetry which deserves special attention since it is the most sensitive to a complex phase of the anomalous coupling $\mathrm{Im}\ g_{\rm R}$; the forward-backward asymmetry,$A^N_{\rm FB}$, in the polar angle with respect to the normal direction,$\cos\theta_N$, is used to set limits on this coupling. A cut-based analysis is used to discriminate the signal events from background. The main background contributions to this analysis come from other top-quark processes ($t\bar{t}$ production and top-quarks singly produced in the s-channel and in association with a W boson)

and W+jets production. Other sources of background contamination come from Z+jets, diboson and multijet production. The shape and normalization of the signal and background processes, except multijet events, are estimated from MC simulations. The multijet background is estimated using data-driven techniques instead. The reconstructed angular distributions are distorted by acceptance and detector effects and therefore an unfolding procedure to deconvolve the angular asymmetry to parton level (unfolding) is needed to be able to compare the results with the theoretical predictions. A special emphasis has been devoted to develop an unfolding procedure that does not rely on any assumptions on $\mathrm{Im}\ g_{\mathrm{R}}$ when unfolding the $\cos\theta_N$ distribution.

The final measurements of the asymmetries and the derived spin observables are

$$
\begin{aligned}
A_{\mathrm{FB}} &= -0.26 \pm 0.02(\mathrm{stat.}) \pm 0.07(\mathrm{syst.}) = -0.26 \pm 0.08\,, \\
A_{\mathrm{EC}} &= -0.25 \pm 0.03(\mathrm{stat.}) \pm 0.05(\mathrm{syst.}) = -0.25 \pm 0.06\,, \\
A_{\mathrm{FB}}^{N} &= -0.04 \pm 0.02(\mathrm{stat.}) \pm 0.03(\mathrm{syst.}) = -0.04 \pm 0.04\,, \\
A_{\mathrm{FB}}^{T} &= 0.39 \pm 0.03(\mathrm{stat.}) \pm 0.09(\mathrm{syst.}) = 0.39 \pm 0.09\,, \\
A_{\mathrm{FB}}^{N,\phi} &= -0.03 \pm 0.03(\mathrm{stat.}) \pm 0.05(\mathrm{syst.}) = -0.03 \pm 0.06\,, \\
A_{\mathrm{FB}}^{T,\phi} &= -0.17 \pm 0.05(\mathrm{stat.})^{+0.11}_{-0.10}(\mathrm{syst.}) = -0.17^{+0.12}_{-0.11}\,,
\end{aligned}
$$

and

$$\langle S_3 \rangle = -0.35 \pm 0.03(\text{stat.}) \pm 0.10(\text{syst.}) = -0.35 \pm 0.10\,,$$
$$\langle T_0 \rangle = -0.55 \pm 0.06(\text{stat.}) \pm 0.12(\text{syst.}) = -0.55 \pm 0.13\,,$$
$$\langle S_1 \rangle = 0.52 \pm 0.04(\text{stat.}) \pm 0.12(\text{syst.}) = 0.52 \pm 0.12\,,$$
$$\langle S_2 \rangle = 0.06 \pm 0.03(\text{stat.}) \pm 0.04(\text{syst.}) = 0.06 \pm 0.05\,,$$
$$\langle A_2 \rangle = -0.05 \pm 0.05(\text{stat.}) \pm 0.09(\text{syst.}) = -0.05 \pm 0.10\,,$$
$$\langle A_1 \rangle = 0.27 \pm 0.07(\text{stat.})^{+0.16}_{-0.17}(\text{syst.}) = 0.27^{+0.17}_{-0.19}\,.$$

These results are in good agreement within uncertainties with the SM predictions. The uncertainties of the measurements are dominated by the limited size of the data sample and the modeling of the t-channel and $t\bar{t}$ processes.

The asymmetry A_{FB}^{N}, which has the highest sensitivity to $\text{Im}\ g_{\text{R}}$ is used, together with the asymmetry A_{FB}^{ℓ} from [1], to extract limits on the anomalous coupling $\text{Im}\ g_{\text{R}}$ at 95% CL, assuming that the rest of the coupling have SM values,

$$\text{Im}\ g_{\text{R}} \in [-0.18, 0.06].$$

In addition, the overall compatibility of the measurements with the Standard Model predictions is evaluated through the extraction of a p-value of 81%.

At the time of publishing this result, it improved the previous limit set by the ATLAS Collaboration from the measurement of double-differential angular decay rates at 7 TeV ($\text{Im}\left[\frac{g_{\text{R}}}{V_{\text{L}}}\right] \in [-0.17, 0.23]$). A more recent study of the triple-differential angular decay rates by the ATLAS Collaboration at 8 TeV gives more stringent limits on the ratio $\text{Im}\left[\frac{g_{\text{R}}}{V_{\text{L}}}\right] \in [-0.07, 0.06]$.

With new data from Run-2, these results are expected to improve. From a simple extrapolation of the results presented in this thesis to a center-of-mass energy of 13 TeV and an integrated luminosity of 100 fb^{-1}, the data statistics uncertainty decreases a factor four, while the total systematic uncertainties remain similar.

The second analysis documented in this thesis has been carried out using data from proton-proton interactions at center of mass energy of 13 TeV delivered by the LHC and collected by the ATLAS detector in 2015 and 2016, resulting in a total

integrated luminosity of 36.1 fb^{-1}. It aims at the search for DM production. These kind of searches at the LHC are signature-based. The final state searched for in this thesis is the lepton channel of the non-resonant mono-top production in which a top quark recoils against an unseen vector boson that decays into a pair of dark matter particles. The data analysis is based on a signal region defined by an event selection that maximizes the sensitivity to the non-resonant DM signal production, and control regions, enriched in the dominant background processes ($t\bar{t}$ and W+jets). The statistical interpretation of the results is based on a simultaneous fit to the signal and control regions to determine a possible signal contribution and constrain the main backgrounds from data, taking into account experimental and theoretical systematic uncertainties. The final fit in the signal and control regions does not show any excess of data when compared to the theory predictions. In the absence of evidence of a non-resonant DM signal, these results have been used to set 95% CL upper limits on the corresponding production cross-section. The combination of the results in the leptonic and hadronic channels enhances the sensitivity of the search and leads to observed (expected) mass limits for the mediator vector of 2.0 (1.9) TeV, which substantially extends the previous results at 8 TeV by the ATLAS Collaboration (650 GeV) and is comparable to the CMS result at 13 TeV (1.75 TeV). The obtained limits are also translated into constraints on the parameter space of the non-resonant model.

At the time of writing this thesis, expected studies in preparation for the new HL-LHC Run at 14 TeV have started. Exciting results are to come with higher energy and statistics and with the improvement of the calibration and reconstruction methods.

Indeed, the high precision of the two analyses presented in this thesis, as well as of all the physics analyses carried out by the ATLAS Collaboration, rely on an excellent understanding of the detector which assist to a proper calibration of the detectors, good reconstruction algorithms and minimization of the systematic uncertainties. This thesis work also includes contributions to the alignment of Inner Detector done during the LS1, to ensure the quality of the data collected in Run-2. During this period, cosmic-rays data were used to study the alignment of the new installed pixel IBL layer. In addition, the alignment process was implemented in

the calibration loop and a web display was created to monitor the output from the alignment.

Resum en valencià

El Model Estàndard (SM) de física de partícules és el marc teòric que millor descriu el món subatòmic. Des de la seua formulació final en la dècada de 1970 fins ara s'ha provat en nombrosos experiments. Això no obstant, encara hi ha fenòmens per als quals el SM no té una explicació satisfactòria. En aquesta tesi es presenten dues anàlisis sensibles a la presència de nova física que utilitzen dades enregistrades amb el detector ATLAS (A Toroidal LHC ApparatuS) [116] de l'accelerador LHC (Large Hadron Collider) [114, 115]. Les dues anàlisis utilitzen esdeveniments[1] relacionats amb el quark cim [2], la partícula fonamental més massiva observada experimentalment.

La primera anàlisi utilitza dades enregistrades al 2012 durant el primer període de funcionament del LHC, anomenat Run-1. La segona anàlisi que es mostra empra les dades de la primera part del Run-2, preses als anys 2015 i 2016. En el temps que l'accelerador va estar parat entre ambdós períodes es van realitzar una sèrie de tasques de manteniment i millora. Part del treball presentat a aquesta tesi consisteix en la posada a punt del procés d'alineament del detector intern d'ATLAS en preparació per al Run-2, fonamental per garantir la qualitat de les dades utilitzades a les anàlisis de física.

[1] S'anomena esdeveniment al resultat d'una col·lisió.

[2] La paraula anglesa, utilitzada d'ara endavant en el present resum és *top*.

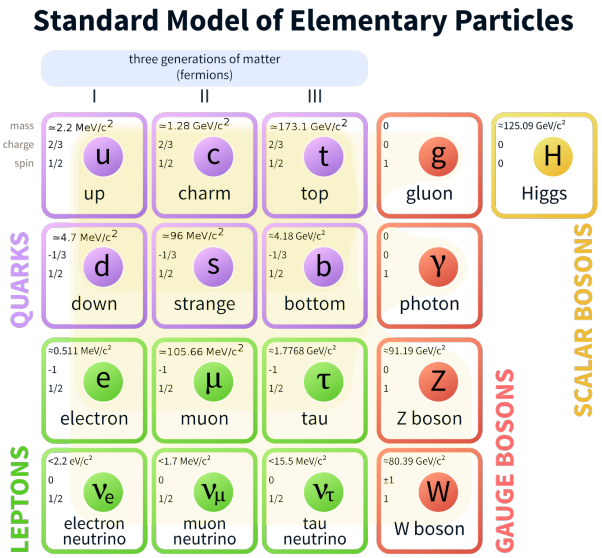

Figure R.1: Resum del contigut de partícules de Model Estàndard de física de partícules.

R.1 Marc teòric

R.1.1 El Model Estàndard de física de partícules

El Model Estàndard de física de partícules és una teoria quàntica de camps que descriu les interaccions entre els components fonamentals de la matèria, anomenats fermions, mitjançant l'intercanvi de partícules portadores de força, anomenades bosons. La Figura R.1 mostra un resum del contingut de partícules descrites pel SM.

Les quatre forces fonamentals són la interacció electromagnètica, descrita per l'electrodinàmica quàntica (QED); la interacció forta, descrita per la cromodinàmica quàntica (QCD), la interacció feble i la interacció gravitatòria (no inclosa en el SM). Dins del marc del SM, totes les forces fonamentals deriven d'un principi general, el qual requereix que el Lagrangià siga invariant sota una transformació de constrast (*gauge*) local basada en el grup de simetria $SU(3)_C \times$

$SU(2)_L \times U(1)_Y$, on el terme $SU(2)_L \times U(1)_Y$ fa referència a la unificació de les interaccions feble i electromagnètica en una teoria electrofeble (EW) [6–8] i el terme $SU(3)_C$ descriu la interacció forta.

Les partícules portadores de càrrega són partícules amb espín 1 que obeeixen l'estadística de Bose-Einstein. Hi ha quatre tipus de bosons associats a cadascuna de les forces descrites pel SM. El fotó (γ) és l'intermediari de les interaccions entre partícules carregades (QED). La força feble està mediada per bosons carregats $W^{\pm}$ i pel boson neutre Z. Finalment, vuit bosons, anomenats gluons (g), intervenen en la interacció forta.

D'altra banda, els fermions són partícules amb espín 1/2 descrites per l'estadística de Fermi-Dirac. Hi ha dos tipus de fermions: quarks i leptons. A més a més, estan subdividits en tres famílies o generacions, on l'única diferència entre les partícules d'una generació i una altra és la seua massa. Les partícules més lleugeres i estables pertanyen a la primera família i són les que conformen tota la matèria estable de l'univers.

Cada generació de leptons està formada per una partícula carregada (electró, muó i tau) i un neutrí neutre i sense massa. Les partícules carregades poden interaccionar per mitjà de les interaccions electromagnètica i feble, mentre que els neutrins només interactuen feblement. En el cas dels quarks, cada família conté un quark carregat positivament ($+\frac{2}{3}$) i un quark carregat negativament ($-\frac{1}{3}$). A més, els quarks tenen una altra càrrega, color, que pot prendre tres valors: roig, verd o blau (rgb). Els quarks poden interaccionar amb qualsevol de les tres forces descrites pel SM. Una característica dels quarks és que no s'observen com a estats lliures a la natura (confinament), sinó que s'agrupen en hadrons formats per una parella quark-antiquark (mesó) o per tres quarks (barió). Com a conseqüència del confinament, quan se separen els quarks en una col·lisió s'augmenta la seua energia potencial fins el punt que es genera una parella quark-antiquark. Aquesta parella es lliga amb el quark original en un procés que es repeteix successivament donant lloc a una cascada d'hadrons que es propaga en la direcció del quark original, i que s'anomena comunament doll [3].

[3] La paraula anglesa, utilitzada d'ara endavant en el present resum és *jet*.

El SM tal i com està descrit pels lagrangians de EW i QCD només pot contenir partícules sense massa. La presència de partícules massives és possible gràcies a un procés de trencament espontani de simetria (SSB) anomenat mecanisme de Higgs [12–14], en el qual el grup de simetria $SU(2)_L \times U(1)_Y$ es descompon en $U(1)_{EM}$. Aquest mecanisme introdueix un nou camp escalar que, quan se situa en un mínim, dóna lloc al trencament de la simetria, donant masses als bosons $W^{\pm}$ i Z i originant un nou camp que correspon al bosó de Higgs, H. La interacció dels fermions amb el bosó de Higgs és l'origen de la seua massa. Un dels majors èxits del SM fou el descobriment del bosó de Higgs al LHC en 2012 [4, 5].

Malgrat la gran quantitat d'evidència experimental que prova la validesa del Model Estàndard, encara hi queden molts interrogants que fan pensar que ha d'haver-hi una teoria més general, de la qual el SM és només una aproximació. Entre d'altres, està el problema de la descripció de la interacció gravitatòria com una teoria quàntica de camps; l'observació d'oscil·lacions de neutrins, que indiquen que aquestes partícules tenen massa; la gran asimetria entre matèria i antimatèria, per a la qual la violació de CP predita pel SM és insuficient; o entendre la natura de la matèria i energia fosques, que constitueixen prop del 25% i 68% del contingut energètic de l'univers, respectivament, i per a les quals encara no hi ha una explicació satisfactòria.

R.1.2 La física del quark top

El quark top forma part de la tercera generació de fermions. Es va predir la seua existència el 1973 [11] però, no va ser fins el 1995 que es va observar per primera vegada a l'accelerador Tevatron [16, 17]. La importància d'aquest quark ve donada per la seua gran massa, que es tradueix en una vida mitjana molt curta, de manera que el quark top es desintegra en un bosó W i un quark b abans que tinga temps d'hadronitzar formant partícules estables. L'alta massa del quark *top* es deu al gran acoblament d'aquest amb el bosó de Higgs, de manera que entendre la física subjacent és fonamental per entendre el mecanisme del Higgs. A més a més, molts models de física més enllà del SM prediuen l'existència de noves partícules que s'acoblen preferentment al quark *top*. És per tant essencial mesurar

amb la màxima precissió possible les propietats i interaccions del quark *top*, així com realitzar cerques directes de nova física en la producció o desintegració del quark *top*.

A les col·lisions hadró-hadró com les que tenen lloc al LHC, el quark *top* es produeix sobretot en parelles mitjançant la interacció forta. No obstant això, també es pot produir de manera única mitjançant la interacció electrofeble amb l'intercanvi d'un bosó W virtual en els canals t i s, i associat a un bosó W real.

El 99.8% de les voltes, el quark *top* es desintegra en un bosó W i un quark b. Atenent a la posterior desintegració del bosó W, es pot classificar la desintegració del *top* en hadrònica (si el W es desintegra en dos quarks) i en leptònica (si el W es desintegra en un leptó i el seu corresponent neutrí).

R.2 Dispositiu experimental

Per tal de produir el quark *top* necessari per als estudis que s'han proposat a la secció anterior, és necessària una gran quantitat d'energia. Aquest tipus de procés es dóna als col·lisionadors de partícules, en els quals dos feixos de partícules s'acceleren a altes velocitats i es fan xocar en punts específics on s'enregistra el resultat de la col·lisió. Avui en dia, l'accelerador de partícules més potent del món és el LHC del CERN (Conseil Européen pour la Recherche Nucléaire, en francés), en el qual es fan col·lisionar dos feixos de protons. El LHC es va dissenyar per fer mesures de precisió de les prediccions del SM així com per a cercar nova física.

R.2.1 El Gran Col·lisionador d'Hadrons

El LHC és l'accelerador de partícules més potent de món. Es tracta d'un anell de 27 km situat a la frontera franco-suïssa, al laboratori CERN [113], en el qual s'acceleren dos feixos de protons. Durant el Run-1 es van accelerar els feixos fins a una energia en el centre de masses de 8 TeV. Durant el Run-2 s'ha quasi duplicat l'energia dels feixos, arribant a 13 TeV. Al llarg de l'anell hi ha quatre punts d'interacció en els quals s'han col·locat quatre detectors. ATLAS i CMS (Compact Muon Solenoid) [117] són detectors de propòsit general, dissenyats per

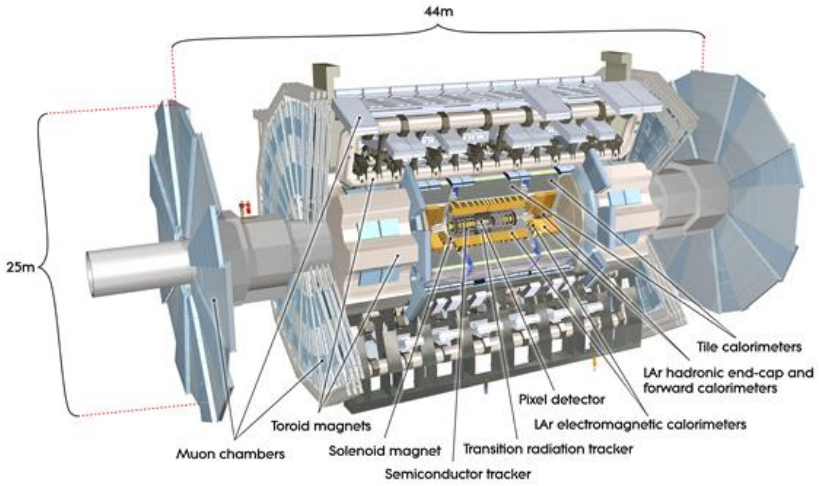

Figure R.2: Vista esquemàtica del detector ATLAS.

a mesurar el bosó de Higgs i cercar nova física, així com per a fer mesures de precisió de les prediccions del SM. Els altres dos experiments són ALICE i LHCb.

R.2.2 El detector ATLAS

El funcionament del detector ATLAS és possible gràcies a l'esforç de col·laboració de 3000 autors científics procedents de 37 estats. Té una forma cilíndrica i els seus distints components, dissenyats per a mesurar propietats específiques de les partícules emergents de les col·lisions, estan ordenats en capes. La Figura R.2 mostra un tall transversal del detector, que té unes dimensions de 44 m de llarg i 25 m de diàmetre. Els principals components del detector ATLAS són:

- **Detector intern**: El sistema més pròxim al punt de col·lisió està dissenyat per mesurar amb molta precisió la trajectòria de les partícules carregades, reconstruir els vèrtexs primaris i secundaris i mesurar el moment de les partícules. Està format per tres subdetectors, dos basats en silici i un en tubs de deriva. Aquest detector es troba immers en un camp magnètic de 2T

creat per un solenoide que corba la trajectòria de les partícules carregades. Entre el Run-1 i el Run-2 es va introduir una nova capa de detector de píxel més pròxima al punt d'interacció, anomenada IBL.

- **Calorímetres**: Envoltant el detector intern es troben dos calorímetres; l'electromagnètic, en el qual es mesura l'energia dels electrons i fotons, i l'hadrònic, en el qual es mesura l'energia dels *jets* i l'energia transversa mancant. El calorímetre electromagnètic utilitza argó líquid com a mitjà ionitzant i té una geometria en forma d'acordió, mentre que el el calorímetre hadrònic utilitza una tecnologia de teula d'escintil·lació.

- **Cambra de muons**: el detector més extern d'ATLAS està dissenyat per a identificar i reconstruir les trajectòries dels muons. Les cambres de muons, immerses en un intens camp magnètic toroïdal, utilitzen quatre tipus de tecnologia diferents, optimitzades per a identificar els esdeveniments més interessants.

- **Sistema de disparador (trigger)**: donats els recursos limitats de computació i emmagatzematge, no tots els esdeveniments produïts es poden guardar. El sistema de disparador és l'encarregat de decidir quins esdeveniments es guarden i quins no, de manera que d'uns 20 (40) milions d'esdeveniments per segon, només en queden prop de 400 (1000) al Run-1 (Run-2).

R.2.3 Reconstrucció d'objectes

La informació proporcionada pels diferents components del detector s'ha de combinar per a transformar els senyals en els detectors en objectes físics reconstruïts (electrons, muons, taus, *jets*, energia transversa faltant i *jets* procedents del quarks b).

- **Electrons**: els electrons es reconstrueixen combinant un dipòsit d'energia en el calorímetre electromagnètic amb una traça al detector intern. Als candidats a electrons reconstruïts d'aquesta manera se'ls aplica una sèrie de talls optimitzats per a identificar electrons provinents de la desintegració del W.

- **Muons**: els muons es reconstrueixen combinant segments de traces reconstruïdes al detector intern i a la cambra de muons i se'ls aplica un criteri similar a l'aplicat als electrons per a assegurar la qualitat dels muons reconstruïts.

- ***jets***: els *jets* es reconstrueixen a partir d'agregats topològics en el calorímetre utilitzant l'algoritme "anti-k_t". Als candidats a *jet* se'ls aplica una sèrie de correccions per tal de reduir els efectes d'apilament, soroll electrònic o la variació del moment segons la regió del detector, entre d'altres.

- b-***jets***: els *jets* originats per quarks de tipus b s'identifiquen mitjançant diferents algoritmes que exploten les propietats d'aquestes partícules, com són el paràmetre d'impacte, la presència de vèrtexs secundaris o la topologia de la desintegració dels quarks b i c.

- **Energia transversa mancant**: a causa de la conservació de moment en el pla transvers al feix, la suma vectorial del moment transvers de tots els productes d'una col·lisió ha de ser zero. Un desequilibri en aquesta quantitat s'anomena moment transversa mancant $E_{\mathrm{T}}^{\mathrm{miss}}$ i indica la presència de partícules que només interaccione feblement. En el marc del Model Estàndard, la $E_{\mathrm{T}}^{\mathrm{miss}}$ es considera una mesura dels neutrins.

R.3 Alineament del detector intern d'ATLAS

Després de la instal·lació i muntantge del detector és possible que la posició dels seus mòduls es conega amb menys precisió que la seua resolució intrínseca. A més a més, canvis en les condicions de funcionament poden variar la seua posició relativa. La finalitat de l'alineament és determinar les posicions dels mòduls del detector intern respecte a la geometria ideal del detector.

El mètode d'alineament utilitza les trajectòries reconstruïdes de les partícules carregades que creuen el detector intern. Els ingredient principals de l'algoritme són:

- **Sistema de referència global** en el qual es determina la posició de cada mòdul del detector.
- **Sistema de referència local** en el qual es reconstrueix el punt d'impacte en cada mòdul.
- **6 paràmetres d'alineament** corresponents a les tres translacions i tres rotacions que determinen els sis graus de llibertat d'un sòlid rígid i que caracteritzen la posició i orientació del mòdul o estructura alineada.
- **Residus** o distància entre el senyal a un mòdul i el punt de la trajectòria reconstruïda a aquest.

La Figura R.3 mostra un esquema simplificat del procés d'alineament, basat en la minimització dels residus. A l'esquerra es presenta la posició real dels mòduls, on el mòdul central està desalineat, i la trajectòria real d'una partícula. Utilitzant aquesta informació, la traça es reconstrueix tal i com representa la fletxa discontínua al centre. Per determinar la geometria real del detector, s'aplica un procés iteratiu de minimització de tots els residus de la partícula. El panel dret mostra la trajectòria reconstruïda amb la geometria actualitzada.

R.3.1 Posada en marxa de l'alineament en preparació per al Run-2

Entre el Run-1 i el Run-2 es van realitzar una sèrie de millores en el detector intern: el detector de píxel es va extraure i renovar i es va afegir una nova capa més pròxima al punt d'interacció (IBL). En preparació per al Run-2 es va realitzar un primer alineament utilitzant dades de raigs còsmics, provinents de l'atmosfera terrestre. La Figura R.4 (esquerra) mostra les distribucions dels residus en el IBL en la direcció x' abans i després de l'alineament.

R.3.1.1 Distorsió de l'IBL i alineament en temps real

Durant la campanya de raigs còsmics es va observar que les dogues de l'IBL es guerxen amb els canvis de temperatura. Açò és pels diferents coeficients de dilatació dels materials que componen l'IBL. Utilitzant dades preses a diferents

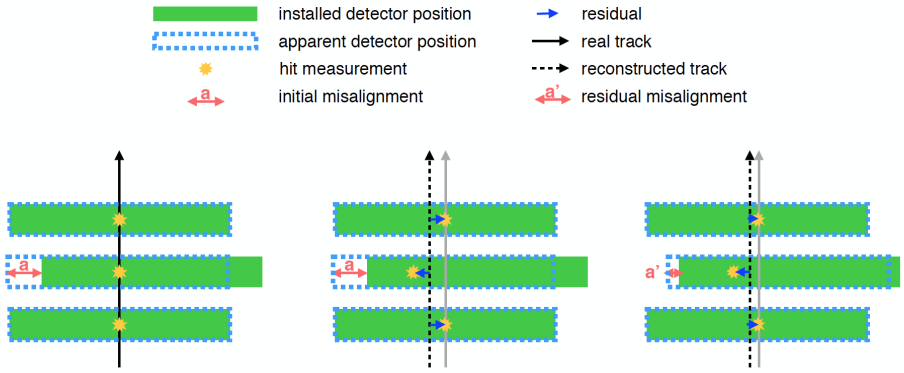

Figure R.3: Esquema del procediment d'alineament.

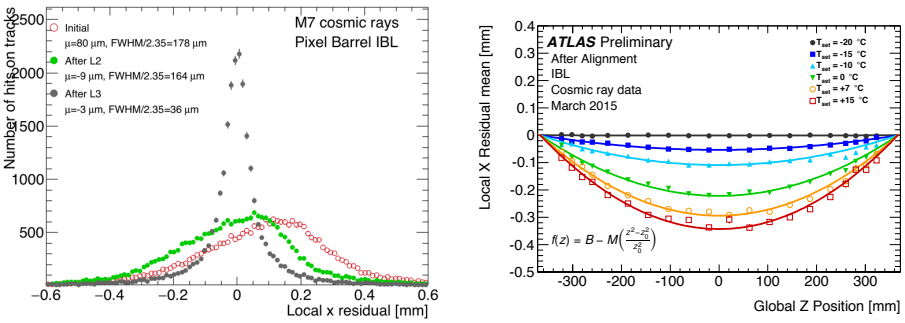

Figure R.4: Esquerra: distribució dels residus de l'IBL en la direcció x' abans i després de l'alineament. Dreta: Deformació de les dogues de l'IBL en funció de la temperatura.

temperatures s'ha trobat que la deformació es pot descriure amb una paràbola on el paràmetre lliure de l'ajust, M, quantifica la grandària de la distorsió (Figura R.4). Durant la campanya de raigs còsmics reflectida en aquesta tesi, es va mesurar que la variació en la temperatura de les dogues de l'IBL era menor que 0.2 K, donant lloc a deformacions negligibles. Durant les primeres col·lisions es va observar que l'efecte era major i es va incloure una rutina de correcció en el cicle de calibratge.

Amb la finalitat de corregir qualsevol moviment o deformació al més ràpid possible, s'ha implementat un alineament en el cicle de calibratge que s'aplica a cada sèrie de dades de manera automatitzada. Per estudiar els resultats s'ha creat una aplicació web que carrega els resultats proporcionats pel cicle de calibratge i crea gràfiques a demanda de l'usuari.

Aquesta tesis reflecteix el treball realitzat en alineament utilitzant raigs còsmics durant 2015. Des d'aleshores, el cicle de calibratge s'ha actualitzat i la configuració és diferent ara. Entre d'altres, s'han canviat els nivells d'alineament per a incloure una correcció de la deformación del IBL.

R.4 Estudi del vèrtex Wtb

El procés principal de producció de quarks *top* de forma individual a les col·lisions protó-protó és el canal t, tal i com es mostra a la Figura R.5. En aquest procés, la interacció d'un quark lleuger amb un quark b mitjançant l'intercanvi d'un bosó W virtual dóna lloc a un quark *top* i un quark lleuger al qual anomenem quark espectador. El quark *top* produït d'aquesta manera té un grau de polarització molt gran al llarg de la direcció del quark espectador. A més, a causa a la seua vida mitjana tan curta, la informació sobre el seu espín es trasllada a les distribucions angulars dels productes de la seua desintegració. Com es veu a la Figura R.5, el vèrtex Wtb apareix tant a la producció com a la desintegració del quark *top*, de manera que es pot estudiar tant mesurant observables relacionats amb la polarització del quark *top* com amb observables relacionats amb l'espín del bosó W. Si hi ha física més enllà del model estàndard responsable del trencament espontani de la simetria, és molt possible que aparega en aquest vèrtex. El lagrangià que el descriu es pot parametritzar dins d'una teoria efectiva com [37, 42]

$$\mathcal{L}_{Wtb} = -\frac{g}{\sqrt{2}}\bar{b}\gamma^{\mu}(V_L P_L + V_R P_R)tW^{-}_{\mu} - \frac{g}{\sqrt{2}}\frac{i\sigma^{\mu\nu}}{M_W}q_{\nu}(g_L P_L + g_R P_R)tW^{-}_{\mu} + \text{h.c.}, \quad \text{(R.1)}$$

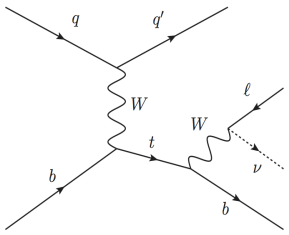

Figure R.5: Diagrama de Feynman a primer ordre de la producció de quarks *top* únics al canal t en col·lisions protó-protó. S'hi mostra també la desintegració leptònica del quark *top* ($t \to Wb$ amb $W \to \ell\nu$).

on g és la constant d'acoblament feble, m_W i q_ν són les masses i quadrimoment del bosó W, $P_{L,R} \equiv (1 \mp \gamma^5)/2$ són els operadors de projecció levogir i dextrogir i $\sigma^{\mu\nu} = [\gamma^\mu, \gamma^\nu]/2$. Dins del SM, l'acoblament V_L és aproximadament la unitat, mentre la resta dels acoblaments, V_R i $g_{R,L}$, també anomenats acoblaments anòmals, són zero. L'observació de valors dels acoblaments anòmals distints de zero podria proporcionar indicis de física més enllà del Model Estàndard. En particular, valors complexos implicarien que la desintegració del quark *top* té una component que viola la simetria CP.

L'espín del bosó W es pot parametritzar en termes del valor esperat de sis observables [32] que determinen per complet la distribució angular dels productes de la desintegració del bosó W. Una manera senzilla de mesurar els valors dels observables esmentats és projectar la descripció completa de la desintegració del W en diferents direccions que permeten obtenir distribucions en només una dimensió amb menys paràmetres. La Figura R.6 mostra les direccions triades en aquesta anàlisi.

D'aquesta manera, els observables relacionats amb l'espín del W es poden relacionar amb asimetries angulars definides respecte a les distribucions dels angles polars i azimutals del moment del leptó carregat provinent de la desintegració del W respecte a cadascuna de les direccions utilitzades (l'eix $\hat{z}$ i les direccions normal i transversal). En l'anàlisi presentada en aquesta tesi s'utilitzen dos tipus d'asimetries angulars, la asimetria avant-arrere (*forward-backward* en anglès) i l'asimetria vora-centre (*edge-central* en anglès)

$$A_{\mathrm{FB}} = \frac{N(\cos\theta > 0) - N(\cos\theta < 0)}{N(\cos\theta > 0) + N(\cos\theta < 0)}, \tag{R.2}$$

$$A_{\mathrm{EC}} = \frac{N(|\cos\theta| > \frac{1}{2}) - N(|\cos\theta| < \frac{1}{2})}{N(|\cos\theta| > \frac{1}{2}) + N(|\cos\theta| < \frac{1}{2})}. \tag{R.3}$$

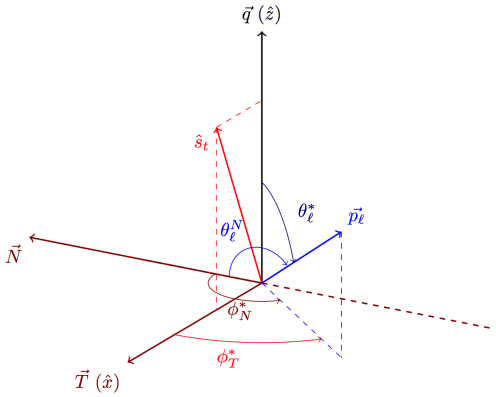

Figure R.6: Sistema de coordenades utilitzat per a definir els observables de l'espín del bosó W. L'eix $\hat{z}$ està definit pel moment lineal del bosó W en el sistema de referència del quark *top* en repós; la direcció de l'espín del quark *top* $\hat{s}_t$, definida al llarg del moment del quark espectador en el sistema de referència del quark *top* en repós, es troba dins del pla $\hat{x} - \hat{z}$. L'eix normal es defineix com la direcció ortogonal al pla definit per l'eix $\hat{z}$ i la direcció de l'espín del quark *top*, mentre que l'eix transvers es defineix com la direcció ortogonal al pla format per la direcció normal i l'eix $\hat{z}$.

A la Taula R.1 es resumeixen les distribucions angulars considerades en l'anàlisi, les asimetries respecte a aquestes, les relacions entre les asimetries i els observables de l'espín del W i els valors predits pel SM. Els valors de les asimetries depenen dels valors dels acoblaments anòmals, essent A_{FB}^{N} i $A_{\mathrm{FB}}^{N,\phi}$ els observables més sensibles a fases complexes de l'acoblament g_{R}.

Aquestes asimetries s'han mesurat amb dades proporcionades pel detector ATLAS durant l'any 2012 a una energia en centre de masses de 8 TeV corresponent a una luminositat integrada de 20.2 fb^{-1}.

Distribució angular	Observables d'espín		Asimetries			
	Observable	Pred. SM	Observable			Pred. SM
$\cos\theta^*_\ell$	$< S_3 >$	-0.30	A_{FB}	=	$\frac{3}{4}\langle S_3\rangle$	-0.23
$\cos\theta^*_\ell$	$< T_0 >$	-0.45	A_{EC}	=	$\frac{3}{8}\sqrt{\frac{3}{2}}\langle T_0\rangle$	-0.20
$\cos\theta^T_\ell$	$< S_1 >$	0.46	$A^T_{\rm FB}$	=	$\frac{3}{4}\langle S_1\rangle$	0.34
$\cos\theta^N_\ell$	$< S_2 >$	0.00	$A^N_{\rm FB}$	=	$-\frac{3}{4}\langle S_2\rangle$	0.00
$\cos\theta^*_\ell\cos\phi^*_T$	$< A_1 >$	0.23	$A^{T,\phi}_{\rm FB}$	=	$-\frac{2}{\pi}\langle A_1\rangle$	-0.14
$\cos\theta^*_\ell\cos\phi^*_N$	$< A_2 >$	0.00	$A^{N,\phi}_{\rm FB}$	=	$-\frac{2}{\pi}\langle A_1\rangle$	0.00

Table R.1: Resum de les asimetries angulars i els observables d'espín del W relacionats amb elles. Es donen també els valors predits pel SM.

R.4.1 Selecció d'esdeveniments

El primer pas de l'anàlisi consisteix a seleccionar els esdeveniments que s'utilitzaran per a mesurar els observables. Aquesta selecció es fa en dues etapes. En primer lloc, se seleccionen aquells esdeveniments que tenen el mateix estat final que la producció de quarks *top* en el canal t amb desintegració leptònica: un *jet* lleuger, un *b-jet*, un leptó carregat (electró o muó) i energia transversa mancant major de 30 GeV corresponent al neutrí. Hi ha diferents processos en el SM que tenen un estat final similar i que per tant poden passar aquests criteris i ser seleccionats com a senyal. Aquest tipus de processos s'anomenen fons i s'estudien mitjançant simulacions de Monte Carlo o dades reals. Els principals fons són:

- Altres processos de producció de quarks *top* (parelles i quarks *top* únics en el canal s i associats a un bosó W)
- Producció de bosons W o Z en associació amb *jets* lleugers o pesats
- Producció de processos dibosònics (WW, ZZ o ZW)
- Esdeveniments amb multijets generats en interaccions de QCD en els quals un dels *jets* es reconstrueix de manera errònia com un leptó

Per a minimitzar la presència de fons de multijets, s'apliquen dos talls addicionals:

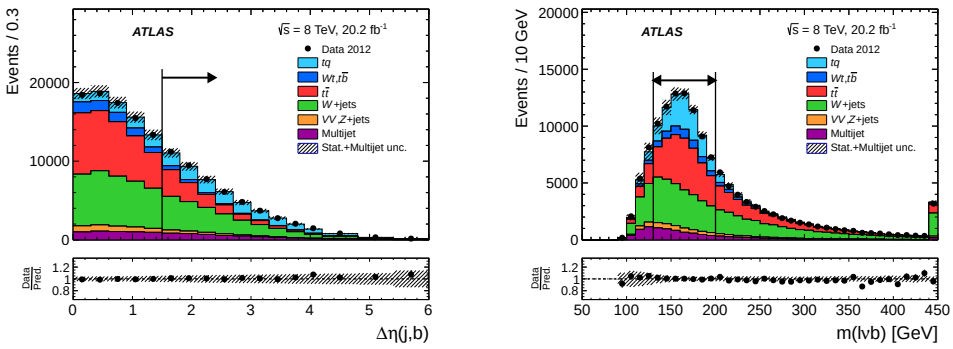

Figure R.7: Comparació entre les dades i les simulacions per a dues variables en la regió de preselecció.

- $m_{\mathrm{T}}(W) = \sqrt{2p_{\mathrm{T}}(\ell)E_{\mathrm{T}}^{\mathrm{miss}}(1-\cos\Delta\phi(\ell, E_{\mathrm{T}}^{\mathrm{miss}}))} > 50GeV$
- $\frac{p_{\mathrm{T}}(\ell)}{1-\frac{\pi-|\Delta\phi(\ell,\mathrm{j})|}{\pi-1}} > 40\,\mathrm{GeV}$, on $p_{\mathrm{T}}(\ell)$ és el moment transvers del leptó i $\Delta\phi(\ell,\mathrm{j})$ és la diferència en angle azimutal entre el moment del leptó i el del *jet* lleuger.

Els esdeveniments que passen aquests criteris de selecció defineixen la regió de preselecció. La Figura R.7 mostra les distribucions de la diferència en pseudorapidesa entre els dos *jets* en el canal d'electrons i la massa del *top* quark reconstruït en el canal de muons per a tots els esdeveniments que han passat els talls de preselecció. Es pot veure que hi ha un bon acord entre les dades mesurades i la predicció de Monte Carlo. En aquest nivell, les distribucions estan dominades pels fons, mentre que el senyal només representa un 15% de la contribució total.

Els angles definits en la Figura R.6 es defineixen a partir del moment del bosó W i del quark *top*, per això és necessari reconstruir el quadrimoment d'aquests. El quadrimoment del W es reconstrueix a partir del quadrimoment de les partícules en les quals es desintegra, és a dir, el leptó carregat i l'energia transversa mancant associada al neutrí. Una vegada reconstruït el W, s'utilitza per a reconstruir el quark *top* juntament amb el *b-jet*.

El segon pas de la selecció consisteix a aplicar talls a algunes variables seleccionades pel seu poder discriminant front als fons. Els talls aplicats i que defineixen la regió de senyal són els següents:

- La pseudo-rapidesa del *jet* lleuger ha de satisfer $|\eta| > 2$
- La diferència entre la pseudorapidesa d'ambdós *jets* ha de ser major que 1.5.
- La massa del quark *top* reconstruït ha d'estar entre 130 GeV i 200 GeV.
- La suma del moment transvers de tots els objectes seleccionats, H_{T}, ha de ser major de 195 GeV.

R.4.2 Estimació de fons

Per estimar-ne la contribució dels dos fons més importants i assegurar-ne una bona descripció es defineixen tres regions en les quals la presència dels fons és més important que la del senyal. Aplicant els talls de selecció amb dos *jets* addicionals s'aconsegueix una regió dominada per parelles de quarks *top*. Imposant una identificació de *b-jets* més relaxada sobre els esdeveniments que passen la preselecció s'obté una regió amb molta presència de W+*jets*. Finalment, la selecció d'esdeveniments que passen els talls de preselecció però no els de selecció (antiselecció) dóna lloc a una regió amb igual contribució de parelles de quarks *top* i de processos de W+*jets* però amb poca senyal. Per a estimar la normalització dels processos de senyal, W+*jets* i parelles de quarks *top* es fa un ajust de màxima versemblança a les regions de senyal, de parelles de *top* i de anti-selecció. La Figura R.8 mostra les distribucions de dues variables a les regions de parelles de *top* i de W+*jets* regions. Es pot veure que hi ha un bon acord entre les dades i les prediccions.

R.4.3 Mesura dels observables d'espín

La Figura R.9 mostra les distribucions angulars en la regió de senyal a partir de les quals s'obtenen les asimetries angulars. Aquestes distribucions estan distorsionades per limitacions experimentals com la resolució del detector i la seua acceptància espacial i els talls de selecció. Per tant, abans d'extraure els valors de les asimetries, les distribucions angulars s'han de corregir per l'efecte d'aquestes distorsions mitjançant un procediment anomenat desdoblament.

El mètode nominal de desdoblament emprat en aquesta anàlisi utilitza la informació d'una mostra simulada de canal t generada amb els acoblaments que

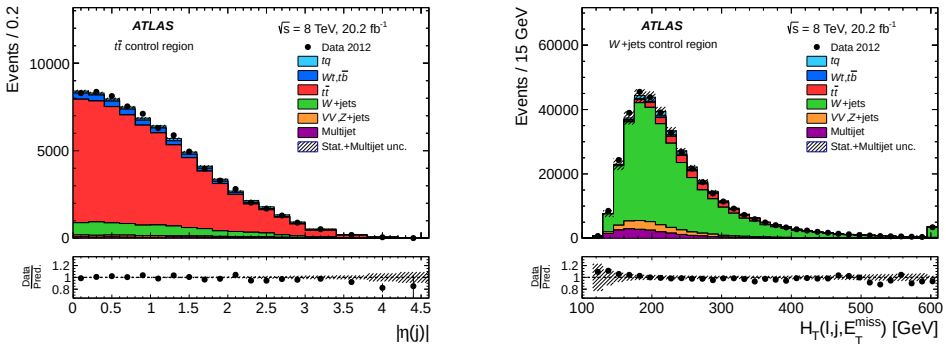

Figure R.8: Comparació entre les dades i les simulacions per a dues variables en les regions de parelles de *top* i W+jets.

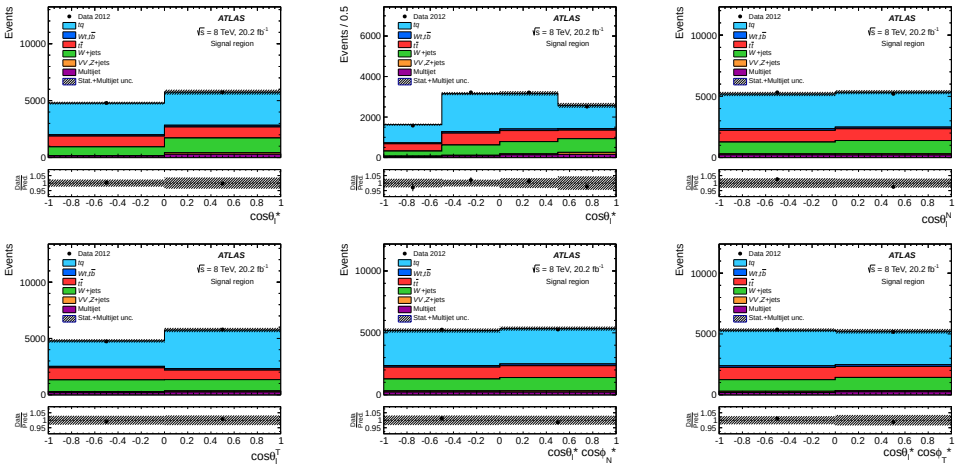

Figure R.9: Distribucions angulars en la regió de senyal per al canal d'electrons usades per a mesurar les asimetries (de dreta a esquerra i de dalt a baix): A_{FB}, A_{EC}, A_{FB}^{N}, A_{FB}^{T}, $A_{\mathrm{FB}}^{N,\phi}$ i $A_{\mathrm{FB}}^{T,\phi}$.

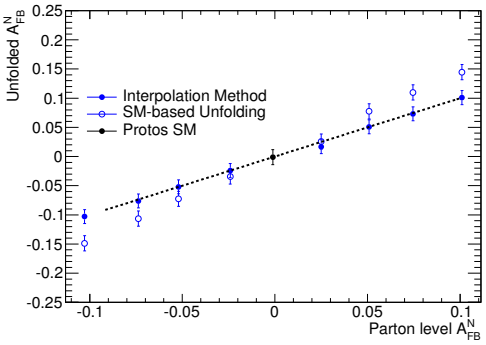

Figure R.10: Valor corregit de A_{FB}^N en funció del valor a nivell de partons. Es comparen el mètode nominal de desdoblament (punts oberts) amb el mètode d'interpolació (punts complets).

prediu el SM i que conté les distribucions angulars a nivell de partons i a nivell de reconstrucció. Una manera de validar el mètode consisteix a aplicar-lo en mostres simulades amb acoblaments anòmals i comparar el resultat amb la asimetria mesurada directament a nivell de partons. El resultat d'aquest test per a la asimetria A_{FB}^N es pot veure als punts oberts de la Figura R.10. Atès que aquesta asimetria és la més sensible a fases complexes de l'acoblament $\mathrm{Im}\ g_{\mathrm{R}}$, s'ha desenvolupat una variació del mètode nominal per a corregir les no-linealitats que s'observen en aquesta figura. El mètode consisteix a utilitzar la informació de cinc mostres simulades amb valors distints de $\mathrm{Im}\ g_{\mathrm{R}}$. La informació de cada mostra té un pes distint en la correcció total depenent de com a prop estiga de la mostra un valor inicial calculat amb el mètode nominal. Aquest mètode s'ha aplicat a mostres de les quals no s'ha utilitzat cap informació addicional i, com es veu als punts complets de la Figura R.10, permet recuperar la linealitat. Aquest mètode permet així proporcionar una mesura sense cap assumpció en el valor de $\mathrm{Im}\ g_{\mathrm{R}}$.

R.4.4 Incerteses sistemàtiques i estadístiques

A banda de la incertesa estadística de les dades, les distribucions angulars també es veuen afectades per efectes instrumentals (per exemple, el calibratge dels objectes) i teòrics (per exemple el càlcul de les seccions eficaces dels processos) que

poden alterar la seua forma i per tant, les asimetries mesurades. La quantificació de l'impacte d'aquests efectes, anomenats sistemàtics, és una part fonamental de l'anàlisi. L'error dominant prové de la quantitat limitada de dades. Altres contribucions importants estan relacionades amb el modelatge dels processos de canal t i de parelles de *top*.

R.4.5 Resultat final

Els valors mesurats de les asimetries són

$$
\begin{aligned}
A_{\mathrm{FB}} &= -0.26 \pm 0.02(\mathrm{stat.}) \pm 0.07(\mathrm{syst.}) = -0.26 \pm 0.08\,, \\
A_{\mathrm{EC}} &= -0.25 \pm 0.03(\mathrm{stat.}) \pm 0.05(\mathrm{syst.}) = -0.25 \pm 0.06\,, \\
A_{\mathrm{FB}}^{N} &= -0.04 \pm 0.02(\mathrm{stat.}) \pm 0.03(\mathrm{syst.}) = -0.04 \pm 0.04\,, \\
A_{\mathrm{FB}}^{T} &= 0.39 \pm 0.03(\mathrm{stat.}) \pm 0.09(\mathrm{syst.}) = 0.39 \pm 0.09\,, \\
A_{\mathrm{FB}}^{N,\phi} &= -0.03 \pm 0.03(\mathrm{stat.}) \pm 0.05(\mathrm{syst.}) = -0.03 \pm 0.06\,, \\
A_{\mathrm{FB}}^{T,\phi} &= -0.17 \pm 0.05(\mathrm{stat.})^{+0.11}_{-0.10}(\mathrm{syst.}) = -0.17^{+0.12}_{-0.11}\,.
\end{aligned}
$$

Aquests valors estan en bon acord amb les prediccions del Model Estàndard (veure la Figura R.11) amb un p-value del 81 %.

La asimetria A_{FB}^{N} és la més sensible a $\mathrm{Im}\ g_{\mathrm{R}}$ i es pot utilitzar per establir els següents límits en aquest acoblament

$$\mathrm{Im}\ g_{\mathrm{R}} \in [-0.18, 0.06].$$

R.5 Cerca de matèria fosca en estats finals amb un sol quark *top* i moment transvers mancant

A la primera meitat del segle XX es va observar per primera vegada inconsistències en la suposició que tot l'univers està format per matèria visible ordinària. Es va proposar com a solució l'existència d'un nou tipus de matèria, la

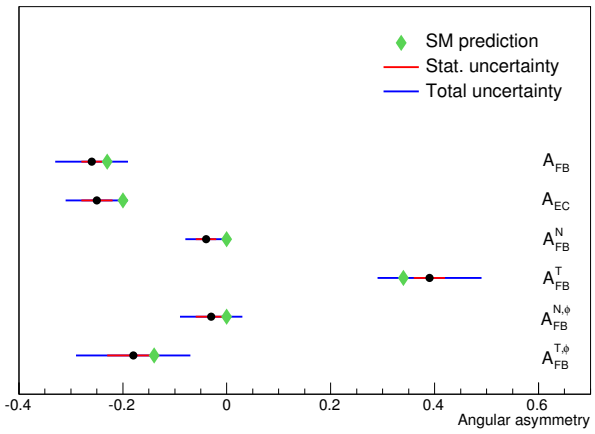

Figure R.11: Resum de les asimetries mesurades en comparació amb les prediccions del SM.

matèria fosca (DM), que només podria interaccionar mitjançant les interaccions gravitatòria i feble.

Des d'aleshores, són moltes les evidències que s'han trobat de la presència de matèria fosca que ompli l'univers. D'una banda, la seua presència s'infereix de l'observació de les corbes rotacionals de les galàxies. Mentre que, d'acord amb la dinàmica de Newton, aquesta corba hauria de decréixer amb el radi, el que s'observa és que la velocitat es manté constant a llargues distàncies, la qual cosa és compatible amb la presència de matèria no visible envoltant la galàxia. Altres fonts d'evidència de l'existència de DM provenen d'observacions de lents gravitacionals o del fons còsmic de microones.

Atès que encara no s'ha detectat directament, en l'actualitat hi ha una ampla varietat de candidats a matèria fosca, tots els quals han de complir una sèrie de condicions. Els candidats a DM han de ser no relativístics en el moment de la formació de galàxies, estables en escales temporals cosmològiques i no han d'interactuar amb la radiació electromagnètica. Alguns dels candidats són forats negres primordials, axions, neutrins estèrils o partícules massives que només interactuen feblement (WIMPs).

Per poder conèixer la natura d'aquest tipus de matèria, a banda d'inferir la seua presència gràcies a la seua interacció gravitatòria amb altres partícules, és necessari dissenyar experiments que proven la seua interacció no-gravitatòria. Als col·lisionadors de partícules es poden produir partícules de DM que no s'espera que interaccionen amb el detector. Tanmateix, la seua presència es pot deduir si hi ha un desequilibri en l'energia final observada. L'estratègia de cerca de DM al LHC doncs, es basa a buscar DM produïda amb radiació addicional provinent dels quarks o gluons inicials que participen en la reacció. El resultat final d'aquest procés és una gran quantitat d'energia transversa mancant (que correspon a la partícula de DM no detectada) i un objecte energètic que pot ser un *jet*, un fotó o un bosó.

L'anàlisi descrita en aquesta tesi presenta la cerca de DM produïda en associació amb un quark *top*, anomenada *mono-top*. El model simplificat que abasta aquest tipus de procés es pot llegir en les referències [104–106]. El mecanisme de producció estudiat en aquesta tesi és la producció no-ressonant que es mostra a la Figura R.12. Aquest mecanisme és diferent a la resta de cerques de DM ja que el quark *top* no prové de la radiació inicial sinó que es produeix associat a un estat vectorial V que pot decaure en una parella de partícules de DM χ. El Lagrangià que descriu la dinàmica d'aquest procés és

$$\mathcal{L}_{int} = [aV_\mu \bar{u}\gamma^\mu P_R t + g_\chi V_\mu \bar{\chi}\gamma^\mu \chi + h.c.]\,, \tag{R.4}$$

on un bosó vectorial massiu V s'acobla a una partícula de fermiònica de DM χ amb un acoblament g_χ. El paràmetre a representa la constant d'acoblament entre vector V i el quark *top*.

Els estats finals de la producció del *mono-top* es classifiquen d'acord a la desintegració del bosó W que prové del quark *top*. L'anàlisi presentada en aquesta tesi se centra en el canal leptònic, en el qual el bosó W es desintegra en un leptó carregat i un neutrí.

La cerca d'esdeveniments de mono-top s'ha realitzat amb dades amb una energia de centre de masses de 13 TeV, recollides als anys 2015 i 2016 corresponents a una lluminositat integrada de $36.1\ \mathrm{fb}^{-1}$.

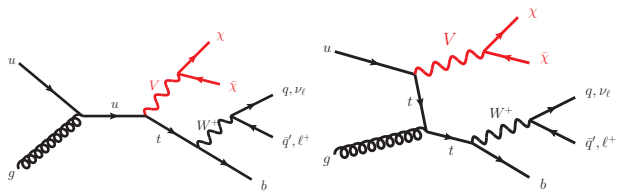

Figure R.12: Producció de *mono-top* en el context d'un model de producció no ressonant de matèria fosca: diagrames de Feynman a primer ordre en els canals s (esquerra) i t (dreta).

R.5.1 Selecció d'esdeveniments

L'estat final dels esdeveniments de *mono-top* es caracteritza per la presència d'un quark top que es desintegra en un quark b i un bosó W i alta energia transversa mancant, $E_{\mathrm{T}}^{\mathrm{miss}}$. En un primer pas, se seleccionen els esdeveniments que tenen aquest mateix estat final, és a dir, un *jet* identificat com provinent d'un quark b, un leptó carregat positivament procedent de la desintegració del W (donada l'estructura del protó, el 90 % del temps es produiran quarks *top* enlloc d'antiquarks *top*) i alta $E_{\mathrm{T}}^{\mathrm{miss}} > 50$ GeV. També s'aplica un tall inferior a la suma de $E_{\mathrm{T}}^{\mathrm{miss}} + m_{\mathrm{T}}(W)$ per a reduir la presència d'esdeveniments de multijets. Els esdeveniments que acompleixen aquests criteris defineixen la regió de preselecció.

La Figura R.13 mostra les distribucions a nivell de preselecció de les dues variables més discriminants. Per comparació del fons amb el senyal, els talls que defineixen la regió de senyal són:

- $m_{\mathrm{T}}(W) > 260$ GeV
- $|\Delta\phi(\ell, b)| < 1.2$

R.5.2 Estimació de fons

El fons dominant en la regió de senyal és la producció de parelles de quarks *top*. La producció de W+jets també té una contribució important. Per estimar la contribució d'aquests dos fons es defineixen dues regions de control anomenades

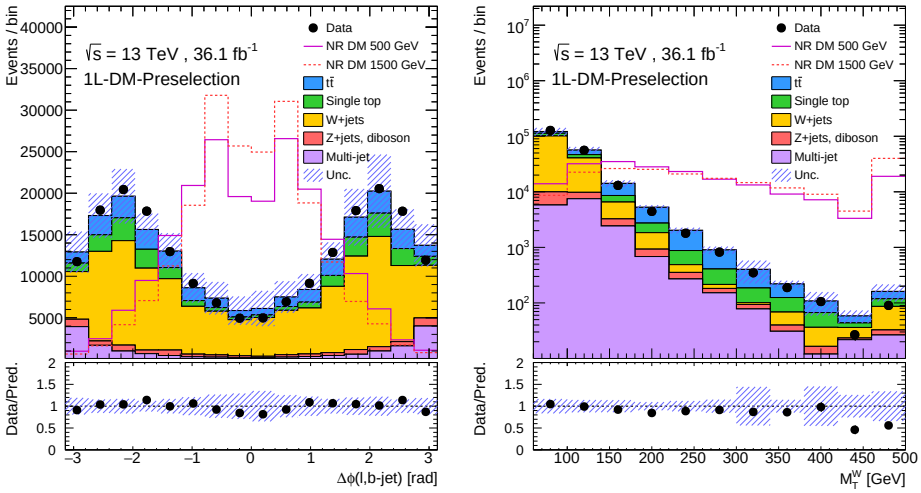

Figure R.13: Distribució de les variables $|\Delta\phi(\ell, b)|$ and $m_{\mathrm{T}}(W)$ en la regió de preselecció. Es mostren també per a tres models de senyal de *mono-top*.

TCR i WCR. Ambdues es defineixen canviant el tall de selecció a $m_{\mathrm{T}}(W)$< 100 GeV i en el cas de la regió de TCR, demanant un *jet* addicional.

Abans d'estudiar les dades en la regió de senyal, s'ajusta la contribució dels fons en les regions de control. El resultat d'aquest ajust es pot veure a la Figura R.14, on s'observa que hi ha un bon ajust entre les dades observades i les prediccions.

R.5.3 Incerteses sistemàtiques

Encara que aquesta anàlisi està limitada fonamentalment per la baixa estadística a la regió de senyal, també s'han tingut en compte les limitacions instrumentals i teòriques que poden afectar la normalització i la forma de les distribucions. L'efecte de cada font d'incertesa s'inclou com un paràmetre de soroll en l'ajust final. L'error dominant, a banda de l'estadístic, és el modelatge dels processos del canal t i de parelles de *top*.

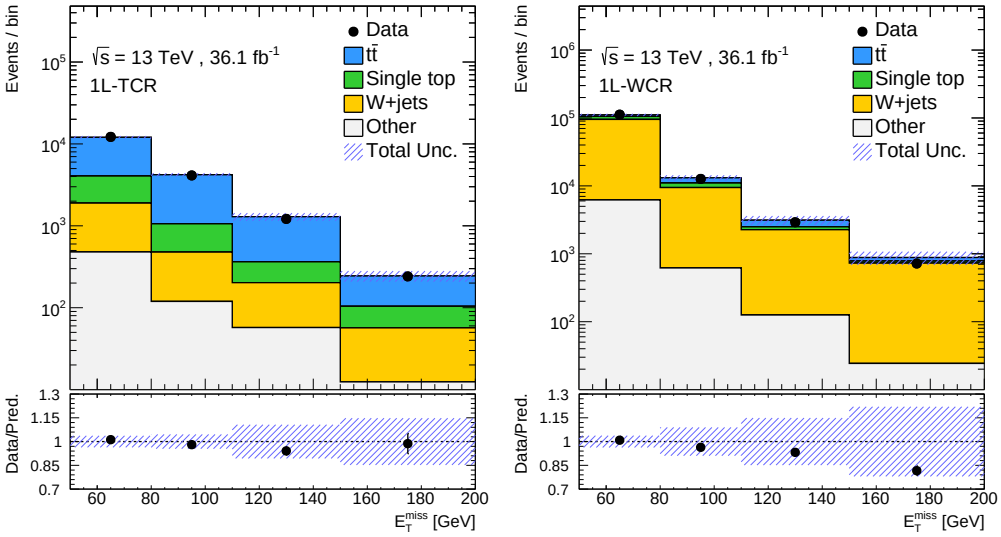

Figure R.14: Comparació entre les dades i les simulacions per a la variable $E_{\mathrm{T}}^{\mathrm{miss}}$ en les dues regions de control després de l'ajust de la contribució dels fons.

R.5.4 Resultats i interpretació

Per tal d'estimar la possible presència de senyal de *mono-top* es fa un ajust de màxima versemblança de la distribució de $E_{\mathrm{T}}^{\mathrm{miss}}$ a les regions de control i de senyal sota la hipòtesi de presència única de fons. El resultat de l'ajust per a un model representatiu es mostra a la Figura R.15, on es veu que les dades són compatibles amb una hipòtesi de només fons.

Atès que no s'ha observat un excés en les dades, els resultats s'han utilitzat per establir un límit inferior en la massa del vector V. Per millorar la sensibilitat de l'anàlisi, els resultats del canal leptònic s'han combinat amb els resultat del canal hadrònic. El límit inferior que s'ha observat és de 2 GeV, com es veu a la Figura R.16.

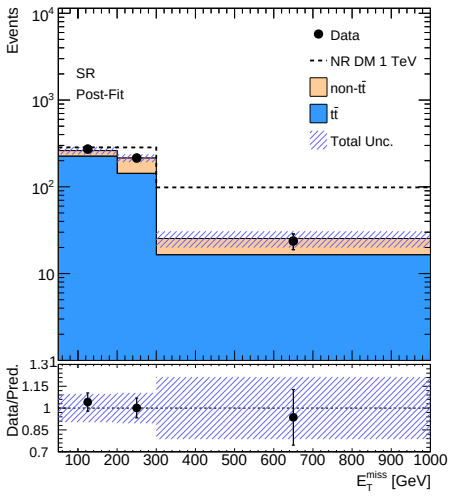

Figure R.15: Resultat de l'ajust de màxima versemblança a la regió de senyal.

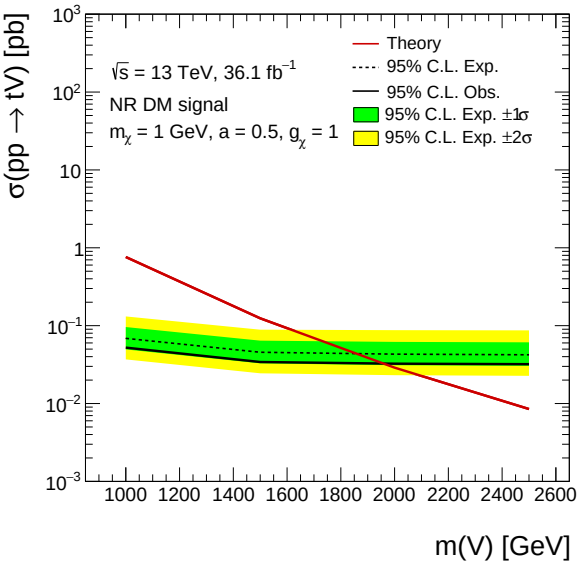

Figure R.16: Límits al nivell de confiança de 95% en la secció eficaç per a diferents punts de massa del model no-resonant de producció de *mono-top*.

R.6 Conclusions

Aquesta tesi doctoral s'ha desenvolupat en el marc del projecte del LHC i presenta una sèrie de resultats obtingut amb el detector ATLAS.

La producció de quarks *top* polaritzats presenta una oportunitat única per estudiar el vèrtex Wtb, molt sensible a la presència de nova física més enllà del Model Estàndard. Una part fonamental del treball d'aquesta tesi ha sigut l'estudi d'aquest vèrtex mitjançant la mesura d'asimetries en les distribucions angulars dels productes de la desintegració del bosó W procedent del quark *top*. L'anàlisi s'ha realitzat amb dades del Run-1 del LHC recollides l'any 2012, amb una energia en centre de masses de 8 TeV. El resultat de la mesura, documentat a [1], s'ha utilitzat per establir límits a l'acoblament anòmal $\mathrm{Im}\ g_{\mathrm{R}}$, que van donar lloc als límits més precisos al moment de la publicació.

Entre el primer i el segon període de funcionament del LHC va haver una parada tècnica durant la qual es van renovar alguns detectors, de manera que va ser necessari actualitzar els procediments de calibratge i reconstrucció dels senyals. Una contribució d'aquest treball en la posada a punt del detector fou l'alineament del detector intern, fonamental per garantir la qualitat de les mesures de precisió [2, 3].

Finalment, amb les dades de la primera part del Run-2 a una energia de 13 TeV, recollides al 2015 i 2016, s'ha cercat nova física en forma de producció de *mono-tops*. La presència d'aquest tipus d'esdeveniments es pot interpretar en el context de models genèrics de matèria fosca. Els resultats obtinguts amb la precisió actual no mostren indicis de l'existència de *mono-tops* i s'han utilitzat per a posar límits a les seccions eficaces de producció d'aquestes senyals, excloent masses de bosó V inferiors a 2 GeV.

Appendix

A Simulated samples

A.1 Simulated samples at $\sqrt{s} = 8$TeV

Table A.1 gives the list of nominal MC samples of the signal and background processes used in the analysis. Table A.2 gives the list of t-channel MC samples implementing different configurations of anomalous couplings. Tables show the cross-section, σ (which includes the leptonic W boson branching ration) and the k-factor which indicates the ration over NLO to LO calculations.

A.2 Simulated samples at $\sqrt{s} = 13$TeV

The list of MC samples, cross-sections and k-factors used in the analysis can be found in Tables A.3 and A.4.

Process	Generator	σ[pb]	k-factor
t-channel (ℓ+jets, t)	POWHEG+PYTHIA P2011C	17.5	1.05
t-channel (ℓ+jets, $\bar{t}$)	POWHEG+PYTHIA P2011C	9.4	1.06
s-channel (ℓ+jets)	POWHEG+PYTHIA P2011C	1.64	1.11
Wt (incl.), DR scheme	POWHEG+PYTHIA P2011C	20.5	1.09
$t\bar{t}$ (no all had.), h_{damp}=m_t	POWHEG+PYTHIA P2011C	114	1.20
$W \to e\nu$ b-filtered	SHERPA	140	1.10
$W \to e\nu$ c-filtered	SHERPA	538	1.10
$W \to e\nu$	SHERPA	10295	1.10
$W \to \mu\nu$ b-filtered	SHERPA	140	1.10
$W \to \mu\nu$ c-filtered	SHERPA	466	1.10
$W \to \mu\nu$	SHERPA	10368	1.10
$W \to \tau\nu$ b-filtered	SHERPA	140	1.10
$W \to \tau\nu$ c-filtered	SHERPA	506	1.10
$W \to \tau\nu$	SHERPA	10327	1.10
$Z \to e^+e^-$ b-filtered	SHERPA	31.0	1.12
$Z \to e^+e^-$ c-filtered	SHERPA	314	1.12
$Z \to e^+e-$	SHERPA	764	1.12
$Z \to \mu^+\mu^-$ b-filtered	SHERPA	31.0	1.12
$Z \to \mu^+\mu^-$ c-filtered	SHERPA	314	1.12
$Z \to \mu^+\mu^-$	SHERPA	764	1.12
$Z \to \tau^+\tau^-$ b-filtered	SHERPA	31.0	1.12
$Z \to \tau^+\tau^-$ c-filtered	SHERPA	314	1.12
$Z \to \tau^+\tau^-$	SHERPA	765	1.12
$WW \to e\nu qq$	SHERPA	7.3	1.06
$WW \to \mu\nu qq$	SHERPA	7.3	1.06
$WW \to \tau\nu qq$	SHERPA	7.3	1.06
$ZZ \to e^+e^-qq$	SHERPA	0.24	1.00
$ZZ \to \mu^+\mu^-qq$	SHERPA	0.24	1.00
$WZ \to e\nu qq$	SHERPA	1.91	1.05
$WZ \to \mu\nu qq$	SHERPA	1.91	1.05
$WZ \to \tau\nu qq$	SHERPA	1.91	1.05
$ZW \to e^+e^-qq$	SHERPA	1.46	1.05
$ZW \to \mu^+\mu^-qq$	SHERPA	1.46	1.05

Table A.1: Baseline signal and background Monte Carlo samples used in the analysis. The cross-section column includes the branching ratio of the W boson leptonic decay channel but not the k-factor.

Process	Couplings $\mathrm{Re}\,V_\mathrm{L}$, $\mathrm{Im}\,g_\mathrm{R}$, $\mathrm{Re}\,g_\mathrm{R}$, $\mathrm{Re}\,V_\mathrm{R}$	Generator	σ [pb]	k-factor
t-channel (ℓ+jets)	1.0, 0.0, 0.0, 0.0	PROTOS+PYTHIA P2011C	28.4	1.00
t-channel (ℓ+jets)	0.958, 0.23, 0.0, 0.0	PROTOS+PYTHIA P2011C	28.4	1.00
t-channel (ℓ+jets)	0.958, -0.23, 0.0, 0.0	PROTOS+PYTHIA P2011C	28.4	1.00
t-channel (ℓ+jets)	0.993, 0.094, 0.0, 0.0	PROTOS+PYTHIA P2011C	28.4	1.00
t-channel (ℓ+jets)	0.993, -0.094, 0.0, 0.0	PROTOS+PYTHIA P2011C	28.4	1.00
t-channel (ℓ+jets)	0.982, 0.144, 0.0, 0.0	PROTOS+PYTHIA P2011C	28.4	1.00
t-channel (ℓ+jets)	0.992, 0.043, 0.0, 0.0	PROTOS+PYTHIA P2011C	28.4	1.00
t-channel (ℓ+jets)	0.982, -0.144, 0.0, 0.0	PROTOS+PYTHIA P2011C	28.4	1.00
t-channel (ℓ+jets)	0.992, -0.043, 0.0, 0.0	PROTOS+PYTHIA P2011C	28.4	1.00

Table A.2: Signal Monte Carlo samples generated with PROTOS used in the analysis. The implemented values of the Wtb couplings are given. The cross-section column includes the branching ratio of the W boson leptonic decay channel but not the k-factor.

Dataset ID	Sample Type	Sample	Generator	x-sec	k-factor	p-tag	SimType	Events
364158	W+b jets	Wmunu + jets	Sherpa	844.198	0.970	p2952	FS	17226200
364161	W+b jets	Wmunu + jets	Sherpa	71.459	0.970	p2952	FS	19639000
364164	W+b jets	Wmunu + jets	Sherpa	36.915	0.970	p2952	FS	9826000
364167	W+b jets	Wmunu + jets	Sherpa	9.609	0.970	p2952	FS	2959500
364172	W+b jets	Wenu + jets	Sherpa	844.638	0.970	p2952	FS	17242400
364175	W+b jets	Wenu + jets	Sherpa	97.738	0.970	p2952	FS	9801900
364178	W+b jets	Wenu + jets	Sherpa	36.997	0.970	p2952	FS	9880900
364181	W+b jets	Wenu + jets	Sherpa	9.657	0.970	p2952	FS	2958000
364186	W+b jets	Wtaunu + jets	Sherpa	854.555	0.970	p2952	FS	17273200
364189	W+b jets	Wtaunu + jets	Sherpa	98.018	0.970	p2952	FS	9857000
364192	W+b jets	Wtaunu + jets	Sherpa	40.062	0.970	p2952	FS	9834000
364195	W+b jets	Wtaunu + jets	Sherpa	9.670	0.970	p2952	FS	2954100
364157	W+c jets	Wmunu + jets	Sherpa	2493.378	0.970	p2952	FS	9847000
364160	W+c jets	Wmunu + jets	Sherpa	219.966	0.970	p2952	FS	9853800
364163	W+c jets	Wmunu + jets	Sherpa	98.437	0.970	p2952	FS	7408000
364166	W+c jets	Wmunu + jets	Sherpa	22.918	0.970	p2952	FS	2958000
364171	W+c jets	Wenu + jets	Sherpa	2492.639	0.970	p2952	FS	9853500
364174	W+c jets	Wenu + jets	Sherpa	215.490	0.970	p2952	FS	9818400
364177	W+c jets	Wenu + jets	Sherpa	98.443	0.970	p2952	FS	7410000
364180	W+c jets	Wenu + jets	Sherpa	22.847	0.970	p2952	FS	2963400
364185	W+c jets	Wtaunu + jets	Sherpa	2477.249	0.970	p2952	FS	9865600
364188	W+c jets	Wtaunu + jets	Sherpa	210.382	0.970	p2952	FS	9860000
364191	W+c jets	Wtaunu + jets	Sherpa	98.578	0.970	p2952	FS	7365000
364194	W+c jets	Wtaunu + jets	Sherpa	22.779	0.970	p2952	FS	2956400
364156	W+light jets	Wmunu + jets	Sherpa	15770.003	0.970	p2952	FS	24723000
364159	W+light jets	Wmunu + jets	Sherpa	637.424	0.970	p2952	FS	14788000
364162	W+light jets	Wmunu + jets	Sherpa	212.555	0.970	p2952	FS	9882000
364165	W+light jets	Wmunu + jets	Sherpa	39.382	0.970	p2952	FS	4940000
364168	W+light jets	Wmunu + jets	Sherpa	15.010	0.970	p2952	FS	5910500
364169	W+light jets	Wmunu + jets	Sherpa	1.234	0.970	p2952	FS	3959000
364170	W+light jets	Wenu + jets	Sherpa	15769.638	0.970	p2952	FS	24740000
364173	W+light jets	Wenu + jets	Sherpa	630.322	0.970	p2952	FS	14660500
364176	W+light jets	Wenu + jets	Sherpa	202.836	0.970	p2952	FS	9879000
364179	W+light jets	Wenu + jets	Sherpa	39.243	0.970	p2952	FS	4923800
364182	W+light jets	Wenu + jets	Sherpa	15.224	0.970	p2952	FS	5916800
364183	W+light jets	Wenu + jets	Sherpa	1.233	0.970	p2952	FS	3947000
364184	W+light jets	Wtaunu + jets	Sherpa	15799.442	0.970	p2952	FS	24784000
364187	W+light jets	Wtaunu + jets	Sherpa	638.546	0.970	p2952	FS	14808500
364190	W+light jets	Wtaunu + jets	Sherpa	202.333	0.970	p2952	FS	9899000
364193	W+light jets	Wtaunu + jets	Sherpa	39.325	0.970	p2952	FS	4931200
364196	W+light jets	Wtaunu + jets	Sherpa	15.046	0.970	p2952	FS	5945000
364197	W+light jets	Wtaunu + jets	Sherpa	1.234	0.970	p2952	FS	3946000
364102	Z+b jets	Zmumu + jets	Sherpa	127.180	0.975	p2952	FS	7902000
364105	Z+b jets	Zmumu + jets	Sherpa	12.389	0.975	p2952	FS	5900600
364108	Z+b jets	Zmumu + jets	Sherpa	6.014	0.975	p2952	FS	12339300
364111	Z+b jets	Zmumu + jets	Sherpa	1.491	0.975	p2952	FS	1971400
364116	Z+b jets	Zee + jets	Sherpa	126.450	0.975	p2952	FS	7883600
364119	Z+b jets	Zee + jets	Sherpa	12.623	0.975	p2952	FS	5855000
364122	Z+b jets	Zee + jets	Sherpa	6.083	0.975	p2952	FS	12330900
364125	Z+b jets	Zee + jets	Sherpa	1.494	0.975	p2952	FS	1976850
364130	Z+b jets	Ztautau + jets	Sherpa	127.733	0.975	p2952	FS	7890600
364133	Z+b jets	Ztautau + jets	Sherpa	12.294	0.975	p2952	FS	5912550
364136	Z+b jets	Ztautau + jets	Sherpa	5.479	0.975	p2952	FS	4932950
364139	Z+b jets	Ztautau + jets	Sherpa	1.503	0.975	p2952	FS	1974950
364101	Z+c jets	Zmumu + jets	Sherpa	223.717	0.975	p2952	FS	4917000
364104	Z+c jets	Zmumu + jets	Sherpa	20.348	0.975	p2952	FS	1969800
364107	Z+c jets	Zmumu + jets	Sherpa	9.275	0.975	p2952	FS	2954400
364110	Z+c jets	Zmumu + jets	Sherpa	2.266	0.975	p2952	FS	986000
364115	Z+c jets	Zee + jets	Sherpa	223.731	0.975	p2952	FS	4940500
364118	Z+c jets	Zee + jets	Sherpa	20.336	0.975	p2952	FS	1972600
364121	Z+c jets	Zee + jets	Sherpa	9.372	0.975	p2952	FS	2962600
364124	Z+c jets	Zee + jets	Sherpa	2.280	0.975	p2952	FS	988900
364129	Z+c jets	Ztautau + jets	Sherpa	223.881	0.975	p2952	FS	4941000
364132	Z+c jets	Ztautau + jets	Sherpa	20.212	0.975	p2952	FS	1961200
364135	Z+c jets	Ztautau + jets	Sherpa	9.328	0.975	p2952	FS	2973000
364138	Z+c jets	Ztautau + jets	Sherpa	2.276	0.975	p2952	FS	986000

Table A.3: Used samples and corresponding cross-sections (part 1)

Dataset ID	Sample Type	Sample	Generator	x-sec	k-factor	p-tag	SimType	Events
364100	Z+light jets	Zmumu + jets	Sherpa	1630.224	0.975	p2952	FS	7891000
364103	Z+light jets	Zmumu + jets	Sherpa	75.016	0.975	p2952	FS	5917000
364106	Z+light jets	Zmumu + jets	Sherpa	24.285	0.975	p2952	FS	4943000
364109	Z+light jets	Zmumu + jets	Sherpa	4.773	0.975	p2952	FS	1973000
364112	Z+light jets	Zmumu + jets	Sherpa	1.788	0.975	p2952	FS	2960500
364113	Z+light jets	Zmumu + jets	Sherpa	0.148	0.975	p2952	FS	988000
364114	Z+light jets	Zee + jets	Sherpa	1627.177	0.975	p2952	FS	7900000
364117	Z+light jets	Zee + jets	Sherpa	76.293	0.975	p2952	FS	5925000
364120	Z+light jets	Zee + jets	Sherpa	25.030	0.975	p2952	FS	4949000
364123	Z+light jets	Zee + jets	Sherpa	4.869	0.975	p2952	FS	1932800
364126	Z+light jets	Zee + jets	Sherpa	1.808	0.975	p2952	FS	2973000
364127	Z+light jets	Zee + jets	Sherpa	0.149	0.975	p2952	FS	988000
364128	Z+light jets	Ztautau + jets	Sherpa	1627.726	0.975	p2952	FS	7907000
364131	Z+light jets	Ztautau + jets	Sherpa	76.026	0.975	p2952	FS	5935500
364134	Z+light jets	Ztautau + jets	Sherpa	24.803	0.975	p2952	FS	4956000
364137	Z+light jets	Ztautau + jets	Sherpa	4.791	0.975	p2952	FS	1973000
364140	Z+light jets	Ztautau + jets	Sherpa	1.810	0.975	p2952	FS	2944800
364141	Z+light jets	Ztautau + jets	Sherpa	0.148	0.975	p2952	FS	980000
410025	s-channel	s-channel	PowhegPythia	2.052	1.005	p2952	FS	997800
410026	s-channel	s-channel	PowhegPythia	1.262	1.022	p2952	FS	995400
410011	t-channel	t-channel	PowhegPythia	43.700	1.000	p2952	FS	4986200
410012	t-channel	t-channel	PowhegPythia	25.800	1.000	p2952	FS	4989800
410013	Wt-channel	Wt-channel	PowhegPythia	34.009	1.054	p2952	FS	4985800
410014	Wt-channel	Wt-channel	PowhegPythia	69.500	1.000	p2952	FS	4985600
410501	top pairs	ttbar no allhad	PowhegPythia	397.110	1.139	p2952	AFII	58829000
361600	Diboson	WWlvlv	Sherpa	10.631	1.000	p2669	FS	998400
361601	Diboson	WZlvll_mll4	Sherpa	4.463	1.000	p2952	FS	983600
361602	Diboson	WZlvvv_mll4	Sherpa	2.778	1.000	p2669	FS	982600
361603	Diboson	ZZllll_mll4	Sherpa	1.257	1.000	p2952	FS	992000
361604	Diboson	ZZvvll_mll4	Sherpa	0.925	1.000	p2669	FS	199400
361606	Diboson	WWlvqq	Sherpa	44.176	1.000	p2669	FS	2993000
361607	Diboson	WZqqll_mll20	Sherpa	3.285	1.000	p2669	FS	292200
361609	Diboson	WZlvqq_mqq20	Sherpa	10.099	1.000	p2669	FS	787800
361610	Diboson	ZZqqll_mqq20mll20	Sherpa	2.274	1.000	p2669	FS	100000
302759	Monotop NR	MTNRl v0a0p2	MadGraph+Pythia	197.580	1.000	p2669	AFII	299000
302760	Monotop NR	MTNRl v25a0p2	MadGraph+Pythia	777.290	1.000	p2669	AFII	290000
302761	Monotop NR	MTNRl v50a0p2	MadGraph+Pythia	245.130	1.000	p2669	AFII	299000
302762	Monotop NR	MTNRl v75a0p2	MadGraph+Pythia	130.600	1.000	p2669	AFII	299000
302763	Monotop NR	MTNRl v100a0p2	MadGraph+Pythia	82.934	1.000	p2669	AFII	298000
302764	Monotop NR	MTNRl v150a0p2	MadGraph+Pythia	41.318	1.000	p2669	AFII	297000
302765	Monotop NR	MTNRl v200a0p2	MadGraph+Pythia	23.405	1.000	p2669	AFII	300000
302766	Monotop NR	MTNRl v250a0p2	MadGraph+Pythia	14.190	1.000	p2669	AFII	299000
302767	Monotop NR	MTNRl v300a0p2	MadGraph+Pythia	9.084	1.000	p2669	AFII	298000
302768	Monotop NR	MTNRl v500a0p2	MadGraph+Pythia	2.147	1.000	p2669	AFII	597900
302769	Monotop NR	MTNRl v750a0p2	MadGraph+Pythia	0.545	1.000	p2669	AFII	298000
302770	Monotop NR	MTNRl v1000a0p2	MadGraph+Pythia	0.180	1.000	p2669	AFII	299000
302771	Monotop NR	MTNRl v1250a0p2	MadGraph+Pythia	0.069	1.000	p2669	AFII	299000
302772	Monotop NR	MTNRl v1500a0p2	MadGraph+Pythia	0.030	1.000	p2669	AFII	598800
302773	Monotop NR	MTNRl v1750a0p2	MadGraph+Pythia	0.014	1.000	p2669	AFII	299000
302774	Monotop NR	MTNRl v2000a0p2	MadGraph+Pythia	0.007	1.000	p2669	AFII	299000
302775	Monotop NR	MTNRl v2250a0p2	MadGraph+Pythia	0.003	1.000	p2669	AFII	298000
302776	Monotop NR	MTNRl v2500a0p2	MadGraph+Pythia	0.002	1.000	p2669	AFII	595600

Table A.4: Used samples and corresponding cross-sections (part 2)

List of Acronyms

2HDM Two Higgs Doublet Model.

AF2 ATLFAST-II.
ALICE A Large Ion Collider Experiment.
ATLAS A Large Toroidal ApparatuS.

BDT Booted Decision Tree.

CB Combined muons.
CDF Collider Detector at Fermilab.
CERN Conseil Européen pour la Recherche Nucléaire.
CKM Cabbibo-Kobayashi-Maskawa.
CL Calibration Loop.
CM Calorimeter-tagged muons.
CMB Cosmic Microwave Background.
CMS Compact Muon Solenoid.
CS Central Solenoid.
CST Calorimeter Soft Term.

DAQ Data Acquisition System.
DIS Deep Inelastic Scattering.
DM Dark Matter.
DY Drell Yan.

ECAL Electromagnetic Calorimeter.
EF Event Filter.
EFT Effective Field Theory.
EW Electroweak theory.

FCNC Flavor Changing Neutral Current.
FWHM Full Width Half Maximum.

GSC Global Sequential Calibration.

HCAL Hadronic Calorimeter.
HLT High Level Trigger.

IBL Insertable B-Layer.
ID Inner Detector.
IP Interaction Point.

JER Jet Energy Resolution.
JES Jet Energy Scale.
JVF Jet Vertex Fraction.
JVT Jet Vertex Tagger.

Lar Liquid Argon Calorimeter.
LEP Large Electron-Positron collider.
LH Likelihood.
LHC Large Hadron Collider.
LHCb LHC beauty.
LS1 Long Shutdown.
LSP Lightest Superparticles.

MC Monte Carlo.
ME Extrapolated muons.
MFV Minimal Flavor Violation.
MOND MOdified Newtonian Dynamics.

MS Muon Spectrometer.
MVA Multivariate Analysis.

NLO Next to Leading Order.
NN Neural Network.
NNLL Next to next to Leading Log.
NNLO Next to next to Leading Order.
NP Nuisance Parameter.

PBH Primordial Black Hole.
PDF Parton Distribution Function.
pdf Probability Density Function.
PDG Particle Data Group.
pQCD Perturbative Quantum Chromodynamics.
PS Proton Synchrotron.

QCD Quantum Chromodynamics.
QED Quantum Electro-Dynamics.

ROI Regions Of Interest.

SA Stand-Alone muons.
SCT SemiConductor Tracker.
SF Scale Factor.
SM Standard Model.
SPS Super Proton Synchrotron.
SSB Spontaneous Symmetry Breaking.
ST Segment-tagged muons.
STVF Soft Term Vertex Fraction.

TileCar Tile Calorimeter.
TRT Transition Radiation Tracker.
TST Track Soft Term.

WIMP Weakly Interacting Massive Particle.

ZMF Zero Momentum Frame.

Bibliography

[1] ATLAS Collaboration, *Probing the W tb vertex structure in t-channel single-top-quark production and decay in pp collisions at $\sqrt{s} = 8$ TeV with the ATLAS detector*, JHEP **04** (2017) 124, arXiv:1702.08309 [hep-ex].

[2] *ATLAS Inner Detector Alignment Performance with February 2015 Cosmic Rays Data*, Tech. Rep. ATL-PHYS-PUB-2015-009, CERN, Geneva, Apr, 2015. https://cds.cern.ch/record/2008724.

[3] *Study of the mechanical stability of the ATLAS Insertable B-Layer*, Tech. Rep. ATL-INDET-PUB-2015-001, CERN, Geneva, Jun, 2015. https://cds.cern.ch/record/2022587.

[4] ATLAS Collaboration, *Observation of a new particle in the search for the Standard Model Higgs boson with the ATLAS detector at the LHC*, Phys. Lett. **B716** (2012) 1–29, arXiv:1207.7214 [hep-ex].

[5] CMS Collaboration, S. Chatrchyan et al., *Observation of a new boson at a mass of 125 GeV with the CMS experiment at the LHC*, Phys. Lett. **B716** (2012) 30–61, arXiv:1207.7235 [hep-ex].

[6] S. L. Glashow, *Partial Symmetries of Weak Interactions*, Nucl. Phys. **22** (1961) 579–588.

[7] S. Weinberg, *A Model of Leptons*, Phys. Rev. Lett. **19** (1967) 1264–1266.

[8] A. Salam and J. C. Ward, *Gauge Theory of Elementary Interactions*, Phys. Rev. **136** (1964) B763–B768, https://link.aps.org/doi/10.1103/PhysRev.136.B763.

[9] Particle Data Group Collaboration, C. Patrignani et al., *Review of Particle Physics*, Chin. Phys. **C40** (2016) 100001.

[10] N. Cabibbo, *Unitary Symmetry and Leptonic Decays*, Phys. Rev. Lett. **10** (1963) 531–533, [,648(1963)].

[11] M. Kobayashi and T. Maskawa, *CP Violation in the Renormalizable Theory of Weak Interaction*, Prog. Theor. Phys. **49** (1973) 652–657.

[12] P. W. Higgs, *Broken Symmetries and the Masses of Gauge Bosons*, Phys. Rev. Lett. **13** (1964) 508–509, https://link.aps.org/doi/10.1103/PhysRevLett.13.508.

[13] G. S. Guralnik, C. R. Hagen, and T. W. B. Kibble, *Global Conservation Laws and Massless Particles*, Phys. Rev. Lett. **13** (1964) 585–587, https://link.aps.org/doi/10.1103/PhysRevLett.13.585.

[14] F. Englert and R. Brout, *Broken Symmetry and the Mass of Gauge Vector Mesons*, Phys. Rev. Lett. **13** (1964) 321–323, https://link.aps.org/doi/10.1103/PhysRevLett.13.321.

[15] S. W. Herb et al., *Observation of a Dimuon Resonance at 9.5-GeV in 400-GeV Proton-Nucleus Collisions*, Phys. Rev. Lett. **39** (1977) 252–255.

[16] D0 Collaboration, S. Abachi et al., *Observation of the top quark*, Phys. Rev. Lett. **74** (1995) 2632–2637, arXiv:hep-ex/9503003 [hep-ex].

[17] CDF Collaboration, F. Abe et al., *Observation of top quark production in $\bar{p}p$ collisions*, Phys. Rev. Lett. **74** (1995) 2626–2631, arXiv:hep-ex/9503002 [hep-ex].

[18] M. Czakon, P. Fiedler, and A. Mitov, *Total Top-Quark Pair-Production Cross Section at Hadron Colliders Through $O(\alpha\frac{4}{S})$*, Phys. Rev. Lett. **110** (2013) 252004, arXiv:1303.6254 [hep-ph].

[19] M. Brucherseifer, F. Caola, and K. Melnikov, *On the NNLO QCD corrections to single-top production at the LHC*, Phys. Lett. **B736** (2014) 58–63, arXiv:1404.7116 [hep-ph].

[20] E. L. Berger, J. Gao, and H. X. Zhu, *Differential Distributions for t-channel Single Top-Quark Production and Decay at Next-to-Next-to-Leading Order in QCD*, JHEP **11** (2017) 158, arXiv:1708.09405 [hep-ph].

[21] N. Kidonakis, *NNLL resummation for s-channel single top quark production*, Phys. Rev. **D81** (2010) 054028, arXiv:1001.5034 [hep-ph].

[22] N. Kidonakis, *Two-loop soft anomalous dimensions for single top quark associated production with a W^- or H^-*, Phys. Rev. D **82** (2010) 054018, https://link.aps.org/doi/10.1103/PhysRevD.82.054018.

[23] M. Czakon and A. Mitov, *Top++: A Program for the Calculation of the Top-Pair Cross-Section at Hadron Colliders*, Comput. Phys. Commun. **185** (2014) 2930, arXiv:1112.5675 [hep-ph].

[24] ATLAS Collaboration, *Summary plots from the ATLAS Top physics group*, https://atlas.web.cern.ch/Atlas/GROUPS/PHYSICS/CombinedSummaryPlots/TOP/tt_xsec_vsroots/tt_xsec_vsroots.pdf.

[25] ATLAS Collaboration, *Summary plots from the ATLAS Top physics group*, https://atlas.web.cern.ch/Atlas/GROUPS/PHYSICS/CombinedSummaryPlots/TOP/singletop_allchanvsroots/singletop_allchanvsroots.pdf.

[26] G. Mahlon and S. Parke, *Single Top Quark Production at the LHC: Understanding Spin*, Phys. Lett. **B476** (2000) 323, arXiv:hep-ph/9912458.

[27] G. Mahlon and S. J. Parke, *Improved spin basis for angular correlation studies in single top quark production at the Tevatron*, Phys. Rev. **D55** (1997) 7249–7254, arXiv:hep-ph/9611367 [hep-ph].

[28] A. Czarnecki, J. G. Korner, and J. H. Piclum, *Helicity fractions of W bosons from top quark decays at NNLO in QCD*, Phys. Rev. **D81** (2010) 111503, arXiv:1005.2625 [hep-ph].

[29] ATLAS Collaboration, *Measurement of the W boson polarisation in $t\bar{t}$ events from pp collisions at $\sqrt{s}$ = 8 TeV in the lepton + jets channel with ATLAS*, Eur. Phys. J. **C77** (2017) 264, arXiv:1612.02577 [hep-ex].

[30] CMS Collaboration, V. Khachatryan et al., *Measurement of the W boson helicity fractions in the decays of top quark pairs to lepton + jets final states produced in pp collisions at $\sqrt{s} = 8$TeV*, Phys. Lett. **B762** (2016) 512–534, arXiv:1605.09047 [hep-ex].

[31] J. A. Aguilar-Saavedra and J. Bernabéu, *W polarisation beyond helicity fractions in top quark decays*, Nucl. Phys. **B840** (2010) 349, arXiv:1005.5382 [hep-ph].

[32] J. A. Aguilar-Saavedra and J. Bernabéu, *Breaking down the entire W boson spin observables from its decay*, Phys. Rev. **D93** (2016) 011301, arXiv:1508.04592 [hep-ph].

[33] R. Schwienhorst et al., *Single top quark production and decay in the t-channel at next-to-leading order at the LHC*, Phys. Rev. **D83** (2011) 034019, arXiv:1012.5132 [hep-ph].

[34] C. Burges and H. J. Schnitzer, *"Virtual effects of excited quarks as probes of a possible new hardonic mass scale"*, Nuclear Physics B **228** (1983) 464 – 500, http://www.sciencedirect.com/science/article/pii/0550321383905552.

[35] C. N. Leung, S. T. Love, and S. Rao, *Low-Energy Manifestations of a New Interaction Scale: Operator Analysis*, Z. Phys. **C31** (1986) 433.

[36] W. Buchmuller and D. Wyler, *Effective Lagrangian Analysis of New Interactions and Flavor Conservation*, Nucl. Phys. **B268** (1986) 621–653.

[37] J. A. Aguilar-Saavedra, *A Minimal set of top anomalous couplings*, Nucl. Phys. **B812** (2009) 181–204, arXiv:0811.3842 [hep-ph].

[38] K. Hsieh, K. Schmitz, J.-H. Yu, and C. P. Yuan, *Global Analysis of General SU(2) x SU(2) x U(1) Models with Precision Data*, Phys. Rev. **D82** (2010) 035011, arXiv:1003.3482 [hep-ph].

[39] Q.-H. Cao, Z. Li, J.-H. Yu, and C. P. Yuan, *Discovery and Identification of W' and Z' in SU(2) x SU(2) x U(1) Models at the LHC*, Phys. Rev. **D86** (2012) 095010, arXiv:1205.3769 [hep-ph].

[40] G. Cacciapaglia, A. Deandrea, D. Harada, and Y. Okada, *Bounds and Decays of New Heavy Vector-like Top Partners*, JHEP **11** (2010) 159, arXiv:1007.2933 [hep-ph].

[41] J. A. Aguilar-Saavedra, R. Benbrik, S. Heinemeyer, and M. Pérez-Victoria, *Handbook of vectorlike quarks: Mixing and single production*, Phys. Rev. **D88** (2013) 094010, arXiv:1306.0572 [hep-ph].

[42] J. A. Aguilar-Saavedra, *Single top quark production at LHC with anomalous Wtb couplings*, Nucl. Phys. **B804** (2008) 160, arXiv:0803.3810.

[43] ATLAS Collaboration, *Measurement of the W boson polarization in top quark decays with the ATLAS detector*, JHEP **06** (2012) 088, arXiv:1205.2484 [hep-ex].

[44] CMS Collaboration, S. Chatrchyan et al., *Measurement of the W-boson helicity in top-quark decays from $t\bar{t}$ production in lepton+jets events in pp collisions at $\sqrt{s} = 7$ TeV*, JHEP **10** (2013) 167, arXiv:1308.3879 [hep-ex].

[45] CMS Collaboration, V. Khachatryan et al., *Measurement of the W boson helicity in events with a single reconstructed top quark in pp collisions at $\sqrt{s} = 8$ TeV*, JHEP **01** (2015) 053, arXiv:1410.1154 [hep-ex].

[46] C. Bernardo, N. F. Castro, M. C. N. Fiolhais, H. Gonçalves, A. G. C. Guerra, M. Oliveira, and A. Onofre, *Studying the Wtb vertex structure using recent LHC results*, Phys. Rev. **D90** (2014) 113007, arXiv:1408.7063 [hep-ph].

[47] ATLAS Collaboration, *Fiducial, total and differential cross-section measurements of t-channel single top-quark production in pp collisions at 8 TeV using data collected by the ATLAS detector*, Eur. Phys. J. **C77** (2017) 531, arXiv:1702.02859 [hep-ex].

[48] CMS Collaboration, *Measurement of the t-channel single-top-quark production cross section and of the $|V_{tb}|$ CKM matrix element in pp collisions at $\sqrt{s} = 8$ TeV*, JHEP **1406** (2014) 090, arXiv:1403.7366 [hep-ex].

[49] ATLAS Collaboration, *Search for anomalous couplings in the Wtb vertex from the measurement of double differential angular decay rates of single top quarks produced in the t-channel with the ATLAS detector*, JHEP **04** (2016) 023, arXiv:1510.03764 [hep-ex].

[50] V. Cirigliano, W. Dekens, J. de Vries, and E. Mereghetti, *Is there room for CP violation in the top-Higgs sector?*, Phys. Rev. **D94** (2016) 016002, arXiv:1603.03049 [hep-ph].

[51] B. Grzadkowski and M. Misiak, *Anomalous Wtb coupling effects in the weak radiative B-meson decay*, Phys. Rev. **D78** (2008) 077501, arXiv:0802.1413 [hep-ph], [Erratum: Phys. Rev.D84,059903(2011)].

[52] J. Aguilar-Saavedra, *TopFit - a program to fit the Wtb vertex*, http://jaguilar.web.cern.ch/jaguilar/topfit.

[53] ATLAS Collaboration, *Analysis of the Wtb vertex from the measurement of triple-differential angular decay rates of single top quarks produced in the t-channel at $\sqrt{s}$ = 8 TeV with the ATLAS detector*, JHEP **12** (2017) 017, arXiv:1707.05393 [hep-ex].

[54] E. Corbelli and P. Salucci, *The Extended Rotation Curve and the Dark Matter Halo of M33*, Mon. Not. Roy. Astron. Soc. **311** (2000) 441–447, arXiv:astro-ph/9909252 [astro-ph].

[55] F. Zwicky, *Die Rotverschiebung von extragalaktischen Nebeln*, Helvetica Physica Acta **6** (1933) 110–127.

[56] H. W. Babcock, *The rotation of the Andromeda Nebula*, Lick Observatory Bulletin **19** (1939) 41–51.

[57] V. C. Rubin and W. K. Ford, Jr., *Rotation of the Andromeda Nebula from a Spectroscopic Survey of Emission Regions*, Astrophys. J. **159** (1970) 379–403.

[58] A. Refregier, *Weak gravitational lensing by large scale structure*, Ann. Rev. Astron. Astrophys. **41** (2003) 645–668, arXiv:astro-ph/0307212 [astro-ph].

[59] M. Bartelmann and M. Maturi, *Weak gravitational lensing*, 2016. arXiv:1612.06535 [astro-ph.CO]. https://inspirehep.net/record/1505136/files/arXiv:1612.06535.pdf.

[60] D. Clowe, M. Bradac, A. H. Gonzalez, M. Markevitch, S. W. Randall, C. Jones, and D. Zaritsky, *A direct empirical proof of the existence of dark matter*, Astrophys. J. **648** (2006) L109–L113, arXiv:astro-ph/0608407 [astro-ph].

[61] R. A. Alpher and R. C. Herman, *On the Relative Abundance of the Elements*, Phys. Rev. **74** (1948) 1737–1742, https://link.aps.org/doi/10.1103/PhysRev.74.1737.

[62] A. A. Penzias and R. W. Wilson, *A Measurement of excess antenna temperature at 4080-Mc/s*, Astrophys. J. **142** (1965) 419–421.

[63] Planck Collaboration, P. A. R. Ade et al., *Planck 2013 results. XVI. Cosmological parameters*, Astron. Astrophys. **571** (2014) A16, arXiv:1303.5076 [astro-ph.CO].

[64] M. Milgrom, *MOND theory*, Can. J. Phys. **93** (2015) 107–118, arXiv:1404.7661 [astro-ph.CO].

[65] L. Bernard, L. Blanchet, and L. Heisenberg, *Bimetric gravity and dark matter*, pp. , 43–52. 2015. arXiv:1507.02802 [gr-qc]. https://inspirehep.net/record/1382322/files/arXiv:1507.02802.pdf.

[66] E. Bugaev and P. Klimai, *Large curvature perturbations near horizon crossing in single-field inflation models*, Phys. Rev. **D78** (2008) 063515, arXiv:0806.4541 [astro-ph].

[67] B. Carr, M. Raidal, T. Tenkanen, V. Vaskonen, and H. Veermäe, *Primordial black hole constraints for extended mass functions*, Phys. Rev. **D96** (2017) 023514, arXiv:1705.05567 [astro-ph.CO].

[68] J. E. Kim and G. Carosi, *Axions and the Strong CP Problem*, Rev. Mod. Phys. **82** (2010) 557–602, arXiv:0807.3125 [hep-ph].

[69] K. Abazajian, G. M. Fuller, and M. Patel, *Sterile neutrino hot, warm, and cold dark matter*, Phys. Rev. **D64** (2001) 023501, arXiv:astro-ph/0101524 [astro-ph].

[70] H. Goldberg, *Constraint on the Photino Mass from Cosmology*, Phys. Rev. Lett. **50** (1983) 1419–1422, https://link.aps.org/doi/10.1103/PhysRevLett.50.1419.

[71] J. Ellis, J. Hagelin, D. Nanopoulos, K. Olive, and M. Srednicki, *Supersymmetric relics from the big bang*, Nuclear Physics B **238** (1984) 453 – 476, http://www.sciencedirect.com/science/article/pii/0550321384904619.

[72] H.-C. Cheng and I. Low, *TeV symmetry and the little hierarchy problem*, JHEP **09** (2003) 051, arXiv:hep-ph/0308199 [hep-ph].

[73] A. Birkedal, A. Noble, M. Perelstein, and A. Spray, *Little Higgs dark matter*, Phys. Rev. **D74** (2006) 035002, arXiv:hep-ph/0603077 [hep-ph].

[74] M. Dine, W. Fischler, and M. Srednicki, *Supersymmetric technicolor*, Nuclear Physics B **189** (1981) 575 – 593, http://www.sciencedirect.com/science/article/pii/0550321381905824.

[75] Snowmass 2013 Cosmic Frontier Working Groups 1–4 Collaboration, D. Bauer et al., *Dark Matter in the Coming Decade: Complementary Paths to Discovery and Beyond*, Phys. Dark Univ. **7-8** (2015) 16–23, arXiv:1305.1605 [hep-ph].

[76] LUX Collaboration, D. S. Akerib et al., *Results from a search for dark matter in the complete LUX exposure*, Phys. Rev. Lett. **118** (2017) 021303, arXiv:1608.07648 [astro-ph.CO].

[77] PandaX-II Collaboration, X. Cui et al., *Dark Matter Results From 54-Ton-Day Exposure of PandaX-II Experiment*, Phys. Rev. Lett. **119** (2017) 181302, arXiv:1708.06917 [astro-ph.CO].

[78] XENON Collaboration, E. Aprile et al., *First Dark Matter Search Results from the XENON1T Experiment*, Phys. Rev. Lett. **119** (2017) 181301, arXiv:1705.06655 [astro-ph.CO].

[79] B. J. Mount et al., *LUX-ZEPLIN (LZ) Technical Design Report*, arXiv:1703.09144 [physics.ins-det].

[80] C. E. Aalseth et al., *DarkSide-20k: A 20 tonne two-phase LAr TPC for direct dark matter detection at LNGS*, Eur. Phys. J. Plus **133** (2018) 131, arXiv:1707.08145 [physics.ins-det].

[81] DARWIN Collaboration, J. Aalbers et al., *DARWIN: towards the ultimate dark matter detector*, JCAP **1611** (2016) 017, arXiv:1606.07001 [astro-ph.IM].

[82] DES, Fermi-LAT Collaboration, F.-L. Collaboration, *Searching for Dark Matter Annihilation in Recently Discovered Milky Way Satellites with Fermi-LAT*, Astrophys. J. **834** (2017) 110, arXiv:1611.03184 [astro-ph.HE].

[83] H.E.S.S. Collaboration, *Search for Dark Matter Annihilations towards the Inner Galactic Halo from 10 Years of Observations with H.E.S.S.*, Phys. Rev. Lett. **117** (2016) 111301, https://link.aps.org/doi/10.1103/PhysRevLett.117.111301.

[84] F. Halzen and S. R. Klein, *IceCube: An Instrument for Neutrino Astronomy*, Rev. Sci. Instrum. **81** (2010) 081101, arXiv:1007.1247 [astro-ph.HE].

[85] ANTARES Collaboration, S. Adrian-Martinez et al., *Limits on Dark Matter Annihilation in the Sun using the ANTARES Neutrino Telescope*, Phys. Lett. **B759** (2016) 69–74, arXiv:1603.02228 [astro-ph.HE].

[86] AMS Collaboration, *First Result from the Alpha Magnetic Spectrometer on the International Space Station: Precision Measurement of the Positron Fraction in Primary Cosmic Rays of 0.5–350 GeV*, Phys. Rev. Lett. **110** (2013) 141102, https://link.aps.org/doi/10.1103/PhysRevLett.110.141102.

[87] L. Bergstrom, T. Bringmann, I. Cholis, D. Hooper, and C. Weniger, *New limits on dark matter annihilation from AMS cosmic ray positron data*, Phys. Rev. Lett. **111** (2013) 171101, arXiv:1306.3983 [astro-ph.HE].

[88] D. Abercrombie et al., *Dark Matter Benchmark Models for Early LHC Run-2 Searches: Report of the ATLAS/CMS Dark Matter Forum*, arXiv:1507.00966 [hep-ex].

[89] ATLAS Collaboration, *Search for dark matter and other new phenomena in events with an energetic jet and large missing transverse momentum using the ATLAS detector*, JHEP **01** (2018) 126, arXiv:1711.03301 [hep-ex].

[90] CMS Collaboration, A. M. Sirunyan et al., *Search for dark matter produced with an energetic jet or a hadronically decaying W or Z boson at* $\sqrt{s} = 13$ *TeV*, JHEP **07** (2017) 014, arXiv:1703.01651 [hep-ex].

[91] ATLAS Collaboration, *Search for dark matter at* $\sqrt{s} = 13$ *TeV in final states containing an energetic photon and large missing transverse momentum with the ATLAS detector*, Eur. Phys. J. **C77** (2017) 393, arXiv:1704.03848 [hep-ex].

[92] CMS Collaboration, A. M. Sirunyan et al., *Search for new physics in the monophoton final state in proton-proton collisions at* $\sqrt{s} = 13$ *TeV*, JHEP **10** (2017) 073, arXiv:1706.03794 [hep-ex].

[93] ATLAS Collaboration, *Search for new phenomena in dijet events using 37* fb^{-1} *of* pp *collision data collected at* $\sqrt{s} = 13$ *TeV with the ATLAS detector*, Phys. Rev. **D96** (2017) 052004, arXiv:1703.09127 [hep-ex].

[94] CMS Collaboration, *Search for dijet resonances in proton–proton collisions at s=13TeV and constraints on dark matter and other models*, Physics Letters B **769** (2017) 520 – 542, http://www.sciencedirect.com/science/article/pii/S0370269317301028.

[95] ATLAS Collaboration, *Search for resonances in the mass distribution of jet pairs with one or two jets identified as b-jets in proton–proton collisions at* $\sqrt{s} = 13$ *TeV with the ATLAS detector*, Phys. Lett. **B759** (2016) 229–246, arXiv:1603.08791 [hep-ex].

[96] CMS Collaboration, *Search for resonances in the mass distribution of jet pairs with one or two jets identified as b-jets in proton–proton collisions at s=13 TeV with the ATLAS detector*, Physics Letters B **759** (2016) 229 – 246, http://www.sciencedirect.com/science/article/pii/S0370269316302118.

[97] *Search for heavy particles decaying to pairs of highly-boosted top quarks using lepton-plus-jets events in proton–proton collisions at* $\sqrt{s} = 13$ *TeV with the ATLAS detector*, Tech. Rep. ATLAS-CONF-2016-014, CERN, Geneva, Mar, 2016. https://cds.cern.ch/record/2141001.

[98] CMS Collaboration, *Search for resonant* $t\bar{t}$ *production in proton-proton collisions at* $\sqrt{s} = 8$ TeV, Phys. Rev. D **93** (2016) 012001, https://link.aps.org/doi/10.1103/PhysRevD.93.012001.

[99] ATLAS Collaboration, *Search for dark matter in association with a Higgs boson decaying to two photons at* $\sqrt{s}$ *= 13 TeV with the ATLAS detector*, Phys. Rev. D **96** (2017) 112004, arXiv:1706.03948 [hep-ex].

[100] ATLAS Collaboration, *Search for dark matter produced in association with bottom or top quarks in* $\sqrt{s} = 13$ *TeV pp collisions with the ATLAS detector*, Eur. Phys. J. **C78** (2018) 18, arXiv:1710.11412 [hep-ex].

[101] ATLAS Collaboration, *Search for an invisibly decaying Higgs boson or dark matter candidates produced in association with a* Z *boson in* pp *collisions at* $\sqrt{s} =$ *13 TeV with the ATLAS detector*, Phys. Lett. **B776** (2018) 318–337, arXiv:1708.09624 [hep-ex].

[102] ATLAS Collaboration, *Search for Dark Matter Produced in Association with a Higgs Boson Decaying to* $b\bar{b}$ *using 36* fb^{-1} *of* pp *collisions at* $\sqrt{s} = 13$ *TeV with the ATLAS Detector*, Phys. Rev. Lett. **119** (2017) 181804, arXiv:1707.01302 [hep-ex].

[103] ATLAS Collaboration, *Search for top-squark pair production in final states with one lepton, jets, and missing transverse momentum using 36* fb^{-1} *of* $\sqrt{s} = 13$ *TeV pp collision data with the ATLAS detector*, JHEP **06** (2018) 108, arXiv:1711.11520 [hep-ex].

[104] J. Andrea, B. Fuks, and F. Maltoni, *Monotops at the LHC*, Phys. Rev. **D84** (2011) 074025, arXiv:1106.6199 [hep-ph].

[105] J.-L. Agram, J. Andrea, M. Buttignol, E. Conte, and B. Fuks, *Monotop phenomenology at the Large Hadron Collider*, Phys. Rev. **D89** (2014) 014028, arXiv:1311.6478 [hep-ph].

[106] I. Boucheneb, G. Cacciapaglia, A. Deandrea, and B. Fuks, *Revisiting monotop production at the LHC*, JHEP **01** (2015) 017, arXiv:1407.7529 [hep-ph].

[107] E. L. Berger, B. W. Harris, and Z. Sullivan, *Single top squark production via R-parity violating supersymmetric couplings in hadron collisions*, Phys. Rev. Lett. **83** (1999) 4472–4475, arXiv:hep-ph/9903549 [hep-ph].

[108] E. L. Berger, B. W. Harris, and Z. Sullivan, *Direct probes of R-parity violating supersymmetric couplings via single top squark production*, Phys. Rev. **D63** (2001) 115001, arXiv:hep-ph/0012184 [hep-ph].

[109] N. Desai and B. Mukhopadhyaya, *R-parity violating resonant stop production at the Large Hadron Collider*, JHEP **10** (2010) 060, arXiv:1002.2339 [hep-ph].

[110] A. Kumar, J. N. Ng, A. Spray, and P. T. Winslow, *Tracking down the top quark forward-backward asymmetry with monotops*, Phys. Rev. **D88** (2013) 075012, arXiv:1308.3712 [hep-ph].

[111] H. Davoudiasl, D. E. Morrissey, K. Sigurdson, and S. Tulin, *Baryon Destruction by Asymmetric Dark Matter*, Phys. Rev. **D84** (2011) 096008, arXiv:1106.4320 [hep-ph].

[112] ATLAS Collaboration, *Search for new phenomena in events with same-charge leptons and b-jets in pp collisions at $\sqrt{s} = 13$ TeV with the ATLAS detector*, arXiv:1807.11883 [hep-ex].

[113] *CERN: Accelerating science*, https://home.cern/.

[114] L. Evans and P. Bryant, *LHC Machine*, JINST **3** (2008) S08001.

[115] M. Benedikt, P. Collier, V. Mertens, J. Poole, and K. Schindl, *LHC Design Report*. CERN Yellow Reports: Monographs. CERN, Geneva, 2004. https://cds.cern.ch/record/823808.

[116] ATLAS Collaboration, *The ATLAS Experiment at the CERN Large Hadron Collider*, JINST **3** (2008) S08003.

[117] CMS Collaboration, S. Chatrchyan et al., *The CMS Experiment at the CERN LHC*, JINST **3** (2008) S08004.

[118] ALICE Collaboration, K. Aamodt et al., *The ALICE experiment at the CERN LHC*, JINST **3** (2008) S08002.

[119] LHCb Collaboration, A. A. Alves, Jr. et al., *The LHCb Detector at the LHC*, JINST **3** (2008) S08005.

[120] C.-T. Collaboration, *CMS-TOTEM Precision Proton Spectrometer*, Tech. Rep. CERN-LHCC-2014-021. TOTEM-TDR-003. CMS-TDR-13, Sep, 2014. https://cds.cern.ch/record/1753795.

[121] LHCf Collaboration, *LHCf experiment: Technical Design Report.* Technical Design Report LHCf. CERN, Geneva, 2006. https://cds.cern.ch/record/926196.

[122] MoEDAL Collaboration Tech. Rep. CERN-LHCC-2009-006. MoEDAL-TDR-001, Jun, 2009. https://cds.cern.ch/record/1181486.

[123] A. D. Martin, W. J. Stirling, R. S. Thorne, and G. Watt, *Parton distributions for the LHC*, Eur. Phys. J. **C63** (2009) 189–285, arXiv:0901.0002 [hep-ph].

[124] NNPDF Collaboration, R. D. Ball et al., *Parton distributions for the LHC run II*, JHEP **04** (2015) 040, arXiv:1410.8849 [hep-ph].

[125] H.-L. Lai, M. Guzzi, J. Huston, Z. Li, P. M. Nadolsky, J. Pumplin, and C. P. Yuan, *New parton distributions for collider physics*, Phys. Rev. **D82** (2010) 074024, arXiv:1007.2241 [hep-ph].

[126] J. Pumplin, D. R. Stump, J. Huston, H. L. Lai, P. M. Nadolsky, and W. K. Tung, *New generation of parton distributions with uncertainties from global QCD analysis*, JHEP **07** (2002) 012, arXiv:hep-ph/0201195 [hep-ph].

[127] CDF Collaboration, R. D. Field, *The Underlying event in hard scattering processes*, eConf **C010630** (2001) P501, arXiv:hep-ph/0201192 [hep-ph].

[128] T. Sjöstrand, S. Ask, J. R. Christiansen, R. Corke, N. Desai, P. Ilten, S. Mrenna, S. Prestel, C. O. Rasmussen, and P. Z. Skands, *An Introduction to PYTHIA 8.2*, Comput. Phys. Commun. **191** (2015) 159–177, arXiv:1410.3012 [hep-ph].

[129] M. Bahr et al., *Herwig++ Physics and Manual*, Eur. Phys. J. **C58** (2008) 639–707, arXiv:0803.0883 [hep-ph].

[130] ATLAS Collaboration, *Luminosity Public Results*, https://twiki.cern.ch/twiki/bin/view/AtlasPublic/LuminosityPublicResults.

[131] ATLAS Collaboration, *Luminosity Public Results*, https://twiki.cern.ch/twiki/bin/view/AtlasPublic/LuminosityPublicResultsRun2.

[132] ATLAS Collaboration, *ATLAS: Detector and physics performance technical design report. Volume 1*,.

[133] ATLAS Collaboration Collaboration„ *ATLAS inner detector: Technical Design Report, 1*. Technical Design Report ATLAS. CERN, Geneva, 1997. https://cds.cern.ch/record/331063.

[134] ATLAS Collaboration, *ATLAS Insertable B-Layer Technical Design Report*, Tech. Rep. CERN-LHCC-2010-013. ATLAS-TDR-19, Sep, 2010. https://cds.cern.ch/record/1291633.

[135] ATLAS Collaboration, *Performance of the ATLAS Trigger System in 2010*, Eur. Phys. J. **C72** (2012) 1849, arXiv:1110.1530 [hep-ex].

[136] ATLAS Collaboration, *ATLAS level-1 trigger: Technical Design Report*. Technical Design Report ATLAS. CERN, Geneva, 1998. https://cds.cern.ch/record/381429.

[137] ATLAS Collaboration, *ATLAS high-level trigger, data-acquisition and controls: Technical Design Report*. Technical Design Report ATLAS. CERN, Geneva, 2003. https://cds.cern.ch/record/616089.

[138] ATLAS Collaboration, *2015 start-up trigger menu and initial performance assessment of the ATLAS trigger using Run-2 data*, ATL-DAQ-PUB-2016-001, 2016, https://cds.cern.ch/record/2136007/.

[139] ATLAS Collaboration, *Performance of the ATLAS Trigger System in 2015*, Eur. Phys. J. **C77** (2017) 317, arXiv:1611.09661 [hep-ex].

[140] ATLAS Collaboration Collaboration„ *Performance of the ATLAS Inner Detector Track and Vertex Reconstruction in the High Pile-Up LHC Environment*, Tech. Rep. ATLAS-CONF-2012-042, CERN, Geneva, Mar, 2012. http://cds.cern.ch/record/1435196.

[141] T. Cornelissen, M. Elsing, S. Fleischmann, W. Liebig, E. Moyse, and A. Salzburger, *Concepts, Design and Implementation of the ATLAS New Tracking (NEWT)*, Tech. Rep. ATL-SOFT-PUB-2007-007. ATL-COM-SOFT-2007-002, CERN, Geneva, Mar, 2007. https://cds.cern.ch/record/1020106.

[142] *Track Reconstruction Performance of the ATLAS Inner Detector at* $\sqrt{s} = 13$ *TeV*, Tech. Rep. ATL-PHYS-PUB-2015-018, CERN, Geneva, Jul, 2015. http://cds.cern.ch/record/2037683.

[143] ATLAS Collaboration, *Reconstruction of primary vertices at the ATLAS experiment in Run 1 proton–proton collisions at the LHC*, Eur. Phys. J. **C77** (2017) 332, arXiv:1611.10235 [physics.ins-det].

[144] *Vertex Reconstruction Performance of the ATLAS Detector at* $\sqrt{s}$ *= 13 TeV*, Tech. Rep. ATL-PHYS-PUB-2015-026, CERN, Geneva, Jul, 2015. http://cds.cern.ch/record/2037717.

[145] ATLAS Collaboration, *Electron reconstruction and identification efficiency measurements with the ATLAS detector using the 2011 LHC proton-proton collision data*, Eur. Phys. J. **C74** (2014) 2941, arXiv:1404.2240 [hep-ex].

[146] *Electron efficiency measurements with the ATLAS detector using the 2012 LHC proton-proton collision data*, Tech. Rep. ATLAS-CONF-2014-032, CERN, Geneva, Jun, 2014. https://cds.cern.ch/record/1706245.

[147] ATLAS Collaboration, *Electron efficiency measurements with the ATLAS detector using the 2015 LHC proton-proton collision data*, Tech. Rep. ATLAS-CONF-2016-024, CERN, Geneva, Jun, 2016. https://cds.cern.ch/record/2157687.

[148] ATLAS Collaboration, *Electron and photon energy calibration with the ATLAS detector using LHC Run 1 data*, Eur. Phys. J. **C74** (2014) 3071, arXiv:1407.5063 [hep-ex].

[149] ATLAS Collaboration, *Electron and photon energy calibration with the ATLAS detector using data collected in 2015 at* $\sqrt{s} = 13$ TeV, Tech. Rep. ATL-PHYS-PUB-2016-015, CERN, Geneva, Aug, 2016. https://cds.cern.ch/record/2203514.

[150] ATLAS Collaboration, *Muon reconstruction efficiency and momentum resolution of the ATLAS experiment in proton-proton collisions at* $\sqrt{s}$ *= 7 TeV in 2010*, Eur. Phys. J. **C74** (2014) 3034, arXiv:1404.4562 [hep-ex].

[151] ATLAS Collaboration, *Measurement of the muon reconstruction performance of the ATLAS detector using 2011 and 2012 LHC proton–proton collision data*, Eur. Phys. J. **C74** (2014) 3130, arXiv:1407.3935 [hep-ex].

[152] ATLAS Collaboration, *Muon reconstruction performance of the ATLAS detector in proton–proton collision data at $\sqrt{s}$ =13 TeV*, Eur. Phys. J. **C76** (2016) 292, arXiv:1603.05598 [hep-ex].

[153] W. Lampl, S. Laplace, D. Lelas, P. Loch, H. Ma, S. Menke, S. Rajagopalan, D. Rousseau, S. Snyder, and G. Unal, *Calorimeter Clustering Algorithms: Description and Performance*, Tech. Rep. ATL-LARG-PUB-2008-002. ATL-COM-LARG-2008-003, CERN, Geneva, Apr, 2008. https://cds.cern.ch/record/1099735.

[154] M. Cacciari, G. P. Salam, and G. Soyez, *The Anti-k(t) jet clustering algorithm*, JHEP **04** (2008) 063, arXiv:0802.1189 [hep-ph].

[155] ATLAS Collaboration, *Jet energy scale measurements and their systematic uncertainties in proton-proton collisions at $\sqrt{s} = 13$ TeV with the ATLAS detector*, Phys. Rev. **D96** (2017) 072002, arXiv:1703.09665 [hep-ex].

[156] ATLAS Collaboration, *Performance of the ATLAS Detector using First Collision Data*, JHEP **09** (2010) 056, arXiv:1005.5254 [hep-ex].

[157] ATLAS Collaboration, *Performance of pile-up mitigation techniques for jets in pp collisions at $\sqrt{s} = 8$ TeV using the ATLAS detector*, Eur. Phys. J. **C76** (2016) 581, arXiv:1510.03823 [hep-ex].

[158] ATLAS Collaboration, *Jet energy measurement with the ATLAS detector in proton-proton collisions at $\sqrt{s} = 7$ TeV*, Eur. Phys. J. **C73** (2013) 2304, arXiv:1112.6426 [hep-ex].

[159] *Tagging and suppression of pileup jets with the ATLAS detector*, Tech. Rep. ATLAS-CONF-2014-018, CERN, Geneva, May, 2014. https://cds.cern.ch/record/1700870.

[160] ATLAS Collaboration, *Characterisation and mitigation of beam-induced backgrounds observed in the ATLAS detector during the 2011 proton-proton run*, JINST **8** (2013) P07004, arXiv:1303.0223 [hep-ex].

[161] *Selection of jets produced in 13TeV proton-proton collisions with the ATLAS detector*, Tech. Rep. ATLAS-CONF-2015-029, CERN, Geneva, Jul, 2015. https://cds.cern.ch/record/2037702.

[162] ATLAS Collaboration, *Data-driven determination of the energy scale and resolution of jets reconstructed in the ATLAS calorimeters using dijet and multijet*

events at $\sqrt{s} = 8\ TeV$, Tech. Rep. ATLAS-CONF-2015-017, CERN, Geneva, Apr, 2015. https://cds.cern.ch/record/2008678.

[163] *Jet Calibration and Systematic Uncertainties for Jets Reconstructed in the ATLAS Detector at* $\sqrt{s} = 13$ *TeV*, Tech. Rep. ATL-PHYS-PUB-2015-015, CERN, Geneva, Jul, 2015. https://cds.cern.ch/record/2037613.

[164] *Calibration of the performance of* b*-tagging for* c *and light-flavour jets in the 2012 ATLAS data*, Tech. Rep. ATLAS-CONF-2014-046, CERN, Geneva, Jul, 2014. http://cds.cern.ch/record/1741020.

[165] ATLAS Collaboration, *Performance of* b*-Jet Identification in the ATLAS Experiment*, JINST **11** (2016) P04008, arXiv:1512.01094 [hep-ex].

[166] ATLAS Collaboration Collaboration„ *Optimisation of the ATLAS* b*-tagging performance for the 2016 LHC Run*, Tech. Rep. ATL-PHYS-PUB-2016-012, CERN, Geneva, Jun, 2016. https://cds.cern.ch/record/2160731.

[167] ATLAS Collaboration, *Measurements of* b*-jet tagging efficiency with the ATLAS detector using* $t\bar{t}$ *events at* $\sqrt{s} = 13$ *TeV*, arXiv:1805.01845 [hep-ex].

[168] ATLAS Collaboration Collaboration„ *Calibration of light-flavour jet* b*-tagging rates on ATLAS proton-proton collision data at* $\sqrt{s} = 13$ *TeV*, Tech. Rep. ATLAS-CONF-2018-006, CERN, Geneva, Apr, 2018. http://cds.cern.ch/record/2314418.

[169] ATLAS Collaboration Collaboration„ *Measurement of* b*-tagging Efficiency of* c*-jets in* $t\bar{t}$ *Events Using a Likelihood Approach with the ATLAS Detector*, Tech. Rep. ATLAS-CONF-2018-001, CERN, Geneva, Mar, 2018. http://cds.cern.ch/record/2306649.

[170] ATLAS Collaboration, *Performance of Missing Transverse Momentum Reconstruction in Proton-Proton Collisions at 7 TeV with ATLAS*, Eur. Phys. J. **C72** (2012) 1844, arXiv:1108.5602 [hep-ex].

[171] *Performance of Missing Transverse Momentum Reconstruction in ATLAS studied in Proton-Proton Collisions recorded in 2012 at 8 TeV*, Tech. Rep. ATLAS-CONF-2013-082, CERN, Geneva, Aug, 2013. http://cds.cern.ch/record/1570993.

[172] *Performance of missing transverse momentum reconstruction for the ATLAS detector in the first proton-proton collisions at at* $\sqrt{s}$*= 13 TeV*, Tech. Rep.

ATL-PHYS-PUB-2015-027, CERN, Geneva, Jul, 2015. https://cds.cern.ch/record/2037904.

[173] *Expected performance of missing transverse momentum reconstruction for the ATLAS detector at* $\sqrt{s} = 13$ *TeV*, Tech. Rep. ATL-PHYS-PUB-2015-023, CERN, Geneva, Jul, 2015. https://cds.cern.ch/record/2037700.

[174] ATLAS Collaboration, *Alignment of the ATLAS Inner Detector and its Performance in 2012*, ATLAS-CONF-2014-047, 2014, https://cds.cern.ch/record/1741021.

[175] P. Brückman, A. Hicheur, and S. J. Haywood, *Global chi2 approach to the Alignment of the ATLAS Silicon Tracking Detectors*, Tech. Rep. ATL-INDET-PUB-2005-002. ATL-COM-INDET-2005-004. CERN-ATL-INDET-PUB-2005-002, CERN, Geneva, 2005. https://cds.cern.ch/record/835270.

[176] C. Escobar, C. García, and S. Marti i García, *Alignment of the ATLAS Silicon Tracker and measurement of the top quark mass.* PhD thesis, Universitat de Valencia, 2010. https://cds.cern.ch/record/1277903.

[177] M. Elsing, L. Goossens, A. Nairz, and G. Negri, *The ATLAS Tier-0: Overview and operational experience*, Journal of Physics: Conference Series **219** (2010) 072011, http://stacks.iop.org/1742-6596/219/i=7/a=072011.

[178] CherryPy, *CherryPy: A Minimalist Python Web Framework*, https://docs.cherrypy.org/en/latest/.

[179] PyROOT, *PyROOT | ROOT a data analysis framwork @ CERN*, https://root.cern.ch/pyroot.

[180] ATLAS Collaboration, *Performance of the ATLAS muon trigger in* pp *collisions at* $\sqrt{s} = 8$ *TeV*, Eur. Phys. J. C **75** (2015) 120, arXiv:1408.3179 [hep-ex].

[181] ATLAS Collaboration, *The ATLAS Simulation Infrastructure*, Eur. Phys. J. C **70** (2010) 823, arXiv:1005.4568 [hep-ex].

[182] GEANT4 Collaboration, S. Agostinelli et al., *GEANT4: A simulation toolkit*, Nucl. Instrum. Meth. **A506** (2003) 250.

[183] ATLAS Collaboration, *The simulation principle and performance of the ATLAS fast calorimeter simulation FastCaloSim*, http://cds.cern.ch/record/1300517.

[184] T. Sjostrand, S. Mrenna, and P. Skands, *A brief introduction to PYTHIA 8.1*, Comput. Phys. Commun. **178** (2008) 852–867, arXiv:0710.3820 [hep-ph].

[185] P. Nason, *A New method for combining NLO QCD with shower Monte Carlo algorithms*, JHEP **11** (2004) 040, arXiv:hep-ph/0409146 [hep-ph].

[186] S. Frixione, P. Nason, and C. Oleari, *Matching NLO QCD computations with Parton Shower simulations: the POWHEG method*, JHEP **11** (2007) 070, arXiv:0709.2092 [hep-ph].

[187] S. Alioli, P. Nason, C. Oleari, and E. Re, *A general framework for implementing NLO calculations in shower Monte Carlo programs: the POWHEG BOX*, JHEP **1006** (2010) 043, arXiv:1002.2581 [hep-ph].

[188] R. Frederix, E. Re, and P. Torrielli, *Single-top t-channel hadroproduction in the four-flavour scheme with POWHEG and aMC@NLO*, JHEP **1209** (2012) 130, arXiv:hep-ph/1207.5391.

[189] S. Frixione, P. Nason, and G. Ridolfi, *A positive-weight next-to-leading-order Monte Carlo for heavy flavour hadroproduction*, JHEP **09** (2007) 126, arXiv:0707.3088 [hep-ph].

[190] E. Re, *Single-top Wt-channel production matched with parton showers using the POWHEG method*, Eur. Phys. J. C **71** (2011) 1547, arXiv:1009.2450 [hep-ph].

[191] ATLAS Collaboration, *Comparison of Monte Carlo generator predictions to ATLAS measurements of top pair production at $\sqrt{s} = 7$ TeV*, Atlas-phys-pub-2015-002, https://cds.cern.ch/record/1981319.

[192] T. Sjostrand, S. Mrenna, and P. Skands, *PYTHIA 6.4 physics and manual*, JHEP **05** (2006) 026, arXiv:hep-ph/0603175.

[193] P. Z. Skands, *Tuning Monte Carlo Generators: The Perugia Tunes*, Phys. Rev. **D82** (2010) 074018, arXiv:1005.3457 [hep-ph].

[194] T. Gleisberg, S. Hoeche, F. Krauss, M. Schonherr, S. Schumann, et al., *Event generation with Sherpa 1.1*, JHEP **0902** (2009) 007, arXiv:0811.4622 [hep-ph].

[195] S. Hoeche, F. Krauss, S. Schumann, and F. Siegert, *QCD matrix elements and truncated showers*, JHEP **0905** (2009) 053, arXiv:hep-ph/0903.1219.

[196] J. Alwall, R. Frederix, S. Frixione, V. Hirschi, F. Maltoni, O. Mattelaer, H. S. Shao, T. Stelzer, P. Torrielli, and M. Zaro, *The automated computation of tree-level and next-to-leading order differential cross sections, and their matching to parton shower simulations*, JHEP **07** (2014) 79, arXiv:1405.0301 [hep-ph].

[197] G. Marchesini, B. R. Webber, G. Abbiendi, I. G. Knowles, M. H. Seymour, and L. Stanco, *HERWIG: A Monte Carlo event generator for simulating hadron emission reactions with interfering gluons. Version 5.1 - April 1991*, Comput. Phys. Commun. **67** (1992) 465–508.

[198] G. Corcella, I. G. Knowles, G. Marchesini, S. Moretti, K. Odagiri, P. Richardson, M. H. Seymour, and B. R. Webber, *HERWIG 6: An Event generator for hadron emission reactions with interfering gluons (including supersymmetric processes)*, JHEP **01** (2001) 010, arXiv:hep-ph/0011363 [hep-ph].

[199] J. M. Butterworth, J. R. Forshaw, and M. H. Seymour, *Multiparton interactions in photoproduction at HERA*, Z. Phys. **C72** (1996) 637–646, arXiv:hep-ph/9601371 [hep-ph].

[200] ATLAS Collaboration, *New ATLAS event generator tunes to 2010 data*, http://cds.cern.ch/record/1345343.

[201] S. Frixione and B. R. Webber, *Matching NLO QCD computations and parton shower simulations*, JHEP **06** (2002) 029, arXiv:hep-ph/0204244 [hep-ph].

[202] S. Frixione, P. Nason, and B. R. Webber, *Matching NLO QCD and parton showers in heavy flavor production*, JHEP **08** (2003) 007, arXiv:hep-ph/0305252 [hep-ph].

[203] S. Frixione, E. Laenen, P. Motylinski, and B. R. Webber, *Single-top production in MC@NLO*, JHEP **03** (2006) 092, arXiv:hep-ph/0512250 [hep-ph].

[204] S. Frixione, E. Laenen, P. Motylinski, B. R. Webber, and C. D. White, *Single-top hadroproduction in association with a W boson*, JHEP **0807** (2008) 029, arXiv:0805.3067 [hep-ph].

[205] ATLAS Collaboration, *Estimation of non-prompt and fake lepton backgrounds in final states with top quarks produced in proton–proton collisions at $\sqrt{s} = 8$ TeV with the ATLAS Detector*, ATLAS-CONF-2014-058, 2014, https://cds.cern.ch/record/1951336.

[206] ATLAS Collaboration, *Measurement of the b-tag Efficiency in a Sample of Jets Containing Muons with 5 fb− 1 of Data from the ATLAS Detector*, Tech. Rep. ATLAS-CONF-2012-043, CERN, Geneva, Mar, 2012. http://cds.cern.ch/record/1435197.

[207] *Calibration of b-tagging using dileptonic top pair events in a combinatorial likelihood approach with the ATLAS experiment*, Tech. Rep. ATLAS-CONF-2014-004, CERN, Geneva, Feb, 2014. http://cds.cern.ch/record/1664335.

[208] ATLAS Collaboration, *Comprehensive measurements of t-channel single top-quark production cross sections at $\sqrt{s} = 7$ TeV with the ATLAS detector*, Phys. Rev. **D90** (2014) 112006, arXiv:1406.7844 [hep-ex].

[209] ATLAS Collaboration, *Measurement of the t-channel single top-quark production cross section in pp collisions at $\sqrt{s} = 7$ TeV with the ATLAS detector*, Phys. Lett. **B717** (2012) 330, arXiv:1205.3130 [hep-ex].

[210] M. Cacciari et al., *Top-pair production at hadron colliders with next-to-next-to-leading logarithmic soft-gluon resummation*, Phys. Lett. **B710** (2012) 612, arXiv:1111.5869 [hep-ph].

[211] P. Bärnreuther, M. Czakon, and A. Mitov, *Percent Level Precision Physics at the Tevatron: First Genuine NNLO QCD Corrections to $q\bar{q} \to t\bar{t} + X$*, Phys. Rev. Lett. **109** (2012) 132001, arXiv:1204.5201 [hep-ph].

[212] M. Czakon and A. Mitov, *NNLO corrections to top-pair production at hadron colliders: the all-fermionic scattering channels*, JHEP **1212** (2012) 054, arXiv:1207.0236 [hep-ph].

[213] M. Czakon and A. Mitov, *NNLO corrections to top pair production at hadron colliders: the quark-gluon reaction*, JHEP **1301** (2013) 080, arXiv:1210.6832 [hep-ph].

[214] M. Botje et al., *The PDF4LHC Working Group Interim Recommendations*, arXiv:1101.0538 [hep-ph].

[215] A. D. Martin, W. J. Stirling, R. S. Thorne, and G. Watt, *Uncertainties on alpha(S) in global PDF analyses and implications for predicted hadronic cross sections*, Eur. Phys. J. **C64** (2009) 653–680, arXiv:0905.3531 [hep-ph].

[216] J. Gao, M. Guzzi, J. Huston, H.-L. Lai, Z. Li, P. Nadolsky, J. Pumplin, D. Stump, and C. P. Yuan, *CT10 next-to-next-to-leading order global analysis of QCD*, Phys. Rev. **D89** (2014) 033009, arXiv:1302.6246 [hep-ph].

[217] R. D. Ball et al., *Parton distributions with LHC data*, Nucl. Phys. **B867** (2013) 244–289, arXiv:1207.1303 [hep-ph].

[218] N. Kidonakis, *Next-to-next-to-leading-order collinear and soft gluon corrections for t-channel single top quark production*, Phys. Rev. **D83** (2011) 091503, arXiv:1103.2792 [hep-ph].

[219] N. Kidonakis, *Two-loop soft anomalous dimensions for single top quark associated production with a W- or H-*, Phys. Rev. **D82** (2010) 054018, arXiv:1005.4451 [hep-ph].

[220] R. Gavin, Y. Li, F. Petriello, and S. Quackenbush, *FEWZ 2.0: A code for hadronic Z production at next-to-next-to-leading order*, Comput. Phys. Commun. **182** (2011) 2388, arXiv:1011.3540 [hep-ph].

[221] R. Gavin, Y. Li, F. Petriello, and S. Quackenbush, *W physics at the LHC with FEWZ 2.1*, Comput. Phys. Commun. **184** (2013) 208, arXiv:1201.5896 [hep-ph].

[222] J. M. Campbell, R. K. Ellis, and C. Williams, *Vector boson pair production at the LHC*, JHEP **1107** (2011) 018, arXiv:1105.0020 [hep-ph].

[223] ATLAS Collaboration, *Measurement of the W production cross sections in association with jets with the ATLAS detector*, Eur. Phys. J. C **75** (2015) 82, arXiv:1409.8639 [hep-ex].

[224] F. Derue, *Estimation of fake lepton background for top analyses using the Matrix Method with the 2015 dataset at $\sqrt{s}$=13 TeV with AnalysisTop-2.3.41*, Tech. Rep. ATL-COM-PHYS-2016-198, CERN, Geneva, Feb, 2016. https://cds.cern.ch/record/2135116.

[225] G. D'Agostini, *A Multidimensional unfolding method based on Bayes' theorem*, Nucl. Instrum. Meth. **A362** (1995) 487–498.

[226] T. Adye, *Unfolding algorithms and tests using RooUnfold*, pp. , 313–318, CERN. CERN, Geneva, 2011. arXiv:1105.1160 [physics.data-an]. https://inspirehep.net/record/898599/files/arXiv:1105.1160.pdf.

[227] A. Armbruster, K. Kroeninger, B. Malaescu, and F. Spano, *Practical considerations for unfolding*, Tech. Rep. ATL-COM-PHYS-2014-277, CERN, Geneva, Apr, 2014. https://cds.cern.ch/record/1694351.

[228] ATLAS Collaboration, *Luminosity determination in pp collisions at $\sqrt{s}$ = 8 TeV using the ATLAS detector at the LHC*, Eur. Phys. J. **C76** (2016) 653, arXiv:1608.03953 [hep-ex].

[229] ATLAS Collaboration, *Jet energy measurement and its systematic uncertainty in proton–proton collisions at TeV with the ATLAS detector*, Eur. Phys. J. **C75** (2015) 3190, arXiv:1406.0076 [hep-ex].

[230] ATLAS Collaboration, *Jet energy resolution in proton–proton collisions at $\sqrt{s} = 7$ TeV recorded in 2010 with the ATLAS detector*, Eur. Phys. J. **C73** (2013) 2306, arXiv:1210.6210 [hep-ex].

[231] ATLAS Collaboration, *Search for invisible particles produced in association with single-top-quarks in proton–proton collisions at $\sqrt{s} = 8$ TeV with the ATLAS detector*, Eur. Phys. J. C **75** (2015) 79, arXiv:1410.5404 [hep-ex].

[232] CMS Collaboration, *Search for monotop signatures in proton–proton collisions at $\sqrt{s} = 8$ TeV*, Phys. Rev. Lett. **114** (2015) 101801, arXiv:1410.1149 [hep-ex].

[233] CMS Collaboration, *Search for dark matter in events with energetic, hadronically decaying top quarks and missing transverse momentum at $\sqrt{s} =$ 13 TeV*, arXiv:1801.08427 [hep-ex].

[234] CDF Collaboration, T. Aaltonen et al., *Search for a dark matter candidate produced in association with a single top quark in $p\bar{p}$ collisions at $\sqrt{s} = 1.96$ TeV*, Phys. Rev. Lett. **108** (2012) 201802, arXiv:1202.5653 [hep-ex].

[235] S. Catani, L. Cieri, G. Ferrera, D. de Florian, and M. Grazzini, *Vector boson production at hadron colliders: a fully exclusive QCD calculation at NNLO*, Phys. Rev. Lett. **103** (2009) 082001, arXiv:0903.2120 [hep-ph].

[236] D. J. Lange, *The EvtGen particle decay simulation package*, Nucl. Instrum. Meth. A **462** (2001) 152.

[237] ATLAS Collaboration, *Summary of ATLAS Pythia 8 tunes*, ATL-PHYS-PUB-2012-003, 2012, https://cds.cern.ch/record/1474107.

[238] A. Alloul, N. D. Christensen, C. Degrande, C. Duhr, and B. Fuks, *FeynRules 2.0 - A complete toolbox for tree-level phenomenology*, Comput. Phys. Commun. **185** (2014) 2250–2300, arXiv:1310.1921 [hep-ph].

[239] C. Degrande, C. Duhr, B. Fuks, D. Grellscheid, O. Mattelaer, and T. Reiter, *UFO - The Universal FeynRules Output*, Comput. Phys. Commun. **183** (2012) 1201–1214, arXiv:1108.2040 [hep-ph].

[240] ATLAS Collaboration, *ATLAS Pythia 8 tunes to 7 TeV data*, ATL-PHYS-PUB-2014-021, 2014, https://cds.cern.ch/record/1966419.

[241] S. Alioli, P. Nason, C. Oleari, and E. Re, *NLO single-top production matched with shower in POWHEG: s- and t-channel contributions*, JHEP **09** (2009) 111, arXiv:0907.4076 [hep-ph], [Erratum: JHEP02,011(2010)].

[242] T. Gleisberg and S. Höche, *Comix, a new matrix element generator*, JHEP **12** (2008) 039, arXiv:0808.3674 [hep-ph].

[243] F. Cascioli, P. Maierhofer, and S. Pozzorini, *Scattering Amplitudes with Open Loops*, Phys. Rev. Lett. **108** (2012) 111601, arXiv:1111.5206 [hep-ph].

[244] S. Schumann and F. Krauss, *A Parton shower algorithm based on Catani-Seymour dipole factorisation*, JHEP **03** (2008) 038, arXiv:0709.1027 [hep-ph].

[245] S. Höche, F. Krauss, M. Schönherr, and F. Siegert, *QCD matrix elements + parton showers: The NLO case*, JHEP **04** (2013) 027, arXiv:1207.5030 [hep-ph].

[246] ATLAS Collaboration, *Topological cell clustering in the ATLAS calorimeters and its performance in LHC Run 1*, Eur. Phys. J. C **77** (2017) 490, arXiv:1603.02934 [hep-ex].

[247] M. Cacciari, G. P. Salam, and G. Soyez, *FastJet User Manual*, Eur. Phys. J. C **72** (2012) 1896, arXiv:1111.6097 [hep-ph].

[248] ATLAS Collaboration, *Measurement of the Inclusive and Fiducial Cross-Section of Single Top-Quark t-Channel Events in pp Collisions at $\sqrt{s} = 8$ TeV*, ATLAS-CONF-2014-007, 2014, https://cds.cern.ch/record/1668960.

[249] J. Butterworth et al., *PDF4LHC recommendations for LHC Run II*, J. Phys. G **43** (2016) 023001, arXiv:1510.03865 [hep-ph].

[250] W. Verkerke and D. Kirkby, *The RooFit toolkit for data modeling*, 2003, arXiv:physics/0306116 [physics.data-an].

[251] G. Cowan, K. Cranmer, E. Gross, and O. Vitells, *Asymptotic formulae for likelihood-based tests of new physics*, Eur. Phys. J. **C71** (2011) 1554, arXiv:1007.1727 [physics.data-an], [Erratum: Eur. Phys. J.C73,2501(2013)].

[252] ATLAS Collaboration, *Measurements of top-quark pair differential cross-sections in the lepton+jets channel in pp collisions at $\sqrt{s} = 13$ TeV using the ATLAS detector*, JHEP **11** (2017) 191, arXiv:1708.00727 [hep-ex].

[253] ATLAS Collaboration, ATLAS Collaboration, *Measurements of $t\bar{t}$ differential cross-sections of highly boosted top quarks decaying to all-hadronic final states in pp collisions at $\sqrt{s} = 13$ TeV using the ATLAS detector*, arXiv:1801.02052 [hep-ex].

[254] ATLAS Collaboration, *Performance of jet substructure techniques for large-R jets in proton-proton collisions at $\sqrt{s}$ = 7 TeV using the ATLAS detector*, JHEP **09** (2013) 076, arXiv:1306.4945 [hep-ex].